ICAF
International Committee on Aeronautical Fatigue and Structural Integrity

Chinese Aeronautical Establishment

A REVIEW OF AERONAUTICAL FATIGUE AND STRUCTURAL INTEGRITY INVESTIGATIONS IN CHINA (2023-2025)

Edited by:

Dr. Sun Xiasheng

Chinese National Delegate

Chinese Aeronautical Establishment

CONTENTS

INTRODUCTION

This review is a summary of the aeronautical fatigue and structural integrity investigations carried out in the China the period June 2023 to May 2025. The review will be presented at the 39th conference of the International Committee on Aeronautical Fatigue and Structural Integrity （ICAF） in the Netherlands and published online on ICAF website.

The report contains summaries of the research, engineering and technology activities in the field of aeronautical fatigue and structural integrity that have occurred at Chinese aerospace industry and universities.

The contributions generously provided by following organizations:

- Shanghai Aircraft Design and Research Institute
- Aircraft Strength Research Institute
- Shenyang Aircraft Design & Research Institute
- Chengdu Aircraft Design & Research Institute
- The First Aircraft Design & Research Institute
- China Helicopter Research and Development Institute
- Chinese Aeronautical Establishment
- Shanghai Aircraft Manufacturing Co., Ltd
- General Huanan Aircraft Industry Co., Ltd
- Chengdu Aircraft Company
- XAC Commercial Co. Ltd
- SF Airline Company Limited
- Changcheng Institute of Metrology&Measurement
- Xi'an Civil Aircraft Industry Company Ltd
- Institute of Mechanics, Chinese Academy of Sciences
- Northwestern Polytechnical University
- Xi'an Jiaotong University
- Beihang University
- Shanghai Jiao Tong University
- Huazhong University of Science and Technology
- Beijing Institute of Technology
- Sichuan University
- Nanjing University of Aeronautics and Astronautics

The topics covered in this review include:

- Sustainable aviation
- Fatigue crack growth and life prediction methods
- Structural integrity of composite structures
- Reliability and risk-analysis of structures and mechanisms
- Fatigue life enhancement methods and repair solutions
- Life extension and management of ageing fleets
- Advanced materials and innovative structural concepts

- NDI inspections and structural load/health monitoring
- Full-scale fatigue testing
- Airworthiness considerations
- Digital Engineering in aeronautical fatigue and structural integrity

1 Sustainable Aviation

1.1 Evaluation technology and its applications on tire-generated water spray of civil aircraft[1]

The taxiing spray test of the aircraft on the water runway is one of the important subjects for the airworthiness certification of civil aircraft. Since 1919, 298 flight accidents have been reported to relate to wet runways or contaminated runways, with a cumulative death toll up to 650 people, which indicates the significance of the safety of aircraft taking off and landing on contaminated runways. In 2012, the full-scale aircraft water spray test was first launched in China, which was a challenging and complex problem at that time. After more than 10 years of exploring, we propose an integral numerical method with several key technologies to simulate the whole process of tire-generated water spray, which mainly involves a two-stage model setup and model verification based on effective experiment. The observations and findings from large number of whole-process simulations are very helpful for Chinese engineers with instructions on this subject, including the available design of detailed tire structures.

Key technology

An indoor full-scale aircraft tire vertical-dropping spray experimental platform is designed and constructed, which could not only accurately control the water depth and falling speed of water spray generation to realize the top priority of model verification in a wide speed range, but also stably observe and capture the differences of the generated spray related to the detail structures of tire. As shown in Figure 1 below, the objective of this study is to accurately characterize the shape and distribution details of water spray generated during civil aircraft taxiing on the water runway.

Figure 1: Spray of C909 aircraft taxiing on the water runway

Support C909 and C919 aircraft to pass the water spray airworthiness certification

Since June 2012, more than 100 flights have been carried out in following 5 years with a total of 17

[1] Northwestern Polytechnical University, Xu Fei, xufei@nwpu.edu.cn

types of tire chines being simulated and analyzed. Combined with the indoor test data, the tire configurations of C909 front wheel were carefully explored and finally determined. At the same time, the breakwater baffle design to suppress the spray for C909 main wheel was approachable. For the C919 aircraft, during its designing modification and verification stage in 2021, our key technologies provided a strong support for spray safety evaluation of several concerned positions, such as the places of the air conditioning, the air duct of fuel tank inserting system and the airframe skins step. The local skin was repaired in advanced based on our simulation results, which contributed to the successful one-time pass of all test points. The proposed evaluation technology on tire-generated water spray of civil aircraft significantly reduced the experimental cost, improved the competitiveness and may prospectively create values for customer. Comparisons between the simulation and test results of C909 and C919 aircraft taxiing spray are shown in the Figure 2. The spray shapes are highly consistent.

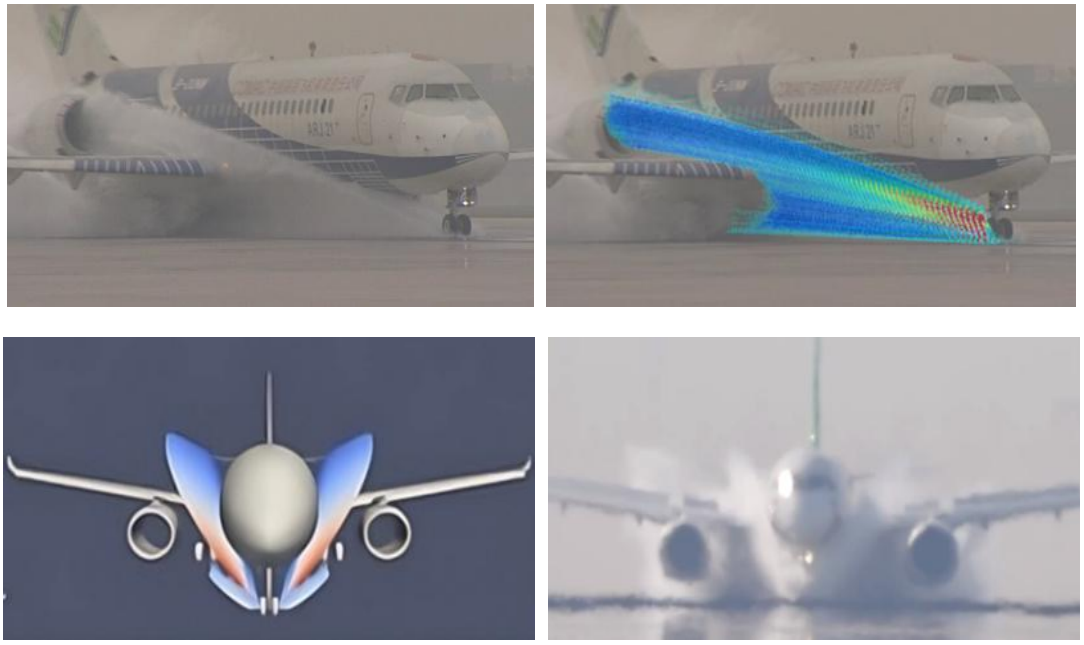

Figure 2: Spray of ARJ21(above) and C919(below) aircraft taxiing on the water runway

Support the spray suppression design in a wide speed range of aircraft taxiing

A spray simulation calculation software with intellectual property rights was developed, and the whole process of aircraft tire-generated water spray calculation was realized for the first time, which filled the gap and may bring new future for more applications. The mechanism of detailed tire structure to suppress spray can be revealed, and the reason of chine failure caused by high-speed taxiing can be observed. New design such as the chine-tire configuration with multi-water bars can be proposed.

1.2 Reshapable, repairable and recyclable (3r) vitrimer composites[2]

The ability to reshape and repair these composites under moderate heat or chemical conditions significantly extends their service life, contributing to a circular economy. In addition, 3R vitrimer composites are fully recyclable, an attribute that aligns with the growing demand for sustainable manufacturing. The dynamic covalent bonds in vitrimers can be broken and reformed, enabling the recovery and reuse of both the polymer matrix and the reinforcing components. This recyclability

[2] Xi'an Jiaotong University , Chen Zhiqiang, zq.chen@xjtu.edu.cn

reduces the environmental footprint of composite materials, which are widely used in industries such as aerospace, automotive, and construction. Moreover, the chemical tunability of vitrimer systems allows for the optimization of material properties, such as stiffness, toughness, and thermal resistance, to meet specific application requirements. By combining functionality with sustainability, 3R vitrimer composites pave the way for innovative designs in materials engineering, fostering progress toward a greener future.

Reshapability of vitrimer composites

The reshaping process of vitrimer composites is driven by the activation of their dynamic covalent bonds, which become labile at elevated temperatures. This thermal activation triggers bond exchange reactions, enabling the material to relax internal stresses and flow without compromising the overall crosslink density. This property is particularly advantageous for the reprocessing of vitrimer composites, as it allows for the efficient reshaping of materials into new forms while retaining their mechanical and functional properties Figure 3. Furthermore, the activation temperature can be fine-tuned by adjusting the chemical composition, offering control over the reshaping conditions to suit specific industrial requirements.

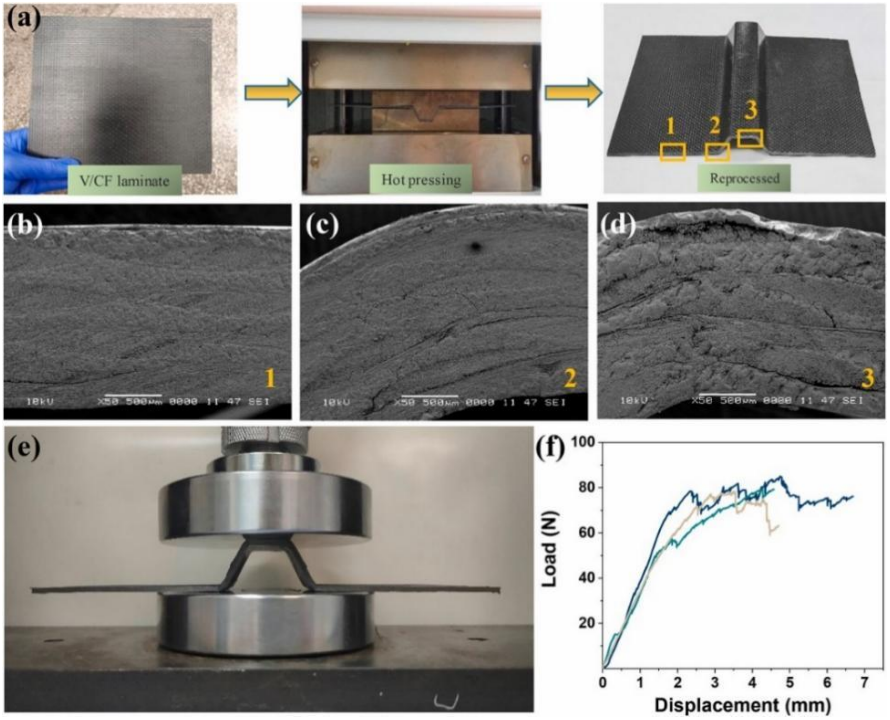

Figure 3: (a) Thermoforming process diagram for complex structural components. The cross-sectional microstructures of (b) plane area 1, (c) hot deformation position 2, and (d) hot deformation zone 3. (e) Compression testing and (f) corresponding load-displacement curves of thermoformed sample.

Recyclability of vitrimer composites

The recycling process for vitrimer composites involves triggering bond exchange reactions by applying heat, catalysts, or solvents. Figure 4 shows the flow chart of preparation and recycling of 3D multiaxial braided vitrimer composite (3DMBC). The depolymerization of the vitrimer network enables the recovery of raw materials or reshaped components. For instance, in fiber-reinforced vitrimer composites, the matrix can be selectively degraded, allowing for the extraction and reuse of high-value

reinforcing fibers, such as carbon or glass fibers. This closed-loop recycling capability not only reduces material waste but also lowers the environmental footprint associated with composite production and disposal. Researchers are continually optimizing recycling protocols to minimize energy input and ensure the scalability of these processes for industrial applications.

The adoption of vitrimer composites in industries such as automotive, aerospace, and construction presents an opportunity to shift towards a circular economy, where materials are continuously reused rather than discarded. By combining superior mechanical properties with efficient recyclability, vitrimer composites align with the growing demand for sustainable materials in high-performance applications. Ongoing research and development aim to optimize the properties of vitrimer composites, making them even more compatible with large-scale recycling technologies. As a result, vitrimer composites have the potential to significantly reduce environmental pollution and resource depletion, contributing to a more sustainable and environmentally conscious future.

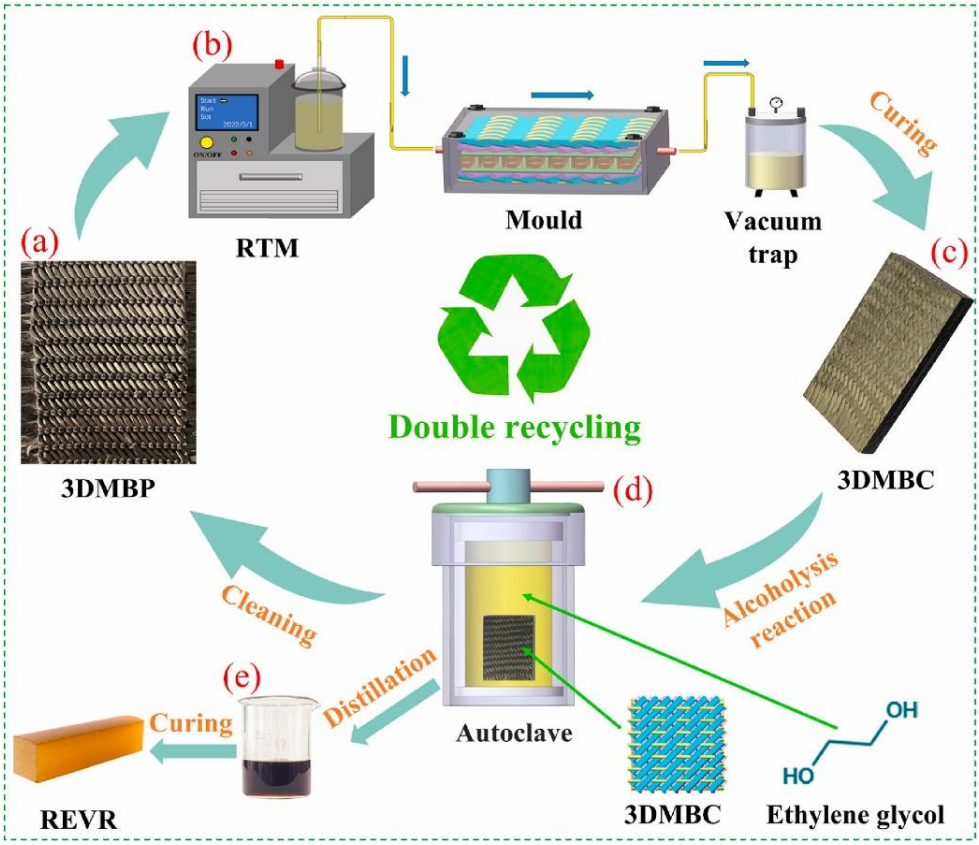

Figure 4: Flow chart of preparation and recycling of 3D multiaxial braided vitrimer composite (3DMBC).

Challenges and prospects

Developing reshapable, repairable, and recyclable (3R) vitrimer composites presents several challenges and opportunities for future advancements. One major hurdle is achieving a balance between mechanical performance and dynamic reconfigurability; high-performance composites often rely on rigid networks that can limit their reshaping and recycling potential. Additionally, the scalability of 3R vitrimer composites remains an obstacle due to the complexity of synthesis and processing methods, which can hinder their large-scale industrial application. Environmental concerns, such as minimizing the use of hazardous chemicals and ensuring full recyclability, also demand innovative solutions.

Future directions include optimizing catalyst systems and dynamic covalent chemistry to improve reprocessing efficiency and recyclability without compromising material properties. Moreover, integrating sustainable raw materials and adopting energy-efficient processing techniques are crucial for aligning with global sustainability goals. Advances in these areas could unlock broader applications for 3R vitrimer composites in industries ranging from aerospace to consumer goods.

1.3 Study on the application of thermoplastic composites[3]

The composites can be classified into thermosetting and thermoplastic composites according to the type of resin. At present, thermosetting composites are widely used in domestic and foreign aircraft. However, the manufacturing of thermosetting composites is usually carried out by hot-pressing pot molding process, which has high manufacturing cost and long molding cycle, and often meets the damage problem caused by impact in the process of manufacture and use. In contrast, thermoplastic composites have a short molding cycle and high production efficiency. In addition, they possess good toughness, damage tolerance, impact resistance, and crack propagation resistance. On the other hand, they are low cost, and do not require low-temperature storage. The waste can be recycled, with reshaping and recyclability, which improves the repairability of parts and reduces the scrap rate. Therefore, thermoplastic composites are an important choice for the application of aircraft structural materials in the future, which can effectively realize energy saving and emission reduction.

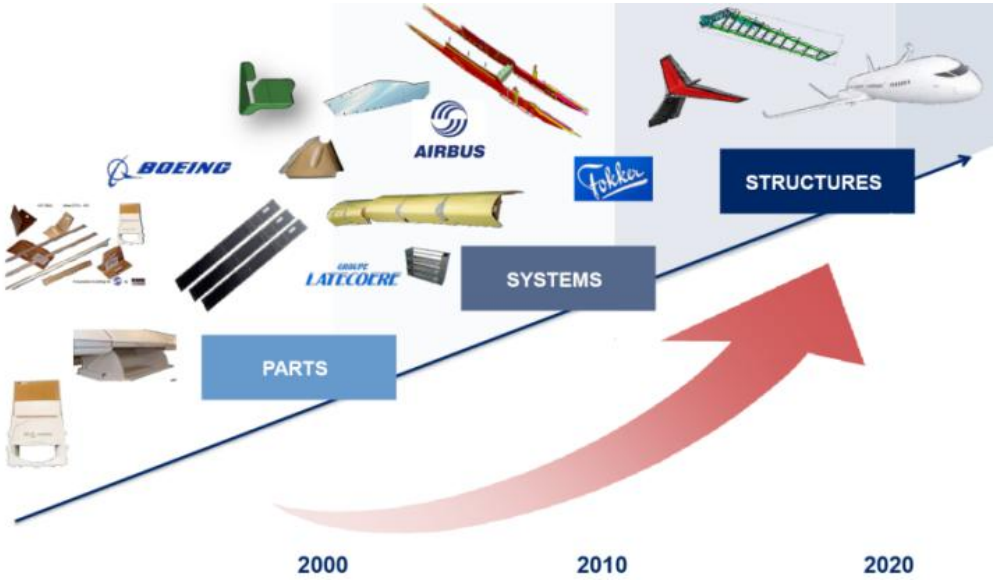

Figure 5: Application of thermoplastic composites

There are two main reasons for restricting the application of thermoplastic composites in aircraft: (1) the molding time of the parts is short, but it needs high temperature and high pressure, so the requirement of equipment and excipients is high; (2) the design maturity is low, and its advantages cannot be fully utilized. Consequently, breaking through the structural design and strength analysis technology, as well as manufacturing technology of thermoplastic composite, is the key to realizing their application.

Manufacturing Technology for the Leading-Edge of Thermoplastic Composites

[3] The First Aircraft Institute Design & Research, Zhang Lei, zhangl025@avic.com

The manufacturing process scheme of the leading-edge structure is shown in Figure 6 In the manufacturing process of the leading-edge, the molding of the skin, long truss/partition, and the welding of the skin and partition are the manufacturing difficulties.

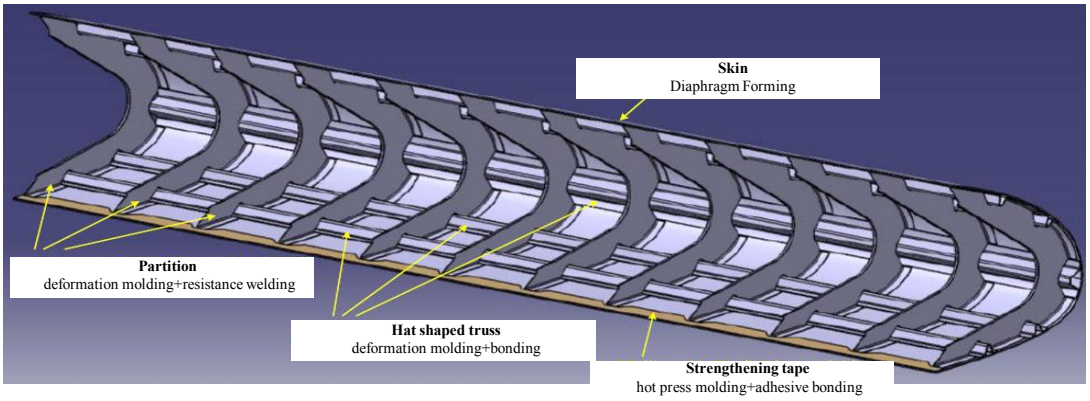

Figure 6: Manufacturing process scheme

The skin is molded by diaphragm process. The large plastic deformation constraint occurs when two layers of diaphragm with high stiffness and high elongation are attached to the surface, which leads to the interlayer slip of the softened prepreg laminates, thus the deformation molding can be realized.

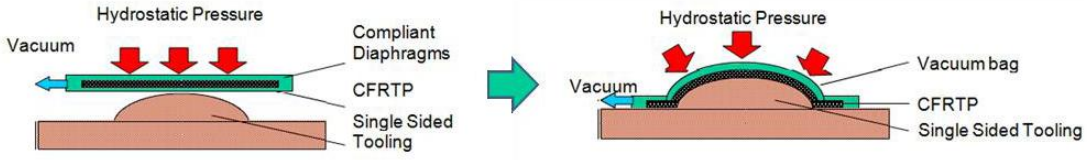

Figure 7: Diaphragm molding

The long truss/partition is molded by hot-pressing. Firstly, prepare the prepreg laminates and heat them up to the molding temperature through an infrared heating furnace. At this point, the resin matrix returns to a viscous flow state, and then they are sent to a low-temperature curved mold for secondary molding and rapid cooling to obtain the final product (see Figure 8).

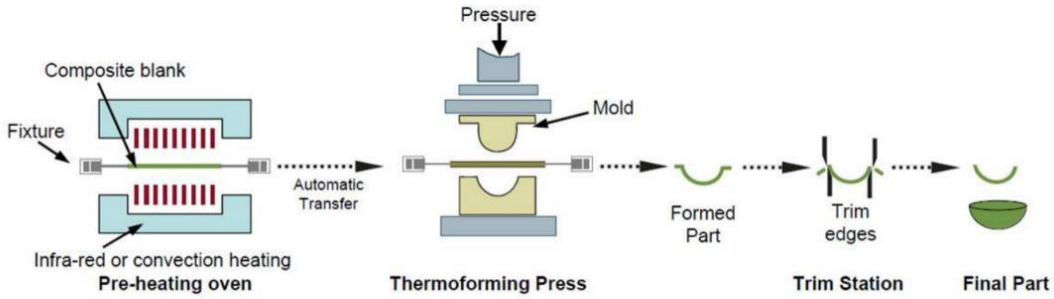

Figure 8: Hot-pressing molding

Verification of the leading-edge of thermoplastic composites

The strength analysis and verification of the leading-edge: For the leading-edge structures, static strength and anti-bird collision are mainly considered. The design of static strength is based on the fact that the skin allows instability after the limited load and does not damage under the ultimate load. The design of anti-bird collision is conducted according to the regulations of CCAR25 (the aircraft must

withstand the impact of a 4-pound bird body without affecting its safe return). Both of them need to be verified by test. The implementation of the test is shown in Figure 9. The test results meet the design requirements of the strength.

Figure 9: Verification of static strength and anti-bird collision tests

1.4 Ice protection system development for composite aircraft[4]

AI/DI is conventionally achieved by bleeding hot air from the engine compressor stages where it is ducted along piping to the inside of the leading edges and the heat transferred to the outside surface by thermal conduction. The spent bleed air is subsequently exhausted through small holes in the wing. This adds weight and maintenance requirements, and is energy inefficient. Such as system is even less efficient for composite wings which are less thermally conductive than metal. Electro-thermal (i.e. resistance heater) systems that are applied to or within the surfaces are an attractive alternative. They can deliver higher energy efficiencies, low maintenance requirements and the absence of bleed exhaust holes, airplane drag and noise are improved.

Electro-thermal heating element development

Various materials have been investigated as the heating element, including carbon nanotubes (CNTs), graphene, carbon fibre (CF), sprayable metal layer, electro-conductive textile, etc. Among the materials, carbon-based electro-thermal heating elements for AI/DI are attractive alternatives to metals as they are compatible with the FRP composites and potentially contribute to the structural properties of the material. CNTs have generated a great deal of interest over recent decades owing to their high thermal and electrical conductivities and extraordinary specific strength and stiffness. Although individually conductive, macroscale assemblies of relatively short CNTs have multiple resistive contacts and thus are a promising material for AI/DI. CNTs grown by chemical vapor deposition (CVD) could be processed into films and integrated into the FRP composites to fabricate the laminate with AI/DI functions via autoclave, as shown in Figure 10, with the glass fibre (GF) layer working as the insulator.

[4] Northwestern Polytechnical University, Yao Xudan, x.yao@nwpu.edu.cn

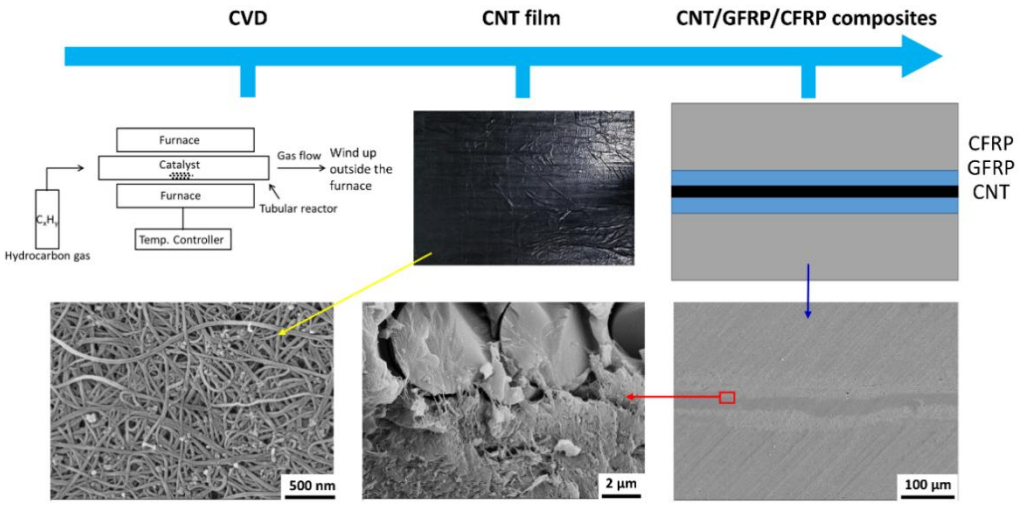

Figure 10: Preparation and morphology of the CNT and CNT/GFRP/CFRP composites.

Thermal fatigue of the composites with AI/DI functions

Due to the difference of thermal expansion between different components, i.e., CNT, GFRP, CFRP, the internal stress between interfaces under the cyclic AI/DI serving environments (Figure 3a, b) will be ignited, and then affect the strength of composite structures. This work will be based on the attenuation of interlaminar shear strength of composite laminates with the service conditions, to study the effect of thermal cycling on interfacial properties of CNT/GFRP/CFRP composites, prior to the airworthiness considerations.

To promote the dominance of interlaminar shear stresses in the composites, and study the interlaminar behaviour of the CNT/GFRP/CFRP, double beam shear tests were applied to composite specimens after different thermal cycles. Thermal cycling of the specimens between -55 ℃ and +80 ℃ led to reductions of the interlaminar shear strength (ILSS) values as a result of the thermal mismatch. To evaluate the strength degradation of the CNT/GFRP/CFRP composites due to thermal fatigue, Bulmanis et al model is used to fit the experimental results, as shown in Figure 11c, d. After the non-linear analysis, parameters were obtained for the Bulmanis et al model, with the R^2 of 0.97, which indicates the model fits the experimental data quite well. Therefore, the model can be used to predict the strength degradation of the composites during thermal fatigue.

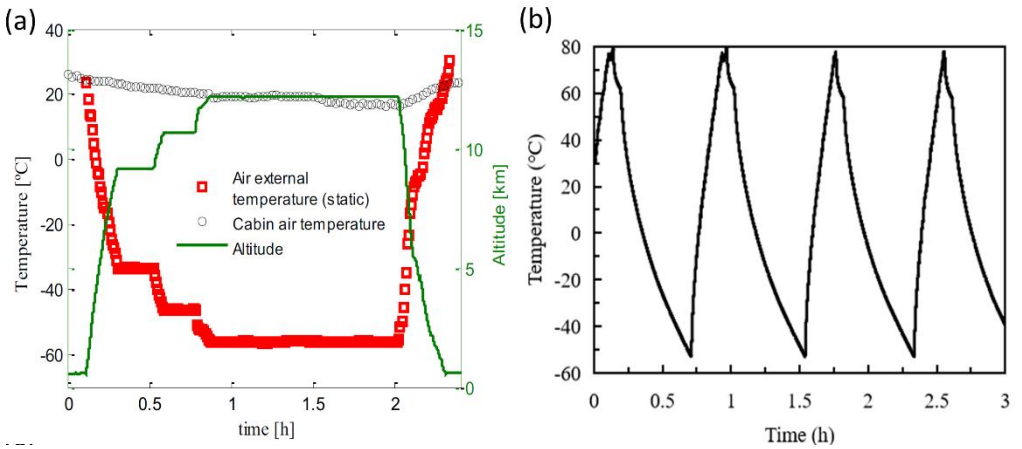

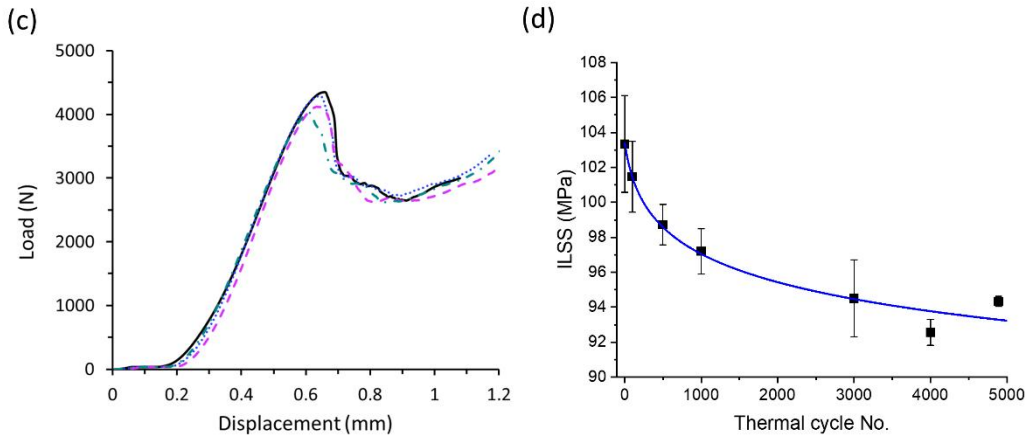

Figure 11: (a) Temperature profile during the flight. (b) Thermal cycles for the composites. (c) Load-displacement curves of the double beam shear tests. (d) Interlaminar shear strength (ILSS) of CNT/GFRP/CFRP composite specimens after different thermal cycles.

1.5 Efficient icephobic coating based on hyperbranched crosslinking[5]

Despite tremendous advancements in icephobic coating technology, icephobic efficacy frequently declines or completely disappears in the actual icing environment (low temperatures, high humidity, and dynamic environments) of aircraft. Here, a hyperbranched vanillin-based composite coating with efficient icephobic properties (HVIC) is prepared by combining vanillin-based phosphazene compounds with oil-stored SiO_2 through imine bonds-HVIC exhibits excellent hydrophobicity, with a water sliding angle of 9°. This coating's exceptional slippery performance imparts outstanding non-adhesive, and deicing properties (τ_{ice}: 8.2 kPa). It is noteworthy that HVIC performs exceptional anti-icing and anti-frosting in low-temperature and high humidity environments. Compared with superhydrophobic coatings (SHC), the icing delay time of HVIC is 9.1 times that of SHC, and the frosting time is extended by roughly 300%. Most importantly, the HVIC-treated propeller experienced two ice-shedding events during the 200s dynamic icing test, while SHC completely lost its icephobic performance. T Compared to the SHC-treated and uncoated cases, this results in a considerable reduction in power usage, requiring just 1/3 and 1/4 of the power, respectively. This study breaks through the bottleneck of anti-/de-icing of aircraft in actual service environment.

Design principle

The presence of silicone oil on the coating's surface results in exceptional hydrophobicity and a low water sliding angle. As a result, HVIC exhibits outstanding hydrophobicity, anti-adhesion, and self-cleaning qualities. Furthermore, the coating containing silicone oil has a smooth surface, resulting in a freezing behavior known as homogeneous nucleation. This characteristic enables it to demonstrate exceptional anti-icing capabilities in conditions with low temperatures and high humidity. HVIC's low sliding angle and smooth features are specifically engineered to effectively overcome the failure issues of SHS in low temperatures, high humidity, or dynamic conditions. More significantly, the unstable performance of conventional icephobic coatings was overcome by covalently bonding inorganic nanoparticles with organic compounds to form a hyperbranched crosslinking network, which led to excellent dynamic icephobic ability of HVIC in propeller icing experiments and continuous ice shedding phenomenon. The preparation diagram of the coating is shown in Figure 12.

[5] Shanghai Jiao Tong University, Liu Hong, hongliu@sjtu.edu.cn

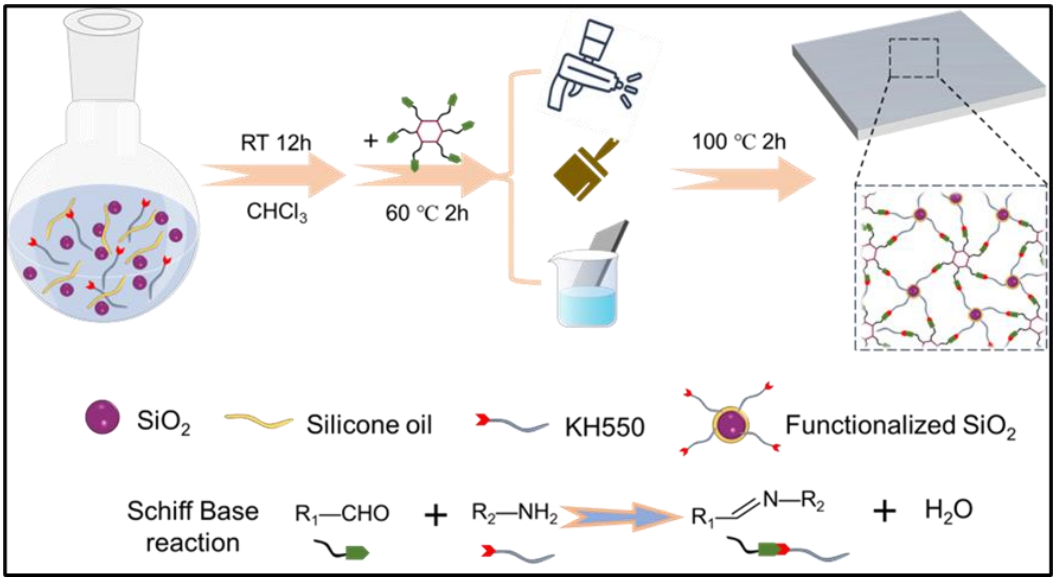

Figure 12: Design and preparation of the icephobic coating

Icephobic performance

With V = 10 m/s, T = -6 °C, and liquid water content (LWC) = 2.0 g/m^3 for the experiment, the three samples were carried out under a typical glaze icing situation in order to comprehend the dynamic icing process and the random ice-shedding phenomenon during the propeller icing. The dynamic ice accumulation over the propeller during the 200 s icing period is seen in Figure 13 As illustrated in Figure 13, it was discovered that the HVIC-treated blade and the SHC-treated one exhibited a comparable ice accretion process during the first 100s of icing, during which the ice quickly deformed the intended geometry and surface roughness. But when the first instance of iceshedding happens at one side of the propeller at 125s, the dynamic icing process is altered. This brief decrease in motor load shows that less force is needed by the propeller coated with an icephobic coating to overcome ice adhesion, allowing the UAV to operate with less impact from ice accumulation. A second ice shedding at 175 s causes even less ice accumulation on the blades after the initial ice shedding at 125 s removed the ice from the propeller.

A symptom of the periodic ice-shedding phenomena, in which all ice structures are shed from the leading-edge (LE) region, which shows the occurrence of the second ice shedding. When compared to the uncoated propeller and SHC-treated cases, the HVIC-treated propeller performs noticeably better, especially when an active warming technique is not being used on the substrate. These ice-shedding processes improve the working conditions at the UAV's designed site, momentarily lowering the loads on the device and increasing its operational viability. The application of the HVIC-coated blade produced a distinct pattern, with two occurrences of ice shedding at 125 and 175 s. This resulted in the drone using less power even though it was still operating in a chilly and humid environment.

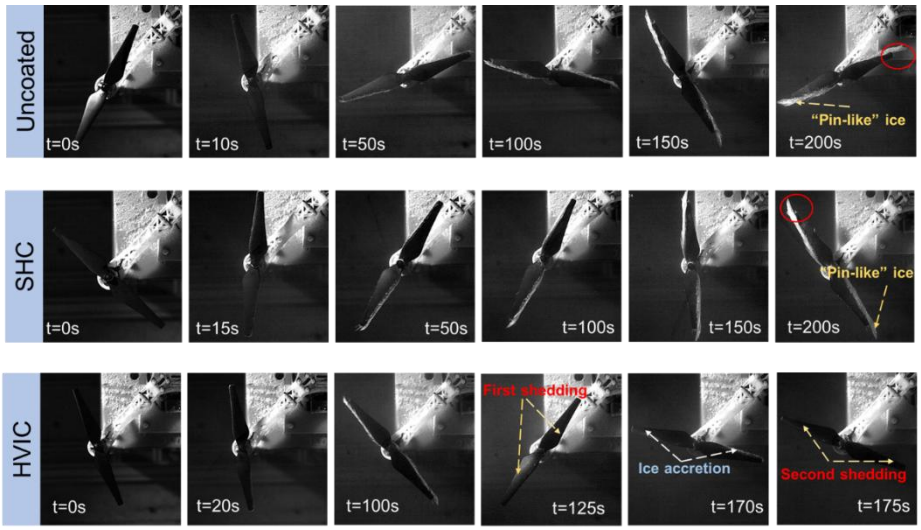

Figure 13: Dynamic icephobic performance. Time-sequenced images of the icing process of Uncoated propeller, SHC, and HVIC, n ≈ 4000 rpm, V = 10 m/s, T = -6 °C, and LWC= 2.0 g/m^3

2 Fatigue Crack Growth and Life Prediction Methods

2.1 Quasi-in situ observation of the microstructural response during fatigue crack growth of friction stir welded aa2024-t4 joint[6]

The reliability of friction stir welded joints is a critical concern, particularly given their potential applications in the aerospace manufacturing industry. This study offers a quasi-in situ observation of the microstructural response during fatigue crack growth (FCG) of a friction stir welded AA2024-T4 joint, aiming to correlate fatigue crack growth behavior with mechanical properties investigated using electron backscatter diffraction (EBSD). Crack propagation occurs within the stir zone, traversing refined grains, which primarily contribute to the highest fatigue life and lowest FCG rate. Additionally, cracks initiate in AS and RS, subsequently expanding into the base metal. Moreover, the study reveals a significant release of residual strain at the joint, particularly notable in the Structural-CT-RS (Str-CT-RS) sample compared to the Str-CT-AS sample during the FCG process. Consequently, the FCG rate of Str-CT-AS is higher than that of Str-CT-RS. These findings have significant implications for improving the reliability and performance of aerospace components.

FCG Behavior at Different Regions

The FCG behavior at different regions, namely the BM, SZ, AS, and RS, can be influenced by microstructural variations, local stress concentrations, or specific welding conditions characteristic of each zone. This study focuses on correlating FCG behavior and mechanical properties with a quasi-in situ observation of microstructural responses. Figure 14 illustrates the measured crack lengths plotted against the counted cycles for various cases. The results indicate that the base metal (CT-BM) exhibits a shorter fatigue life (i.e., lower fatigue cycles, ~10 5 cycles) compared to the welding zones (SZ ~ 3.5 × 10^5 cycles, AS ~ 2.5 × 10^5 cycles, and RS ~ 3.0 × 10^5 cycles), suggesting greater resistance to crack propagation in the welding zones. Among the SZ, AS, and RS, SZ (i.e., Str-CT-SZ) demonstrates the highest fatigue load cycle. Furthermore, it is observed that the SZ, AS, and RS exhibit similar FCG

[6] Aircraft Strength Research Institute, Yang Jun, yangj175@avic.com

behavior compared to the BM. The smooth and continuous crack growth curve for CT-BM suggests stable crack propagation behavior. In contrast, the curves for Str-CT-SZ, Str-CT-AS, and Str-CT-RS display noticeable stages, which will be discussed and characterized using the Paris model in the subsequent analysis.

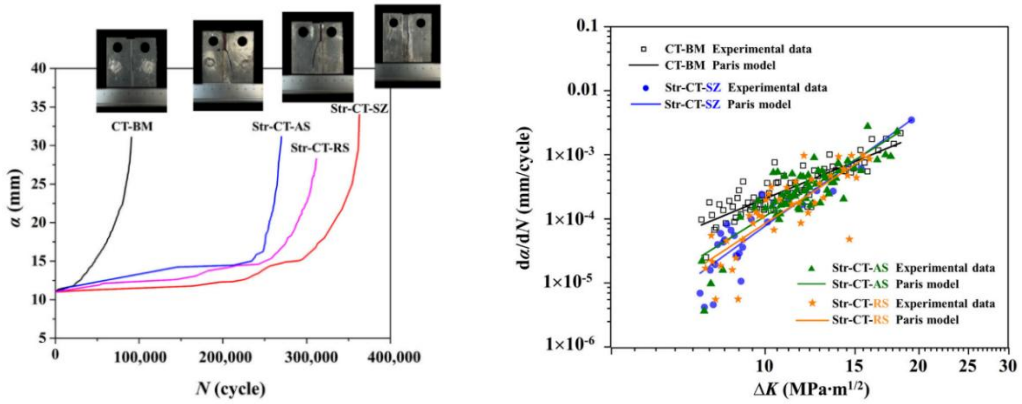

(a) (b)

Figure 14: (a) The relationship of fatigue crack length a and cycle index N;(b) FCG rate curves described by experimental data and Paris model.

Microstructural Response of the Joint during the FCG Process at the AS and RS

The microstructure along the crack path in the AS and the RS exhibit similar features. However, it is noteworthy that the FCG rate of the Str-CT-AS sample is slightly higher than that of Str-CT RS. This suggests that residual strain can also influence the FCG rate, in addition to microstructural factors such as grain size and distribution. Figure 15 presents the kernel average misorientation (KAM) maps illustrating the residual strain of the FSW AA2024 joint. The results reveal that residual strain is predominantly concentrated in the AS (as shown in Figure 15 d) and RS (as shown in Figure 15c) compared to the SZ (as shown in Figure 15b). To further distinguish the FCG rate of the AS and RS, stop-action during the FCG test was employed to capture the microstructural response during the during the FCG process when the crack extended to two-thirds of its final length.

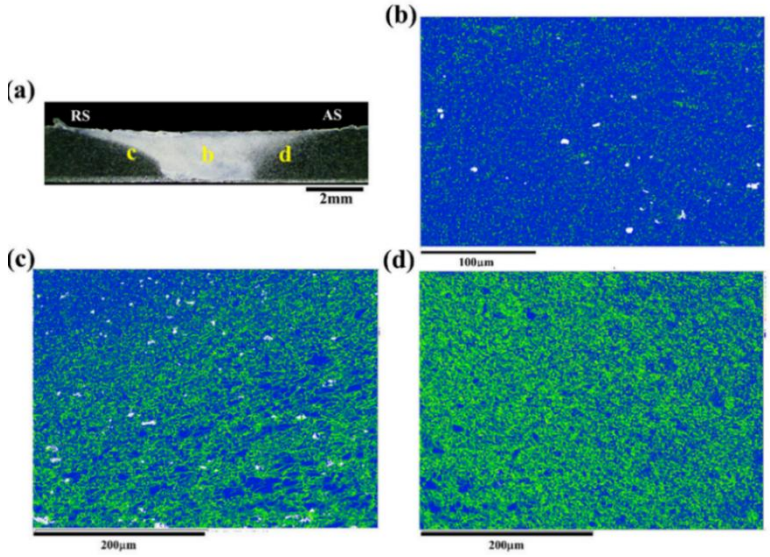

Figure 15: The KAM maps showing the residual strain of the FSW AA2024 joint: (a) the morphology, (b) the KAM map of the SZ, (c) the KAM map of the RS, and (d) the KAM map of the AS.

The study focused on the quasi-in situ observation of the microstructural response during fatigue crack growth of friction stir welded AA2024-T4 joints to correlate FCG behavior with mechanical properties. Notched CT specimens corresponding to the SZ, AS, and RS were designed. FCG performances at different regions were obtained and characterized using the Paris model. EBSD was employed to examine the microstructure along the fatigue crack propagation path. The microstructural response of the joint during crack propagation at the AS and RS was compared to analyze differences in crack growth behavior between these regions.

2.2 Fatigue behavior and life by phase-field modeling[7]

Phase-field model (PFM) has become a popular tool to simulate fatigue fracture phenomena in aeronautical structures, which can describe crack evolution by an order parameter without explicit crack tracking and extra crack criterion. To tackle the crucial problem of computational time when simulating repetitive loading in high-cycle fatigue (HCF), envelope loading, cycle jump techniques, temporal homogenization method, and staggered solution strategies are applied into HCF and FCG calculations. A macroscopic phase-field framework for fatigue fracture is proposed, where fatigue damage under cyclic loading is introduced to the PFM by classic fatigue theory. PFM that covers both fatigue crack initiation (FCI) and growth shows promising advantages in predicting fatigue of aeronautical structures.

Classical fatigue theory informed phase-field fatigue fracture model

PFM for fatigue has recently attracted intensive efforts, but its extension to HCF with efficient computation still remains a challenge. We propose a PFM for predicting HCF life and FCG by leveraging the power of classical fatigue theory that integrates local stress-strain approach and cumulative fatigue damage theory. Six PFMs including three classical fatigue-life formulae (strain-, stress-, and energy-based approaches) and two equivalent-stress criteria (Neuber's and Glinka's rules) are presented. Therein the phase-field damage variable governing the fracture energy degradation is cumulatively calculated from a local lifetime as loading cycles increase. To bypass the direct-cyclic calculation that is computationally expensive, envelope loading and cycle jump techniques are utilized to efficiently calculate HCF life. Our PFM realizes the prediction of FCG behavior by using S-N data as input and is promising for HCF and FCG issues in aeronautical engineering problems.

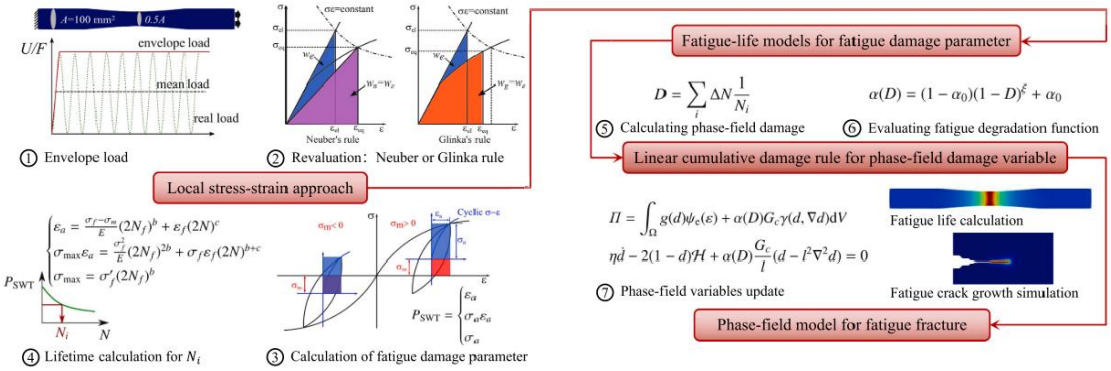

Figure 16: Illustration of the classical fatigue theory informed PFMs for calculating HCF life and FCG.

Phase-field modeling for predicting three-dimensional fatigue crack initiation and growth under

[7] Nanjing University of Aeronautics and Astronautics, Yi Min, yimin@nuaa.edu.cn

laser shock peening induced residual stress

Laser shock peening (LSP) has emerged as a promising technique for retarding fatigue cracks and improving fatigue performance. To numerically investigate fatigue fracture behavior in LSPed metals, a three-dimensional (3D) phase-field model incorporating LSP-induced residual stress is utilized, with the model parameters readily determined by experiments. In a typical LSPed titanium alloy TC4, 3D high-cycle fatigue crack initiation (FCI) and growth (FCG) behaviors in fatigue specimens are predicted by phase-field simulation, showing good agreement with experimental results. Predictions for fatigue life fall within the ±2 times error band. This phase-field modeling framework provides an insightful and efficient approach for predicting fatigue performance of LSPed metals in aeronautical engineering.

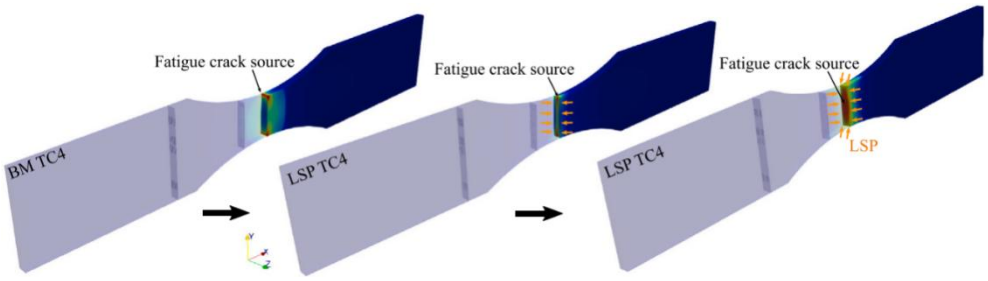

Figure 17: Transfer of the fatigue source after LSP in phase-field simulation.

Macroscopically modeling fatigue life of additively manufactured metals: Pore-defect informed phase-field model

Fatigue crack growth (FCG) behavior and fatigue life of additively manufactured (AM) materials are highly sensitive to AM-induced pore defects, thus challenging the traditional fatigue models. A model customized for predicting fatigue/fracture behavior of AM materials is indispensable. Here we propose a pore-defect informed phase-field model (PFM) for the macroscopic modeling of fatigue crack initiation (FCI), FCG, and fatigue life of AM metals. The macroscopic PFM integrates pore-defect fatigue (PDF) model of AM metals, local stress–strain approach and cumulative fatigue damage theory. The PDF model correlates AM pore features (i.e., size, location, and morphology) with fatigue life and its parameters can be readily determined by fatigue test of standard specimens of AM metals. Our PFM is confirmed to be capable of predicting both S(E)-N curves and Paris' law of AM metallic (nickel base superalloy Hastelloy X, titanium alloy TC4 and TC17) specimens over low- and high-cycle fatigue regimes, and the predictions are found to agree well with experiments. For a simulated compressor blade fabricated by laser AM, our three-dimensional PFM simulations of FCI and FCG behaviors could correctly predict the critical crack length and fatigue limit, which accord with experimental results obtained by X-ray computer tomography and vibration fatigue test. The pore-defect informed PFM framework here could provide a practicable toolkit for the rapid evaluation of fatigue life of AM components, as well as for the computational prediction and design of fatigue-resistant AM components.

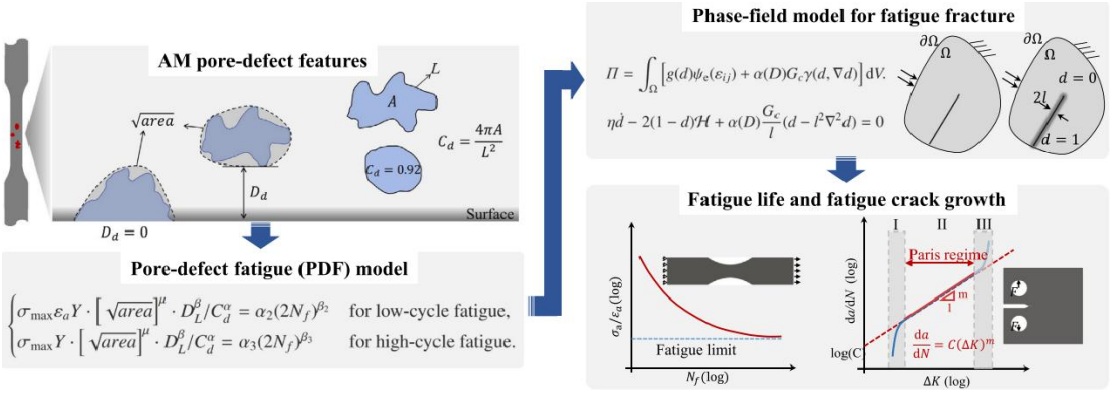

Figure 18: Pore-defect informed PFM including definitions of the various AM pore-defect features and the parameters of defect, pore-defect fatigue (PDF) model, and phase-field fatigue fracture model.

2.3 Numerical analysis of crack propagation in an aluminum alloy under random load spectra[8]

In the proposed damage program for enhanced load spectrum analysis presented in this study, the model for crack propagation under a constant amplitude load spectrum employs the Paris model and Willenborg–Chang model, the crack propagation model is a constant amplitude load spectrum, which can be considered a specific case in the random load spectrum. The weighted load spectrum is scaled up by α factor of equal proportions and then processed by the rainflow method to obtain the weighted load spectrum. Stress intensity factors are obtained through finite element simulations and analyses of the structural components. By the K_c fracture toughness criterion for determining whether the crack continues to expand, if the crack propagates further, proceed to the next iteration; otherwise, terminate the process and output the results. Determine whether the crack cycle undergoes hysteresis according to if hysteresis is calculated by substituting into the crack hysteresis model; if not, substitute into the Paris grain extension model to calculate the crack extension length increment a calculation, until the cycle is terminated. Output the results. Based on the above load spectrum enhancement method, the crack propagation program for random load spectrum enhancement is compiled.

Creating calculation model

This study employs finite element modeling to analyze two different sizes of wall plate structures. The finite element model is depicted in Figure 19(a).Loading Original Spectrum and Enhanced Spectrum: Based on the fracture test of large and small wall plate the stress intensity calculation, critical crack and crack extension analyses under constant amplitude spectrum and random spectrum are carried out, the load spectrum used in the simulation analysis is the experimental spectrum, and the weighting coefficients are selected by following the guideline of consistency of the main damage site and damage mode.

[8] Nanjing University of Aeronautics and Astronautics, Tong Mingbo, tongw@nuaa.edu.cn ,

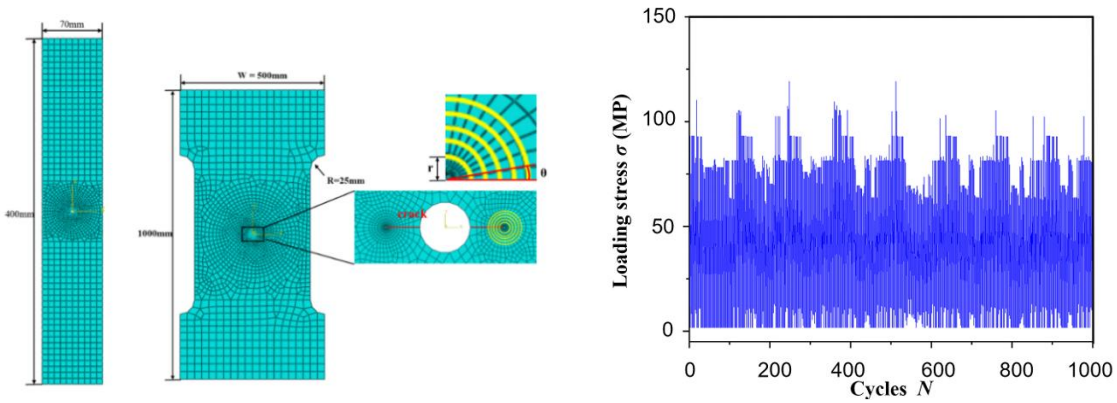

(a) (b)

Figure 19 (a) Small wall panel and big wall panel, (b) crack propagation spectrum under random load.

Simulation and result analysis

The crack extension life N corresponding to the critical crack size under the original spectrum of the large and small wall plate and different aggravation coefficients are calculated. Noriginal is the life corresponding to the fracture of the structure with the original spectrum load, spectrum load, and Nenhancement/Noriginal is the spectrum ratio. Nenhancement/Noriginal ratio and the α−Nenhancement/Noriginal spectrum ratio curve is plotted as shown inFigure 20. The results show that when the enhancement factor is less than 1.25, the Nenhancement/Noriginal ratio coincides with different spectral types and sizes with the increase in the enhancement factor. The fitting formula is:

$$\frac{N_{enhancement}}{N_{original}} = 6.94917 - 8.91763\alpha + 2.97061\alpha^2$$

The error δ is

$$\delta = \frac{|N_{formula} - N_{progrom}|}{N_{program}}$$

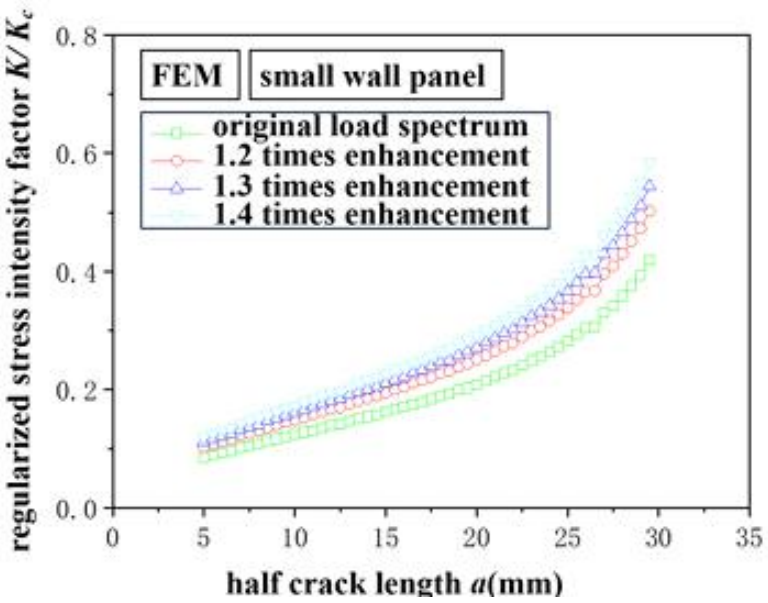

Figure 20 Load spectrum enhancement α-$N_{enhancement}/N_{original}$ original spectrum curves

2.4 Study on High Temperature Fatigue Performance of TC4 Titanium Alloy Superplastic Forming Specimen[9]

For the thin-wall structures commonly used in aircraft structures, superplastic forming and diffusion-welded parts have been applied in aircraft structures in recent years due to their advantages of large out-of-plane stiffness, weight reduction and high production efficiency. At present, the research on high temperature fatigue performance of titanium alloy test parts mainly focuses on standard test parts, and the research on special-shaped components is relatively lacking. In this paper, the specimen is connected by a 0.8mm thick plate and 1.0mm thick plate through diffusion welding process. Solder resistance is placed in the rib area of the rib-type test specimen and the specimen is placed in a specific mold after welding to form the rib area.

Test result

Figure 21 shows the maximum principal stress distribution contour of a superplastic forming test specimen with a rib structure under a stress level of 300MPa at room temperature. It can be observed that the flat plate of the test specimen is subjected to a tensile stress of approximately 300MPa, and the maximum stress does not occur on the surface of the specimen. The surface of the rib structure is subjected to compressive stress. From Figure 21 (c) and Figure 21 (d), the stress in the test specimen is in the connection area between the lower flat plate and the rib structure, with a maximum stress of 729.5MPa. This indicates that there is a significant stress concentration phenomenon in this region of the test specimen. Under cyclic loading, this region is more likely to initiate fatigue cracks earlier, and further crack propagation will lead to fracture failure of the test specimen. The distribution pattern of the maximum principal stress in the test specimen is consistent under different test temperatures and stress levels.

[9] The First Aircraft Design & Research Institute, Li Shiyu, lisy68@avic.com

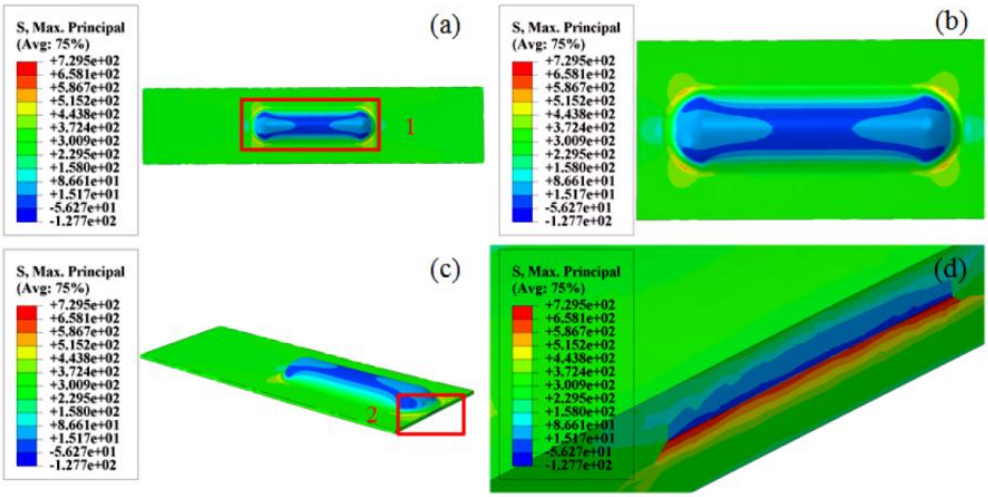

Figure 21: Maximum principal stress distribution

Figure 22 presents the fatigue life data of the test specimens under different experimental conditions. As can be seen from the figure, the fatigue life of the specimens decreases with the increase in test temperature and stress level, and the influence of stress level on fatigue life is significant. When the test temperature rises from room temperature to 200°C, the fatigue life of the specimens does not change significantly. However, when the test temperature increases from 200°C to 400°C, the fatigue life of the specimens decreases substantially. The variation trend of the DFR (Detailed Fatigue Rating) value of the specimens with test temperature is consistent with that of the fatigue life with test temperature. The DFR values of the specimens are essentially the same under different stress levels, which is due to the fact that the DFR value is an inherent property of the specimens.

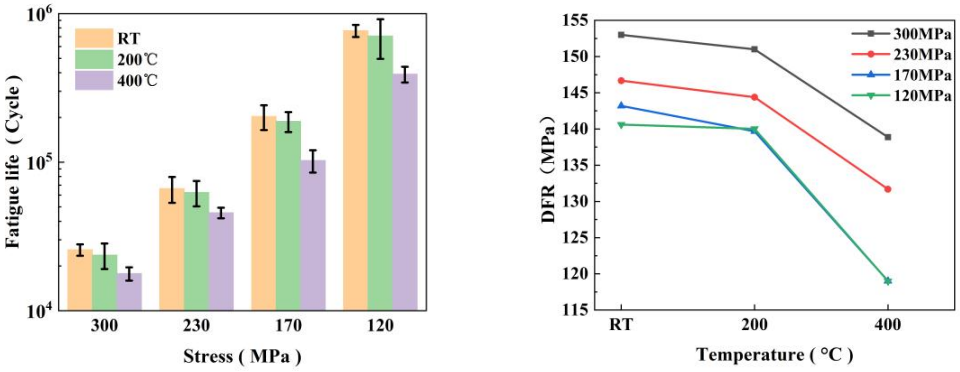

Figure 22: Fatigue test results and DFR values at different temperature and stress levels

Figure 23 displays the microscopic morphology of the crack propagation zone in the test specimens under different test temperatures and stress levels. In the figure, fatigue striations can be clearly observed occupying most of the plane, and the arrangement of these striations exhibits a distinct directly. Each fatigue striation represents one cycle of alternating load that the structure has endured. The spacing between the fatigue striations is positively correlated with the crack propagation rate. As the test temperature increases, the spacing between the fatigue striations also increases, and the striations become more pronounced. There is no significant difference in the spacing of fatigue striations at room temperature and 200°C, whereas the spacing at 400°C is noticeably larger than that at room temperature and 200°C, which is consistent with the trend of the specimens' fatigue life changing

with temperature. Under the same temperature but different load levels, the microscopic morphology of the crack propagation zone in the test specimens also follows a similar pattern.

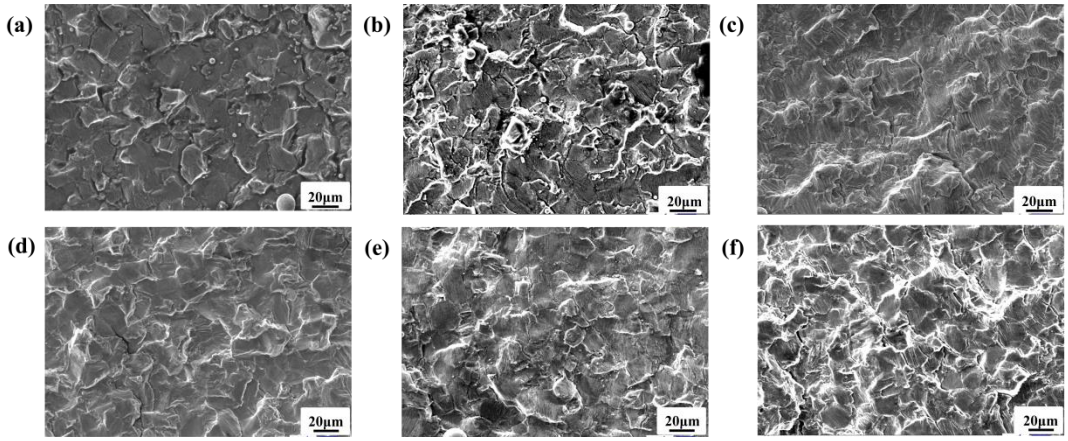

Figure 23: (a) RT, 170MPa; (b) 200°C, 170MPa; (c) 400°C, 170MPa; (d) 40°C, 120MPa; (e) 400°C, 230MPa; (f) 400°C, 300MPa.Micromorphology of crack growth zone of specimens at different temperature

2.5 Predicting Fatigue Lifetime of Additively Manufactured Specimens: Combining Simulation Data and Experiment Data[10]

Due to the excellent capabilities of near-net shape forming for parts with complex geometries, additive manufacturing (AM) showed great attraction in aeronautical industry. However, intrinsic defects lead to intricated fatigue performances and lack of reliable evaluation method, which hinders the large-scale application of AM to aeronautic primary structures. It is believed the effects of killer defects on fatigue lifetimes are the key to fatigue analysis, which are unlikely to be fully revealed by limited number of experiment data due to quite large scatter. Our work proposed an innovate approach of combining high-efficiency simulation data and high-fidelity experiment data, in which simulation data are utilized to establish descriptive function for defect effects in semiquantitative sense, while experiment data are utilized to recalibrate the function coefficients to the real fatigue lifetimes. This method improves the efficiency and accuracy of fatigue life prediction and is expected to provide a new methodology to establish the fatigue life model for AM metallic parts.

The combined method of simulation and experiment

As for simulation work, two-dimensional peridynamics are conducted to simulate the whole process of fatigue failure in smooth specimens with a single defect, in which the impacts of stress levels, defect features (sizes and locations) on failure modes and fatigue lifetimes are obtained to establish the descriptive function. As for experimental work, fatigue experiments as well as fractographic analysis are conducted on Laser Powder Bed Fusion (L-PBF) Ti-6Al-4V smooth specimens, in which the real data of fatigue lifetimes and killer-defect features are both exploited for recalibration of function coefficients. The results of both numerical and experimental studies remind us that it is of great significance to consider the impact of multi-mode failures and their competitions, for which we modify the coefficient for effects of defect locations in the conventional Murakami model to be the coefficient for effects of failure modes, and the value of the coefficient is dominated by both defect locations and

[10] Beihang University, Bao Rui, rbao@buaa.edu.cn

defect sizes.

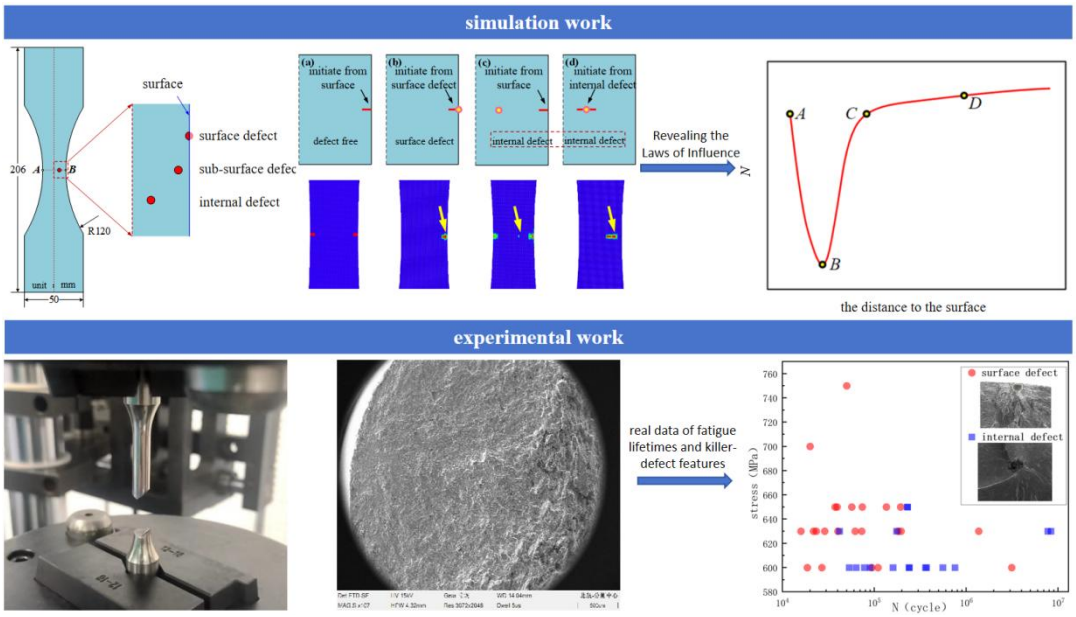

Figure 24： The combined method of simulation and experiment

Effectiveness of the method

For additive manufacturing components, this study leverages the advantages of simulation technology to reveal the variation trends of fatigue life with defect characteristics, guide the development of models, and identify the defect characteristics that require special attention. This approach reduces workload while improving prediction accuracy. Compared with experiment data in this work, 41% of the predictions by conventional Murakami model lie outside ±2 error band, while all the predictions by the proposed model lie within ±2 error band, which demonstrates a notable progress. This work is expected to provide a new methodology to establish the fatigue life model for AM metallic parts.

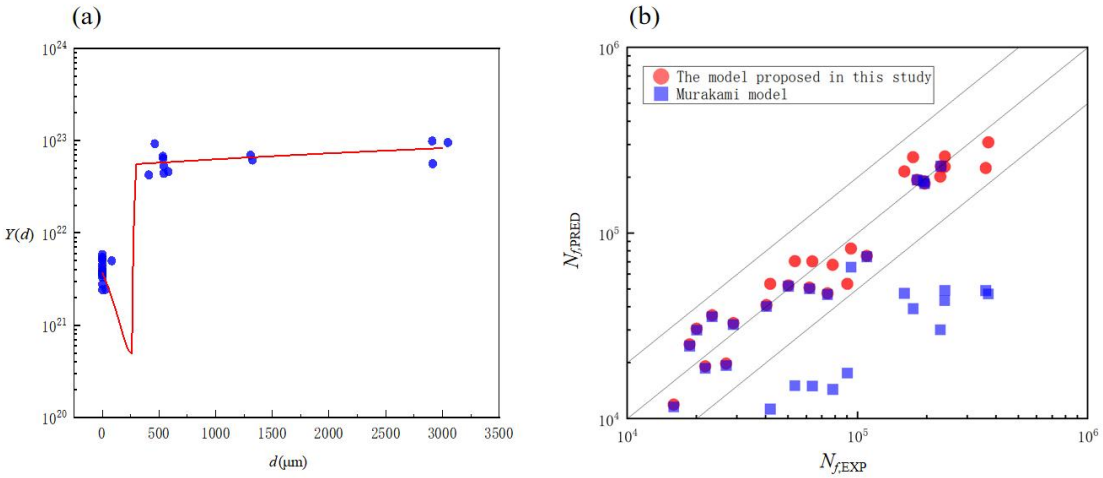

Figure 25:Establish the fatigue life prediction model: (a) Recalibration of function coefficients. (b) Comparison of predicted results

2.6 Fatigue crack growth behavior and simulation of diffusion-bonded laminated plates[11]

Dissimilar metal laminated plates have been widely applied in engineering due to their excellent comprehensive performance and gradient material properties. Studies have shown that the laminated interface formed during the welding of different metal materials can, under certain conditions, slow down the fatigue crack growth (FCG) rate perpendicular to the interface. When two different titanium alloys are welded into a dissimilar titanium alloy laminated plate, the laminated interface can be utilized to optimize the damage tolerance characteristics of the titanium alloy, thereby extending the FCG life of titanium alloy structures. To evaluate the FCG life of dissimilar metal laminated plates, it is necessary to study the complex three-dimensional FCG process in such plates and establish precise and efficient FCG simulation and life prediction methods.

Key technology

Fractographic analysis and stress intensity factor (SIF) calculations were conducted based on FCG test results to analyze the mechanical behavior of FCG in diffusion-bonded dissimilar titanium alloy laminated plates. The results indicate that the variation in SIF range is the primary factor governing FCG in diffusion-bonded dissimilar titanium alloy laminated plates. T-stress was introduced to correct the discrepancies in FCG behavior due to geometric factors, yielding a unified da/dN-ΔK relationship. On this basis, a FCG simulation and life prediction method for dissimilar titanium alloy laminated plates was developed using the finite element method (FEM), achieving automatic finite element parametric modeling and automated FCG simulation.

Application of technology

The object of the study is the TC4/TC1 bilayer diffusion-bonded laminated plates. The specimen configurations and schematic diagram are shown inFigure 26.

The FCG rates and SIF ranges at different characteristic points on the laminated plate did not exhibit strong regularity. This discrepancy arises due to differences in the geometric configuration of the locations, the degree of crack front constraint, and the extent of stress relaxation, all of which affect the actual FCG rate. By introducing T-stress to eliminate the influence of geometric position on FCG rate:

$$\left(\frac{da}{dN}\right)_{CI} = \left|\frac{T\sqrt{\pi a}}{K_I}\right| \frac{da}{dN}$$

The double logarithmic relationship between the corrected FCG rate and ΔK for the five groups of characteristic points is shown in Figure 27. The fitted curves for the hole-containing TC4 and TC1 titanium alloy plates are also presented. The figure demonstrates that after eliminating geometric factors affecting the FCG rate, the da/dN-ΔK relationships of the two different materials exhibit significant differences. However, for the same material, the da/dN-ΔK relationships of different characteristic points show good linear correlation. This confirms that the variation in the SIF range is the dominant factor controlling FCG in dissimilar titanium alloy laminated plates.

[11] Beihang University, He Xiaofan, xfhe@buaa.edu.cn

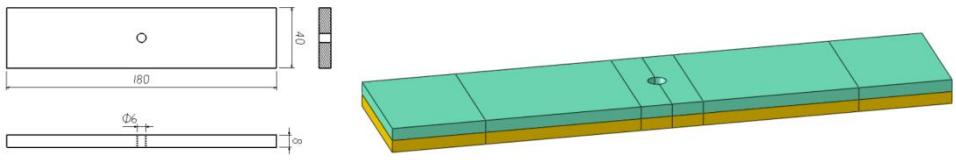

Figure 26: TC4/TC1 specimen configurations and schematic diagram

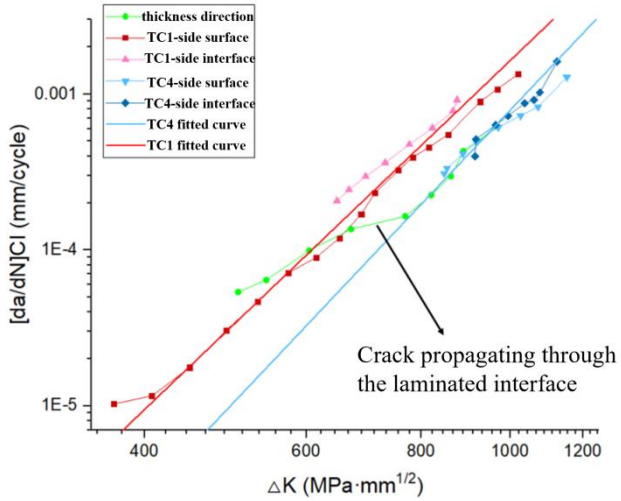

Figure 27: Relationship between the corrected FCG rate and ΔK

Based on the study of FCG characteristics in diffusion-bonded dissimilar titanium alloy laminated plates, FEM was employed for FCG simulations. A Python script was developed to achieve automated FCG simulation, establishing a FCG simulation and life prediction method for dissimilar titanium alloy laminated plates. The programming framework is illustrated in Figure 28.

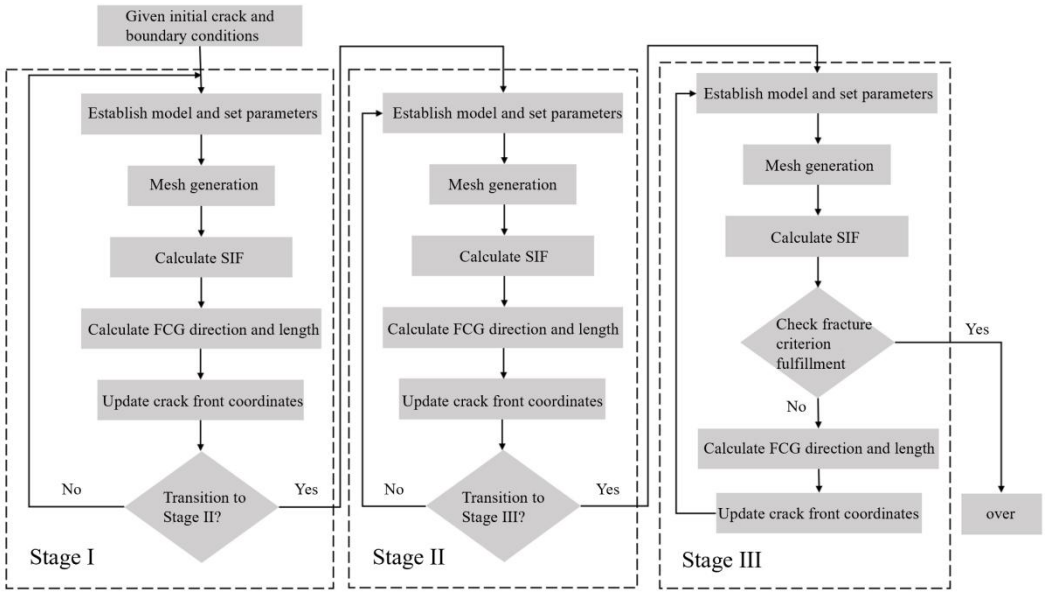

Figure 28: Programming framework of FCG simulation

The FCG simulation method was applied to the TC4/TC1 laminated plate with crack initiation on the TC4 side, and the simulated FCG process was compared with the actual fracture surface of the

specimen. Although the FEM-based FCG simulation could not reproduce the geometric details of the actual fracture surface, it effectively captured the overall FCG behavior in the laminated plate. The experimentally obtained median FCG life was 42,154 cycles, while the simulation result was slightly higher than the measured median life, with an error of approximately 25.08%.

2.7 Complex loading method on very high cycle fatigue testing[12]

While pursuing higher requirement on the safety and integrity, the aircraft structure platform is required to have the fatigue resistance on the very high cycle regime that the repetitions of loading could beyond 10^9 cycles. Although the fatigue test at such high number of cycles already conducted by accelerated loading at ultrasonic frequency of 20 kHz, the uniaxial property in material level couldn't directly applied in the aircraft structure design. The complex loading case, for example in composite loadings or the multiaxial loading, are more consistent to the conditions in service. Therefore, the complex loading method with ultrasonic frequency, which capable to conducting different cyclic deformation, were developed. In addition, to have further understanding the influence of complex loading and the effect of the loading frequency, the fracture mechanism under complex loading were investigated.

Composite loading at very high cycle regime

Components in aero-engine are likely excited in multiple resonance models in dynamic loads. This study proposes an accelerated fatigue testing method that combines the vibration test with ultrasonic loading to develop a feasible experimental system for combined cycle fatigue (CCF), and explore the CCF characteristics in the high cycle fatigue (HCF) associated with very high cycle fatigue (VHCF) conditions. A thin plate specimen of 7075-T6 aluminum alloy with two natural frequencies of 2kHz and 20kHz is designed for the experiment. The influences of composite loads are demonstrated by exploring the characteristics of the S-N curves and fracture morphology.

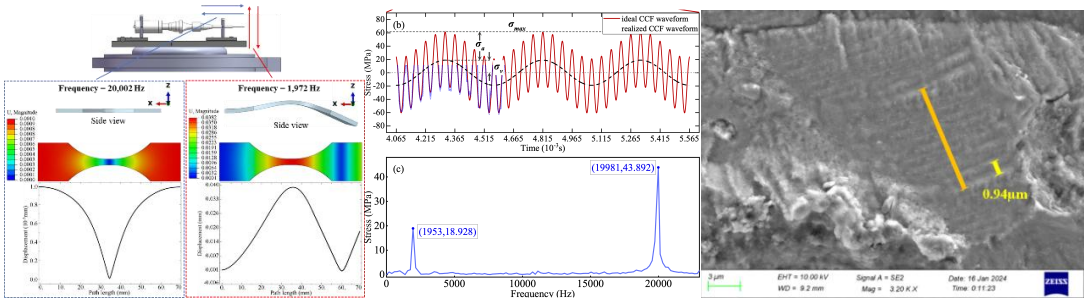

Figure 29: Vibration-Ultrasonic Combined Fatigue on 7075-T6 Aluminum Alloy

Multiaxial loading at ultrasonic frequency

Thin-well metal elements frequently encounter multiaxial fatigue during its service environment. In this study, a novel test method on biaxial is proposed with ultrasonic fatigue technology. Based on the principle of harmonic vibration, a cruciform specimen of TC4 titanium alloy was designed to a natural frequency of 20 kHz, featuring vertically superimposed fourth-order and third-order bending modes. Results of S-N curves, crack propagation paths and fracture morphologies are analyzed, revealing the failure features of biaxial bending fatigue in very high cycle regime with different loading conditions. It was found that, in contrast to uniaxial bending, the facets appeared in biaxial bending fatigue

[12] Sichuan University, Wang Qingyuan & Wang Chong, wangqy@scu.edu.cn, chongwang@scu.edu.cn

presents a batten pattern as in the service cases caused by multiaxial fatigue failure.

Figure 30: Biaxial ultrasonic testing for very high cycle fatigue

Another multiaxial ultrasonic fatigue is conducted under tensile and torsional fatigue on TC17 titanium alloy with bimodal microstructure. It is found, like the tensile cracks, torsional cracks were substantiated to nucleate from specimen surface or interior sites and presented in a fatigue life-dependent mode. Internal tensile and torsional fatigue cracks with faceted morphology were analyzed using focus ion beam and unraveled to initiate in modes II + III that driven by maximum shear stress. Particularly, short crack branching and deflection beneath the crack initiation rough area can be observed for torsional loading condition.

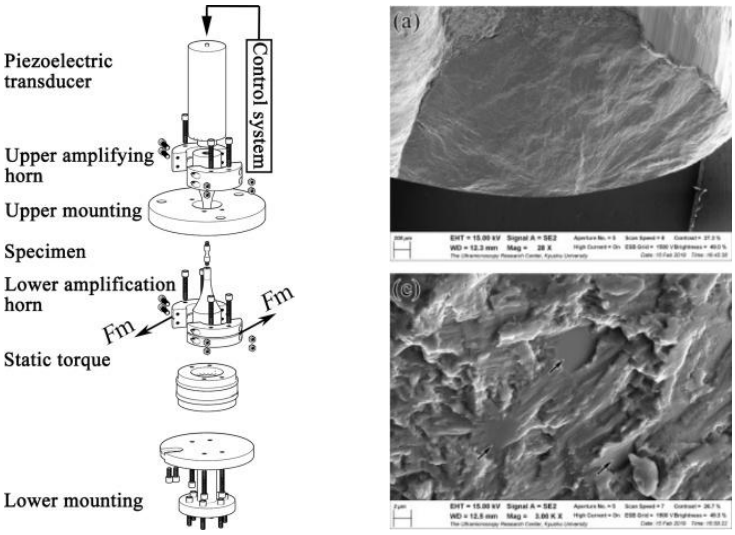

Figure 31: Combined tensile-ultrasonic torsion fatigue and internal crack initiation.

2.8 In-situ ultrasonic testing and crack propagation at very high cycle fatigue[13]

According the resonant model, another advantage of the ultrasonic testing method is that the gauge section, where the stress is the maximum, is also the stagnation section of the displacement. This feature provides the ultrasonic fatigue testing a privilege on In-situ observation condition while the specimen under cyclic loading. In addition, very high cycle fatigue provides the opportunity of the real-time observation time scale by sufficient long cycle either on the crack initiation or the crack propagation. Therefore, different observation technology could be employed to perform the in-situ test for investigating the dynamic behavior on the damage accumulation or crack propagation by optical

[13] Sichuan University, Wang Chong, chongwang@scu.edu.cn ,

microscopy, scanning electrical microscopy, infrared camera, even synchrotron radiation, or their combine. Two particular examples on short crack propagation and internal crack inspection has been successfully study.

Evaluation of the short crack propagation

An in-situ thermographic methodology based on the temperature field is utilized to determine the crack tip position during the very high cycle fatigue test of pure iron and deduce the corresponding fatigue crack growth rate. Two cameras are placed on each side of the plate sample, an infrared one for measuring the temperature fields on the specimen surface and an optical one for visualizing the crack tip verification. The center section of the specimen is notched to initiate the crack. The temperature field is converted into intrinsic dissipation to quantify the inelastic strain energy according to energy conservation. The maximum value of intrinsic dissipation in each thermal image is related to the position of the crack tip and thus allows monitoring of the crack evolution during the fatigue test. It is observed that the intrinsic dissipation has a low-constant level during the initiation and the short cracking, then sharply grows during the long cracking. This transition is visible on the polished surface of the sample, where the plasticity appears during the long cracking and slightly before. The material parameters in the Paris equation obtained from the intrinsic dissipation in the short crack growth are close to the results available in the literature as well as those obtained by the optical camera.

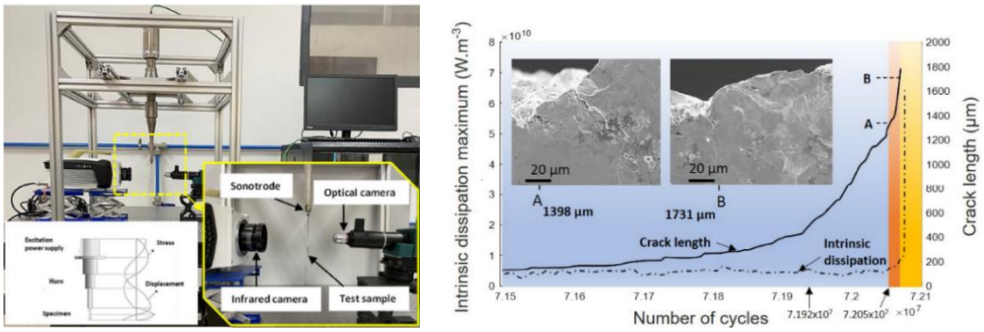

Figure 32: Ultrasonic in-situ setup of infrared and vision microscopies, and the determination of the short crack propagation

Furthermore, because of the in-situ observation, more detail during the short crack propagation could be obtained to analysis the crack growth behavior by considering the microstructural feature of each grain. This also provides a big data for the machine learning study on the fatigue crack growth. In the present study, a physics-informed neural network model based on Bayesian hyperparameter optimization is proposed for the prediction of short crack growth paths. A large number of cyclic loadings at a lower amplitude were applied to an α titanium sample by an ultrasonic fatigue machine to ensure a sufficient amount of data for machine learning. The grain size, grain orientation and grain boundary direction on the path, as well as crack growth direction, were selected as feature data for training the prediction model. The optimizations of the size ratio and the angle operation were conducted to compare different data processing methods, respectively. After evaluation, eventually, a model for predicting crack growth path is obtained with a reliable performance of 10% tolerance on the path angle at each grain boundary. And the prediction effect of the proposed model is better than that of some classic machine learning models and slip trace analysis.

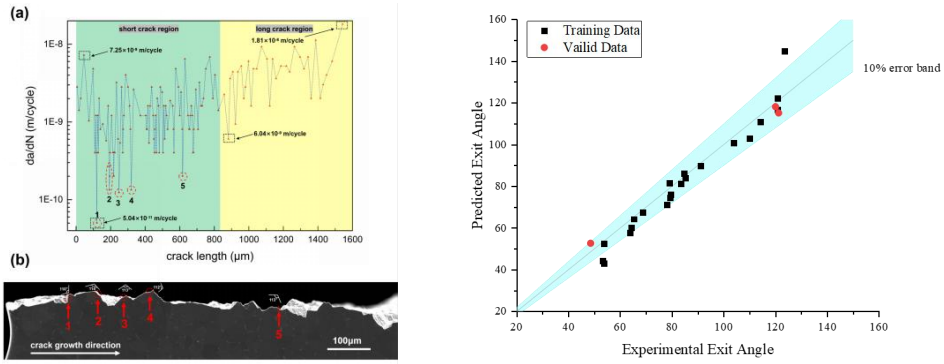

Figure 33: a&b) Correspondence between crack propagation and microstructure of grains, c) Crack path prediction by machine learning.

In-situ determination of internal crack growth and failure prediction

This work presents a thermodynamic characterization method for estimating the internal crack growth rate, which has been a puzzle in very high cycle fatigue research. A theoretical approach of surface temperature is discussed with crack size, initiation site, and time for thin sheet material. Infrared thermography is used to study the inner crack behavior and the heat dissipation phenomenon under 20 kHz vibration loading on high-strength stainless steel. A numerical simulation reveals the consequent temperature elevation on the surfaces by the heat generation at the crack tip and the heat conduction. Ultimately, the internal crack growth rate and final fatigue failure prediction are obtained by combining the calculation of heat dissipation and the observed evolution of the surface temperature field.

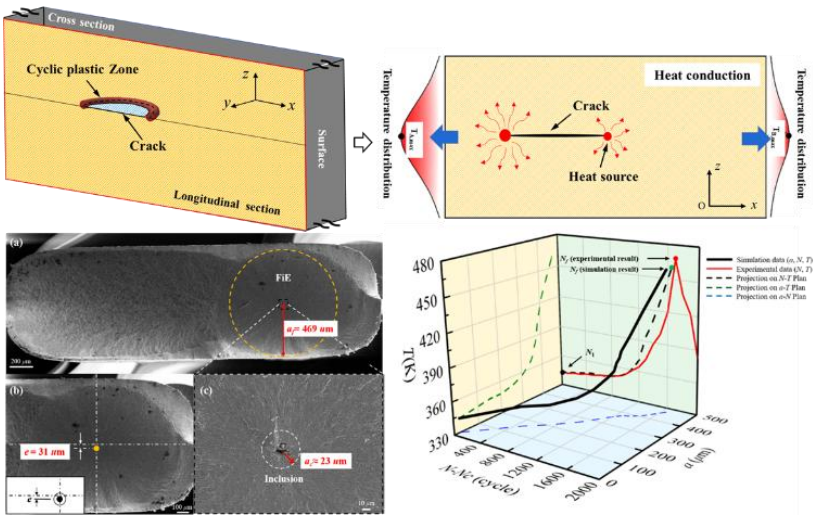

Figure 34: Thermal detection of inter crack growth and its failure predection

2.9 Fatigue crack growth prediction model for aerospace structures[14]

Fatigue Crack Growth (FCG) is a key factor affecting the integrity and safety of aerospace structures. Accurate prediction of crack growth behaviour is essential for extending structural life and optimising maintenance schedules. Traditional crack propagation prediction models mainly focus on long crack behaviour. However, in real engineering structures, short crack propagation is greatly influenced by

14 Chinese Academy of Sciences, Qian Guian , qianguian@imech.ac.cn

micro-mechanisms, showing significantly different growth characteristics from long cracks and accounting for a larger portion of the fatigue life. The study of fatigue short crack growth (SFCG) is essential to improve the accuracy of structural health management. In order to achieve this goal, in-situ fatigue experiments are used to obtain the characteristics of short crack growth and expansion and experimental data, combined with the feature engineering screening characteristics of the actual working conditions. Data expansion technology and the establishment of a machine learning model are used to achieve the accurate prediction of short crack growth.

Key technology

The in-situ fatigue short-crack experimental method is able to track and record the crack growth behaviour in real time during the fatigue experiments, thus providing rich experimental data support for the accurate establishment of crack extension models. Meanwhile, ensemble learning algorithms, such as the gradient boosting machine (XGBoost) technique, provide a powerful tool for processing complex experimental data. For the multi-dimensional crack extension data collected in situ, the machine learning model is able to mine the non-linear relationships and implicit laws in the data to optimise the prediction effect of the model. Combining machine learning and in-situ fatigue experiments, the growth trend of fatigue short cracks can be predicted more accurately, providing a scientific basis for health monitoring and life prediction of aerospace structures.

Application of technology

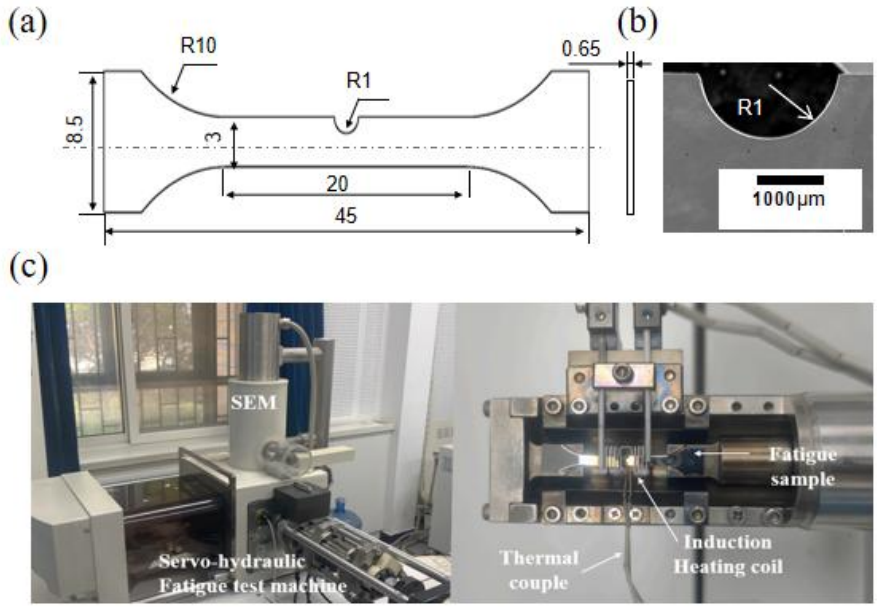

Figure 35: In-situ fatigue experimental system

This study focuses on material-level fatigue, which can reveal the microscopic fatigue behaviour of materials under different loads, environments and load cycles, and thus provide key theoretical support for the fatigue design and reliability analysis of aerospace structures. The in-situ fatigue experimental system is shown in Figure 36.

After the initiation of the crack, it enters the short crack growth stage. During this stage, crack length and cycle data were recorded, and the short crack growth rate was calculated using the secant method. The amplitude of the stress intensity factor was then determined, followed by the plotting of the

d*a*/d*N*-Δ*K* curve. Experimental conditions were carefully documented throughout the process. By gathering these data, an initial experimental dataset was created, which was later expanded using spline interpolation. Once the dataset was established, a machine learning model was developed, and its optimal parameters were identified through training. The resulting rate predictions were obtained using these optimal parameters. The overall process is illustrated below,Figure 37.

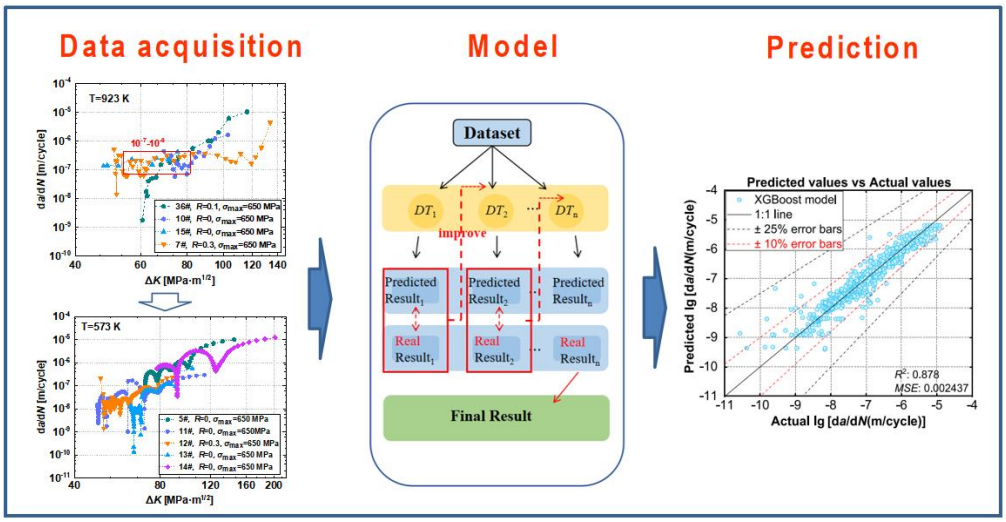

Figure 36: Fatigue crack growth prediction model

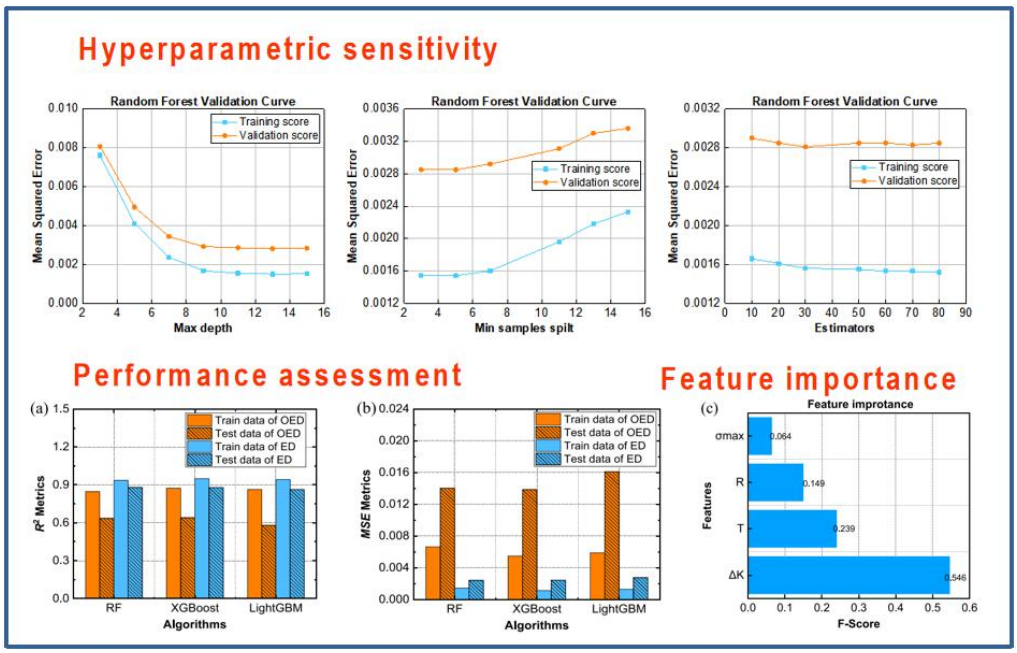

Figure 37: Post-modelling assessment analysis results

The structure and configuration of the machine learning model is then optimised to improve the accuracy and interpretability of the model through hyperparametric sensitivity analysis, performance evaluation and feature importance analysis. These analyses provide strong support for the prediction of fatigue crack extension rates, helping engineers in the aerospace sector to better understand the fatigue behaviour of structures and to effectively perform health monitoring and safety assessments. The overall results are illustrated in Figure 38.

2.10 Stress intensity factors and fatigue crack growth analysis for corner/surface crack in ugs[15]

Lug is one of the most important lap joints in many engineering structures, especially airframes. Through thickness and part-through cracks emanating from pin-loaded lug hole is frequently encountered due to stress concentration. Stress intensity factors for various crack geometries are the prerequisite for damage tolerance design of attachment lug. In this paper, an efficient 3D slice synthesis weight function method (SSWFM) is developed to determine 3D SIFs of hole-edge corner/surface crack in straight and tapered lugs under various pin-loadings. The resulting 3D SIFs are verified by comparisons to the numerical FEM/Franc3D solutions and literature data. The SSWFM is about 3-4 orders of magnitude faster than the numerical FEM/Franc3D in SIF calculation and fatigue life prediction.

3D slice synthesis weight function analysis for corner/surface crack

The basic idea of the SSWFM is to decompose the 3D crack problem into two 2D orthogonal slices, the basic slice and spring slice being parallel with the major- and minor-axis, respectively. For a part-through corner and surface crack emanating from a pin-loaded lug, the basic slice is the hole-edge cracked lug shown in Figure 39(a). The spring sliced are edge and center crack in a finite sheet with elastic constraint boundary, as shown in Figure 39(b).

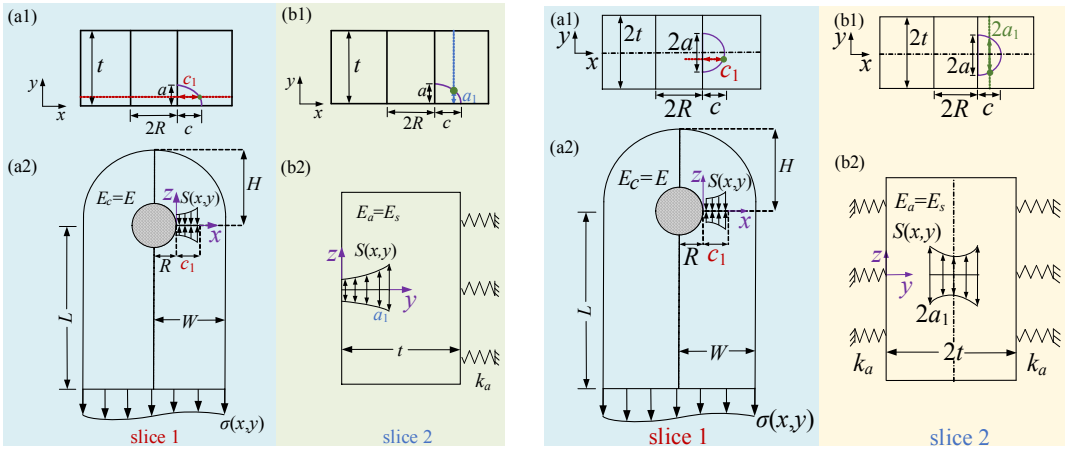

Figure 38: Slice model for surface crack at a pin-loaded lug; (a) corner crack and (b) surface crack

Using the SSWFM, the 3D SIFs are calculated by

$$K(\varphi_j) = 1/(1-\eta^2)\cdot\left\{K_c^4(c_j)+\left[E/E_s\cdot K_a(a_j)\right]^4\right\}^{1/4}(-1)^n \tag{1a}$$

$$E_s = E\left[\Phi/(1-\nu^2)-1\right]\cdot c/a,\ a/c\le 1;\quad E_s = E\left[\Phi/(1-\nu^2)-c/a\right],\ a/c>1 \tag{1b}$$

$$\Phi=\left[1.0+1.464(a/c)^{1.65}\right]^{1/2},\ a/c\le 1;\quad \Phi=\left[1.0+1.464(c/a)^{1.65}\right]^{1/2},\ a/c>1 \tag{1c}$$

where E and E_s are Young's modulus of the basic and spring slices, respectively. η=0 for free surface and $\eta=\nu$ for points inside the body. n=2 for $K_i>0$ ($i=a$, c), otherwise n=1. The subscript j represents the j^{th} slice. K_c and K_a are SIFs of the basic and spring slices, which can be obtained by the 2D WFM Eqs.(2a) and (2b), respectively.

[15] Shanghai Jiao Tong University, Xu Wu, xuwu@sjtu.edu.cn

$$K_c(c_j) = \int_0^{c_j} \left[\sigma(x,y) - S(x,y) \right] \cdot m_c\left(W, R, c_j, x\right) \cdot \mathrm{d}x \quad (2a)$$

$$K_a(a_j) = \int_0^{a_j} S(x,y) \cdot m_a\left(a_j/t, y/t\right) \cdot \mathrm{d}y \quad (2b)$$

where $\sigma(x, y)$ is from a 3D stress analysis of the un-cracked body subjected to pin load. m_c is the WF of a hole-edge cracked lug, m_a is the WF of an edge/center crack in a finite width plate with elastic constraint as shown in Figure 39(b). The spring stress $S(x, y)$ represents the interaction between the basic slice and spring slice.

SIFs and fatigue crack growth analysis

The 3D SIFs of straight lugs are calculated using the SSWFM, the result is normalized by,

$$f = K \cdot \Phi \Big/ \left(\sigma_{\mathrm{br}} \cdot \sqrt{\pi a} \right) \quad (3)$$

where, K is the 3D SIF from Eq. (3), a is the crack depth, $\sigma_{\mathrm{br}} = P/(2Rt)$, P is total pin load, Φ is given in Eq.(1c). Its accuracy will be verified by the FEM/Franc3D.

Using SSWFM, typical corner and surface cracks of straight/tapered lugs subjected to pin load are determined and shown in Figure 40. Also shown in the figures are the results from XFEM by Naderi and Iyyer (triangle symbol) for comparison. The results from SSWFM, XFEM and FEM/Franc3D are generally in good agreement, with the maximum difference being less than 10%.

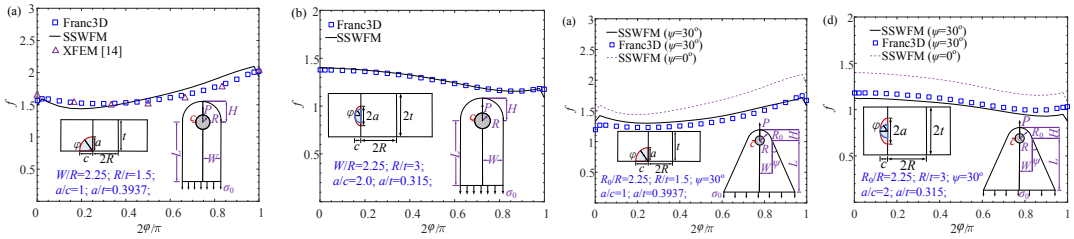

Figure 39: SIFs of corner and surface cracks of straight and tapered lugs under pin load

Fatigue crack growth (FCG) tests and predictions under constant amplitude cyclic pin-loading were made for a hole-edge corner crack in a lug as shown in Figure 41(a). Fatigue mark loads were applied periodically to leave striation marks at crack surface, Figure 41(b), and crack lengths along the two axes were recorded. The changes of crack size and shape are predicted based on the SIF-solutions computed by using SSWFM and the Paris law. The predicted shape evolutions agree well with the striation marks in Figure 41(c); the predicted crack sizes (a and c) by using SSWFM and the numerical Franc3D, respectively, are in quite good agreement as shown in Fig.3(d). In contrast, the computational time required by the two methods are less than 1 minute and about 12 hours, respectively, the difference being 720 times.

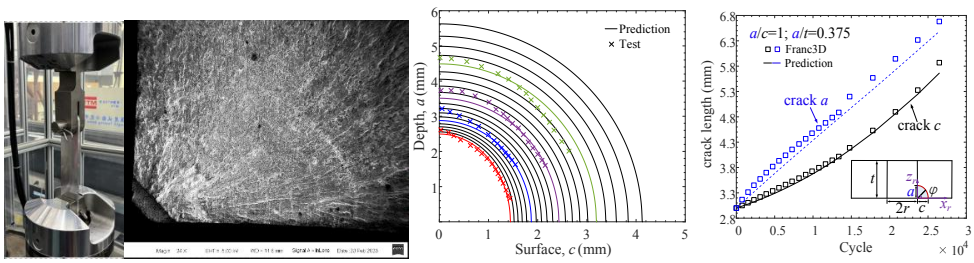

Figure 40: Fatigue crack growth of a hole-edge corner crack in a lug. (a) fatigue test setup, (b) crack striation marks, (c) comparison between predicted evolution of crack size/shape and crack face striations, (d) predicted crack sizes (a and c) based on the SIF-solutions from SSWFM and Franc3D,

respectively.

2.11 Fatigue crack growth in additive manufactured Titanium alloys[16]

Breakthrough in Additive Manufacturing (AM) technologies of large-scale-high- performance metallic integral structures is a significant milestone and a leading direction in the 3-D printing field; the application to the aerospace industry will revolute the methods to achieve further structural weight reduction and manufacturing cost saving. However, the difference in material microstructure between the AM alloys and conventional wrought or casting alloys sets new challenges to the damage tolerance evaluation, consequently, restricts the wide application of AM components in the primary load-bearing aircraft structures. In this project, experimental investigations and numerical simulations will be carried out to study the crack growth behavior and the corresponding mechanical parameters under the fatigue loading for samples manufactured by the Laser Metal Deposition (LMD) process.

Fatigue crack growth path - Microstructure effect

The material textures in AM Ti-alloy made by LMD process are different from those in conventional wrought or casting alloys. The columnar grains and equiaxed grains are alternately arrayed due to the LMD technology, while their mechanical properties of different zones and with respected to different orientations are different as shown in Figure 42.

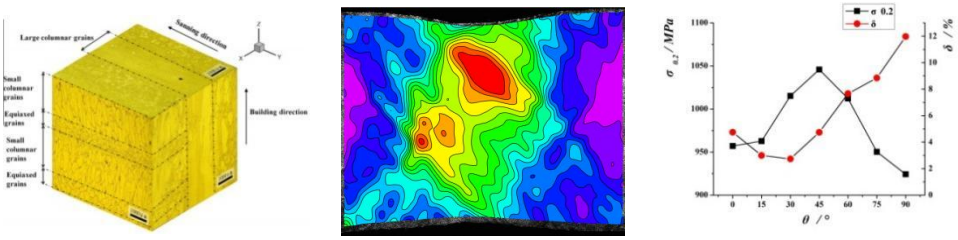

(a) (b) (c)

Figure 41: Material-structure characteristics and its effect on static properties: (a) alternately arrayed columnar grains and equiaxed grains, (b) strain field in different zones, (c) yield stress and critical elongation rate with respected to different orientations.

The crack path deflection is observed in the CT specimens with different orientations. When the angle between columnar grains and crack growth direction decreases, the straight crack path may deflect as shown in Figure 43. The scanning electron microscope (SEM) results in Figure 44 show that the deflection is affected by the angle γ between the expected crack growth direction and α p laths orientations. The fatigue crack tends to propagate along α p laths when is small; as γ increases, the effect of α p laths is no longer strong enough to completely deflect the crack path along α p laths, but the path still deflects locally; When γ is sufficiently large, the crack will pass through the α p laths directly. This indicates that the crack path might be "guided" by controlling α p laths orientations to extend fatigue lifetime. As shown in Figure 45, the possible crack paths with different α p laths orientation distributions are predicted by per dynamics (PD).

[16] Northwestern Polytechnical University, Li Yuexuan, liyuexuan@nwpu.edu.cn

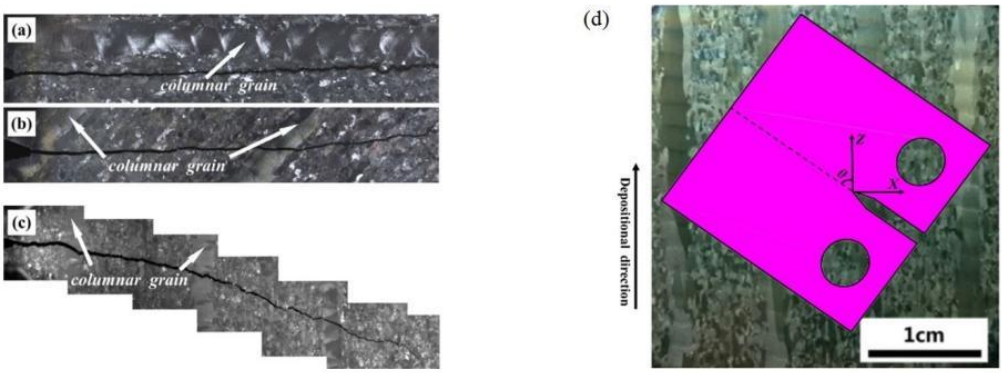

Figure 42: Crack growth paths in different oriented CT specimens, (a) θ=0° 、(b)θ=45° 、(c)θ =90° and (d) specimen orientation.

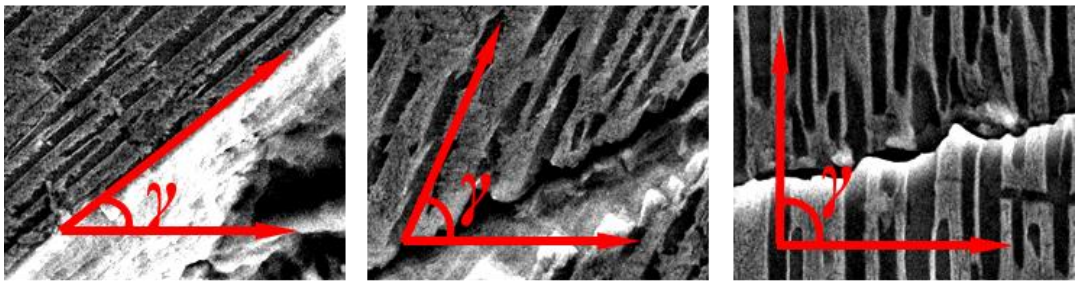

Figure 43: The crack deflection is affected by the angle between crack growth direction and α laths orientations.

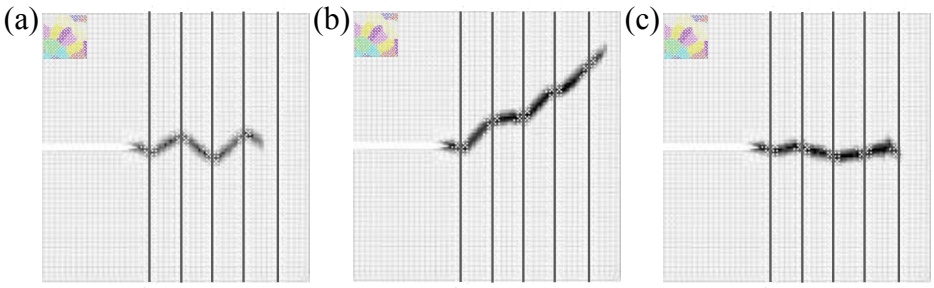

Figure 44: The crack path might be "designed" by controlling α p laths orientations (Peridynamic simulations: (a) 45/-45/45/-45; (b) 45/0/45/0; (c) 75/-75/75/-75).

Crack growth rate - Spectrum loading effects

Aimed at studying the mechanical parameters of crack propagation in different microstructures, the digital image correlation (DIC) method is adopted to measure the crack-tip strain fields before and after overload (OL). Due to the differences in plastic properties, the overload effects on crack closure are different in columnar grains and equiaxed grains, as shown in Figure 46. It is observed that the OL retardation distances are consistent with the intersection points of strains corresponding to the maximum load between the before and after OL, which is shown in Figure 47; that is, the retardation of crack growth rate can be characterized by the variations of crack-tip strain fields before and after OL. The above discoveries can be used to modify retardation models and thus improve the accuracy for lifetime prediction under spectrum loading.

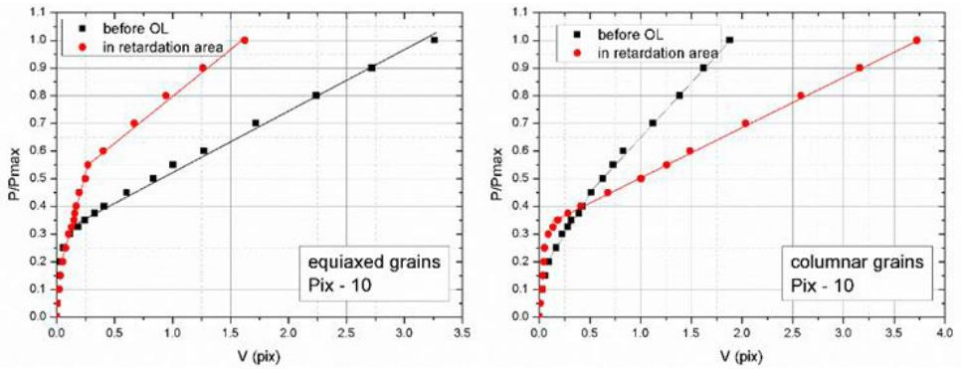

Figure 45: The overload effects are different in columnar grains and equiaxed grains.

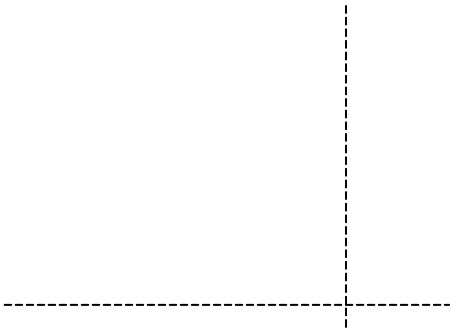

Figure 46: The retardation of fatigue crack growth rate can be characterized by the variations of crack-tip strain fields before and after OL.

3 Structural integrity of composite structures

3.1 Analysis and experimental evaluation framework for buckling and post-buckling of composite stiffened panels[17]

The post-buckling evaluation method for composite stiffened panels proposed in this section includes panel experimental techniques involving compression, shear, and combined compression and shear loads on panels, numerical analysis based on a refined model, and a rapid analysis method for buckling and post-buckling envelope based on interaction formulas. Experiments can directly obtain the buckling and post-buckling performance of panels, thus serving as a means to validate numerical analysis methods and interaction formulas. Numerical analysis, as a supplementary analysis based on experiments, enables further investigation into the damage process, failure modes, and failure mechanisms, thereby facilitating a more comprehensive assessment of post-buckling performance. Interaction formulas are used to predict the buckling correlation curve and the post-buckling failure envelope of the panel under arbitrary proportions of combined loads through uniaxial compression and shear load test results or numerical simulation results. This approach enables a more comprehensive evaluation of post-buckling behavior.

[17] Aircraft Strength Research Institute, Chen Xiangming, chenxiangming@cae.ac.cn

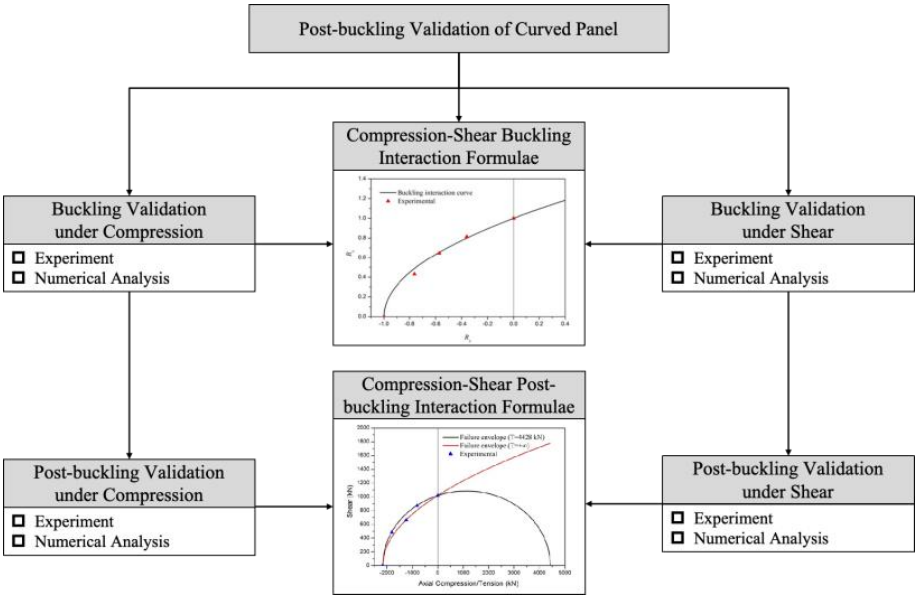

Figure 47: Post-buckling assessment process of composite curved panels

Experimental technology for curved Panels under combined loads

Combined loading experiments were conducted on the second-generation experimental system(Figure 49), which consisted of uniaxial, shear, and pressure-circumferential loading components. The experimental system allows for achieving unitary loads or combined loads with arbitrary proportions. As shown in Figure 2, uniaxial loads are applied by the actuators on both sides of the uniaxial loading component, while shear loads are applied on the specimen boundaries by the shear loading component. By subjecting the specimen to a multipoint distributed shear load on its sides, the shear condition is passively achieved by transferring the load to the resultant force point located at the curved edge via rotation of the shear self-balancing frame.

The load self-balancing and self-following methods were utilized in the fuselage panel combined loading experimental device to actively apply shear loads, which achieving a wider range and more uniformly distributed stress/strain field. By designing a single force path based on a movable pivot lever system, bearings, and motion guides, issues of deformation coordination and nonlinear load coupling effects caused by the complex loads on large panels are effectively avoided. Five identical curved panels (CP1~ CP5) were subjected to different ratios of combined loads respectively. The experiments include buckling loads tests and failure loads tests.

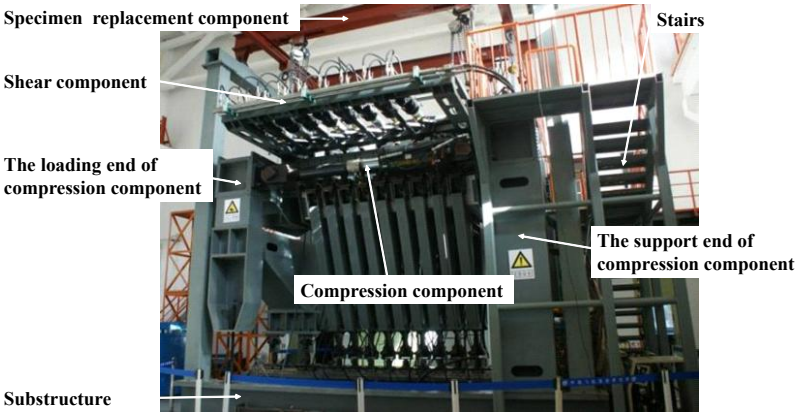

Figure 48: The second-generation experimental system

FEM evaluation

The failure prediction of composite fuselage curved panels were performed by the finite element method, using an improved Tsai-Wu failure criterion and the interlaminar failure criterion.

The finite element analysis of curved panels under compression loads and shear loads was conducted respectively. The panel CP1 failed at 2145 kN between the second and third frames. The comparison of failure modes between FEM and experimental results is shown in Figure 50(a). The estimated failure load is 2264 kN, with errors of - 5.5%. At the load of 1019 kN, the skin of panel CP2 eventually failed along 45° , resulting in debonding between the stiffener and skin at failure areas. The comparison of failure modes between FEM and experimental results is shown in Figure 50(b). The estimated failure load is 1156 kN, with errors of -13.4%.

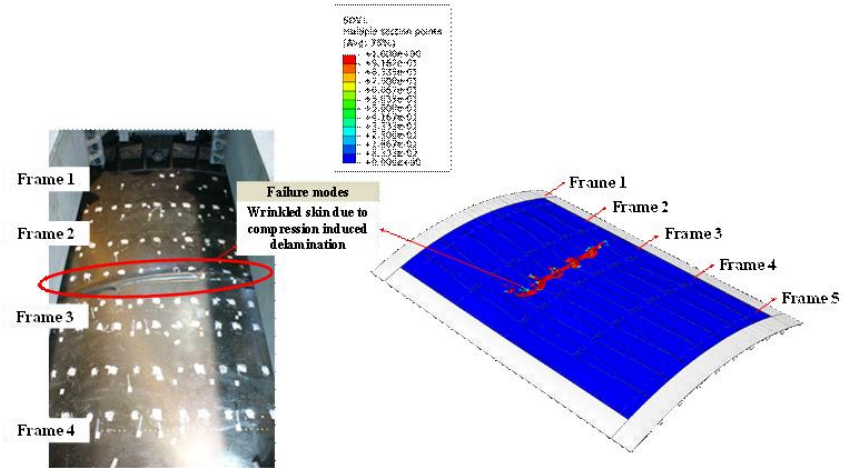

(a) Compression failure

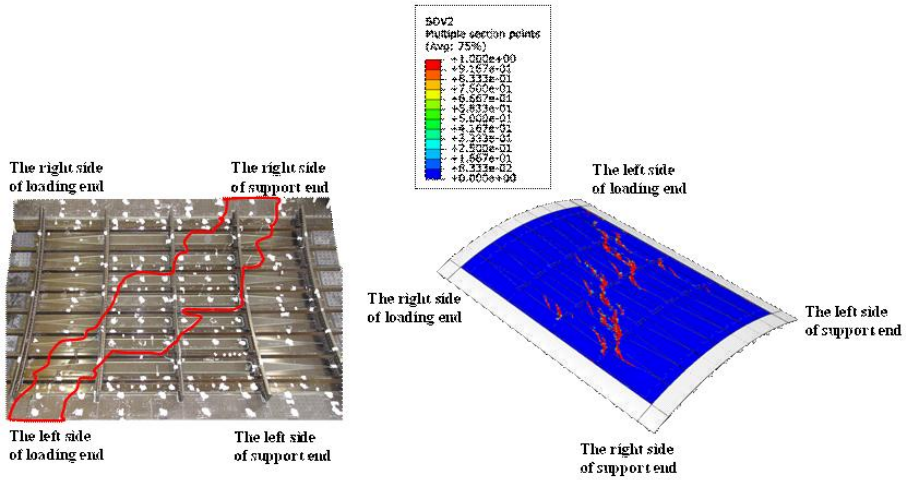

(b) Shear failure

Figure 49: Failure mode of fuselage curved panel

Evaluation of the rapid analysis method based on interaction formulas

By utilizing the buckling interaction formulas proposed in reference, the buckling load and failure load

of curved panels under different combined loading ratios were calculated. Figure 51illustrates a comparison between the predicted buckling correlation curve and the experimental loads, demonstrating a good consistency. Using the post-buckling failure interaction formulas to predict the failure envelope. The tensile strength of the fuselage curved panel, which was not available in this paper, was calculated as 4428 kN by FEM. The failure envelope predicted by interaction formulas for stiffened panels is illustrated in Figure 4. It demonstrates great predictive accuracy, except for certain errors of CP3. When approximating the tensile strength to infinity, there is a slightly larger error in the failure envelope prediction. However, the error remains conservative and falls within the acceptable range of engineering.

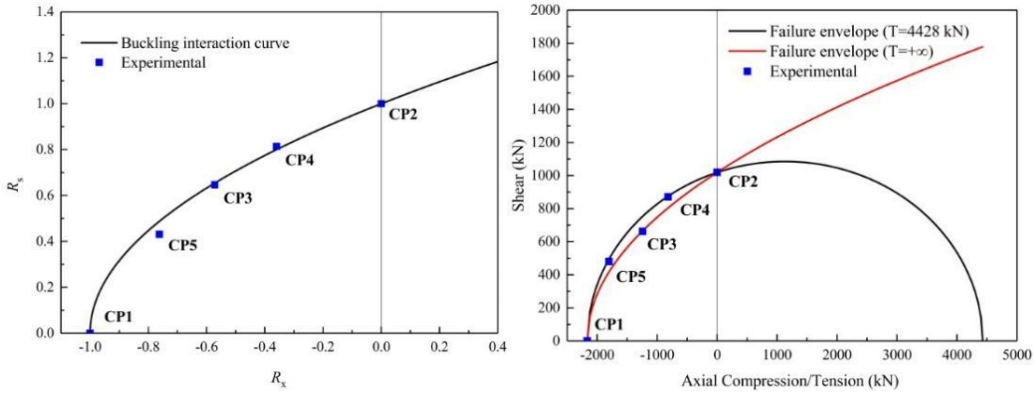

Figure 50: Comparison of the predicted and experimental buckling interaction curves and failure envelope

The post-buckling analysis and experimental research of composite fuselage curved panels under compression, shear, and combined compression and shear loads have been carried out. Experimental technologies for curved panels subjected to complex loads were introduced, enabling the application of axial tension, axial compression, in-plane shear, and combined loads. These techniques can be effectively employed for design and verification tests of fuselage panels.

3.2 A finite crack growth energy release rate for interlaminar fracture analysis of composite material at different temperatures[18]

The interlaminar fracture toughness of unidirectional fiber reinforced polymer composite material is temperature and crack growth history dependent. The non-constant interlaminar fracture toughness hinders the wide application of the linear elastic fracture mechanics-based approach for interlaminar crack growth analysis of composite material and structures. In addition, a quantitive relationship between the ductility of the matrix and interlaminar fracture toughness of the fiber reinforced composite is still highly desirable. In this paper, both pure resin and composite double cantilever beam (DCB) are tested at different temperatures. A finite crack growth energy release rate is used to analyze the interlaminar crack growth behavior of composite material at different temperatures. The plasticity of the composite DCB is modeled by Hill' s anisotropic plasticity, with the properties determined from multiscale analyses. It is found that a single constant finite growth energy release rate can well predict the interlaminar mode I crack growth of composite material at different temperatures. The roles of the ductility of matrix, thickness of the DCB, and crack growth history on the interlaminar mode I fracture toughness of composite material are quantitively determined by using the present method.

[18] Shanghai Jiao Tong University, Xu Wu, xuwu@sjtu.edu.cn

A finite crack growth-based energy release rate

It is reasonable to assume that the surface energy density γ is an intrinsic material property of fracture. Despite it is much smaller than γ_p for ductile material, it cannot be ignored. Therefore, the surface energy density γ should be considered in the analysis of ductile crack growth, i.e. $2\gamma=(\delta W\text{-}dU(Ue+Up))/(t\bullet\Delta a)$. To distinguish Griffith's energy release rate, a finite crack growth energy release rate was proposed recently by one of the authors. A finite crack growth Δa was assumed, which is very useful for finite element analysis of the crack growth. Eq. (1) becomes,

$$G_{\Delta a}=\frac{\delta W-dU_e-dU_p}{t\cdot\Delta a}=G^C_{\Delta a} \tag{1}$$

The driving force is termed $G_{\Delta a}$, and $G^C_{\Delta a}$ is the fracture resistance for a crack growth Δa. For fixed displacement, $\delta W=0$, Eq. (1) become,

$$G_{\Delta a}=-\frac{dU_e+dU_p}{t\cdot\Delta a}=G^C_{\Delta a} \tag{2}$$

That is, the elastic strain energy stored in the body is partially consumed by the new plastic deformation and crack surface during the crack growth Δa.

Elastic-plastic modeling of the composite material

The stress-strain relationship of the resin at high temperature is highly nonlinear. In contrast, the carbon fiber T300 still behaves linear elasticity under the temperatures from -25° C to 120° C. Therefore, the composite material would be anisotropic plasticity.

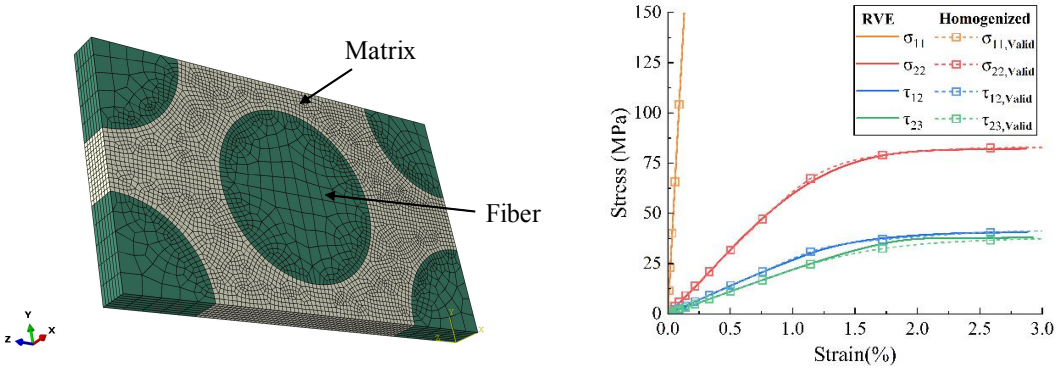

(a) (b)

Figure 51: Elastic-plastic modeling of finite element method (a) RVE of the present composite material;(b) stress-strain curves from micro- and macro- finite element analyses

Determination of the critical $G^C_{\Delta a}$

The DCB tests at room temperature (23℃) are used to calibrate the critical energy $G^C_{\Delta a}$. A trial energy $G^C_{\Delta a}$ was used to simulate the crack growth, and the load-displacement relationship obtained from the simulation is then compared to the experimental results. A good agreement between the simulation from $G^C_{\Delta a}$ = 0.206 N/mm and test results is observed. Consequently, the energy $G^C_{\Delta a}$ of 0.206 N/mm is used as a critical energy for the crack growth analysis. It is subsequently used to predict the DCB tests at temperatures of -25℃, 90℃ and 120℃.

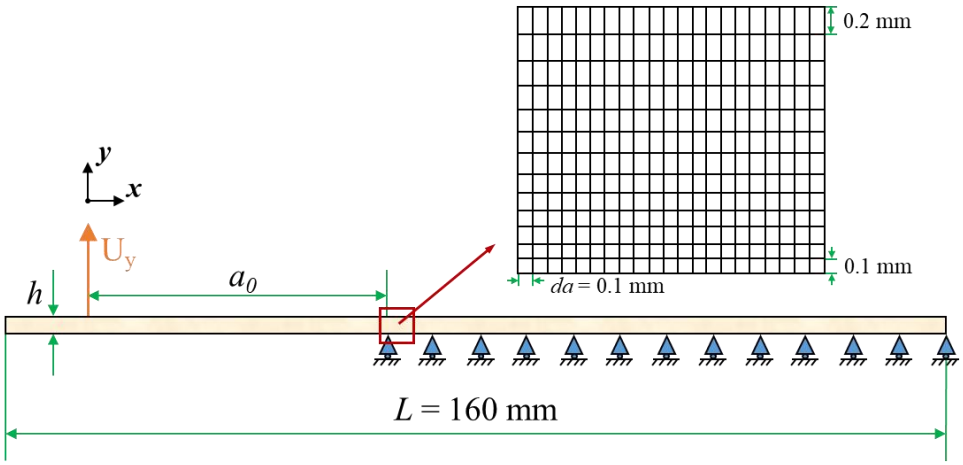

Figure 52: Geometry and boundary conditions of the DCB model

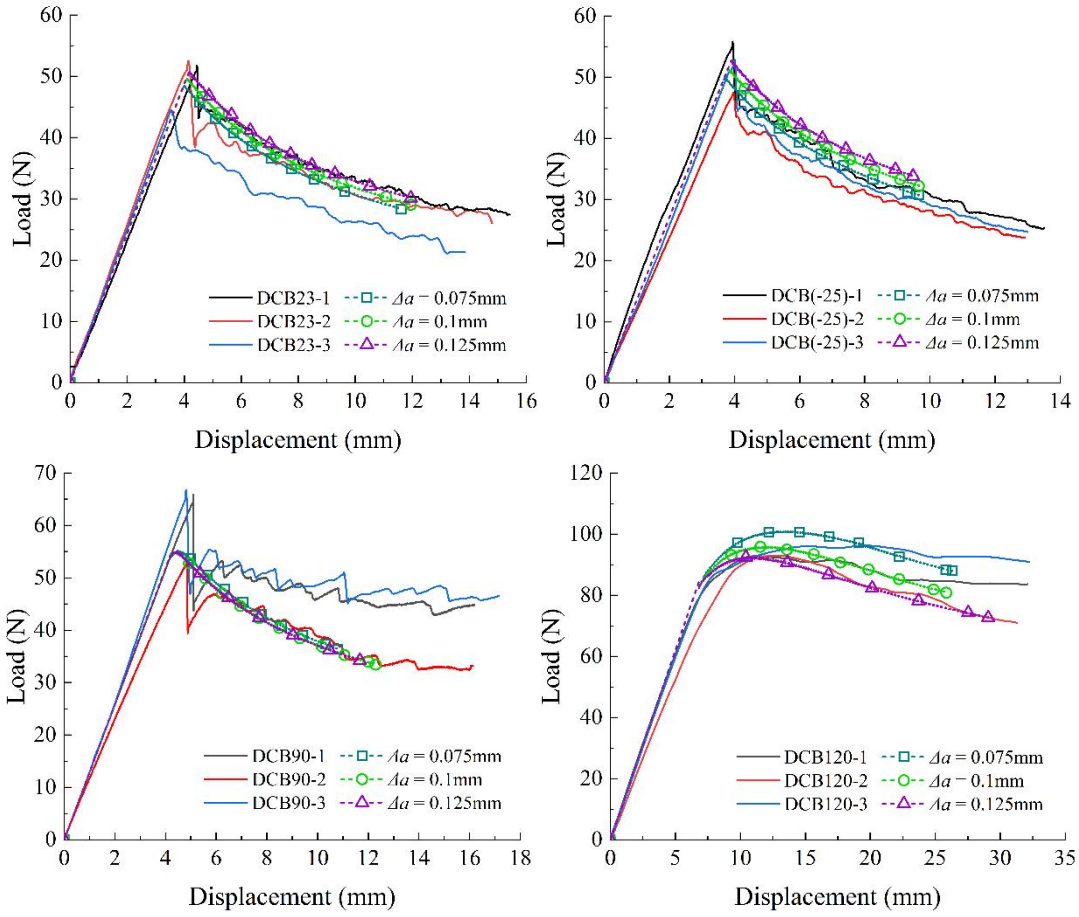

Figure 53: Load displacement obtained from experiments and FEM in different temperatures

3.3 Progressive damage analysis of 3D woven composite SENT test using a ternary model[19]

Single edge notch tension (SENT) test method is available for the crack propagation of 3D woven composite (3DWC). It is of great significance to study the failure mechanism of 3DWC SENT test. In

[19] Shanghai Jiao Tong University, Xu Wu, xuwu@sjtu.edu.cn

this paper, a ternary model is proposed to analyze the damage and fracture of 3DWC. The matrix cracking, yarn rupture, and interface failure between the yarn and matrix are considered in the ternary model. First, the ternary model is verified by the uniaxial tensile test. Subsequently, the SENT finite element (FE) model is established using the ternary model. Progressive damage analysis of SENT tests was conducted. A good consistency of the load-displacement relationships from the SENT FE models and tests is achieved. The failure mechanisms of warp and weft SENT tests are revealed. Finally, the influences of interface failure and yarn fracture toughness on the mechanical behaviors of SENT FE models are discussed. The proposed ternary model can consider the influence of interface failure on the mechanical behavior of 3DWC, compared to the binary model. It is much more efficient than the conformal modeling method.

Ternary model

The concept of the ternary model is shown in Figure 55. Like the binary model, the yarn is modeled by beam element, the matrix is modeled by solid element. An interface element is devised to consider the interface failure in the ternary model. A local coordinate system is necessary for each interface element to ensure that the direction of interface failure is along the yarn. The interface is defined using the VUEL user-defined element. The local coordinate system for each interface element is calculated according to the current node coordinates in the VUEL subroutine.

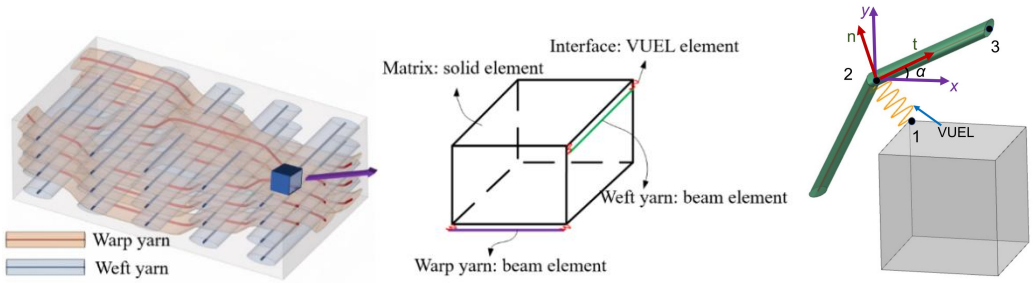

Figure 54: Ternary model and VUEL element

SENT test and FE model

SENT tests were employed to obtain the fracture behavior of the warp and weft 3DWC. The size of SENT specimens is shown in Figure 2. All the tests are performed at room temperature 25℃ and under quasi-static tensile loading at a constant speed 1 mm/min. DIC technology was employed to measure the full-field surface displacement. Speckle was sprayed on the surface to capture the surface morphology. Meanwhile, a camera was used to record the deformation of the SENT specimens.

The SENT FE model shown in Figure 56was established to implement the progressive damage analysis of 3DWC SENT tests. Due to the asymmetry of the weave structure of the SENT specimen, it is necessary to establish a complete SENT FE model. The SENT FE model is divided into two regions: the homogenization model region far from the notch and the ternary model region close to the notch. The homogenization region is assumed to be the linear elastic material. The mesh of the ternary model region was very fine to capture the yarn fracture, matrix crack, and interface failure. The matrix node of the ternary model was moved to the closest yarn node to insert the zero-thickness VUEL interface element.

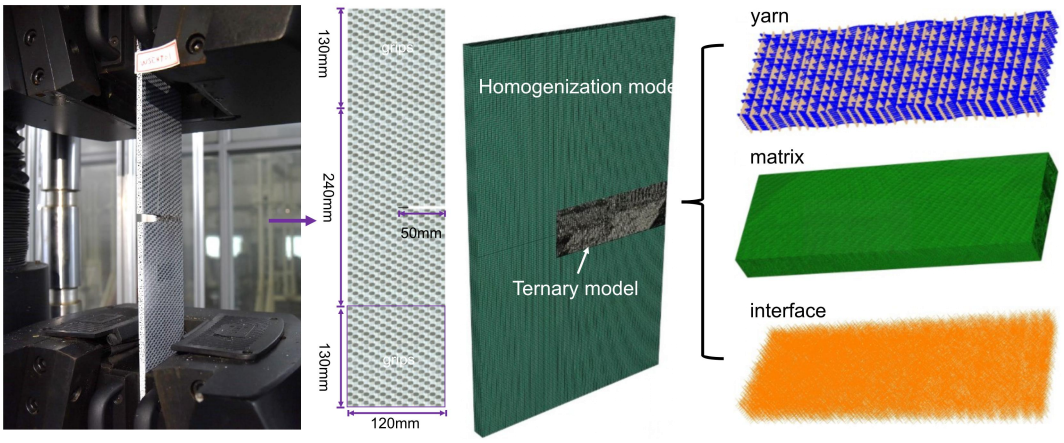

Figure 55: SENT test and FE model

Results and validation

The SENT FE model is firstly validated by comparing the experimentally measured and numerically predicted load-displacement curves. As shown in Figure 3, the SENT FE model does well in predicting the load-displacement response, capturing both the initial stiffness and damage-induced nonlinearity behavior. After crack propagation, the load starts to fluctuate due to the fiber bridging phenomenon.

In order to understand the failure mechanism of the SENT tests, the progressive damage process of the SENT FE model is intuitively displayed in Figure 57. Extensive bridging can be observed in both the warp and weft SENT FE models. With the loading of displacement, the gradual tearing of yarns and the damage propagation of matrix can also be seen in Figure 3. The predicting failure mode is in good agreement with the test. The proposed ternary model is efficient, robust, and suitable for large-scale calculations of 3DWC.

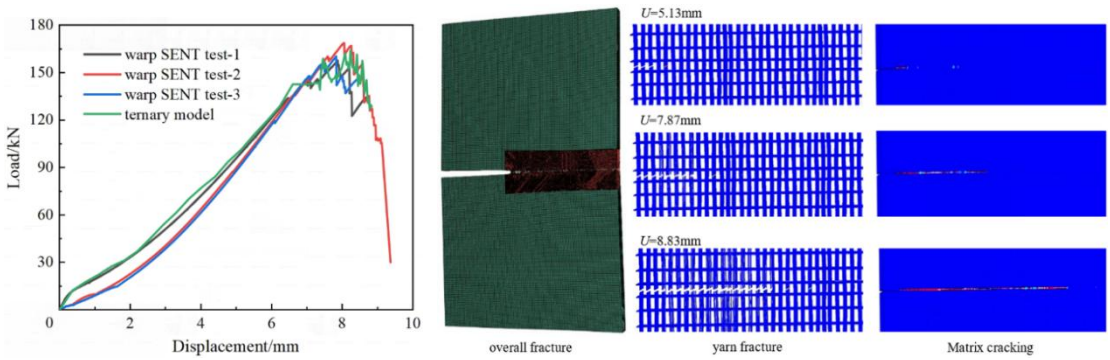

Figure 56: load-displacement relationship and progressive damage process

3.4 The methods to predict the strength of Composite Scarf Repairs Bonded with ductile adhesive[20]

Composite Scarf Bonding is a highly effective structural connection and repair technique widely used in aerospace structures, however, accurate strength prediction of such repairs remains challenging. Now most of the simulation and analytical methods focus on the Composite Scarf Repairs Bonded with

[20] Chinese Aeronautical Establishment, Yan Bing, yanbing@cae.ac.cn

brittle adhesive. In practical applications, selecting ductile adhesives is usually a priority way to obtain higher strength for bonded structures. The mechanical behaviors of brittle adhesives and ductile adhesives are different, which makes their strength prediction strategies different: For joints bonded with brittle adhesives, the maximum adhesive stress determines the joint strength, and assessing stress concentration accurately in bondline is critical to predicting the strength of scarf joints; For ductile adhesives, the failure of scarf joints is governed by maximum strain or fracture toughness, which requires further research.

Strength prediction frameworks

Two strength prediction methodologies for ductile adhesive-bonded composite scarf joints are proposed: a conventional approach and an efficient trace-based approach. Comparative analysis between two-stage and three-stage adhesive models demonstrates that three-stage models achieve superior prediction accuracy in strength estimation. The trace-based model significantly simplifies the prediction process by requiring only the composite material system and its longitudinal elastic modulus, enabling rapid strength assessment during preliminary design stages. This simplified approach can effectively replace conventional non-trace-based models. Validation through experimental data and various simulations shows prediction errors of the proposed models predominantly within 10%. The methodology reveals the mechanical mechanisms of how adhesive ductility enhances structural strength. The framework of the research project is shown in Figure 58.

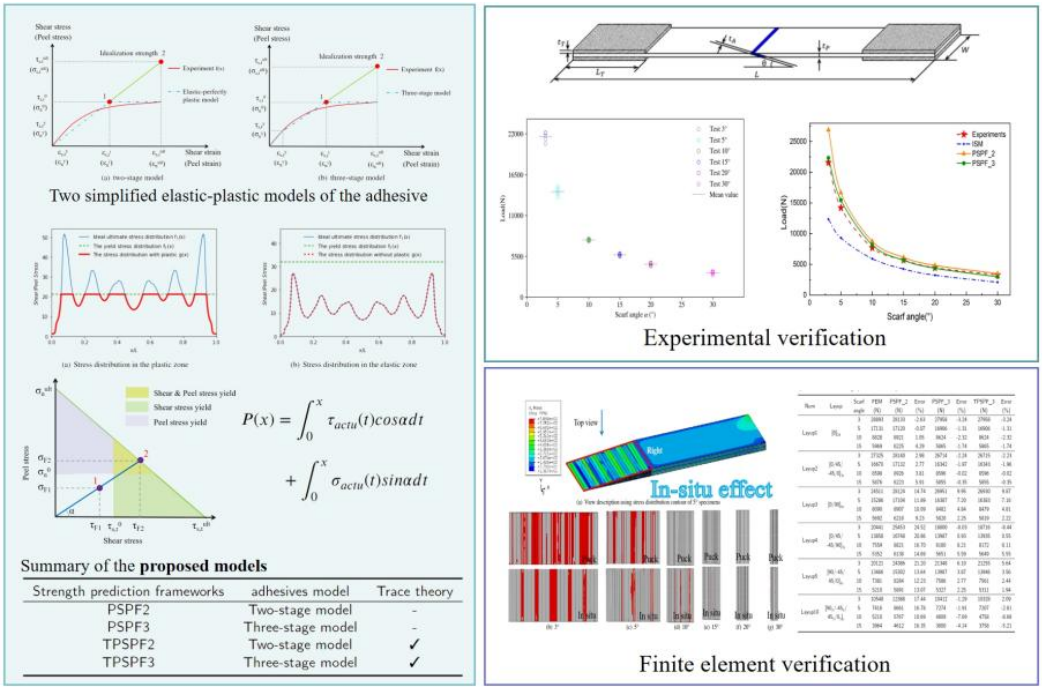

Figure 57: The framework of the research project

Verification of the Strength prediction frameworks

Figure 59 offers a visually comprehensive comparison of the experiments, the PSPF3 model (with three-stage adhesive models), the PSPF2 model (with two-stage adhesive models), and the ISM method which only be used in scarf joints bonded with brittle adhesive. The PSPF3 model perform the best in prediction, and the errors is within 10%. The ISM method are significantly lower than the results of experiments and PSPF3 model, with a maximum error approaching 50%. Therefore, for the scarf joints

with significant ductile adhesive, the PSPF3 model proposed can obtain more precise strength estimation, and it can well characterize the influence of toughness in shear and peeling.

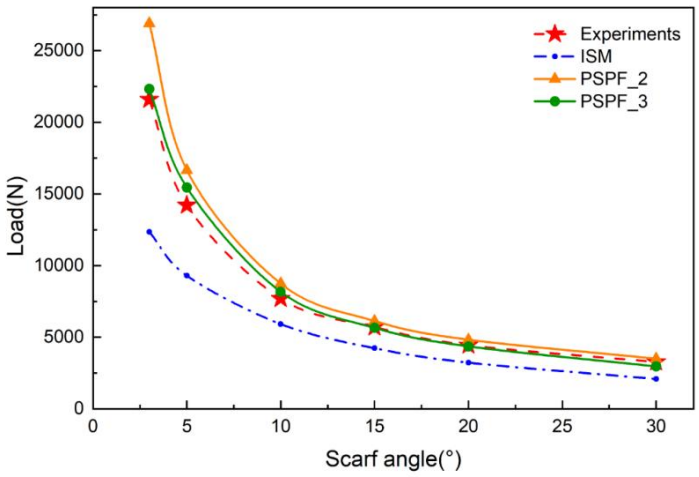

Figure 58: The comparison of prediction performance

The PSPF3 model can also offer insights into the distribution of shear/peeling stresses within the adhesive when joints fail. For instance, considering the 3° and 30° specimens, Figure 60 illustrates the predicted distributions of shear and peeling stresses using the PSPF3 model. For the 3° specimen, there is a noticeable stress concentration phenomenon at the adhesive position corresponding to the 0° ply, and obvious plastic areas can be observed at the outer 0° ply, as shown in Figure 3(a). With the scarf angle increases to 30°, as depicted in Figure 3(b), the stress concentration phenomenon gradually diminishes, approaching the stress distribution characteristics of scarf joints using an isotropic adherend. Additionally, the role of peeling stress in load capacity becomes more pronounced as the scarf angle increases, as indicated by the green line in Figure 15(b).

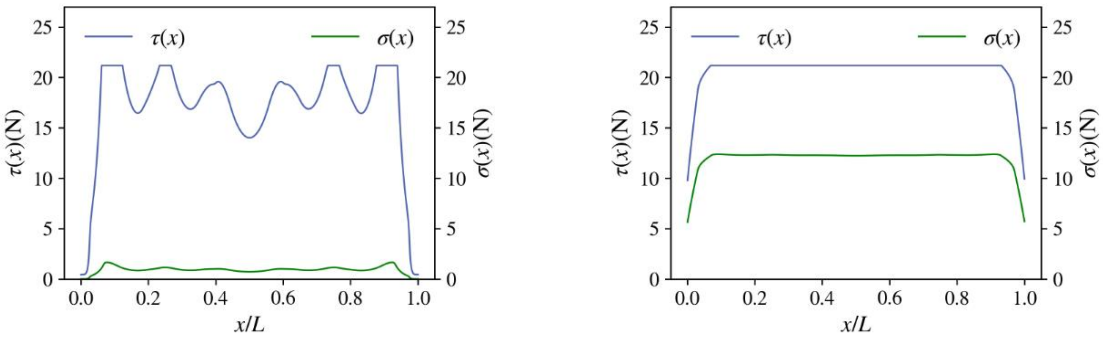

(a) 3° scarf angle (b) 30° scarf angle

Figure 59: The distribution characteristics of adhesive peeling stress and shear stress when 3° and 30° specimens fail

3.5 Micromechanics-based composites failure criteria and applications[21]

Carbon fiber-reinforced polymer (CFRP) composites are widely used in aerospace due to their

[21] Beihang University, Wang Xiaodong, xiaodongwang@buaa.edu.cn

excellent mechanical properties and design flexibility. However, composites exhibit multiphase, multiscale structural characteristics, leading to significant anisotropy and complex failure mechanisms, which makes it highly challenging to predict the strength under complex loading conditions.

A micromechanics-based failure criterion is proposed based on micromechanics failure mechanisms through multi-scale simulation. Besides, an efficient computational method for proposed criterion is proposed to improve their application.

Micromechanical Simulation Methods and Failure Mechanism Analysis

A new random generation algorithm was proposed inspired by molecular dynamics to generate accurate geometric model. Long-range force is introduced between fibers to control fiber distribution. Statistical analysis results proved that the generated distribution is statistically equivalent to that of real composites. Besides, this method can generate arrangements with fiber volume fraction up to 80%.

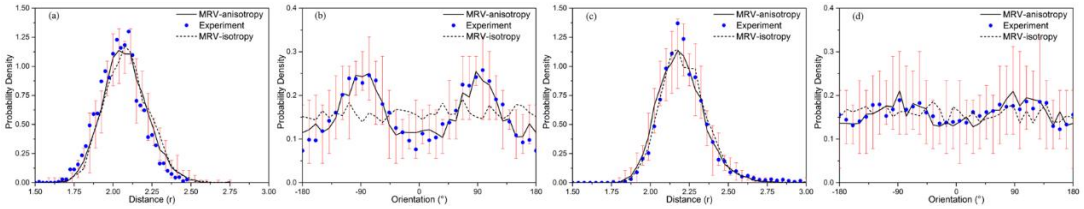

Figure 60: Comparison of the statistical distribution between generated arrangements and real composites

Micromechanical simulation results show that transverse failure, inter-fiber properties (interface and matrix properties) dominated failure, initiates from stress concentration caused by the modulus difference between fibers and matrix. Besides, under longitudinal compressive load, there is a competitive mechanism between two failure modes: inter-fiber property-dominated kink-band failure and fiber property-dominated fiber bending failure.

Failure Criteria Based on Micromechanics and Constituent Failure

Novel failure criteria were proposed based on the failure mechanism. According to the failure modes, the failure criteria are divided into transverse failure criterion and longitudinal failure criterion.

In the transverse failure criterion, the calculation formula for the fiber/matrix interfacial stress under macroscale stress was derived based on Eshelby's inclusion theory. The failure of interface was determined using the Mohr-Coulomb criterion, thereby predicting the strength of composites under transverse stress. In the longitudinal compression criterion, considering the initial misalignment of fibers, analytical formulas for macroscale stress, inter-fiber stress, and intra-fiber stress were established through stress analysis. Two failure mode-based criteria were developed according to inter-fiber failure and fiber bending failure.

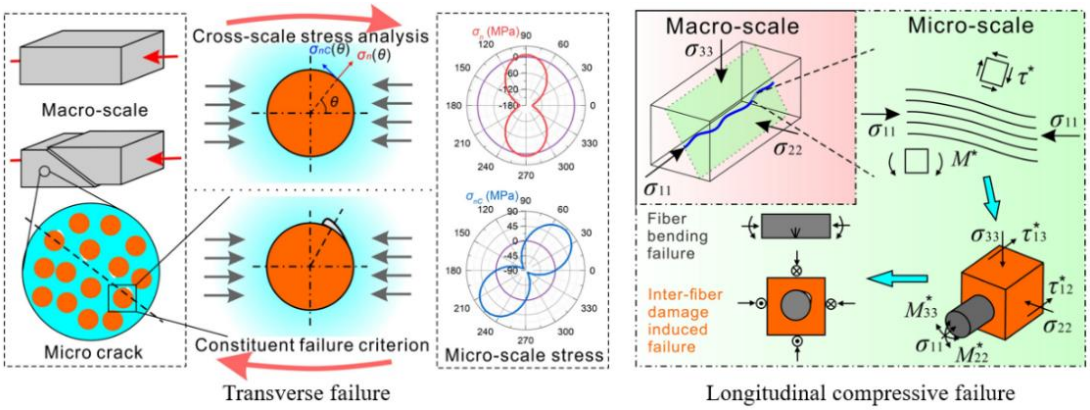

Figure 61: Schematic diagram of failure criterion based on micromechanics and constituent failure

The comparisons with existing experimental results demonstrate that the proposed criteria have good accuracy on predicting the strength of composites.

Efficient Fracture Surface Search Algorithm and Application

To improve the computational efficiency of the proposed failure criteria in searching for fracture surfaces, an algorithm based on the characteristics of failure index curve, classified local golden section search (CLGSS) algorithm, was proposed. The time cost of failure criteria using this algorithm is only 10% of that using the original algorithm.

The failure behavior of composites of Iosepescu test was simulated, the stress-strain curves and failure modes showed excellent agreement with experimental results, demonstrating the effectiveness and accuracy of this method in predicting the failure behavior of composites under complex loading conditions.

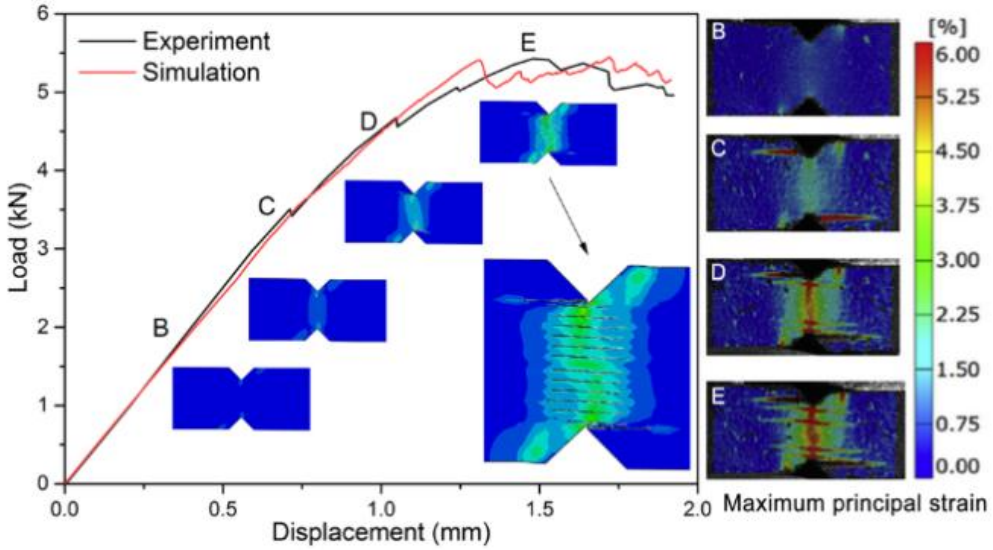

Figure 62: The comparison of experimental and simulated results of composites under longitudinal shear test

3.6 Design and fabrication of high-performance multifunctional composite structures[22]

[22] Northwestern Polytechnical University, Li Yuexuan, liyuexuan@nwpu.edu.cn

The high-performance electromagnetic capabilities of weaponry and equipment primarily rely on external structural designs and functional materials. While external structural design can effectively reduce the radar cross-section (RCS) of aircraft, aerodynamic shape constraints limit its improvement in electromagnetic performance. Furthermore, most existing functional materials are applied as coatings on the surface of aircraft structures. These electromagnetic functional coatings often exhibit limited absorption bandwidth and are prone to cracking and peeling under extreme service conditions, which significantly compromise the electromagnetic stealth performance of the aircraft. Therefore, new-generation aircraft urgently need to evolve toward low detectability, structural/functional integration, and intelligent design to meet the demands of rapid interconnection and operational collaboration across domains such as air, space, cyberspace, sea, and land.

Lightweight and multifunctional design of composite sandwich structures

To address varying electromagnetic functional requirements, the study leverages the load-bearing advantages and electromagnetic design potential of various composite sandwich structures. By incorporating the functional characteristics of different meta-structures, several types of electromagnetic functional load-bearing structures were designed and subjected to multi-level evaluations of their electromagnetic and mechanical performance.

Figure 64 illustrates the unit cell of the square honeycomb enhanced absorbent honeycomb structure (SHEAHS). This structure comprises three main components: glass fiber face panels, glass fiber square honeycomb grid structure with excellent mechanical performance, carbon fiber meta-structure attached to the grid, along with a carbon fiber reflective base plate.

The SHEAHS was developed by embedding a square honeycomb structure (SHS) into an absorbent honeycomb structure (AHS). From an electromagnetic perspective, the integrated synergistic structure uses a high-performance absorbent honeycomb structure as its base and exploits the highly designable electromagnetic properties of meta-structures. This approach significantly improves the absorption performance of the honeycomb structure, resulting in broader bandwidth, larger incident angles, and higher electromagnetic wave absorption efficiency.

From a mechanical perspective, the grid structure with excellent mechanical properties is embedded into the absorbent honeycomb structure. This integration utilizes the synergistic effect between the two components to enhance mechanical characteristics, such as specific compressive strength and energy absorption. The proposed SHEAHS demonstrates an average electromagnetic wave absorption rate of 94.9% across the 2~18 GHz range, far exceeding the performance of the original AHS and SHS structures. Compared to the original absorbent honeycomb structure, the integrated structure achieves: a 57.8% reduction in average electromagnetic wave reflectivity over the 2 – 18 GHz range. A 75.2% reduction in reflectivity in the 3~5 GHz low-frequency range, with significantly reduced fluctuation. These results highlight the superior electromagnetic and mechanical performance of the proposed SHEAHS design.

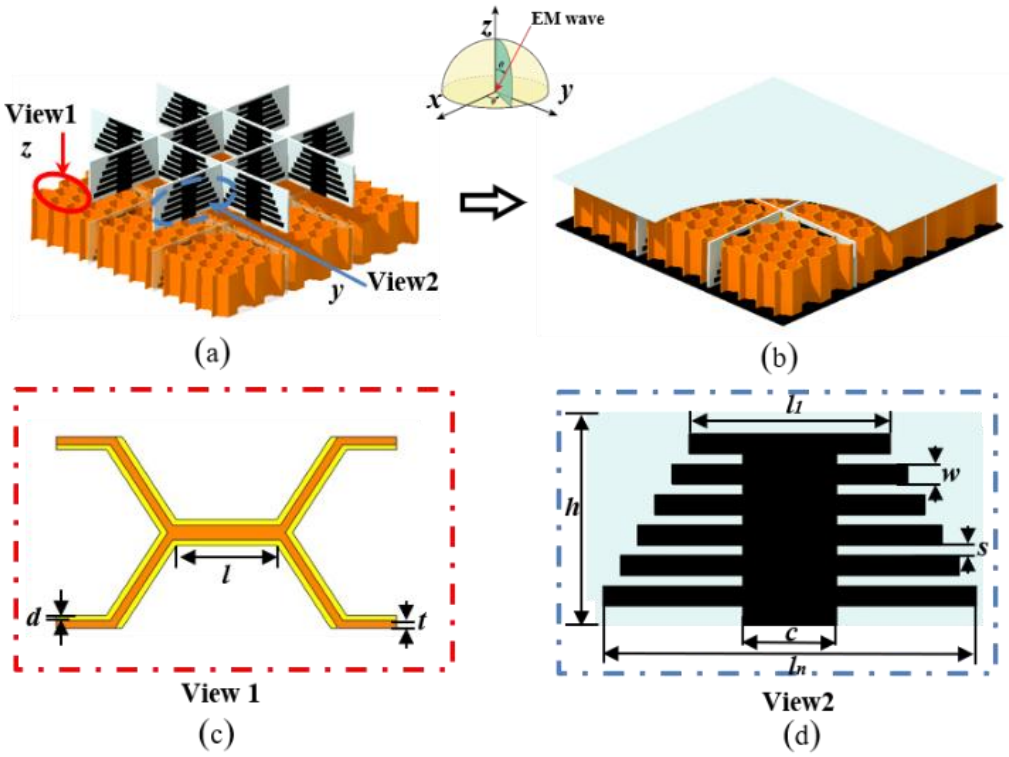

Figure 63:. Structural forms of unit design: (a) grille-enhanced honeycomb core, (b) integrated structure, (c) honeycomb unit cell diagram and dimensions, (d) carbon fiber meta-structure diagram and dimensions.

Based on a similar design approach, the study introduces a carbon fiber meta-material array sewn into a multi-level corrugated core structure, resulting in a carbon fiber enhanced multi-level corrugated wave-absorbing structure, as shown in Figure 65. Leveraging the unique electronic/mechanical properties of carbon fibers, in addition to constructing surface-selectively plasmonic patterns (SSPPs) to achieve efficient, artificially tunable electromagnetic performance, the structure exhibits broadband (4~12GHz), high intensity (average absorption rate > 90%) electromagnetic wave absorption capabilities. Furthermore, by reducing the buckling wavelength of the core's wall panels, the failure mode of the core was altered, leading to a 16.7% increase in the structure's specific compressive.

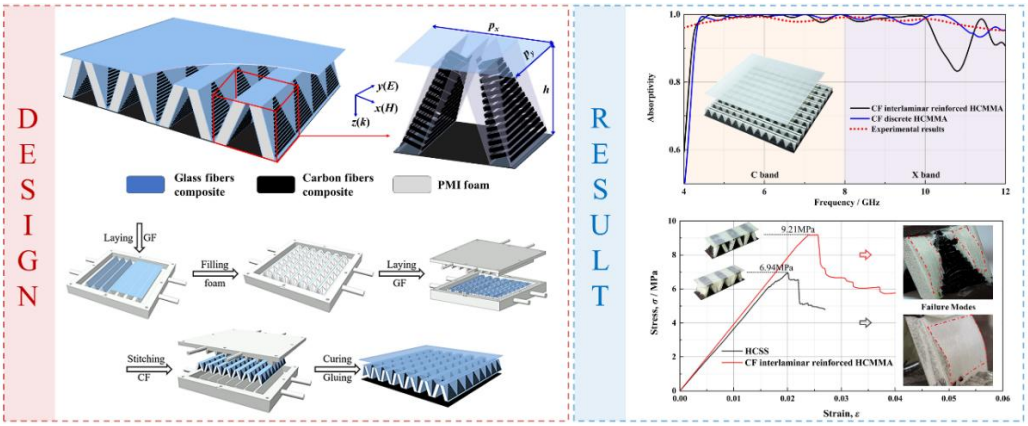

Figure 64: Preparation Process and Electromechanical Performance Characterization of Carbon Fiber Sewn-Enhanced Multi-Level Corrugated Wave-Absorbing Structure

Additionally, to address the issue of low transmission rate in traditional PMI foam core sandwich

structures, which affects radar antenna performance, the study fills the foam core with FR-4 grid wall panels that feature a parabolic meta-material structure on the surface. By optimizing the structural configuration of the metamaterial on the grid wall surface, the proposed novel anti-reflection load-bearing integrated structure achieves more than 80% broadband enhancement (from 8 GHz to 18 GHz) compared to the original foam core sandwich structure. Furthermore, its compressive strength and energy absorption per unit volume are improved by 95% and 72%, respectively, compared to ordinary PMI foam core structures. This leads to an integrated design that enables multi-angle, broadband electromagnetic wave transmission and high-strength load-bearing performance, as shown in Figure 66.

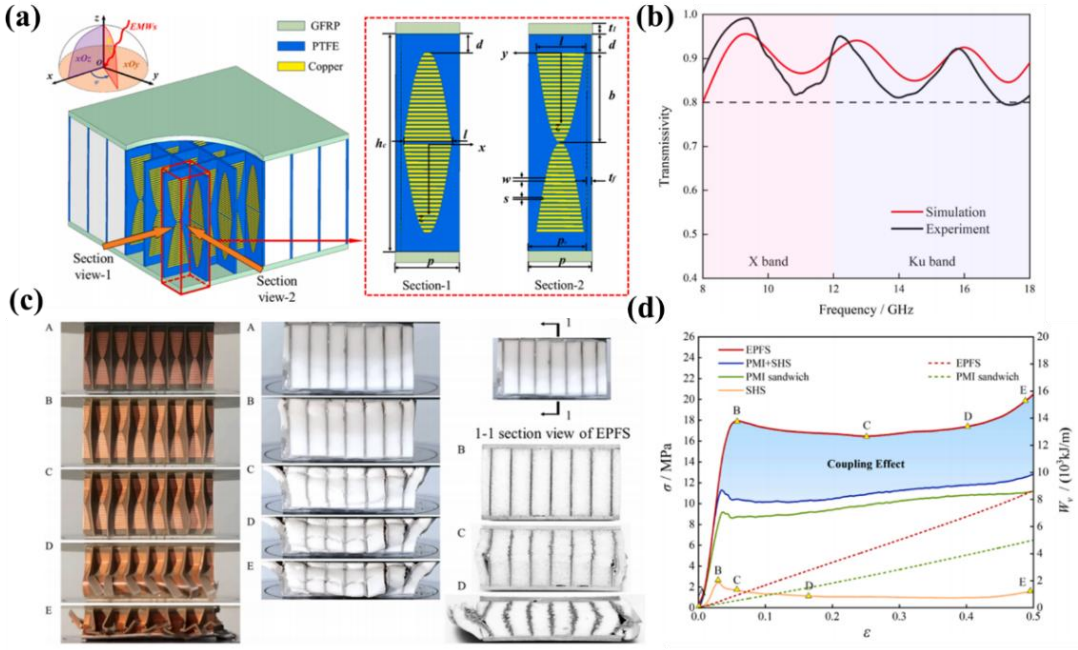

Figure 65: Anti-Reflection/Load-Bearing Integrated Electromagnetic Functional Structure: (a) Unit structure, (b) Transmission performance, (c) Failure process of the structure during compression, (d) Quasi-static compression stress-strain diagram.

3.7 A High-Confidence Lightweight Composite Wing Design Method Integrating Static and Dynamic Loads[23]

Traditional Optimization Methods and Their Limitations

In the iterative design process of aircraft structures, due to the complexity of professional expertise and the intricate nature of repetitive design iterations, current size definition workflows are inadequate to meet the high-efficiency demands of aircraft design. When performing size optimization for large structural components, traditional optimization design methods based on GFEM (Generalized Finite Element Method) are typically employed, characterized by: Optimization based on GFEM models; application to typical aerospace structural element characteristics (e.g., stiffened panels) and inconsistent models across different disciplines (statics vs. dynamics). For smaller aircraft, their typical structural features are not as pronounced compared to the unit sizes of GFEM models. This leads to

[23] Chinese Aeronautical Establishment, Sun Qixing, sunqixing@cae.ac.cn

significant limitations when optimizing based on structural units in critical areas.

Present Work

Taking the wing of the principle verification machine as the research object, this study fully considers the structural details of the wing. It builds a high-confidence dynamic model for the tilt rotor aircraft wing by simulating real boundaries, designing precise layup zones, implementing multi-material layup design, and accurately simulating structural mechanical connections and adhesive layer connections. This provides engineering estimates and precise analysis evaluations for wing structure design, as well as necessary structural parameter inputs for calculating air elastic stability in rotary flutter.

The present work used integrated static and dynamic wing structure lightweight design technology and constructed a detailed integrated static and dynamic structural model DFEM (Detailed Finite Element Method). Low-cost structural optimization design for four-tilt civilian high-speed rotorcraft was also conducted

Regarding inertial load calculation, parameters are balanced using total aerodynamic force, torque, center of pressure, structural weight, centroid location, and moment of inertia data. Overload and angular acceleration under current aerodynamic conditions are computed, along with nodal inertial forces based on overall aircraft mass distribution. The process effectively integrates both aerodynamic and inertial loading into the structural analysis, providing accurate simulation of real-world operating conditions during the optimization phase.

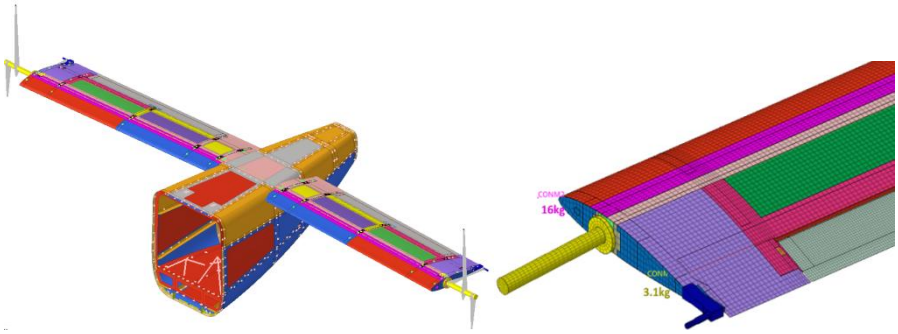

Figure 66: True boundary simulation DFEM model and concentrated mass distribution model

Constrained optimization problems must satisfy the Kuhn-Tucker conditions at their optimal points. To find the optimal solution, two main approaches can be employed: direct methods and dual methods. The appropriate mathematical programming method is automatically selected based on specific problem requirements, differing from traditional optimization criterion-based methods.

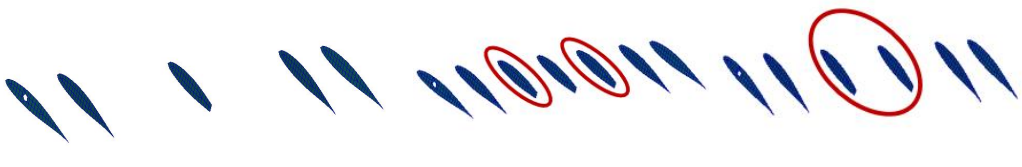

Figure 67: Comparison of three cases of rib designs

After comparing the three rib configurations, adding more rear wing ribs has a very slight positive effect on the mode but is not beneficial for structural weight reduction. It is recommended to use the

configuration with the fewest ribs.

Subsequently, fine modeling and finite element analysis of the model were carried out. The cloud maps of static deformation, structural dynamic response, and comparisons before and after optimization are shown in the figure below. At the low-frequency stage, dynamic stiffness approaches static stiffness, indicating that stiffness dominates in the low-frequency region. At the high-frequency stage, mass terms primarily dominate above the resonance frequency range. A significant decrease in the amplitude of dynamic stiffness occurs at the resonance frequency, suggesting that damping control is dominant at the resonance frequency.

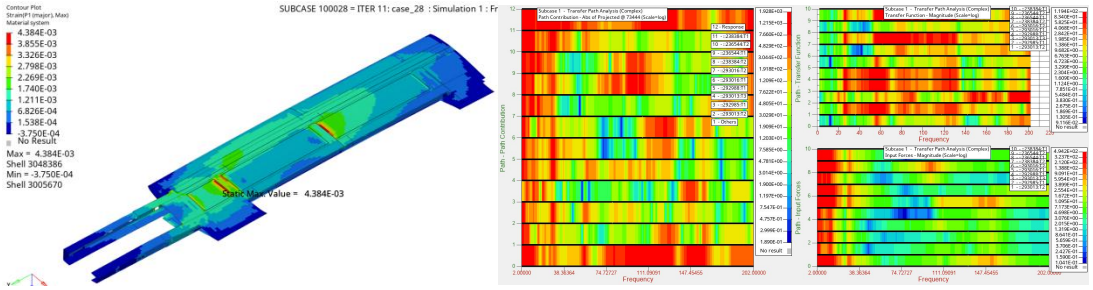

Figure 68: Contour maps of static deformation and dynamic response results of the structure

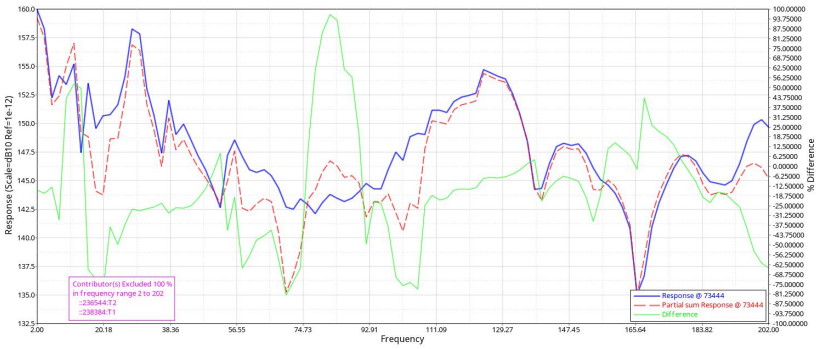

Figure 69: Comparison of optimization (before and after)

Through refinement of the DFEM optimization model and subsequent analysis and verification of its optimized results, it was confirmed that both static strain and stability in the detailed model meet design requirements. This validation demonstrates the feasibility and practical significance of the optimized DFEM model. The project achieved the goal of high-confidence lightweight coupled dynamic-static optimization design for composite materials, ultimately reducing the structure weight by 19%.

4 Reliability and risk-analysis of structures and mechanisms

4.1 Generative adversarial surrogate modeling framework for aerospace engineering structural system reliability design[24]

To effectively realize the reliability design of engineering structural system, a generative adversarial surrogate modeling (GASM) concept is proposed by innovating generative adversarial theory into surrogate modeling methods, which realize the aerospace engineering structural system reliability

[24] Northwestern Polytechnical University, Feng Yunwen, fengyunwen@nwpu.edu.cn

design adversarial modeling. Under the GASM concept, the generative adversarial polynomial chaos expansion (GAPCE) method is developed to achieve aerospace engineering structural system reliability design. The effectiveness of presented GAPCE is verified by the reliability design of flap deflection angle reliability estimation. The reliability level of flap deflection angle is 0.9998, when the allowable values are 9°. Besides, the introduced approach possesses advantages of modeling performance (i.e., modeling accuracy and efficiency) and simulation properties (i.e., simulation precision and efficiency) by comparing with various methods. The efforts of this paper can provide a valuable reference for the operational safety of flap systems and the development of reliability design theory.

Generative adversarial polynomial chaos expansion method

The GAPCE method is proposed under the GASM concept for aerospace engineering structural system reliability design by combining the polynomial chaos expansion and generative adversarial theory. In this method, the polynomial chaos expansion is utilized as a basis function to approximate the functional relationship between input variables and output response; the generative adversarial theory is applied to optimize and determine the final GAPCE model by confrontation analysis and feedback evolution.

Reliability analysis of flap deflection angle

The reliability design of flap deflection angle is adopted to illustrate the effectiveness of GAPCE method from the perspective of engineering application. Based on the composition and working principle of the flap system (Figure 70), the fault logic diagram are determined respectively combining the functional hazard assessment, failure mode and effects analysis, and fault tree analysis. Then the relationship between flap angle and influencing factors can be described. The 900 samples of quick access recorder are obtained for the reliability evaluation of flap deflection angle, the mean and standard deviation of the influencing parameters are obtained. The 600 samples are used as training samples to establish the GAPCE model, and the remaining 300 samples are taken as testing samples to verify the effectiveness of the GAPCE model. According to the training samples, the functional relationship of flap deflection angle and related influencing parameters are determined by the GAPCE approach. The reliability degree of flap deflection angle is converging to 0.9998 with the number of samples increasing.

The modeling performances and simulation properties of the GAPCE model are validated by various methods, which contain the response surface method (RSM), Kriging, back propagation-artificial neural network (BP), polynomial chaos expansion (PCE), and polynomial chaos Kriging model (PCK) methods. The RSM, Kriging, BP, PCE, PCK, and GAPCE models are established by 600 training samples, and the modeling accuracy and modeling efficiency are represented in Figure 71 andFigure 71: Modeling accuracy analysis Figure 72: Modeling efficiency.

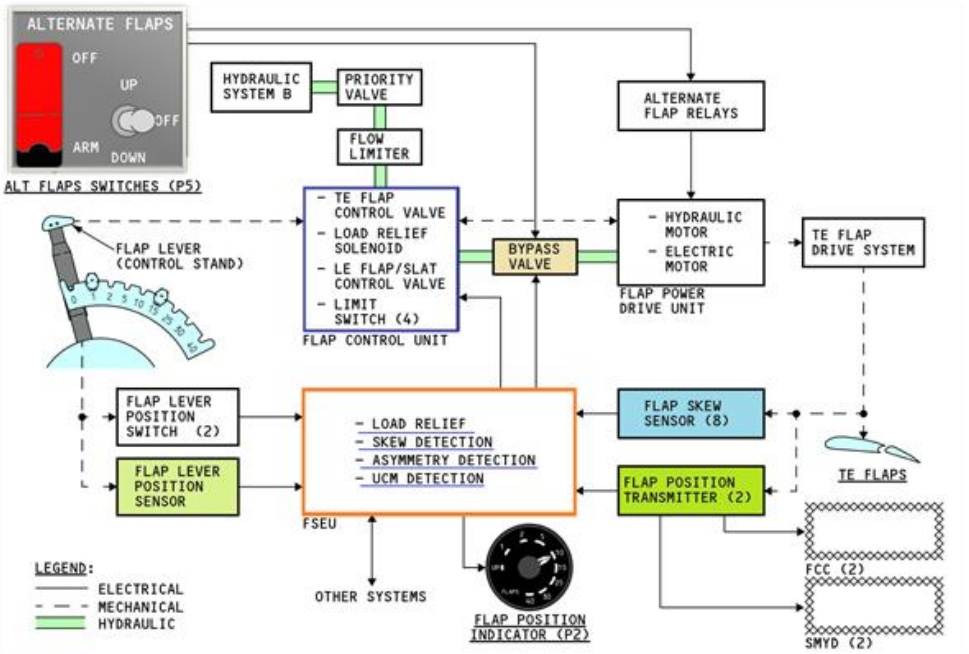

Figure 70: Working principle of the flap system

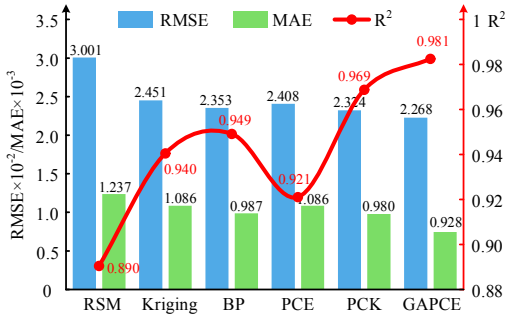

Figure 71: Modeling accuracy analysis

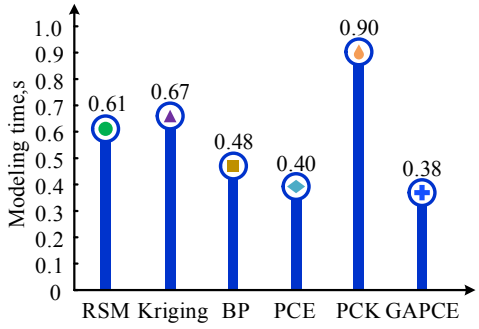

Figure 72: Modeling efficiency

To verify the simulation properties of GAPCE method, the reliability analysis of flap deflection angle is performed by the RSM, Kriging, BP, PCE, and PCK methods. The simulation accuracy and efficiency under different simulation times are shown in Figure 73 and Figure 74, respectively.

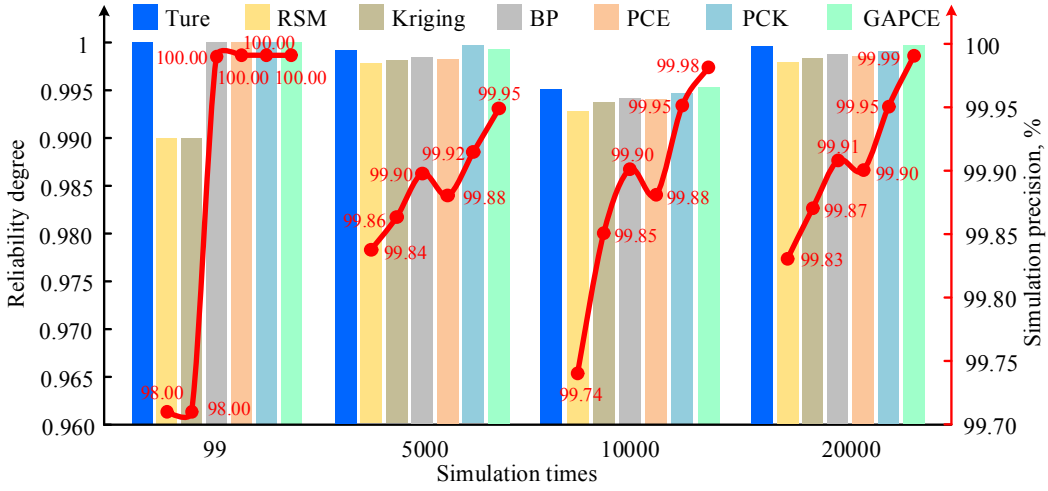

Figure 73:Simulation precision with different methods and simulation times

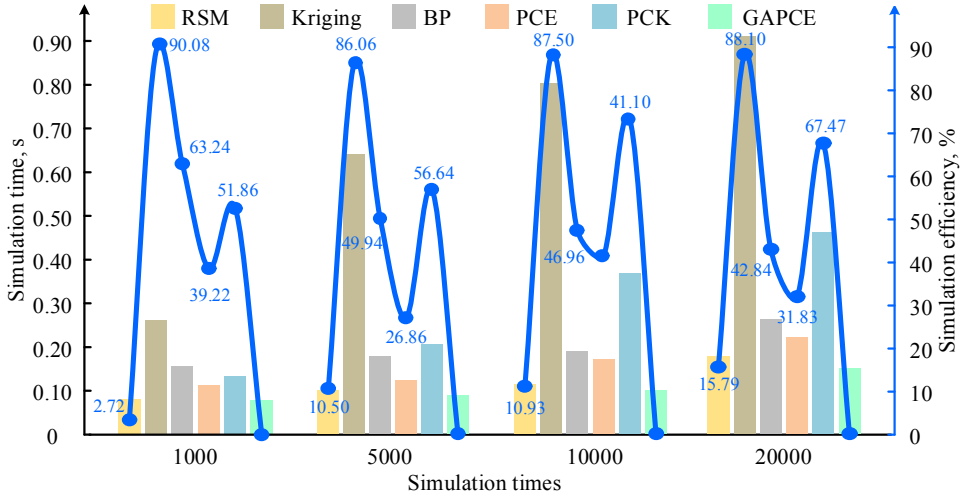

Figure 74: Simulation efficiency with different methods and simulation times

As a result, the proposed GAPCE model has certain simulation properties advantage for the reliability analysis of flap deflection angle by comparing the RSM, Kriging, BP, PCE, and PCK methods.

4.2 Intelligent vectorial surrogate modeling framework for multi-objective reliability estimation of aerospace engineering structural systems[25]

To improve the computational efficiency and accuracy of multi-objective reliability estimation for aerospace engineering structural systems, the intelligent vectorial surrogate modeling concept is presented by fusing the compact support region, surrogate modeling methods, matrix theory, and Bayesian optimization strategy. Under this concept, the intelligent vectorial neural network (IVNN) method is proposed based on deep neural network to realize the reliability analysis of multi-objective aerospace engineering structural systems synchronously. The landing gear brake system temperature multi-failures is used to verify the applicability of IVNN method. The results indicate that the proposed approach holds advantages in modeling properties and simulation performances. The efforts of this paper can offer a valuable reference for the improvement of multi-objective reliability assessment theory.

Reliability assessment of landing gear brake system temperature with multi-failures

To verify the effectiveness of proposed IVNN model in the engineering system field, the reliability assessment of landing gear brake system temperature (LGBS) temperature with multi-failures is performed. Based on the LGBS composition and working principle (Figure 75), the LGBS temperature fault logic diagram is constructed to clarify the fault-related parameters of the brake temperature. 1500 samples are obtained from the aircraft quick access recorder of a certain flight, which are further divided into 1000 training samples and 500 testing samples. Based on the training samples, the functional relationship of left LGBS temperature difference, right LGBS temperature difference, and left and right LGBS temperature difference with correlation parameters established synchronously by the IVNN model. The reliability degree of LGBS temperature gradually converges to 0.9982 as the number of simulation times increases. The analysis results can provide guidance for the fault monitoring and optimized design of the landing gear system.

[25] Northwestern Polytechnical University, Feng Yunwen, fengyunwen@nwpu.edu.cn

The response surface method (RSM), Kriging model, support vector machine (SVM), Back Propagation (BP)-artificial neural network, and Vectorial BP (VIBP), and IVNN models are determined by the 1000 training samples. the modeling accuracy and efficiency of various methods with 500 testing samples are illustrated in Figure 76 and Figure 76: Taylor diagram of various methods Figure 77: Modeling time of various methods

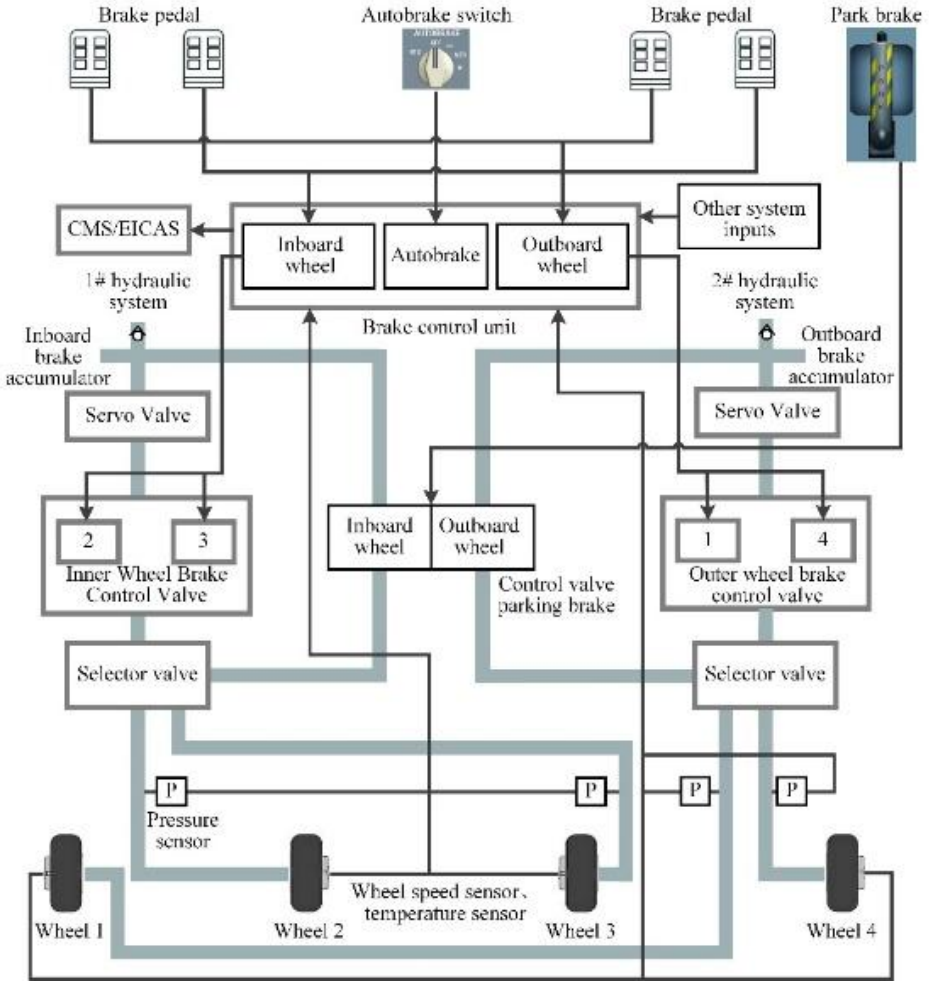

Figure 75: Working principle of LGBS

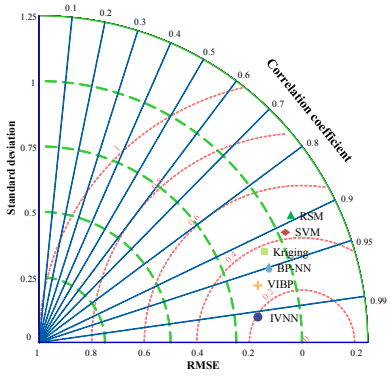

Figure 76: Taylor diagram of various methods

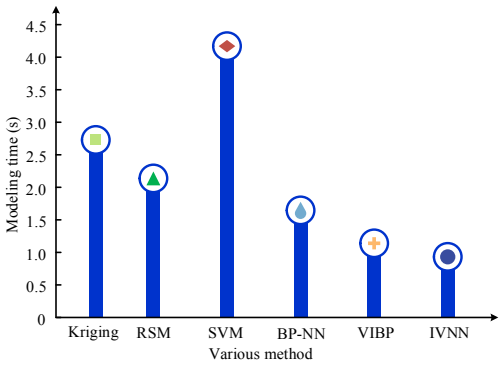

Figure 77: Modeling time of various methods

Combined with the established limit state equation of the LGBS temperature, the reliability analysis of different methods is realized with $5\times10^3$and 2×10^4 simulation times, and the simulation precision and

efficiency are shown in Figure 78and Figure 79, respectively.

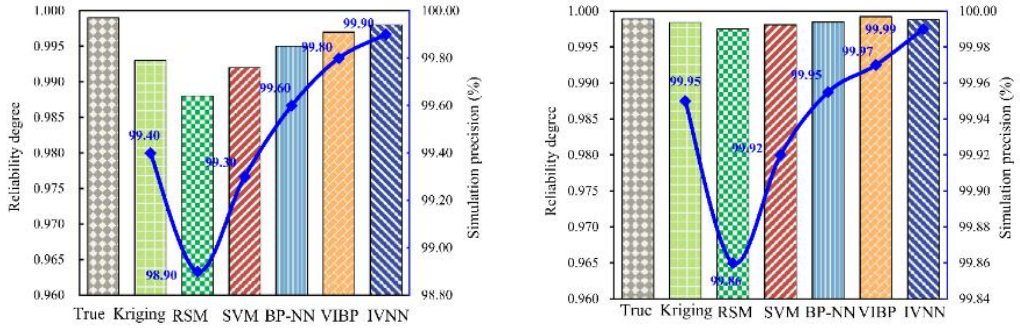

(a) 5000 simulation times (b) 20000 simulation times

Figure 78: Simulation precision of different methods for LGBS temperature

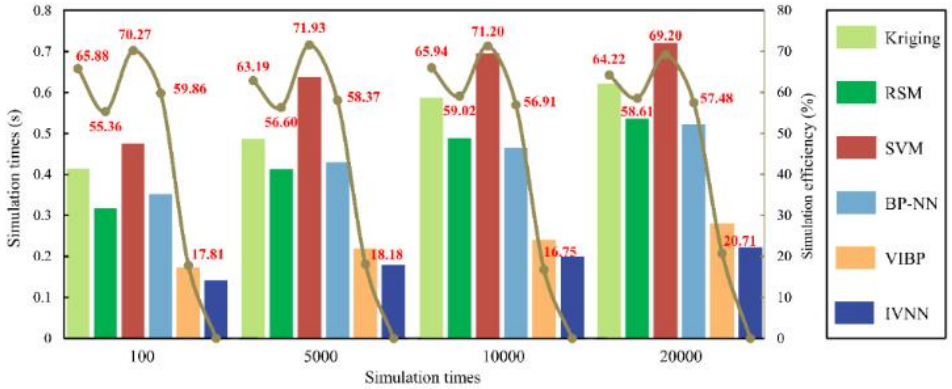

Figure 79: Simulation efficiency of different methods for LGBS temperature

Therefore, the proposed IVNN model has the modeling performances and simulation properties for the reliability assessment of LGBS temperature with multi-failures.

4.3 Fatigue reliability analysis of complex flap hinge mechanism [26]

The decomposition-coordination surrogate model can decompose multiple components of a complex mechanism into individual components where relationships between the output response of each single component and its relevant variables are separately established. By integrating the relationships between the output responses of all components and the total output response it coordinates individual component output responses with the total output response to determine the mathematical model linking the total output response to all variable parameters. This complex mathematical model is then replaced and computed via the surrogate model. The stochastic degradation process simulation technology combines performance degradation data from crack propagation and wear with crack propagation simulation curves and hinge wear curves. Through selected degradation models integrated with the decomposition-coordination surrogate model it calculates the lifespan of the flap hinge structure based on crack propagation failure and wear failure. The reliability under different failure modes is subsequently derived through further computations.

Application of technology

This research has been applied to the fatigue reliability analysis of hinge mechanism in a complex flap

[26] Aircraft Strength Research Institute, Li Chen, lic373@avic.com

mechanism, and its structure is shown in the figure below.

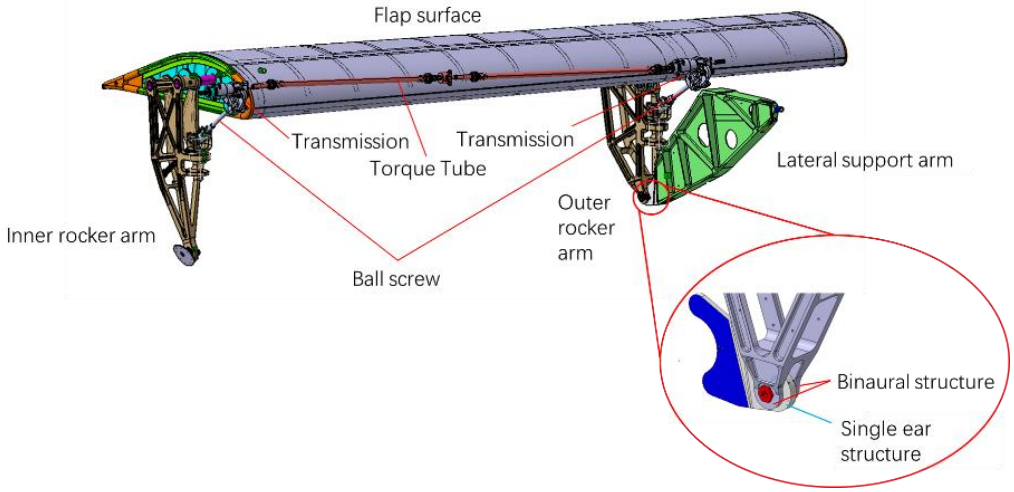

Figure 80: Schematic diagram of complex flap hinge mechanism

Based on the structural composition and load-bearing characteristics of the flap hinge mechanism, the primary failure modes are initially identified as crack propagation failure in the hinge lug and wear-induced failure in the bearing respectively. Corresponding failure physics models and stochastic processes are determined through failure mechanism analysis and comparative studies of stochastic degradation processes. Subsequently, crack propagation curves and wear displacement curves for both failure modes are obtained via software simulations. Finally, a fatigue reliability analysis methodology is established by applying the Gamma stochastic degradation process and analytical coordination strategy to the hinge lug and bearing structures. This methodology leverages the decomposition-coordination surrogate model and employs log-normal distributions to derive reliability curves for both crack propagation failure and wear-induced failure in the hinge mechanism under different operational conditions.

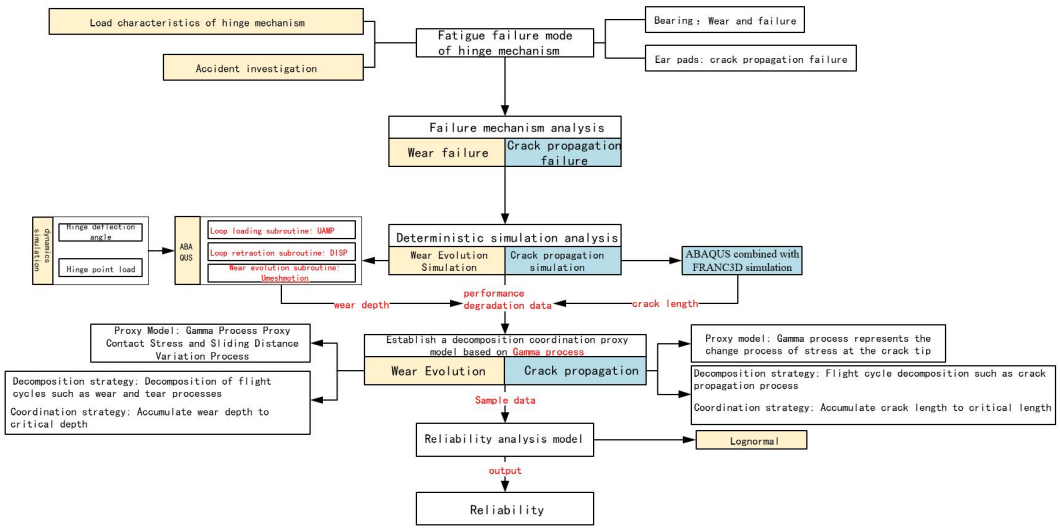

Figure 81: Reliability analysis of flap hinge mechanism based on decomposition coordination proxy model

Reliability analysis of flap hinge mechanism based on decomposition coordination proxy model Based on the decomposition-coordination surrogate model and stochastic degradation process simulation

technology, fatigue reliability analysis of complex flap hinge mechanisms can be conducted which enables early detection of potential issues in flap systems ensures flight safety reduces operational and maintenance costs and provides data support for design optimization and material selection of flap mechanisms.

5 Fatigue life enhancement methods and repair solutions

5.1 Effect of residual stress distribution on fatigue crack path of LPBF Ti6Al4V [27]

Residual stress (RS) in laser powder bed fusion (LPBF) additive manufactured structures can significantly affect mechanical performance, potentially leading to premature failure. The complex distribution of residual stresses, combined with the limitations of full-field measurement techniques, presents a substantial challenge in conducting damage tolerance analyses of aircraft structures. To address these challenges, this study developed a comprehensive simulation framework to analyze the 3D distribution of residual stresses and fatigue crack growth in LPBF parts. The 3D residual stress profiles of as-built samples were computed and compared to experimental data. The fatigue crack propagation behavior considering 3D residual stress was predicted, and the effects of RS redistribution under cyclic loading were discussed. It shows that the anisotropy of RS can lead to mixed-mode fracture and subsequent crack deflection. Tensile residual stress in the near-surface region and compressive stress in the inner region can cause an inverted elliptical crack front and accelerate fatigue crack growth.

Application of technology

X-ray diffraction is limited to measuring only surface residual stresses, making it difficult to assess the effect of 3D residual stress state on fatigue crack propagation and AM structural integrity. To address this, a combined approach involving both experimental measurements and numerical simulations provides a comprehensive and effective method. The flowchart of model is shown in Figure 82.

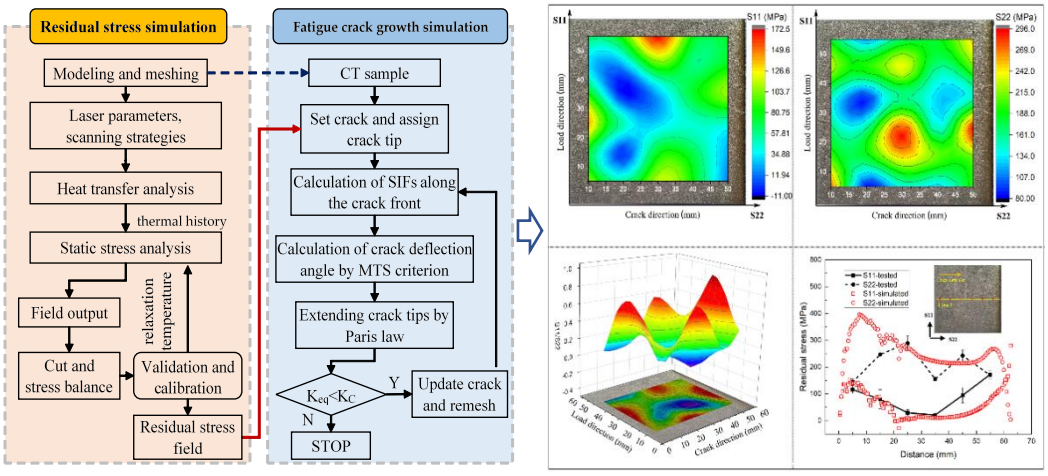

Figure 82: Flowchart of simulation model and validation of residual stress

The fracture surface, crack path, and K_{res} distribution along the crack length were analyzed and

[27] Northwestern Polytechnical University, Sun Wenbo, Ma Yu'e, wenbo-sun@nwpu.edu.cn

compared with experimental observations. In the early stage of crack propagation, the surface tensile residual stress accelerated the FCGR, while the compressive residual stress in the center enhanced the fatigue resistance, leading to an inverted elliptical crack front shape. As the crack propagated, the RS gradually released, and its impact on fatigue crack growth vanished. Consequently, the crack front gradually changed into an elliptical shape. The observed fracture surface exhibited a profile that was higher in the middle and lower on both sides, and this feature was also reproduced in the numerical model.

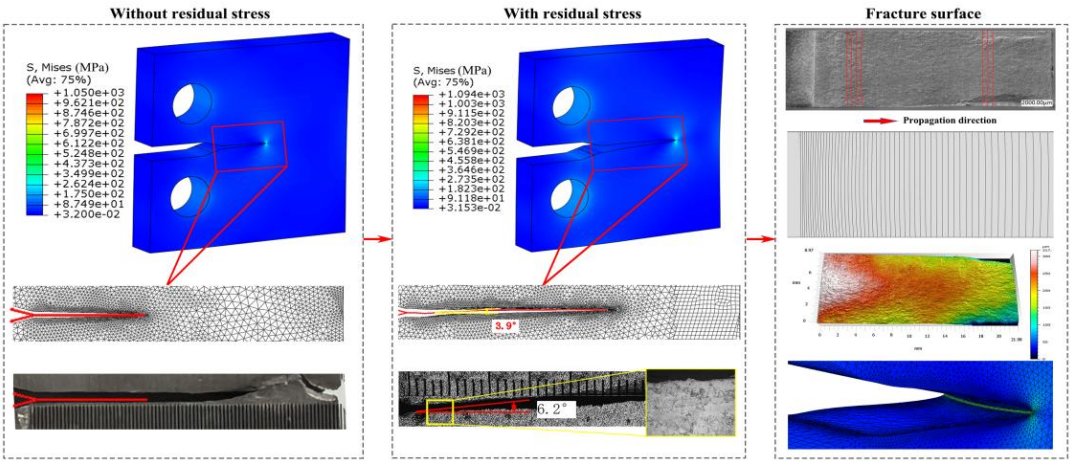

Figure 83: Simulated and experimental crack path and fracture surface

The anisotropic residual stress state, especially in the AM metal structure with a large thickness, has a significant influence on the fatigue fracture behavior. The altered stress state can induce a transition in the fracture mode, resulting in mode II or mode III cracks. The coexistence of tensile and compressive residual stresses along the depth will cause a more complex fracture mode. When residual stresses were not considered, the CT sample exhibited a pure mode I fracture. When the RS was directly superimposed to calculate the SIF, higher tensile residual stresses near the free surface caused pronounced crack deflection and exhibited significant deviations from the experimental results. When the effects of stress relaxation were considered in the model, the RS gradually released and its effect on fatigue cracking gradually decreased and disappeared as the fatigue cycles increased and cracks propagated. Although residual stresses slightly reduced the fatigue crack growth life, this effect was most prominent in the early stage, as shown by the *a*–*N* curves

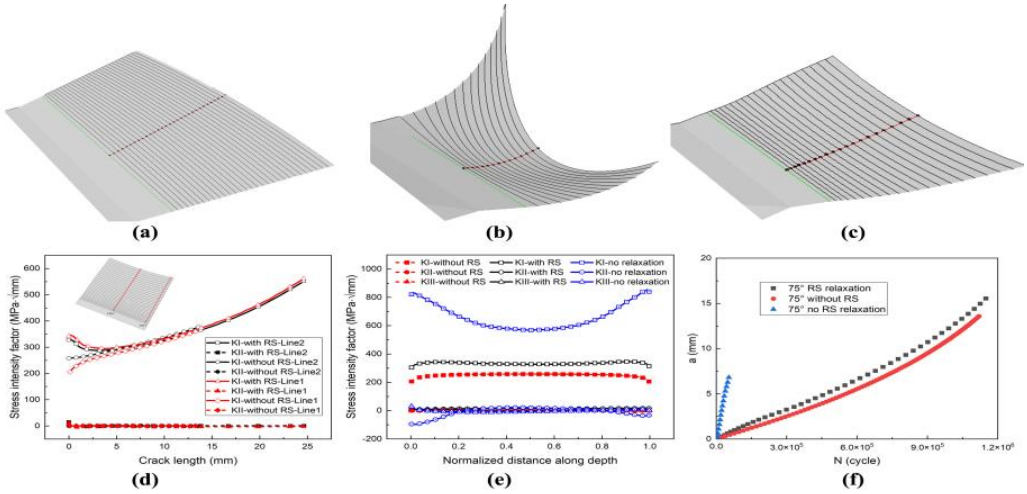

Figure 84: Fatigue crack growth behaviors: (a) fracture surface of the model without RS, (b) fracture surface of the model without RS relaxation, (c) fracture surface of the model with RS relaxation, (d) SIFs along the crack direction, (e) SIFs of the initial crack, and (f) a–N curves.

5.2 A framework for the preliminary design of the scarf bonding structure[28]

With the increasing application of scarf bonding in aircraft primary structures and repair structures, it is of considerable importance that an accurate reliability-based scarf bonding structural design methodology is developed. This section focuses scarf bonding structure design, especially on the adherends of the structure should be ply-by-ply matched with the original structure. The design of a Composite Scarf Bonded (CSB) structure is a complex engineering task since multiple factors need to be considered: (1) The coupling influence of the adherend and adhesive material properties on the final design structural strength should be considered. A well-designed scarf bonded structure should ensure that the adherend and adhesive fail simultaneously. For this reason, the CSB should be designed as to include mutually balanced adhesive and adherend material. (2) The impact of the pre-existing defects, such as interface disbonds at the adhesive-composite interface and discrete damage, as well as uncertainties related to material properties and geometry, on structural strength need to be considered in the design methodology. These pre-existing defects and uncertainties can lead to sudden structural failure, so finding a rational and systematic damage-tolerant design method is of fundamental importance. (3) The stress concentration along the adhesive's bond line, which is induced by the non-uniform stiffness distribution of the ply-by-ply laminate configuration along the thickness. In addition, for fast preliminary structural design, a strength prediction method with few mechanical property tests is needed.

Theory-guided machine learning framework

The development of a theory-guided machine learning framework can be divided into the following steps:: (1) Database preparation: To build an effective machine learning model, a comprehensive database containing input and output variables must be defined and collected, as shown in Figure 85. A suitable sampling method and effective feature selection are essential. (2) Surrogate model construction: Select and compare the performance of various machine learning algorithms using 5-fold cross-validation (CV). A reliable scoring method is required to evaluate model performance with different hyper-parameter combinations, and the grid search method is used to select the optimal hyper-parameters, as shown in Figure 86. (3) Use the best-performing surrogate model to predict structural strength and design structures. The XGBoost estimator has been verified to deliver the best performance.

[28] Chinese Aeronautical Establishment, Yan Bing, yanbing@cae.ac.cn

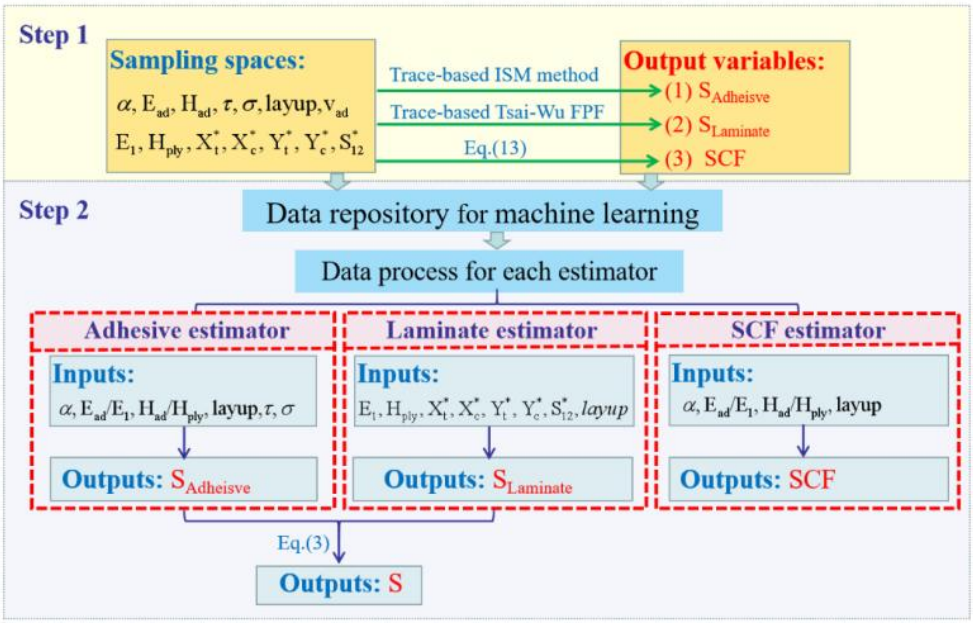

Figure 85: The database generation and process

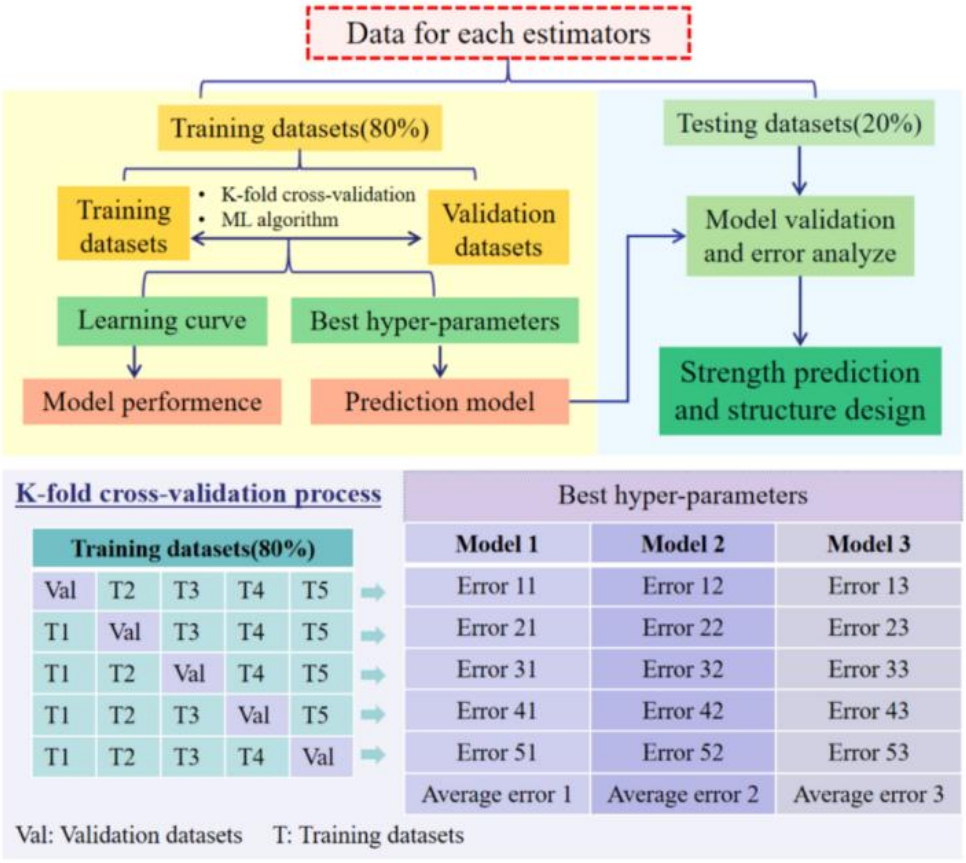

Figure 86: The flowchart to establish an ML estimator

Design space with uncertainties quantification

The design space with uncertainties for laminates made from fabric prepregs is shown in Figure 7. The

green points show a laminate failure mode, and the blue points correspond to adhesive failure. An interesting result is that there is a mixed failure mode region between the orange dotted lines from 2.22° to 2.94° in Figure 15, where laminate failure and adhesive failure can occur. By observing the failure mode in the 2.8° scarf angle experiments, as shown in Figure 7(b), the accuracy of the failure mode predicted by the ML models is verified. For the 1.9° scarf angle and 5.7° scarf angle structures, the failure mode predicted is within the range of laminate failure and adhesive failure, respectively, which corresponds to the observed failure mode in the experiments Figure 87(a) and Figure 87 (c).

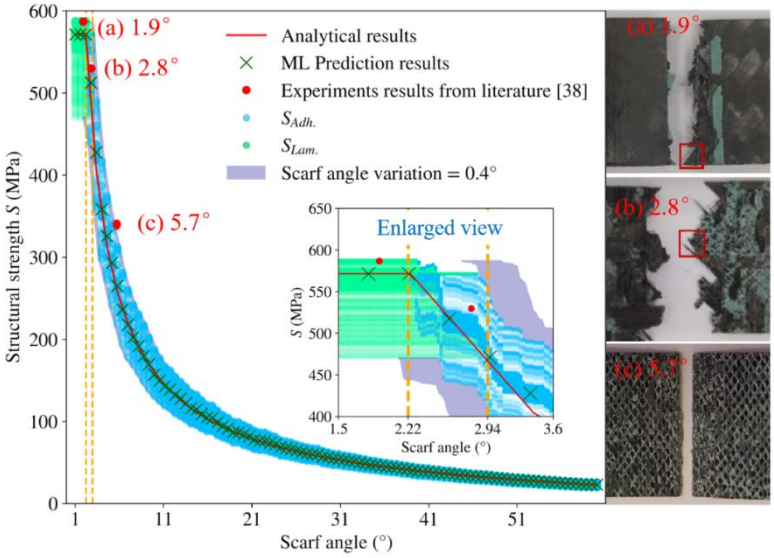

Figure 87: Design space with uncertainties for fabric laminate

For UD composite scarf joints [9], a design space considering uncertainties was obtained, as shown in Figure 8. A mixed failure mode region from 1.0° to 1.36° is obtained from the uncertainties design space as noted by the orange dotted lines in Figure 8, which means the prediction failure mode of all of the cases studied is adhesive failures. This kind of failure mode is consistent with the observations of failure mode A in the experiments as shown in Figure 8. However, only specimens with 15°, 25°, and 45° scarf angle show this failure mode. Observing the failure mode B of 2°, 3°, 6°, 9° in the experiments as shown in Figure 88, where interlaminar/intralaminar failure occurs in 90° ply, and adhesive failure occurs in 0° ply, simultaneously. The interlaminar/intralaminar failure is attributed to the failure of the weak composite sublayer (90° ply) under the higher bonding adhesion, which cannot be accounted for in the current theoretical framework and requires the application of a more detailed model. However, in the design space generated by the ML framework, all of the uncertainties (including material properties and geometry, debonding, weak bonding, porosity in adhesive and laminates, and interlaminar flaw) incorporated into the variation of the inputs, and damage tolerance-based structural design parameters can be obtained.

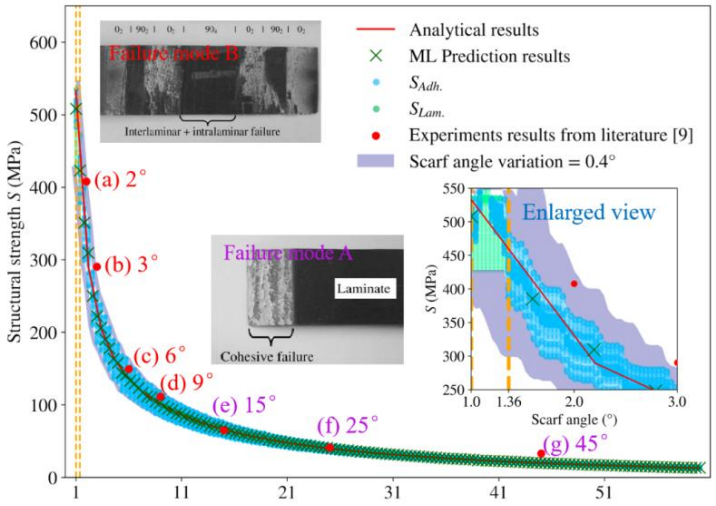

Figure 88: Design space with uncertainties for UD laminate

5.3 Fatigue Life Enhancement Method for Aircraft Large Opening Corners Based on Finite Element Analysis[29]

Large openings, such as doors and windows, are inevitably integrated into the fuselage design of civil aircraft to meet the requirements for passenger and cargo access, operational convenience, and emergency evacuation. However, these large openings, particularly the corners of door openings, often become weak points in the structure due to stress concentration, leading to a reduction in fatigue life. To address this issue, this paper proposes a finite element-based method for locating hazardous areas and predicting the fatigue life of large opening corners. The method's high accuracy is validated by comparing the results with full-scale fatigue test data from the entire aircraft. Based on the results of this method, the paper further presents a fatigue life enhancement approach for the door opening corners, considering the current assembly process level. Experimental and analysis results demonstrate that this method significantly improves the fatigue life of the door opening corners, providing valuable references for the design and maintenance of large opening structures in civil aircraft.

Fatigue life assessment of large opening corners based on finite element analysis

A submodel of the door opening region was extracted from the full-aircraft finite element model, and the corner area was locally refined with detailed meshing (as shown in Figure 89). A refined finite element model of the door opening corner for a specific aircraft was developed. Strain gauges were placed on the critical areas during full-scale fatigue testing to validate the model, confirming its high fidelity.

On this basis, stress distribution was analyzed, and rivet loads were extracted. The fatigue strength for the critical areas was calculated, followed by an evaluation of the fatigue margins and the target service life of the corner rivet holes under the operational flight load spectrum.

[29]Shanghai Aircraft Design and Research Institute, Bao HaiSheng, Baohaisheng1@comac.cc

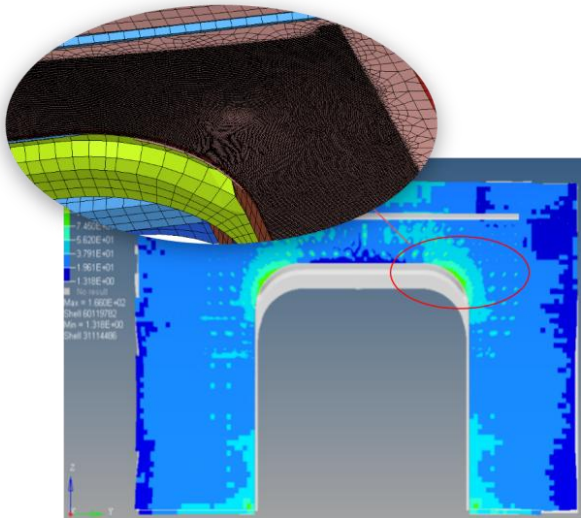

Figure 89: Refined finite element model of the door opening corner

Life Improvement Analysis and Implementation

Analysis indicates that the rivet loads and stress fields at the rivet holes in the door opening corners are relatively high, leading to significantly reduced fatigue life. This conclusion has been validated through full-scale fatigue tests, with the crack patterns from the full-scale tests shown in Figure 90.

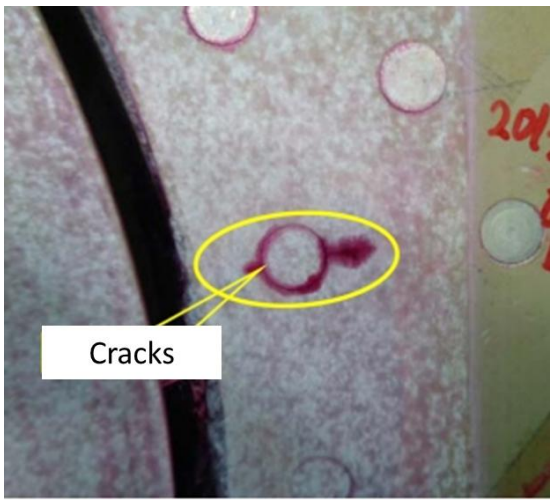

Figure 90: Cracks of full-scale fatigue test at the skin rivet holes in the door opening corner

The ratio of the flight cycles at which cracks were detected to the predicted flight cycles was 92.8%, further validating the high accuracy of the fatigue life analysis based on finite element methods. It was also observed that the fatigue life of the door opening corners in the full-scale test was slightly lower than the predicted life.

A detailed structural analysis revealed the following: The door opening corner comprises a three-layer structure: the outer layer is a 1.6 mm thick skin, the middle layer is a 2 mm thick reinforcement plate, and the innermost layer is another 1.6 mm thick reinforcement plate. To reduce stress concentration at the corners, a large reinforced area was designed, and the three layers were joined using rivets. However, some rivets were found to be insufficiently tightened. Under prolonged exposure to combined pressurization loads and flight loads, fretting fatigue occurred at the connection points,

further reducing the fatigue life of the structure.

To address this issue, the rivets in the affected area were replaced with high-lock bolts. These bolts can apply and maintain precise preload forces, effectively limiting the relative displacement of the multilayer structural components and ensuring a more uniform load distribution. With this improvement, the fatigue life of the door opening corners was significantly increased by 48%, demonstrating substantial economic benefits.

5.4 A platform for recording and analyzing aircraft structural defects and damage data[30]

Inevitably, various defects and damages occur to aircraft structures during the processes of production and operation. Such defect and damage data constitute significant data assets for aircraft design, manufacturing, and operational entities. This data aids relevant departments in improving aircraft structural design, optimizing manufacturing process workflows, and determining maintenance priorities and cycles for aircraft. How to properly aggregate and preserve this data is a critical issue that must be addressed by aircraft design and manufacturing organizations.

This section introduces a web-based platform for recording and analyzing aircraft structural defect and damage data. Upon a single deployment, the platform facilitates swift access within the network. Leveraging database technology enables the storage and retrieval of extensive data volumes. With a visual interactive interface, it ensures convenient entry and bulk import of damage and defect data. Utilizing charts, it achieves the visualization of data analysis results.

Technical pathway of the platform

The aircraft structural defect and damage data recording and analysis platform can be divided into a front-end and a back-end. The front-end is responsible for the presentation of web content, while the back-end handles data storage and responds to web requests. Web development primarily relies on the Vue3 framework, complemented by the ElementPlus library, enabling the creation of an interactive and aesthetically pleasing website interface with relatively low time costs. Additionally, to display 3D models within the webpage, the three.js library is utilized, and for the drawing and presentation of various analytical charts, the echarts library is employed. These third-party libraries significantly enhance the efficiency of website development.

The back-end of the web platform mainly comprises a database and intermediaries for communication between the front-end and back-end. The database used is MySQL, a mature, stable, and freely available open-source database. Furthermore, to facilitate communication between the front-end website and the back-end database and to handle request responses, the Node.js tool is utilized. The specific technical pathway is illustrated in Figure 91.

[30]Nanjing University of Aeronautics and Astronautics, Tong Mingbo, tongw@nuaa.edu.cn ,

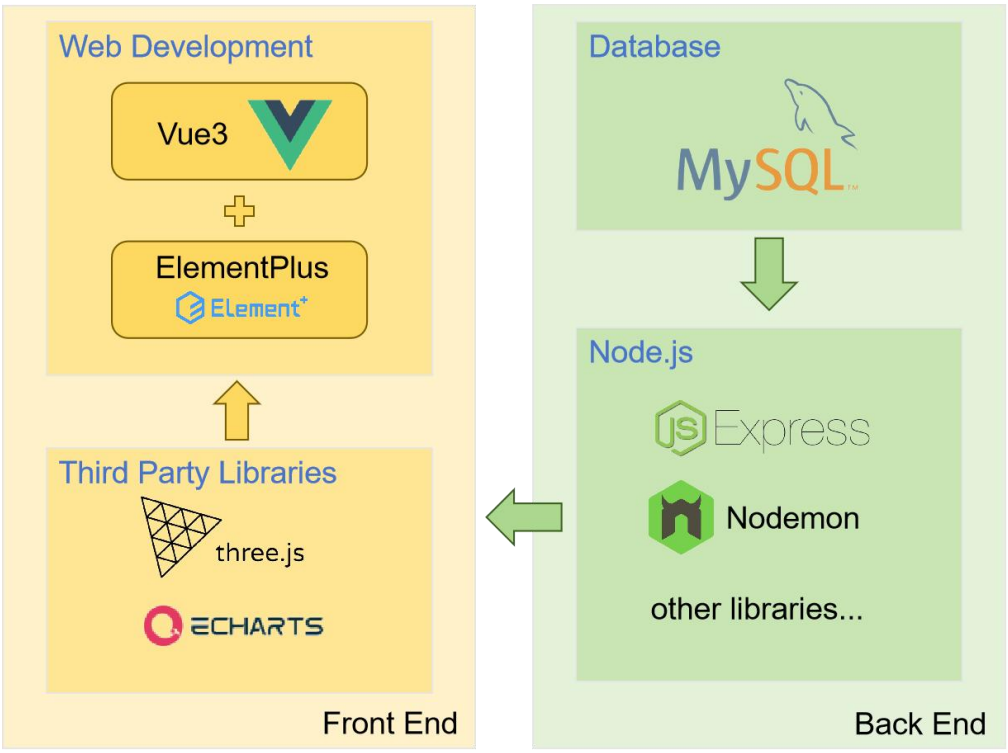

Figure 91: Technical Pathway of the Platform

6 Life extension and management of ageing fleets

6.1 Probability analogy method for individual aircraft life based on structure total inherent fatigue damage[31]

Aircraft service life monitoring is an important task required by the structural integrity program of military aircraft, aiming to manage the service life of individual aircraft to realize their full potential and extend the service life of the entire fleet. The key challenge is how to provide a relatively reliable structural service life prediction for individual aircraft under actual usage conditions. This study proposes a probability method for aircraft service life prediction, with its core in the service life analogy method and probability scatter factor calculation.

Life analogy method and total inherent fatigue damage

The fatigue life analogy method is widely used in engineering because of its high accuracy of life prediction, which is based on the relative Miner criterion, assuming that for the same or similar structural details (same material), the total fatigue damage corresponding to the fatigue cracking of the structure is approximately equal under a similar loading spectrum, thus eliminating the error caused by the certain value of critical value of damage when using theoretical algorithm to calculate fatigue life.

According to the Miner linear fatigue damage accumulation criterion, it can be considered that the total fatigue damage is equal to damage rate multiplies by fatigue life, then

$$D_{cr} = DR \times t,\ \overline{D}_{cr} = DR \times \overline{t} \tag{1}$$

[31] Chengdu Aircraft Design & Research Institute, Liao Yu, liaoy008@avic.com

Where, $DR$is the fatigue damage per unit time(flight hour or sortie) under a certain loading spectrum, called fatigue damage rate;t is the fatigue life under a certain loading spectrum. Considering the dispersion of material properties, manufacturing and assembly quality, t is a random variable, approximately obeying a lognormal distribution, $\lg(t)\sim N(\lg\bar{t},\sigma_{stru}^2)$, and $\bar{t}$is the expected value of fatigue life; D_{cr} is the total inherent fatigue damage, which is a random variable and approximately obeys a lognormal distribution,$\lg(D_{\mathrm{cr}})\sim N(\lg\bar{D}_{\mathrm{cr}},\sigma_{stru}^2)$,and $\bar{D}_{\mathrm{cr}}$ is the expected value of total inherent fatigue damage; σ_{stru} is log standard deviation representing structural fatigue dispersion.

Substituting the design spectrum, the baseline service spectrum and the individual aircraft spectrum into Equation (1),

$$DR_{\mathrm{desi}}\times t_{\mathrm{desi}}\approx DR_{\mathrm{base}}\times t_{\mathrm{base}}\approx DR_{\mathrm{indi}}\times t_{\mathrm{indi}} \tag{2}$$

Where, t_{desi} is the fatigue life of the structure under the design spectrum; DR_{desi} is the fatigue damage rate under the design spectrum, usually obtained by fatigue analysis or simulated specimen fatigue test; t_{base} is the fatigue life of the structure under the baseline service spectrum, also called the baseline service life; DR_{base} is the fatigue damage rate under the baseline service spectrum, usually obtained by fatigue analysis or simulated specimen fatigue test; t_{indi} is the fatigue life of the structure under the individual aircraft spectrum, also called the individual aircraft service life; DR_{indi} is the fatigue damage rate under the individual aircraft spectrum, usually obtained by fatigue analysis.

Baseline service life

The total structural inherent fatigue damage of critical location is determined by the full-scale fatigue test life t_{desi} and damage rate DR_{desi} under the design load spectrum. If the fatigue analysis method is used to determine DR_{desi}, the parameters of the fatigue analysis model need to be verified by the simulated specimen and/or full-scale fatigue test.

The key to the baseline service life evaluation based on total inherent fatigue damage is to determine the ratio of the fatigue damage rate between the baselineservice spectrum and the design spectrum, i.e. DR_{base}/DR_{desi}. Generally, the simulated specimen comparison test and fatigue analysis are both used to determineDR_{base}/DR_{desi}, so as to ensure the accuracy of baseline service life.From equation (2),

$$t_{\mathrm{base}}\approx\frac{D_{cr}}{DR_{\mathrm{base}}}=\frac{DR_{\mathrm{desi}}}{DR_{\mathrm{base}}}\times t_{\mathrm{desi}},\ \frac{DR_{\mathrm{base}}}{DR_{\mathrm{desi}}}\approx\left(\frac{DR_{\mathrm{base}}}{DR_{\mathrm{desi}}}\right)_{\mathrm{analysis}}\ \mathrm{or}\left(\frac{DR_{\mathrm{base}}}{DR_{\mathrm{desi}}}\right)_{\mathrm{test}} \tag{3}$$

Probabilistic expected life of individualaircraft

For each criticallocation of individual aircraft,the probability analogy method is used to calculate the expectedremaining life (RLE) of criticallocations,

$$RLE=\frac{t_{base}-EFH}{k_{future}}=\frac{t_{base}-k\cdot AFH}{k_{future}} \tag{4}$$

Where,AFH is actual flight hours.Other parameters are as follows：

1)Baseline service lifet_{base}.

t_{base}obeys lognormal distribution,

$$\lg(t_{base})\sim N(\overline{t}_{base},\sigma_{stru}^2) \tag{5}$$

2)Flight severity factor*k*.

For a structural detail,the analogy equation is as follows:

$$\hat{t}_{indi} = \frac{DR_{base}}{DR_{indi}} \times t_{base} \tag{6}$$

Where, $\hat{t}_{indi}$ represents the prediction fatiguelife under the individualaircraft spectrum, and *DR* represents the damage rate under the corresponding load spectrum calculated by the fatigue damage model.

The probability distribution of ($\hat{t}_{indi}/t_{indi}$), obeysa lognormal distribution with mean value of zero,

$$\lg(\hat{t}_2 / t_2) \sim N(0, \sigma_{pred}^2) \tag{7}$$

σ_{pred} reflects the uncertainty of life prediction；

Theflight severity factor$k=t_{base}/t_{indi}$. Since t_{indi}typically lacks full-scale fatigue test data, $\hat{k}$ can only be calculated based on the analogy method. Therefore,$\hat{k}=t_{base}/\hat{t}_{indi}=DR_{indi}/DR_{\text{base}}$. It is evident that *k* also obeys a log-normal distribution, as shown below.

$$\lg(k) \sim N(\lg \hat{k}, \sigma_{pred}^2) \tag{8}$$

Actually, it is assumed that the stress spectrum of critical location of individual aircraft is indirectly obtained through the ‘flight data-load-stress’ model, and the influence of load prediction uncertainty on the fatigue damage calculation shall be considered. Due to $DR \propto S^m$(*S* means local stress), it can be derived

$$\lg(k) \sim N(\lg(\hat{k}), \sigma_{pred}^2 + m^2(\sigma_{stress}^2 + \sigma_{force}^2)) \tag{9}$$

Where, *m* is stress damage index, i.e. slope of the S-N curve; σ_{stress} represents stress prediction error of ‘force-stress’ model; σ_{force} represents load prediction error of ‘flight data-force’ model.

6.2 The structural management practice of SF Airline[32]

Establishment of structure management platform ASMS

The structure management platform ASMS is established from the difficulties of structure data collection management, configuration management caused by repair and modification of aging aircraft fleet and structure reliability management.

The technology of three-dimensional interaction and two-dimensional code is used to optimize information collection and solve the difficult problem of data collection and recognition, meanwhile, ensure the integrity and accuracy of structural data by the system process constraints.

Establish the relationship between the structural business information and the spatial location of the aircraft three-dimensional model, so that engineers can timely obtain the aircraft configuration and the latest status information, so that problems can be correctly dealt with.

Quantitative structural damage data, the application of mathematical statistics, thermal maps and other technical methods to achieve structural reliability management, grasp the single aircraft and fleet continued airworthiness safety key indicators trend.

[32]SF Airline Company Limited, Yuan Qingming

Continuously manage the effect of improvement measures through reliability alarm, engineering investigation, implementation of improvement measures and follow-up of the effect of measures.

Application case: An improvement measures Make for the high corrosion rate of the bottom of the lower cargo cabin, B737 aircraft corrosion position map is shown in Figure 92.

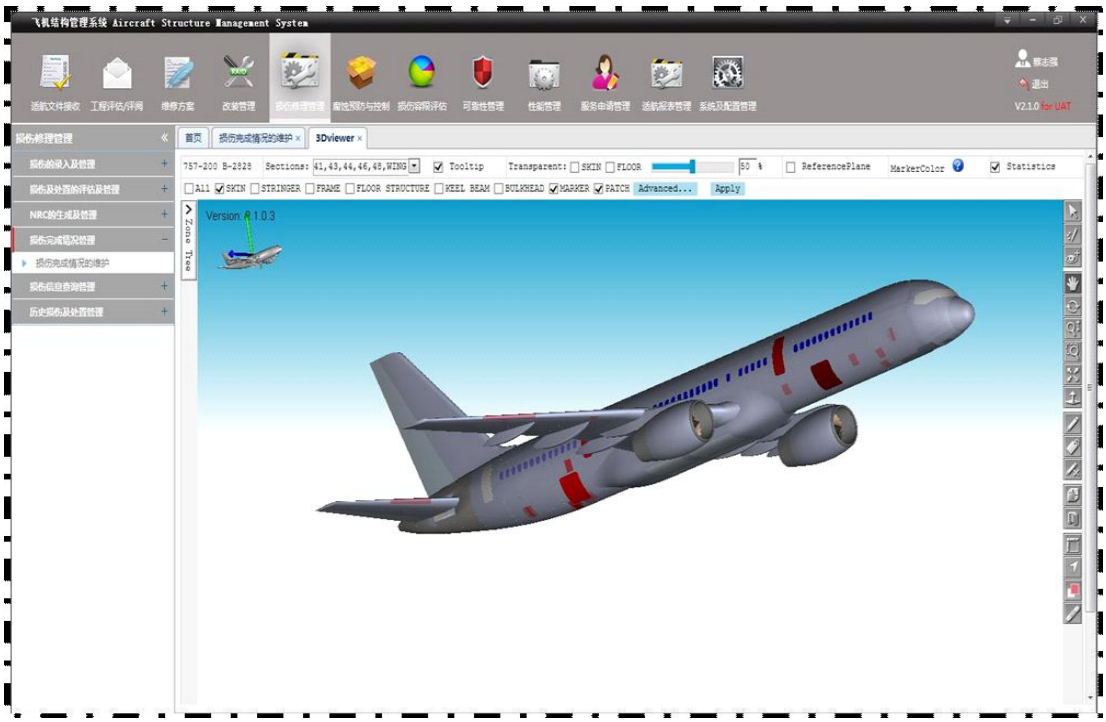

Figure 92: Corrosion position map

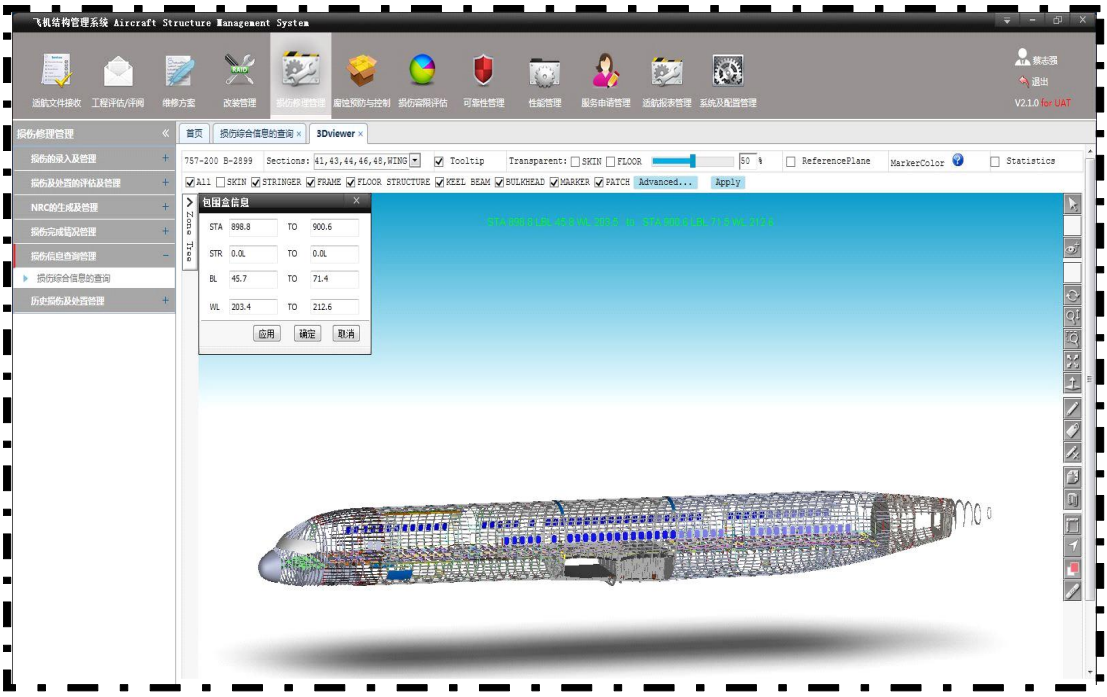

Figure 93: B737 inner structural bounding

Enhance the ability of structural independent engineering

Through the aircraft structure load acquisition system to obtain the actual load response of the structure,

using the technical method of mutual verification between theoretical analysis and measured data, a solid foundation for independent structural repair and modification design is established.

6.3 A surrogate model-based method for rapidly determining the average behavior of widespread fatigue damage[33]

Aiming at the problem that the prediction process of the average behavior of widespread fatigue damage is complex and takes a lot of time, the probabilistic initiation model of widespread fatigue damage and the model of crack propagation are established. In the process of crack propagation, the stress intensity factor at the leading edge of hole edge crack in seven-hole plate is solved by ABAQUS secondary development, the average behavior of widespread fatigue damage is obtained by Monte Carlo method, and the training set of widespread fatigue damage simulation program is established by machine learning. The stress level, random crack initiation parameters and random crack propagation are constructed as design variables, and the polynomial response surface model and Gaussian process regression model are established respectively. The results show that the error of the average behavior of widespread fatigue damage is less than 6% compared with the experimental data. Compared with the polynomial response surface proxy model and the Gaussian process regression proxy model, the accuracy of the Gaussian process regression model is higher, and the error is less than 10%. Compared with the traditional method, the calculation time cost can be saved by 90%. The Gaussian process regression model can accurately determine the average behavior of widespread fatigue damage.

Rapid Analysis Method Based on surrogate Model

The basic idea of the surrogate model is to regard the complex simulation program as a "black box", and use appropriate experimental design method to obtain the sampling matrix, in which the value of each group of design variables is an input vector. Sampling matrix is inputted into the simulation program to obtain the corresponding one-time random failure life value, the corresponding relationship between sampling point and program response value is established as the training set of the surrogate model, and the selected surrogate model is trained to obtain the fitting or interpolation relationship.

The steps to build the proxy model are as follows.

The first step is to determine the design variables and variable space.

The second step is to select the appropriate design of experiment (DOE) to obtain the sampling matrix of design variables.

Thirdly, the simulation program is executed to obtain the output response corresponding to the input sample points.

Fourth, select the appropriate agent model, establish the agent relationship, and train the agent model through the training set.

The fifth step is to check the accuracy.

To avoid entering too many dimensions, filter the input parameters. Firstly, the design variables in the surrogate model are determined, and three parameters, stress level S, crack random initiation parameter m and crack random propagation parameter n, are selected as the design variables. Secondly, we need to determine the variable space of three parameters, the parameters m and n obey normal distribution, the theoretical variable space should be $(-\infty, +\infty)$, in general cases, we choose the variable space as $[\mu - 5\sigma, \mu + 5\sigma]$, where μ is the mean and σ is the standard deviation. The stress level chooses

[33] Chengdu Aircraft Company, Pan Wei, panw14@avic.com

the variable space according to the engineering practice. See Table 1.

Table 1:Variable Space of Design Variable

Variable name	Variable space
Material parameter，m	[3.5,6.2]
Crack propagation parameter,n	[2,4]
Stres level,S/MPa	[50,100]

The training set is trained based on Gaussian process regression model and polynomial response surface model (RSM) respectively, and machine learning verification is carried out through cross-validation method, and the verification accuracy index is shown in Table 2.

Table 2: Machine Learning Verification Accuracy Index

Surrogate model method	**determination coefficient**	**Mean square error**	**Root of Mean square error**
		MSE	**RMSE**
Polynomial response surface model	0.98	0.00558	0.0747
Gaussian process regression model	1	0.00055	0.0234

As can be seen from Table 1, the Gaussian process regression model has higher accuracy and better fitting effect, and the response results of the Gaussian process regression model are shown in Figure 94.The Gaussian process regression model is tested by the test data, and the results show that the error is less than 10%, which saves a lot of time and computing cost.

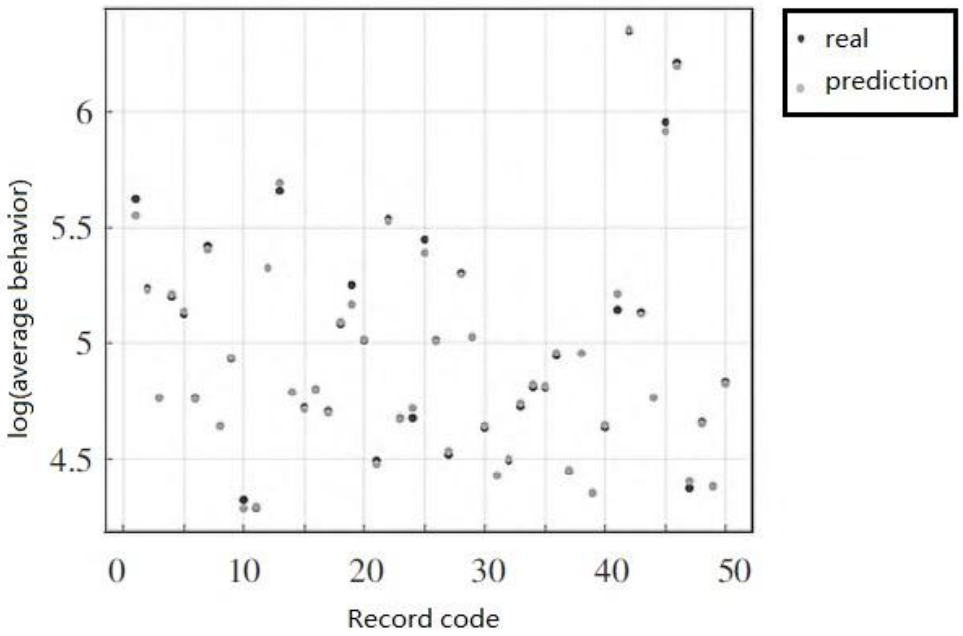

Figure 94: The response results of the Gaussian process regression model

6.4 Practice of structural integrity safeguard technology[34]

With the aging of aircraft, structural fatigue and corrosion become an increasingly significant threat to the safe operation of the fleet, continued airworthiness and structural integrity. According to the requirements of CCAR Part25 Revision 4, subpart E of CCAR Part26, and FAA Amendment 132 to FAR25.571, based on the damage inspection and statistical analysis of test data and aircraft operational data collected from civil aircraft service history ,and the durability and damage tolerance test results of typical structural repair, an aircraft structural integrity safeguard system was established, which includes a modified statistical method for fatigue crack and corrosion analysis. Thus, the airworthiness compliance validation process of structural repair, alteration and the repair of alteration was developed, and a strategy for assessment of widespread fatigue damage was defined based on aircraft fatigue tests and operational data. Furthermore, these structural integrity safeguard measures were incorporated to the instructions for continued airworthiness documents, and then the operational safety is guaranteed and operation cost is reduced.

Typical structure repair damage tolerance test VS analysis

Considering the complexity of the structural repair and modification scheme ,a damage tolerance assessment methodology of combining 3D detail finite element analysis and experiment was developed for different kinds of typical structural repair, which solved the key problem of crack propagation model simplification, including the knowledge of crack growth mechanism and relationship between different parameters. A comparison of a typical structural repair crack growth test and analysis is shown in Figure 95, and following conclusions can be drawn:

1) The crack initial region is identical;

2) The crack growth rate curve is very close;

3) The analysis results of crack growth life is shorter than test, which is conservative.

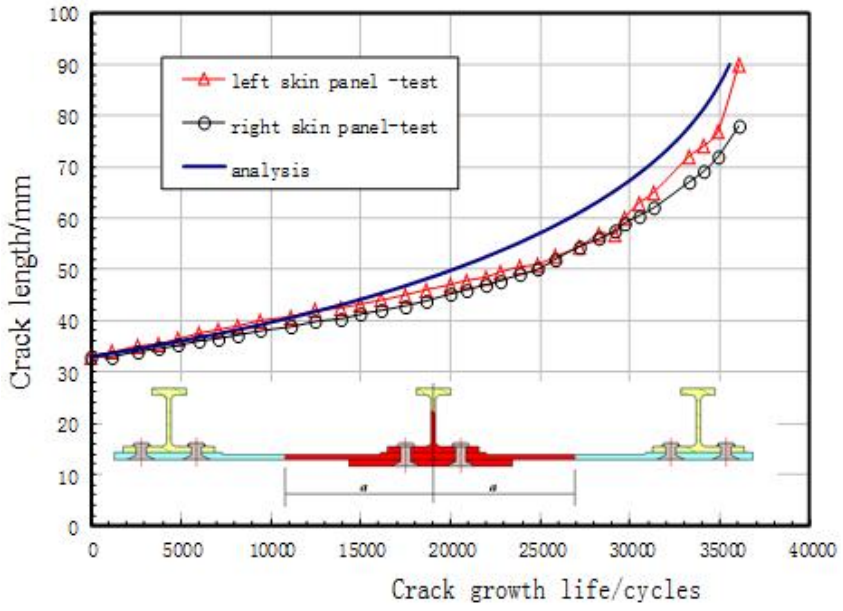

Figure 95: A comparison of a typical structural repair crack growth test and analysis

[34] XAC Commercial Co. Ltd, Zhang Nina, zhangnn@avic.com

WFD Assessment Strategy

A widespread fatigue damage assessment strategy has been developed based on the classic widespread fatigue damage methodology and data collect from several different sources,such as research and development test, operation ,fleet damage monitoring, scheduled inspection ,repair and maintenance. The basic logic is shown in Figure 96.

At present, the specific WFD methodology is being validated by full scale fatigue tests.

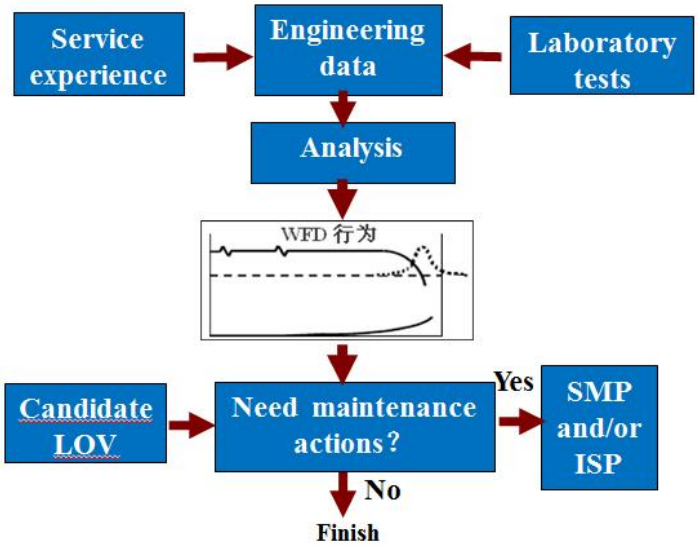

Figure 96: WFD assessment strategy

Full Scale Fatigue test verifed

Figure 97: MA600F Fuselage Structure Full Scale Fatigue Test

After 125000 simulated flights of fatigue, crack growth test, residual stress test and teardown inspection, there was without widespread fatigue damage immerged and the major load-bearing structures were intact(Figure 97), so it was shown that the WFD assessment approach is correct and

reliable.

7 Advanced materials and innovative structural concepts

7.1 Effect of geometric defects on the mechanical properties of additive manufactured Ti6Al4V lattice structures[35]

Lattice structures realized by additive manufacturing (AM) have the great potential for a broad range of engineering applications. However, the lattice structures are involved in geometric defects. This paper focuses the effect of geometric defects on the mechanical properties of Ti6Al4V lattice structures manufactured by laser powder bed fusion (L-PBF), face and body centered cubic with vertical struts (FBCCZ) were studied. X-ray computed tomography was used to extract the shape and the distribution of process-induced geometric defects of these three kinds of samples. Probability density distributions of geometric defects in each layer were also established to analyze the effect of the printing sequence on geometric defects. Then these distributions of geometric defects were inputted into Abaqus to build the modified statistical models to study the effect of geometric defects on mechanical properties. It is shown that the deviation of the cross-section radius exhibits normal distribution and the deviation of the center axis offset exhibits logarithmic distribution. And the middle layer of the sample has a better manufacturing precision. The strut thickness deviation had a more significant effect on the mechanical properties than the strut waviness.

Statistical analysis of geometric defects

X-ray computed tomography (X-CT) was employed to capture the morphological characteristics of as-fabricated lattice samples. Fig.1 shows the X-CT reconstructed samples of BCCZ, FCCZ, and FBCCZ respectively. The struts of the lattice samples were divided into three directions (35°, 45° and 90°). Notably, significant discrepancies in shape were observed between the as-fabricated and as-designed samples, with geometric defects becoming more pronounced as the strut orientation increased.

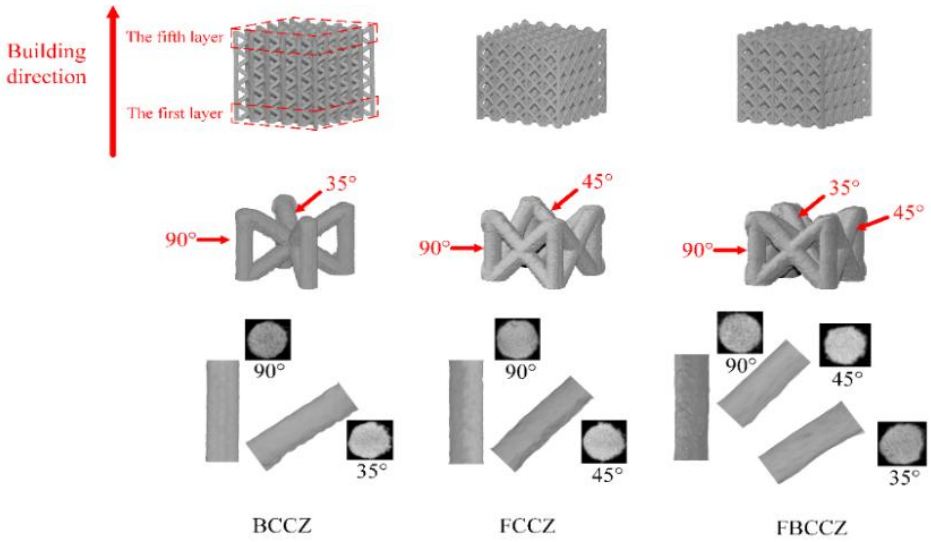

[35] Northwestern Polytechnical University, Ma Yu'e, ma.yu.e@nwpu.edu.cn

Figure 98: X-CT reconstructed samples

For all three lattice samples, the cross-section radius deviation demonstrates a normal distribution, while the offset of the strut center-axis follows a logarithmic distribution. The fitting equations of the normal distribution function and logarithmic distribution function are shown in equations (1) and (2) respectively. The mean value μ of the strut thickness variation is positive, indicating that the cross-section radius of the as-fabricated struts exceeds the design specifications. It confirms that the strut is over melted. And both strut thickness variation and strut waviness decrease as the strut building angle increases. When the effect of the printing sequence is taken into consideration, it can be seen that the mean value μ of the strut thickness in the last layer usually has the lowest value, which can be attributed to the accumulation of unmelted powder. However, there is little difference in the variation of the strut thickness in each layer. In addition, it is observable that the mean value μ of the center-axis offset of the middle layer is always the lowest, which can be due to the characteristics of the additive manufacturing. The upper and lower sides of the structure may cool faster than the middle part. Rapid cooling can cause the material to harden too quickly, which may lead to poor bonding between powder layers and affect the molding quality. Therefore, the middle layer of the sample has better manufacturing accuracy.

$$f(x,\mu,\sigma) = f_0 + \frac{1}{\sigma\sqrt{2\pi}} e^{-\frac{(x-\mu)^2}{2\sigma^2}} \#(1)$$

$$f(x,\mu,\sigma) = f_0 + \frac{1}{x\sigma\sqrt{2\pi}} e^{-\frac{(\ln\frac{x}{\mu})^2}{2\sigma^2}} \#(2)$$

Evaluation of single geometric defect

In order to simulate the mechanical behavior of the lattice samples more accurately, the modified statistical models were built. The geometric defects have a large effect on the mechanical response of the lattice structures, as shown in Figure 99 and Figure 100. And compared with the effect of strut waviness on the elastic modulus and the compressive strength, the strut thickness varication has a more significant effect on the mechanical properties.

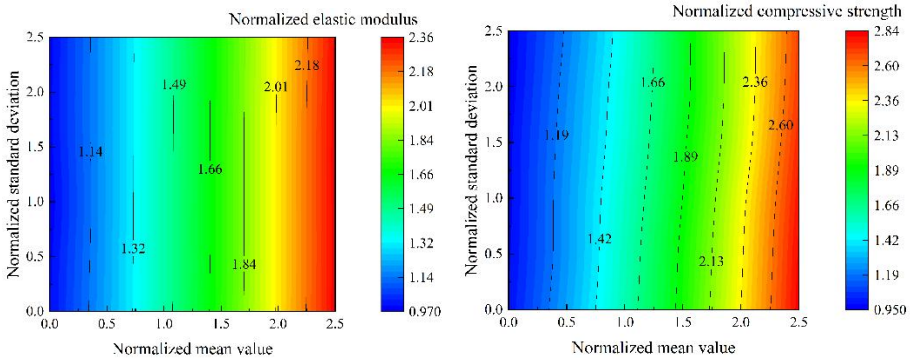

(a) Normalized elastic modulus (b) Normalized compressive strength

Figure 99: Contour plots where only thickness variation is considered for the FBCCZ structure

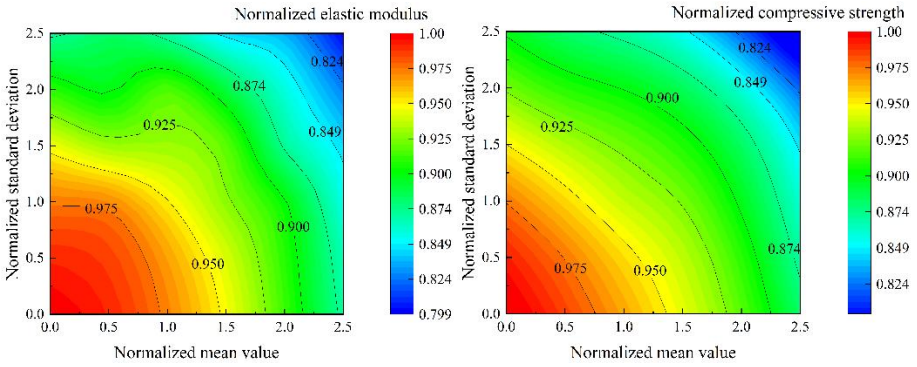

(a) Normalized elastic modulus (b) Normalized compressive strength

Figure 100: Contour plots where only strut waviness is considered for the FBCCZ structure

7.2 Crystal plasticity finite element simulation of crack initiation in titanium alloys under very high cycle fatigue loadings[36]

Fatigue failure in titanium alloys is the result of competition of multiple crack initiation mechanisms in most cases. For example, in very high cycle fatigue (VHCF) regime, micro cracks can form due to nanograin formation as well as factors irrelevant to nanograin formation due to microstructural inhomogeneity and deformation incompatibility. Numerical simulation is a feasible approach to elucidate the competition of fatigue failure mechanisms. By incorporating multiple cracking mechanisms, a slip-twinning-coupled crystal plasticity finite element model is built and used for simulating the fatigue cracks in titanium alloys under VHCF loadings, which presents a new way to simulate the microscopic process of crack initiation and early growth accompanied by microstructure evolution.

Method Introduction

The crystal plasticity finite element model is established based on the framework of Asaro and Kalidindi. Deformation twinning is modeled as pseudo slip, the evolution of its critical resolved shear stress includes the interaction between dislocation and twinning. Two crack initiation mechanisms are introduced in the model, i.e., crack initiation due to grain refinement and crack initiation due to cleavage on slip planes. The grain refinement process and the resultant initiation are determined by the stored energy of a localized region and a grain, respectively. The latter crack initiation criterion is the accumulated shear strain on all slip systems. Effects of grain size are reflected not only in the constitutive model but also in the failure criterion. The computation is accelerated by a cycle-jump approach after several cycles of simulation. The crack propagation after initiation is modeled by the cohesive zone method.

Application

The proposed crystal plasticity method is employed to simulate two cracks on the specimen under VHCF loadings. The material of the specimen is TC17 titanium alloy, the chemical composition of which is 4.97 Al, 4.19 Cr, 4.12 Mo, 2.09 Sn, 1.90 Zr, 0.11 O, <0.10 Fe, and balanced Ti in weight percent. The alloy was at first under beta forging, then solid solution for 4 hours at 800 °C and cooled

[36] Institute of Mechanics, Chinese Academy of Sciences, Sun Chengqi, scq@lnm.imech.ac.cn

by water, and finally under aging treatment for 8 hours at 620 °C. Fatigue test was conducted by an ultrasonic fatigue testing system USF-2000A with a frequency of 20 kHz in air and at room temperature, the stress amplitude σ_a = 588 MPa, and stress ratio R = -1.

After 1.37×108 loading cycles, two micro cracks can be observed on the specimen surface. The fatigue cracks used for model validation are shown in Figure 101, of which SEM, IPF, and phase maps are presented. Two cracks present different crack initiation mechanisms. Formation of nanograins is observed in location I, which increases the microstructural inhomogeneity in local regions, and leads to the fatigue crack initiation within nanograin regions or at the boundaries between nanograins and coarse grains. However, for location II, the main part of the micro crack forming within α grains, and a few nanograins can be found along the crack path.

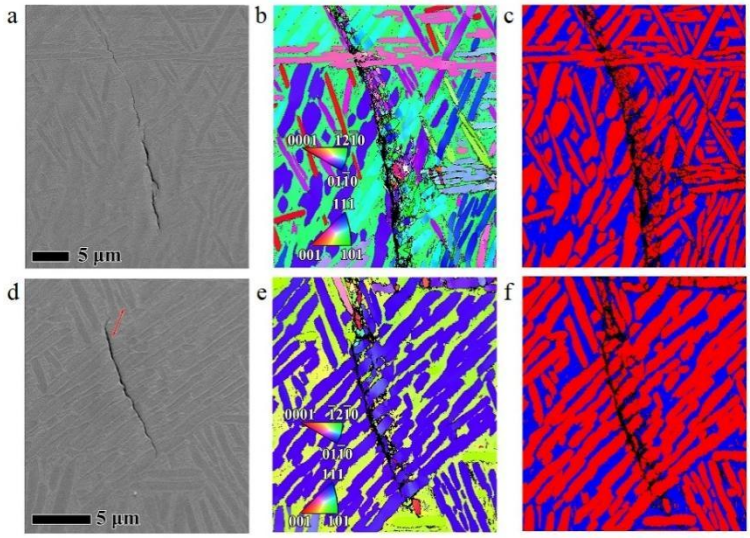

Figure 101: Experimental results for model validation. a-c: SEM, IPF, and phase image for location I; d-f: SEM, IPF, and phase image for location II. The arrow in e presents the slip direction of one prismatic plane. Red and blue in c and f denote α phase and β phase, respectively.

Figure 102 presents the comparison of microstructure between the experiment and simulation for locations I and II. Simulation shows that a crack was initiated in location I due to grain refinement in localized regions. Then the crack further propagated along the boundary of two grains (e.g., a nanograin and a coarse grain, two nanograins, or two coarse grains) or through the coarse grains due to microstructural inhomogeneity. For location II, the accumulation of shear strain of slip systems promoted cleavage on slip planes, and the crack propagated due to further accumulation of shear strain on crack tips. The accordance between simulation and experiment reveals the feasibility of the crystal plasticity finite element method in capturing the competition of different mechanisms in VHCF regime, demonstrating its wide prospect of application in fatigue simulation.

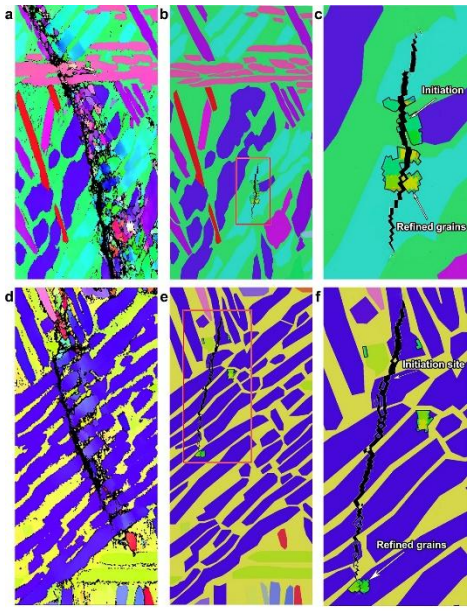

Figure 102: Comparison of microstructure between the experiment and simulation for location I and II. a-c: location I; d-f: location II; a and d: experiment; b and e: simulation; c and f: close-up of rectangular area in b and e, respectively.

7.3 Design and validation of variable camber wing structures for large-scale civil aircraft[37]

Climate change and the rising demand for air travel are driving the aviation industry to rapidly develop technological innovations. Among these advancements, morphing wing leading edges show great promise. To support this, the Chinese Aeronautical Establishment and the Aircraft Strength Research Institute of China have collaboratively conducted extensive research through several national projects. In this research, the CAE-GBJ developed by the Chinese Aeronautical Establishment, serves as a potential platform for integrating morphing leading edges. The aircraft's anticipated morphing leading-edge layout is depicted in Figure 103. This intercontinental business jet features twin tail-mounted engines, a wingspan of 33.5 meters, and a length of 33 meters, with a cruise Mach number of 0.87. Building on this aircraft, the Aircraft Strength Research Institute of China has proposed two variable camber leading edge concepts, along with a corresponding design methodology.

[37] Aircraft Strength Research Institute, Wang Zhigang, wangzhigang@cae.ac.cn

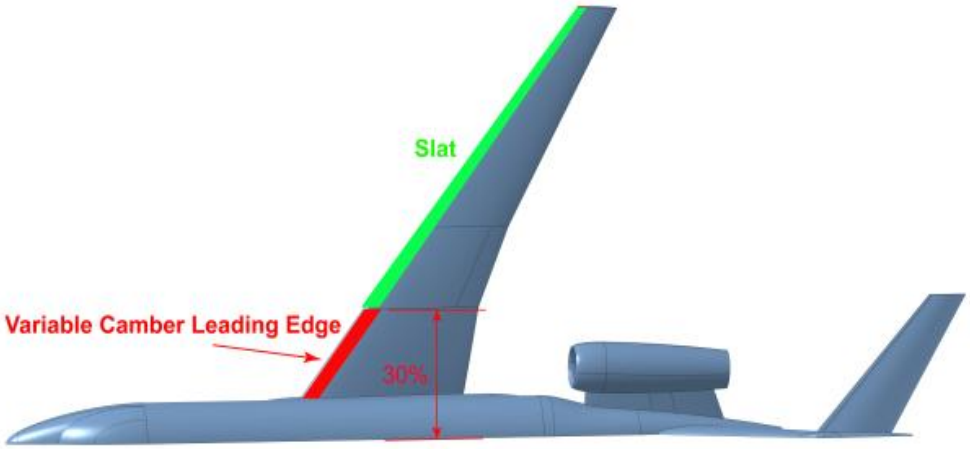

Figure 103: The model of the green jet business jet and the layout of the high-lift device proposed by the Chinese Aeronautical Establishment (CAE)

Design and testing of variable camber leading

The first variable camber leading edge concept utilizes an open-kinematic-chain mechanism. The study introduces a design optimization method for this leading edge, which features an outer composite compliant skin with variable thickness and an inner open-kinematic-chain mechanism. The optimization process applies a fiber continuity model based on ply-drop, guiding, and thickness sequences to characterize the composite skin, ensuring the generation of a composite layup sequence that adheres to fiber continuity requirements. Furthermore, the design methodology for the inner mechanism accounts for rigid-flexible coupling effects and examines the number of driving ribs along the span-wise direction. Finally, a physical mock-up of the variable camber leading-edge based on an open-kinematic-chain mechanism is developed and tested in ground to demonstrate its morphing capacity and accuracy. The final test results show that the developed variable camber leading-edge can be deflected into the target profile determined by CFD optimization result with a maximum deviation of 8mm.

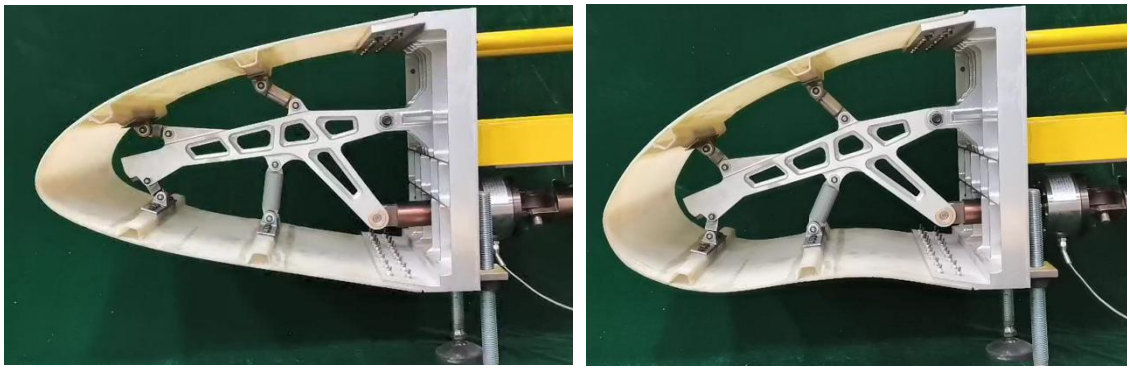

(a) initial profile (b) drooped profile

Figure 104: Variable camber leading-edge based on an open-kinematic-chain mechanism

The second variable camber leading edge concept relies on a closed-kinematic-chain mechanism. The study outlines a two-step design process: first, optimizing the outer variable-thickness composite compliant skin, followed by optimizing the inner kinematic mechanism. For the skin design, a variable

thickness composite skin optimization is introduced using a laminate continuity model, incorporating constraints for laminate continuity and manufacturing. This model employs guiding and ply-drop sequences to describe the stacking arrangement of plies in different thickness regions of the skin. For the inner mechanism, a coupled four-bar linkage system is proposed and optimized to generate specific trajectories at the actuation points on the stringer hats, ensuring that the compliant skin deflects into an aerodynamically optimal shape. Lastly, a morphing leading edge is fabricated and tested, with experimental results compared to numerical predictions, demonstrating the viability of both the concept and the design methodology. As shown in Figure 105, the corresponding maximum deviation is around 7mm and the physical mock-up has realized a continuous and smooth profile.

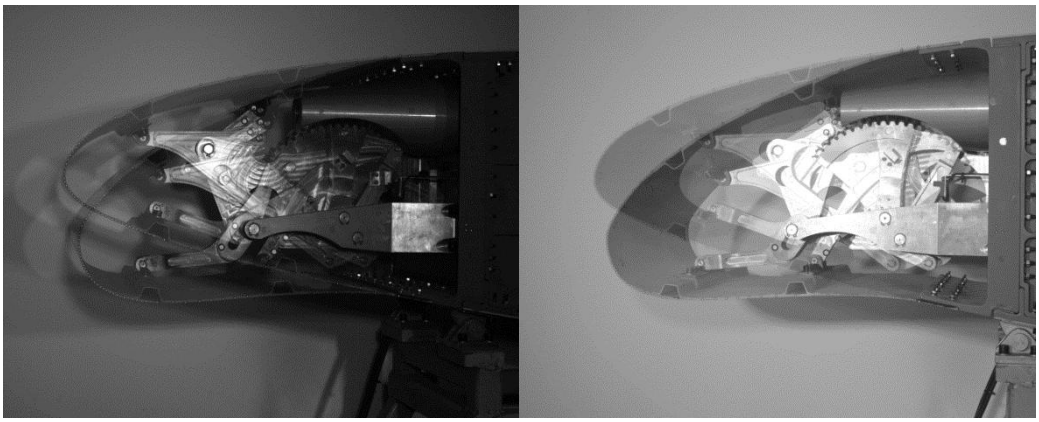

(a) Left camera image (b) Right camera image

Figure 105: Captured results of the left and right camera for the morphing leading-edge based on a closed-kinematic-chain mechanism

Full-scale variable camber leading edge

Based on the design and ground test results, a full-scale physical prototype for a large-scale civil aircraft is developed and experimented in the FL-10 wind tunnel, demonstrating that the variable-camber leading edge can smoothly and precisely achieve its target shape and hold its final profile under the corresponding aerodynamic loads, thereby validating the proposed design methodology.

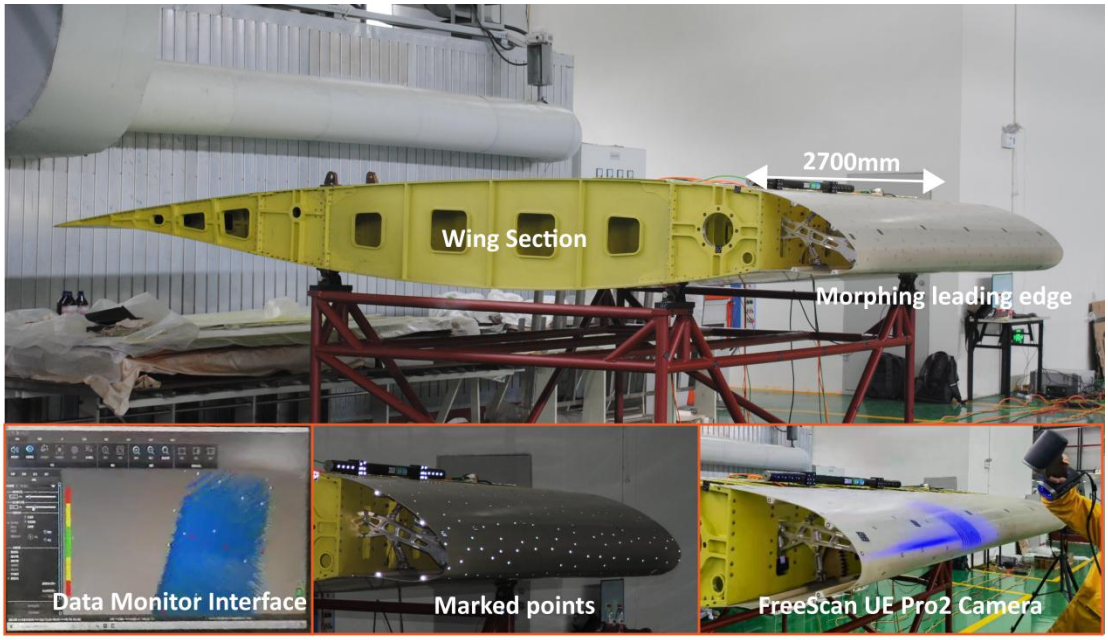

Figure 106: Three-dimensional full-scale physical prototype of the variable-camber leading edge

Figure 107: Comparison of the profiles before and after drooping

7.4 Retarding creep fatigue crack growth of GH4169 by PBF-EB [38]

The polycrystalline Ni-base superalloy, GH4169, exhibiting similar excellent high temperature mechanical properties to Inconel 718, is widely used in gas turbines and aerospace industry. Electron-beam powder-bed-fusion (PBF-EB), one of the main additive manufacturing (AM) approaches, is established as a reliable means to process GH4169. The existing studies have demonstrated the crystallographic texture, grain morphology, and other microstructure features in PBF-EB alloy often differ from those of their wrought counterparts. The microstructural features in PBF-EB GH4169 usually exhibit larger grain size and fewer grain boundaries, which may have more advantages in high temperature applications.

Improvement on the creep fatigue cracking resistance

A comparative study on the creep fatigue crack growth behavior at 650 ° C with 2160s hold time was performed between the electron-beam powder-bed-fusion (PBF-EB) and wrought GH4169. As shown

[38] Beihang University, Bao Rui, rbao@buaa.edu.cn,

in Fig 1, the creep fatigue crack growth rate of PBF-EB H-type (in which loading is perpendicular to columnar grain boundaries) specimen is only tenth of that of wrought specimen. Moreover, the creep fatigue crack growth rate of PBF-EB V-type (in which loading is parallel to the columnar grain boundaries) specimen is only one hundredth of that of wrought specimen. Such great improvements in cracking resistance should be attributed to the different grain boundary structures, including grain size, low angle grain boundary content and grain boundary δ phases precipitate.

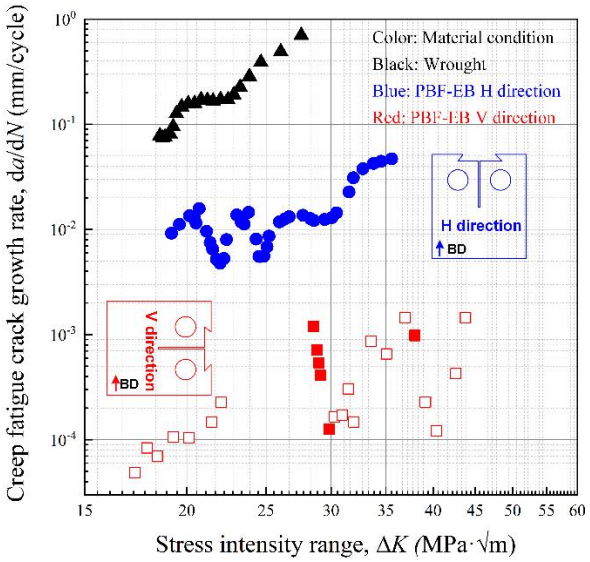

Figure 108: Creep fatigue crack growth rates of the AM and wrought GH4169 specimens.

Anisotropic fatigue cracking resistance in PBF-EB

The crack propagation rate of PBF-EB V specimen is significantly slower than that of PBF-EB H specimen. Considering the main difference of two specimens is the orientation of grain morphology, we can say the upright columnar grains play an important role in retarding the creep fatigue crack growth.

Combined with the EBSD results inFigure 109, it can be seen that the cracking mode is transgranular during pure fatigue loading while intergranular during creep fatigue loading for the PBF-EB V specimen. The main fatigue crack is deflected downward by 90° when it reaches the location of high angle grain boundary, followed by the trigger of intergranular cracking. Under the creep fatigue condition, wrought GH4169 and PBF-EB GH4169 have the same mainly intergranular crack propagation mode. While the differences lies in the grain morphology and size, the grain in wrought GH4169 is usually equiaxed and the grain size is smaller than that of the PBF-EB counterpart.

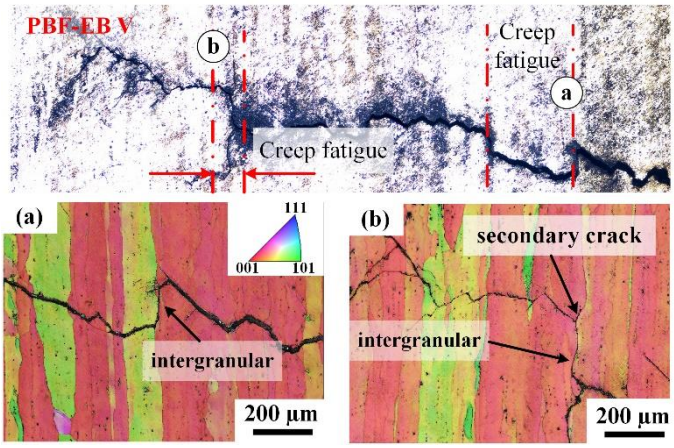

Figure 109: EBSD orientation maps around the fatigue crack growth path of PBF-EB V specimen.

High angle grain boundaries are also vulnerable to be intergranularly cracked in the PBF-EB H specimen,Figure 110. The crack of PBF-EB H specimen strongly prefers growing along high angle grain boundaries, which leads to typical intergranular cracking along the whole path. Different to the PBF-EB V specimen, due to the horizonal orientation of columnar grains, the macroscopic crack path is thus perpendicular to the loading direction.

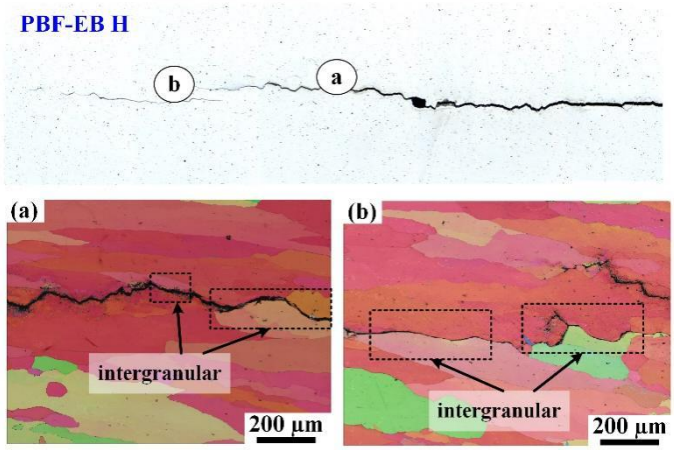

Figure 110: EBSD orientation maps around the fatigue crack growth path of PBF-EB H specimen.

7.5 Residual stress prediction for quality control in advanced manufacturing[39]

Understanding the thermal-metallurgical response in advanced manufacturing is important to interpret the residual stress distribution in components. Accurate prediction of residual stress has significant impacts on aerospace structural fatigue and long-term performance. To accomplish the aforementioned objectives, it is imperative to properly characterize the cooling rate dependent phase transformation in manufacturing process, as well as to reveal the evolution law of microstructures and its relationship to the residual stress distribution. It is also of considerable significance to develop robust methods for evaluating residual stresses both in small scales and macroscale components with complex geometry. These aspects are essential for optimal design and quality control in advanced manufacturing processes.

Key technology

[39]Huazhong University of Science and Technology, Zhang Zhen, z.zhang@hust.edu.cn

A 3D thermo-metallurgical-mechanical finite element modeling approach is proposed by considering varying cooling rate in solid-state phase transformation during advanced manufacturing. The numerical procedure is implemented through the KJMA model so as to incorporate the non-kinetics and non-isothermal phase transformation. In the context of residual stress prediction, a dual-variable influence function-based method is proposed to predict residual stress with small scale and high stress gradient. In order to deal with complex residual stress prediction across dimensions, radial basis function is adopted to reconstruct the full scale eigenstrain by solving an inverse eigenstrain problem. The residual stress reconstruction can be established in three different dimensions.

Application of technology

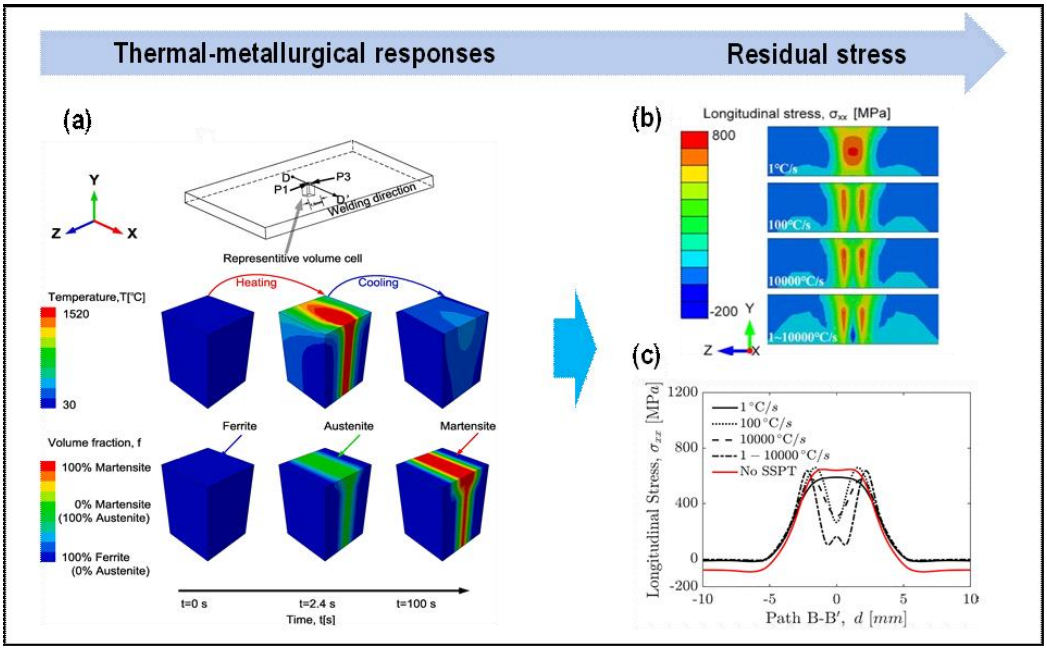

Figure 111: Thermo-metallurgical-mechanical modeling considering varying cooling rate in solid-state phase transformation: (a) thermal-metallurgical responses, (b) residual stress distribution contour, (c) longitudinal residual stress with respective to cooling rate

The KJMA model is formulated into a thermal-metallurgical-mechanical numerical procedure. Both the solid-state phase transformation (SSPT) and thermal elastic–plastic responses are computed in the updated temperature field. As shown in Figure 1, the results indicate that predicted residual stress, when considering SSPT and cooling rate, agree well with the available neutron diffraction experiment. It has been found that lower cooling rate inhibits austenite decomposition. This promotes the formation of retained austenite. While the austenitic phase transformation is well represented, the residual stress distribution along the weld line exhibits a distinctive double-peak profile due to high cooling rate. The austenitic transformation volumetric strain has been discovered to have much less influence on the final residual stress than the martensitic transformation volumetric strain.

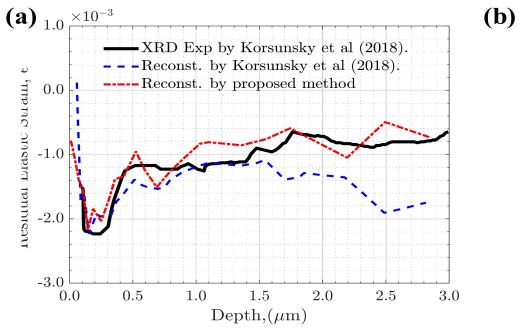

Figure 112: Comparison between XRD residual strain relief measurement with the result obtained by proposed method. (a) overall results obtained by averaging of results for different ring-core diameters, (b)results for different ring-core diameters

The proposed dual-variable influence function-based ring-core method has been validated through available microscale FIB-DIC experiment data conducted on multi-layer nanocrystalline TiN thin films. As shown in Figure 112, an excellent agreement has been found between the proposed method and the XRD experimental data.

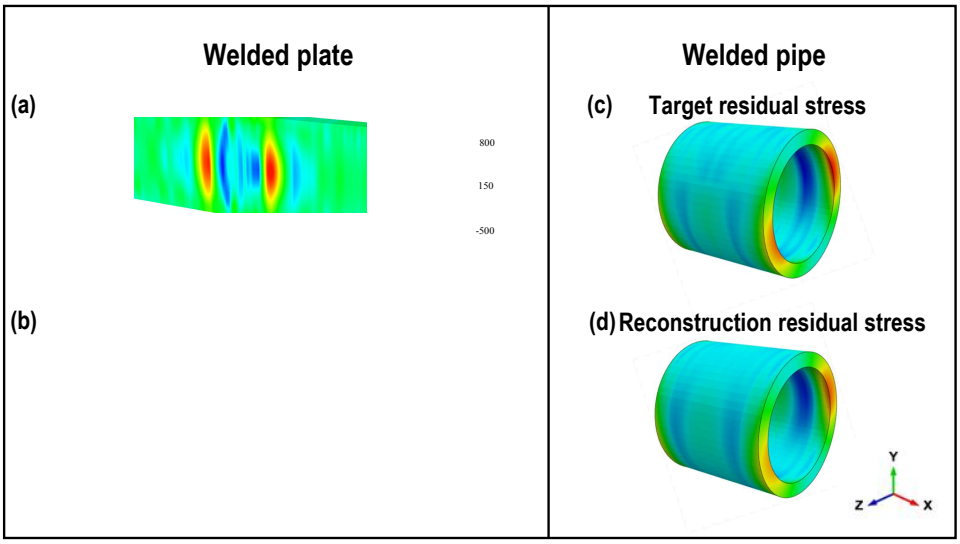

Figure 113: Residual stress prediction based on radial basis function reconstruction in welded plate and pipe: (a) residual stress contour, (b) comparison of prediction results, (c) target residual stress and (d) reconstruction result

The radial basis function reconstruction method is used to reconstruct complex residual elastic strain distribution. As shown in the Figure 113, the presented method performs better than the SIMTRI method proposed by Jun and Korsunsky. With limited accessible measurements obtained from most existing experimental techniques, the proposed reconstruction method can reproduce complex residual stress field accurately in the whole component.

7.6 Multi-physics and multi-scale numerical methods for metal additive manufacturing[40]

For the simulation of metal AM processes, a novel local multi-mesh finite volume method is proposed for heat transfer and fluid flow problems. A multi-physics material point method and a multi-physics finite element-material point method are proposed for solving thermo-fluid-solid coupling problems.

[40]Beijing Institute of Technology, Lian Yanping, lianyanping@bit.edu.cn

For the simulation of microstructure evolution in AM, a parallelized 3D cellular automaton computational model is developed to predict grain morphology, an extended cellular automaton finite volume method is proposed for predicting the melt pool flow and grain structure evolution in Ti6Al4V during the AM process, and a microscale cellular automaton method is proposed to simulate the microstructure evolution process for Ti6Al4V, specifically the $\beta \rightarrow \alpha$ / α' phase transformation process within a few β grains. For the simulation of mechanical properties in AM, a crystal plasticity finite cell-self-consistent clustering analysis method is proposed to efficiently predict the mechanical properties of AM materials.

Application of technology

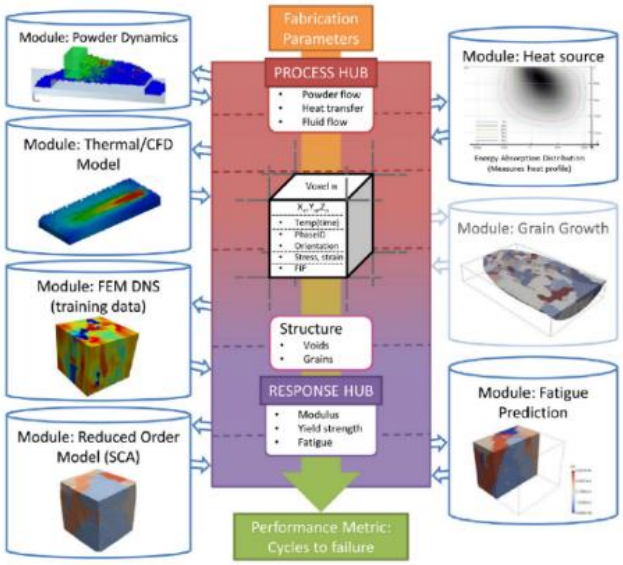

Figure 114: The modeling framework for process-structure-property relatinship in metal AM

The seamless integration of the numerical methods for the manufacturing process, as-built material microstructure formation, and mechanical properties is achieved, which is termed as integrated multi-physics and multi-scale modeling framework. As shown in Figure 114, the modeling framework is capable of the prediction of the resultant mechanical properties from given manufacturing process parameters, mechanical performance (e.g., fatigue property), thereby reducing uncertainty in the material built. In particular, the multi-physics material point method is proposed for solving thermo-fluid–solid coupling problems at powder scale, as shown in Figure 115. A set of numerical examples, including the benchmark problems and the selective laser melting AM problems was conducted, achieving good agreements with the experimental data available in the literature, revealing the powder scale manufacturing defects and thermal stress evolution mechanism.

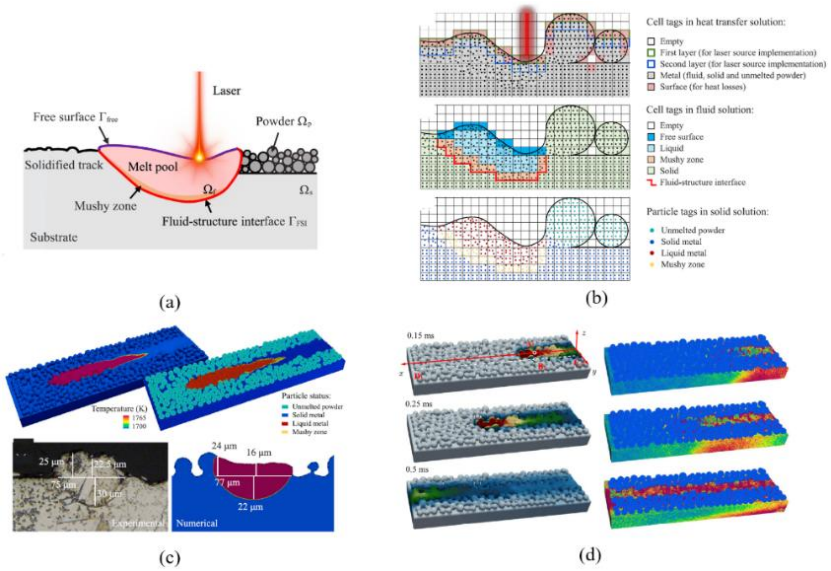

Figure 115: (a) The domain considered in the selective laser melting process, (b) the cell and particle tagging for heat transfer, fluid, and solid domains, (c) thermo-fluid coupling simulation of the selective laser melting problem, (d) surface morphology and von Mises stress at different time points for the SLM problem with powder layer thickness of 30 μm.

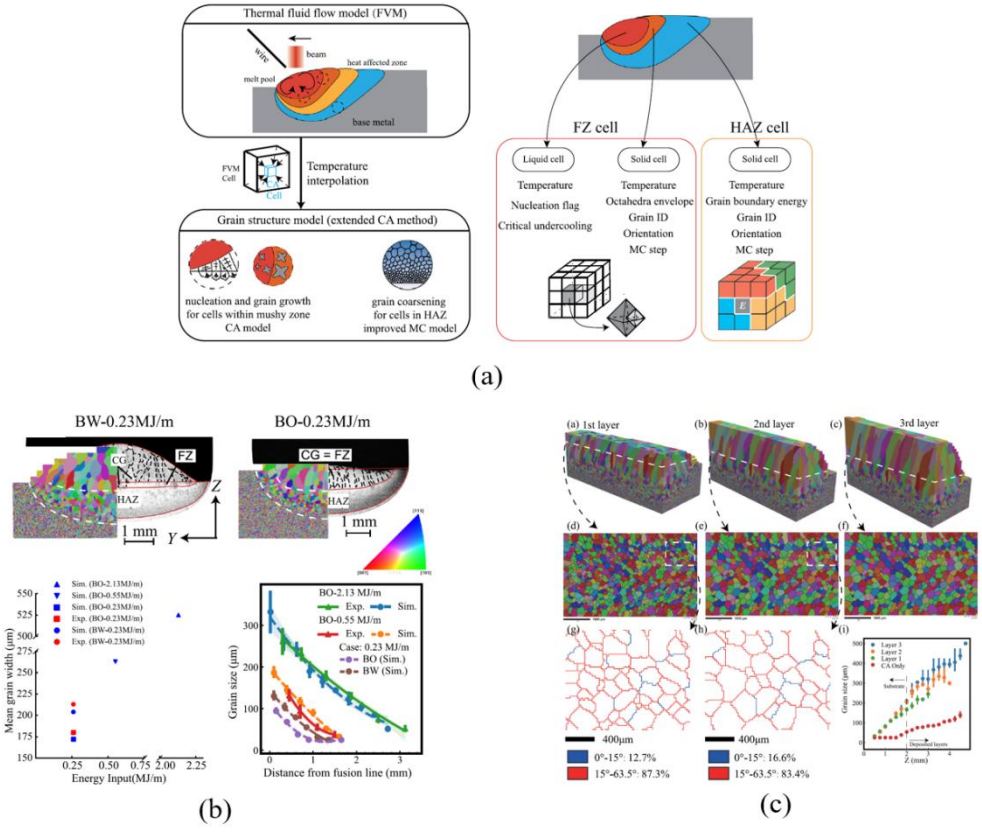

Figure 116: (a) Illustration of the xCAFVM, (b) comparison of simulation results and experimental data, (c) The predicted grain structure results

In the microstructure simulation stage, the cellular automaton model for grain evolution within the mushy zone is extended to predict the grain coarsening in the heat affected zone (HAZ) by coupling it with an improved Monte Carlo (MC) model, as shown in Figure 116. A one-way coupling scheme is

applied to integrate the grain structure prediction method and the finite volume method and multi-physics MPM for the heat and fluid flow in the process. The numerical results provide insights into the relationship between the process and the as-built microstructure. In particular, it is identified that grain coarsening plays a crucial role in determining grain size and shape for Ti6Al4V.

In the mechanical property prediction stage, a crystal plasticity finite cell-self-consistent clustering analysis (CPFC-SCA) method is proposed. It consists of two distinct calculation stages: an offline stage for data preparation and an online stage for rapid calculations. During the offline stage, the CPFC and a clustering method are integrated to discretize the representative volume element (RVE) of the as-built material microstructure. Subsequently, during the online stage, the SCA derived from the subdomain weighted residual formulation and crystal plasticity involving the Hall-Patch effect are utilized to solve the Lippmann-Schwinger equation of the RVE, and the numerical results are further utilized to determine the effective mechanical properties through the homogenization of stress and strain. With the established method, the as-built mechanical properties of additively manufactured IN625 using selective laser melting were addressed. The numerical results shed light on the relationship between the process parameters, as-built microst and the mechanical properties. It is demonstrated that the proposed method is a promising numerical simulation tool with high efficiency in predicting the mechanical properties of materials fabricated by metal additive manufacturing.

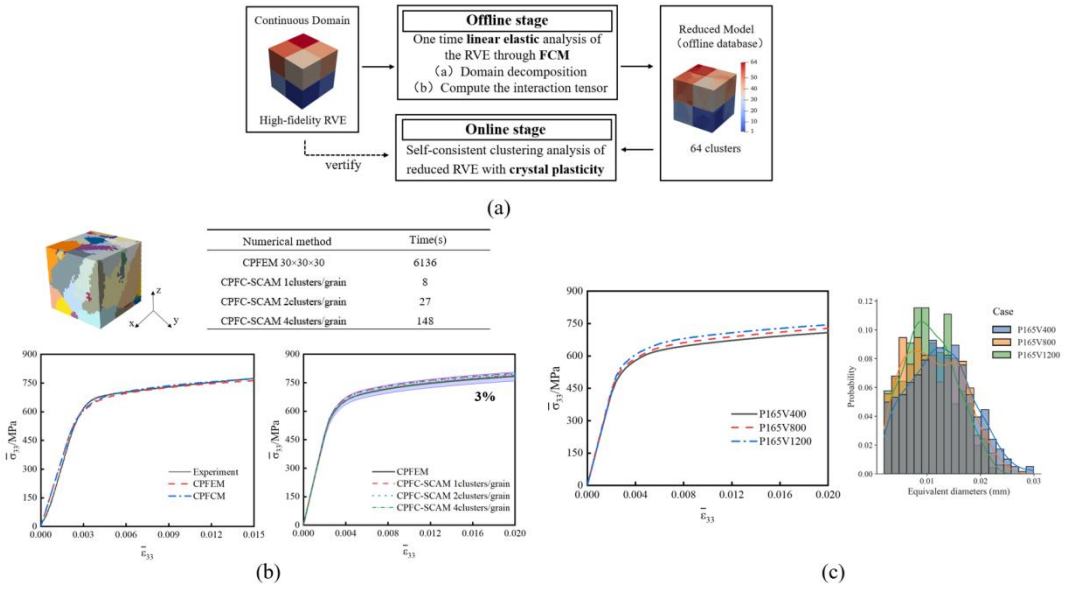

Figure 117: (a) Framework of the CPFC-SCAM, (b) validation of algorithm efficiency and accuracy, (c) effective stress-strain curves of the as-built material between different scan speeds with constant laser power

7.7 A novel cross-scale impact damage and fatigue model for advanced metal materials and structures[41]

Background and Mechanism

Impact damage and fatigue are emerging challenges in defense industry and civil infrastructure, including aerospace and rail transportation. Grounded in the plastic mechanics of metals during impact

[41] Chinese Aeronautical Establishment, Yu Zhijie, yuzhijie@cae.ac.cn

damage and fatigue processes, the present work establishes a delocalized, cross-scale impact constitutive relationship and model for metallic materials, and results in a convenient numerical simulation method for the impact damage and fatigue of multi-scale microstructured metals aimed at advanced manufacturing and novel structures. The results from the novel model align with the intrinsic balance between strength and ductility toughness in metallic materials.

The plastic performance predominantly dictates the service capability of metallic materials under extreme environmental conditions, with the accumulation and evolution of dislocations governing the plastic properties of these materials. Additive manufacturing, along with various manufacturing processes and parameters, yields distinct microstructures within the material, as illustrated in the figure below. These microstructures significantly influence the accumulation and evolution of dislocations, thereby endowing materials fabricated through advanced manufacturing techniques, such as additive manufacturing, with more pronounced size effects compared to traditional materials. Strain gradient theory is a theory based on the physical mechanism of dislocations that can effectively describe the size effect in metallic materials with microstructures. For the first time, we have coupled a lower-order strain gradient theory (CMSG) with models of impact damage and impact fatigue in the present work.

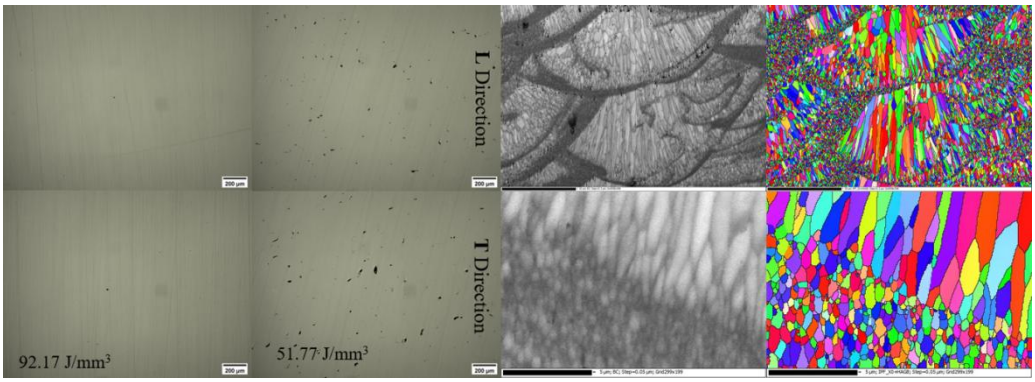

Figure 118: AM materials microstructures of different laser energies (left 4 subfigures) and EBSD information near a melting pool edge (right 4 subfigures)

Method and Model

The combination of the Johnson-Cook model and the strain gradient model provides a form of equivalent stress suitable for metal materials with cross-scale features at medium strain rates under impact. And by combining the definition and evolution of the damage in the Lemaitre model, the constitutive relationship and damage evolution law of the new model can be obtained.

$$\sigma_{eq} = \sqrt{[\sigma_{ref} f(\varepsilon^p)]^2 + l\eta^p} \cdot [1 + C\log(\dot{\varepsilon}^p)] \cdot (1 - D)$$

$$\dot{D} = \left\{ \frac{\sigma_{ref}^2 [f^2(\varepsilon^p) + l\eta^p] [1 + C\log(\dot{\varepsilon}^p)]^2 R_v}{2ES(1-D)^2} \right\}^m \dot{\varepsilon}^p$$

Based on this cross-scale impact damage evolution model, after integrating the time within a single impact process and integrating within the number of impacts, and with parameter reform and proper approximation, a formula for the cross-scale impact fatigue life can be obtained below, which can be used to predict the impact fatigue life for different impact strain loads at medium strain rates.

$$N = \frac{1}{2(2m+1)(1+C_3 m)}\left[\frac{2ES}{K^2 C_1 (1+C_2)^2}\right]^m \cdot \Delta\varepsilon^{p^{-(2mr+1)}}$$

Validation and Application

The aforementioned cross-scale impact damage constitutive relationship can be conveniently implemented in explicit finite element simulations. Figure 119(a) and Figure 119(b) show the stress distribution cloud diagrams before and after damage failure in a U-notch bending impact. The comparison with theoretical and implicit simulation shown in Figure 119(c), as well as the influence of different damage parameters on the stress-strain relationship shown in Figure 119(d), indicate that the new method of the present work can be effectively used for impact damage simulation of metal materials. The results shown in Figure 119(e) indicate that more significant size effects and rate effects will increase the strain of the material under impact load in the first few impacts. Figure 119(f) to (h) show the relationship between impact fatigue life and impact load (strain) with the influence of stress triaxiality, strain rate, and size effect in the impact fatigue life model, respectively. It can be seen from the results that the influence of all three factors on fatigue life is significant, with stress triaxiality and strain rate being the most significant factors.

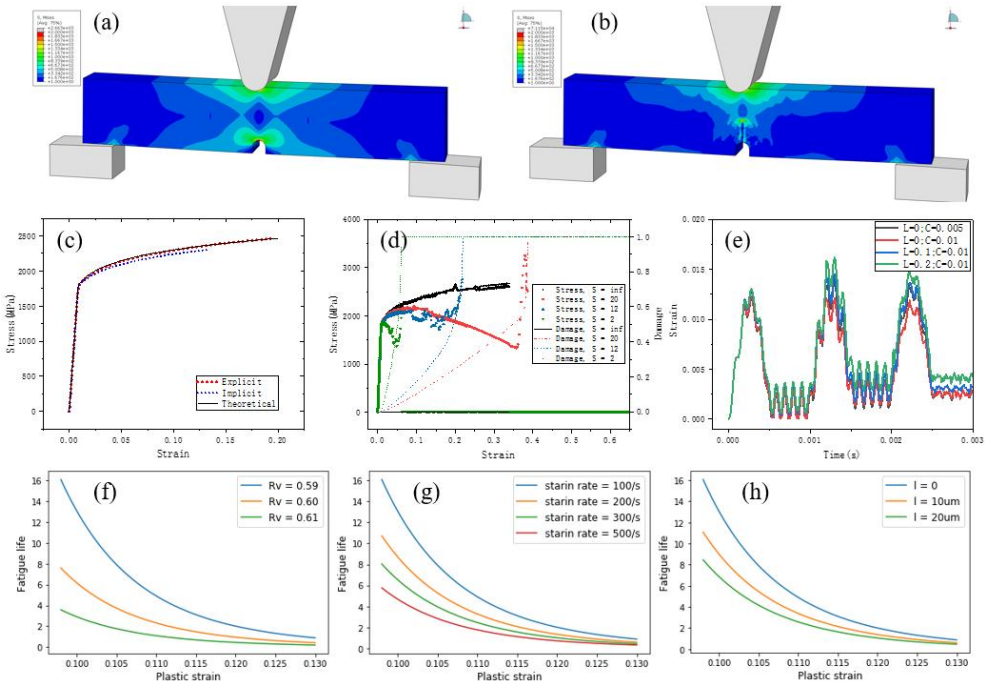

Figure 119: Stress contour (a) before and (b) after damage; (c) Verification of the mode; (d) Damage parameter and (e) influence of size effect and rate effect; impact fatigue life model with different (f) stress triaxiality (g) strain rate and (h) intrinsic material length (size effect)

8 NDI inspections and structural load/health monitoring

8.1 Ultrasonic nondestructive characterization of impact damage and compression after impact for CFRP based on multi-mode imaging[42]

For CFRP laminates with impact damage, delamination damage may occur near the impact point and along the thickness direction of the test piece, resulting in significant uncertainty in the number and location of echoes in the time-domain signal. For example, in the undamaged position, only surface and bottom echoes appear, while in the delamination position, the amplitude of echoes will vary with the size and depth of the delamination, and interference signals such as structural noise and electromagnetic noise will be added to the detection signal, further increasing the difficulty of accurately characterizing delamination damage. A CFRP impact damage characterization method combining multiple imaging modes is proposed to address the above issues. Firstly, ultrasound B-scan imaging is used to reproduce the cross-sectional distribution, expansion, and depth of internal damage in CFRP. By setting and selecting the scanning section, ultrasound images of any cross-section of the tested CFRP in the thickness direction can be obtained with a given step size, as shown in Figure 120.

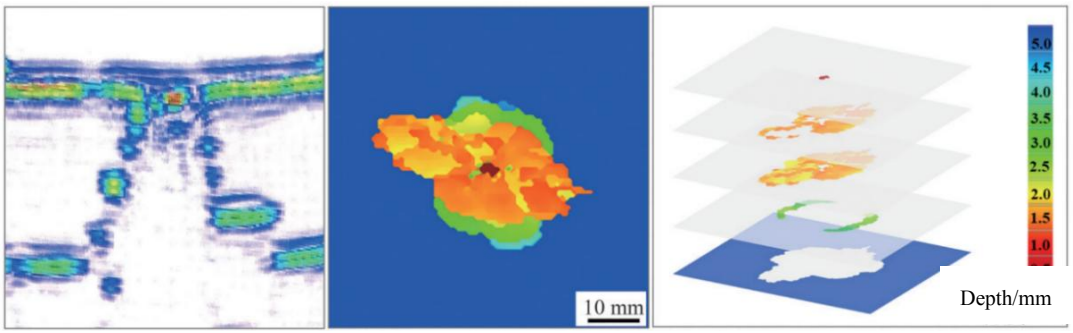

(a)B-scan image (b)C-scan image of sound path (c)Chromatography C-scan image

Figure 120: Multi-mode ultrasound imaging for impact damage

Impact damage imaging and damage characteristics

Based on the phased array ultrasonic testing test, Figure 121 shows the phased array ultrasonic B-scanning imaging results of CFRP test piece under 60J impact energy, where F represents the reflected echo on the surface of the test piece, B represents the reflected echo on the bottom surface of the test piece, and Di represents the reflected echo on the interface of the I-th layered damage. It can be found that in the undamaged area, the bottom reflection echo is clearly visible, and the image distribution between the bottom reflection echo and the surface reflection echo is uniform. In the damaged area, multiple interface reflection echoes caused by layered damage appear after the surface echo, and gradually expand to both sides. In addition, since ultrasonic waves are similar to total reflection at the layered interface, This results in the formation of an acoustic shadow region S, which is impenetrable to sound waves, after reflecting the echoes at the layered interface.

[42]Aircraft Strength Research Institute, Zhang Wei, zhangw395@avic.com

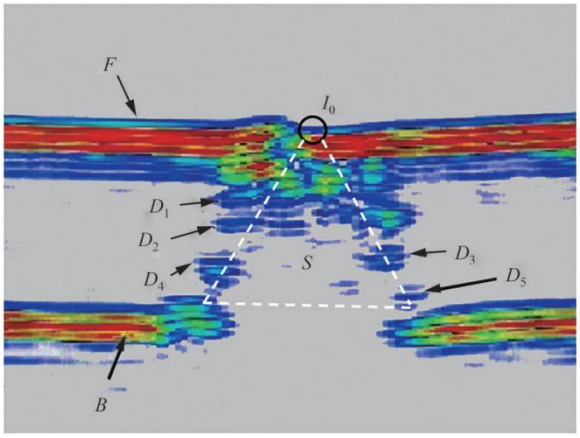

Figure 121: B-scan image of phased array ultrasonic testing

According to the analysis, under the impact load, near-surface delamination comparable to the diameter of the impact head is first generated near the impact point I0. As the impact energy is transmitted along the thickness direction of the test piece, new delamination damage is gradually generated at the layering positions of different depths inside the CFRP, and the impact point I0 is the center. The stratified damage showed an obvious pyramidal diffusion distribution in the thickness direction.

In order to further analyze the damage characteristics of CFRP under impact load, the phased array acoustic path C-scan images of the two groups of CFRP test pieces under impact energy of 35J and 60J are presented respectively, that is, the two-dimensional distribution of layered damage in layering direction and the overlay area projection. It can be found from the figure that the damage area of the acoustic path C-scan image under 60J impact energy is larger than that of the 35J impact energy, but the damage characteristics of the detected images are basically the same. Taking the acoustic path C-scan imaging results with impact energy of 60 J as an example, there are obvious acoustic path changes near the impact point. In the center of the impact area, the acoustic path of the ultrasonic interface reflection echo is relatively short, and the delamination damage mainly occurs in the thickness range of 0.5 ~1.0mm of the test piece, and the area is small. With the impact point as the center, the impact damage depth and area show a trend of gradually increasing and expanding outwards along the circumference, which further reflects the pyramidal diffusion distribution of layered damage in the thickness direction of CFRP.

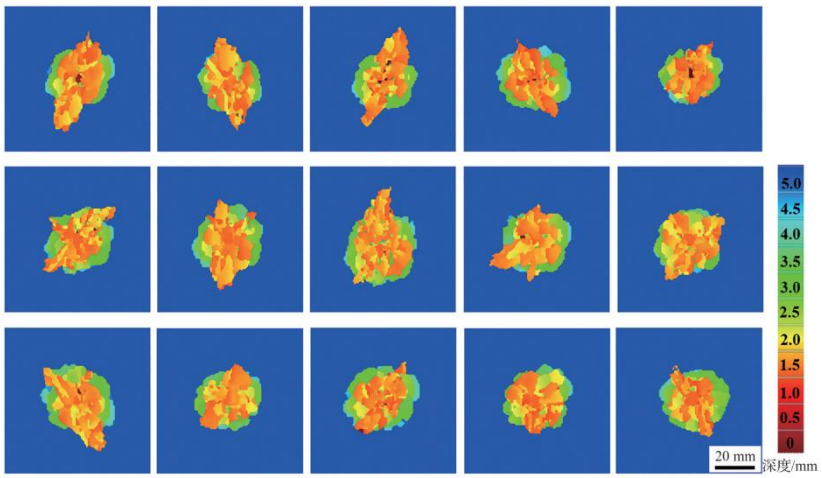

Figure 122: Depth C-scan images of CFRP laminates(impact energy 35J)

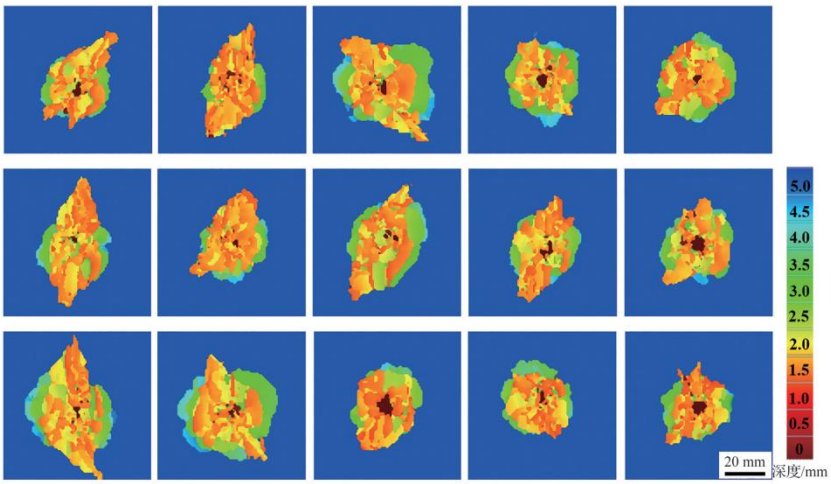

Figure 123: Depth C-scan images of CFRP laminates (impact energy 60J)

8.2 High-efficiency automated and intelligent damage inspection[43]

Currently, the field of full-scale ground test damage detection faces two core technical challenges: Firstly, for large-scale aircraft structures with complex geometries, how to achieve efficient and highly reliable full-area scanning and detection of damage features; secondly, within topologically complex enclosed/confined spaces, how to ensure accurate online identification of micro-damage under multi-physical field coupling conditions. In recent years, emerging technologies such as intelligent robotic systems, machine vision, and deep convolutional neural network algorithms have provided a new paradigm for constructing efficient and intelligent damage detection systems. Among these, the automated ultrasonic detection system for composite structures, by integrating multi-axis robotic arms, phased array ultrasonic probes, and intelligent signal processing algorithms, enables adaptive scanning of complex geometries and precise identification of delamination defects. Meanwhile, the machine vision-based damage inspection technology, utilizing high-resolution industrial cameras and intelligent image recognition algorithms, can rapidly locate surface damage and achieve intelligent classification of damage types.

Automated Ultrasonic Inspection Technology for Composite Materials

Composite materials, with their high specific strength and stiffness, corrosion resistance, fatigue resistance, and other advantages, are increasingly replacing metallic materials in modern aviation. The mature application of composite design processes and performance requires extensive building-block testing and validation, coupled with mandatory 100% ultrasonic non-destructive testing (NDT). This demands urgent advancements in efficient, high-precision detection technologies and capabilities both before and during composite testing, posing significant challenges. While automated ultrasonic testing has achieved large-scale engineering use in batch inspections of simple-configuration composite products, challenges persist in composite testing validation. Due to the progressive scaling of specimen size and complexity in building-block validation, test components vary widely in dimensions, geometries, and assembly states. Manual ultrasonic testing remains dominant in this field, suffering from inefficiency, low accuracy, and poor reliability.

[43] Aircraft Strength Research Institute, Yang Yu, yangyu@cae.ac.cn

To address these issues, the team at the Aircraft Strength Research Institute of China developed a computer-based closed-loop interactive method for synchronized motion and detection control. This innovation enables batch continuous testing of standard composite specimens of varying thicknesses and multi-mechanism collaborative testing of curved panels. They pioneered an automated conveying and testing coordination device for standard composite specimens, reducing the combined cycle time for transport and testing to 8 seconds per specimen. Additionally, they created an automated array ultrasonic testing system for curved composite panels, achieving a testing efficiency of 0.2 m²/min for large-scale curved structures—a 30% improvement over traditional manual methods. These breakthroughs effectively resolve long-standing bottlenecks in manual testing, such as excessive workload, prolonged cycles, and reliability concerns.

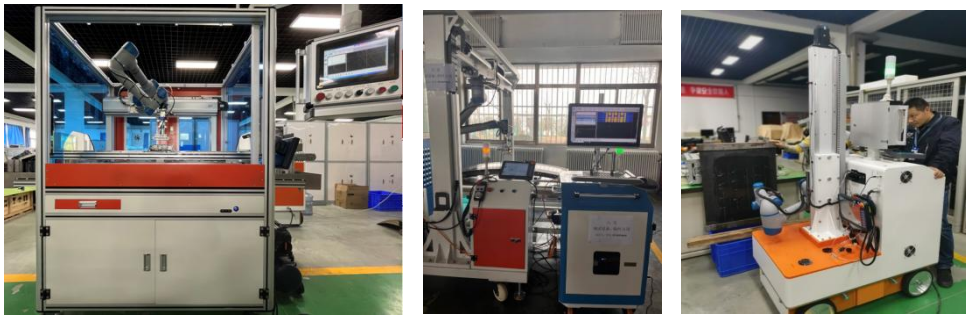

Figure 124: Serialized automated ultrasonic inspection Systems developed by ASRI

Machine Vision Damage Inspection Technology

The full-aircraft ground test is characterized by complex fuselage structures, numerous and dispersed inspection areas, confined spaces, and harsh environments. Especially in narrow and enclosed fuselage structures, non-destructive testing personnel face significant challenges in conducting detailed visual inspections due to spatial limitations and detection accessibility issues. This significantly elevates the risk of missed damage detection, rendering these narrow and enclosed structures prone to high-incidence areas for missed damage detection. An effective approach to addressing this issue is the adoption of a flexibly deployable, miniaturized visual inspection system for automated damage detection in narrow/enclosed structures, thereby replacing human inspectors.

Machine vision damage inspection system is a lightweight intelligent monitoring device equipped with functions for area patrol and real-time damage monitoring. It can be deployed within confined spaces to autonomously identify stress concentration areas, detect structural damages, and provide feedback on inspection results, effectively addressing the issue of uncontrollable damages in inaccessible areas. The core modules of this system comprise: (1) Highly flexible and miniaturized visual terminal platform, which is capable of autonomously reaching regions of interest within narrow and confined spaces and acquiring images from multiple angles; (2) Proprietary monitoring software embedded with a series of self-developed artificial intelligence algorithms, including the high-reliability automatic detection algorithm for stress concentration areas, the automatic segmentation algorithm for micro-crack, and the high-precision crack propagation tracking algorithm, enabling accurate identification and propagation tracking measurement of micro-cracks in complex environment; (3) Edge computing system that supports rapid, low-cost, and distributed deployment of the machine vision damage inspection system, as well as remote viewing of monitoring process. This system has been implemented in the full-aircraft ground tests of multiple military and civilian aircraft. It has

successfully assisted in the manual identification of crack initiation, tracking of crack propagation, and acquisition of key parameters for structural durability and damage tolerance analysis. Consequently, it can effectively reduce inspection time and labor costs for monitored areas.

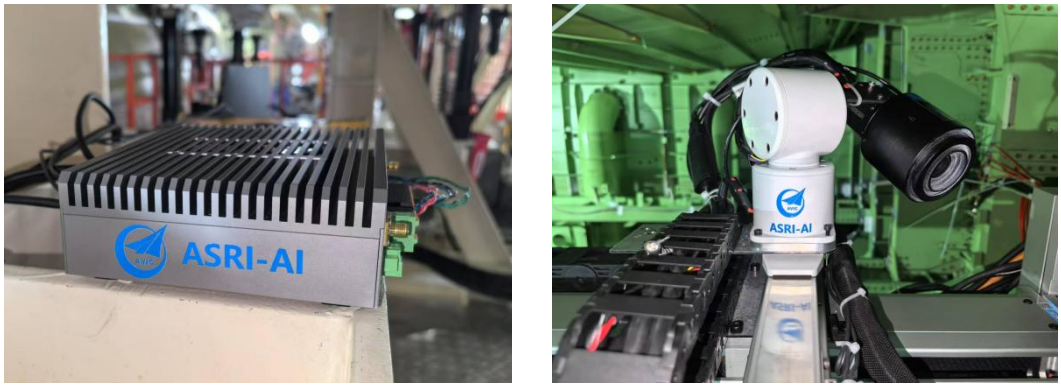

(a) (b)

Figure2: (a)ASRI-AI Edge computing module. (b)ASRI-AI Visual terminal platform

8.3 Multi-parameters monitoring of composite structures using optical fiber sensor[44]

Fiber Bragg grating (FBG) reflects a specific wavelength of light and sensitive to both strain and temperature, thus, strain and temperature can be calculated according to the FBG wavelength shift. The multipoint sensing can be achieved using wavelength division and time division methods. FBG sensors with different orientations were embedded into a full-size composite wing leading edge for creep monitoring after demolding as shown in Figure 125. An algorithm based on multi-parameter decoupling and Burger model was developed to reconstruct creep curve in 710 h, achieving time error < only 3 h. An embeddable multifunctional FBG sensor with temperature resistance up to 340 ℃ and pressure resistance up to 2 MPa was also developed as shown in Figure 126. The monitoring was applied to different composites including carbon fiber reinforced plastics, carbon fiber reinforced thermoplastics and glass fiber reinforced thermoplastics. The forming process was divided into five stages, each with distinct characteristics in spectrum. The differences of measured temperature between encapsulated FBG and thermocouple was smaller than approximately 3 ℃. The in-plane and transverse strain were also evaluated with different trends like remaining stable or approximately linear relationship in five stages, suggesting that PSFBG is a promising method for in-situ monitoring during composite forming process.

[44]Nanjing University of Aeronautics and Astronautics, Wu Qi, wu.qi@nuaa.edu.cn

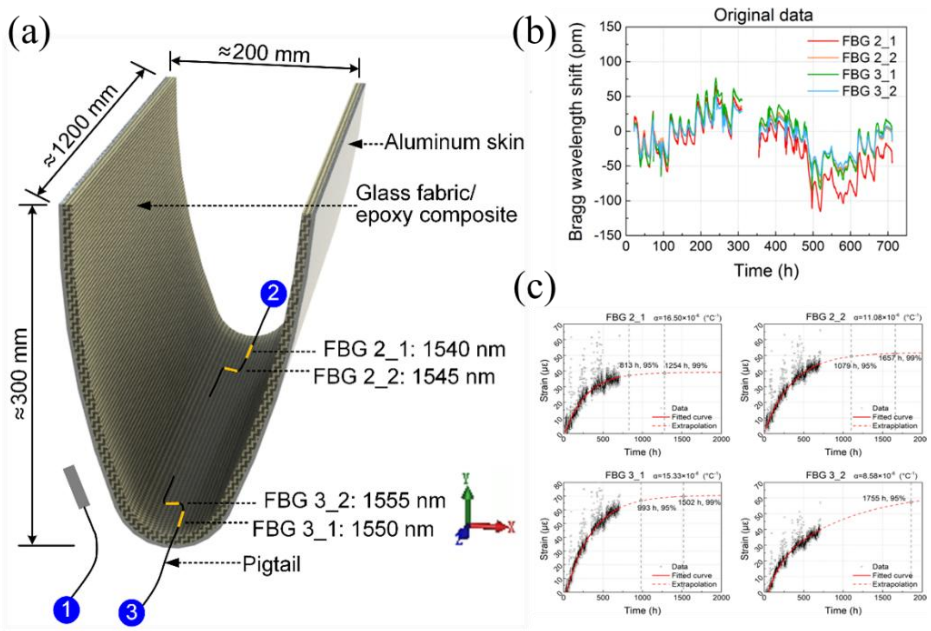

Figure 125: Creep monitoring of composite wing leading edge (a) composite wing leading edge embedded with FBGs (b) original coupled data (c) reconstructed creep curve

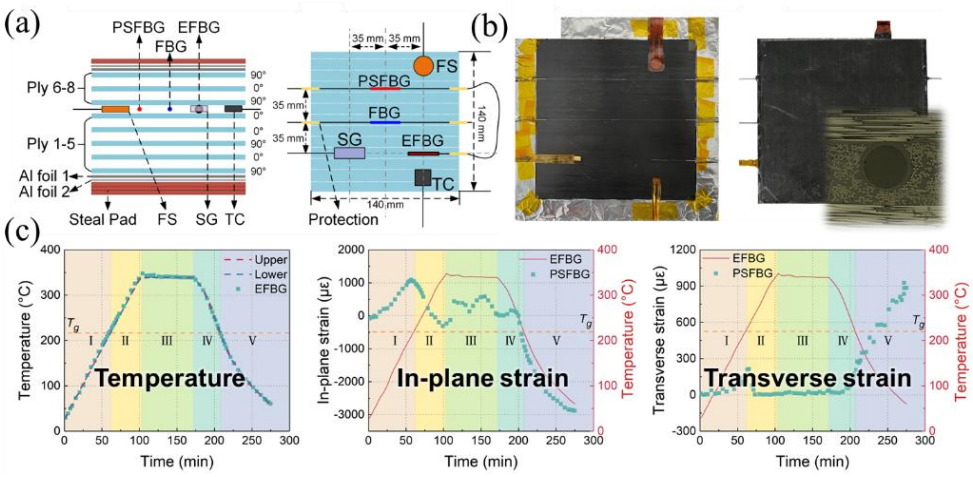

Figure 126: In-situ monitoring of composite forming (a) sensor layer (b) photo of FBG embedded composite (c) curves of temperature, in-plane strain and transverse strain

Ultrasonic monitoring of composite materials

Phase-shifted fiber Bragg grating (PsFBG) is made by inserting a phase shift into the middle of an FBG. It has high ultrasonic sensitivity and broad bandwidth, which makes it suitable for ultrasonic monitoring. The acoustic emission (AE) testing was conducted on the composite at room temperature and low temperature as shown in Figure 127. Different AE statistic features such as cumulative hits or energy distribution were extracted for damage analysis. The modes of Lamb wave were also analyzed in time and frequency domains. Six kinds of signals were distinguished and corresponded to composite damage including matrix crack, delamination, etc. Meanwhile, the AE signals at low temperature appear earlier and increase in number than that at room temperature, indicating the increase of CFRP brittleness. AE monitoring of complex composite structure was also realized on T-joint as shown in

Figure 128. It was found that T-joint did not produce matrix cracks and other small damage before debonding. Temperature changes during the forming can have an impact on ultrasonic monitoring due to the fact that FBG is sensitive to static strain. Thus, encapsulation technology, which used metal tubes to isolate strain, was used to monitor ultrasonic guided waves during the composite forming using acousto-ultrasonic system as shown in Figure 128. Normalized spectrum peaks of ultrasonic guided wave were analyzed to accurately assess the degree of cure of composite prepreg.

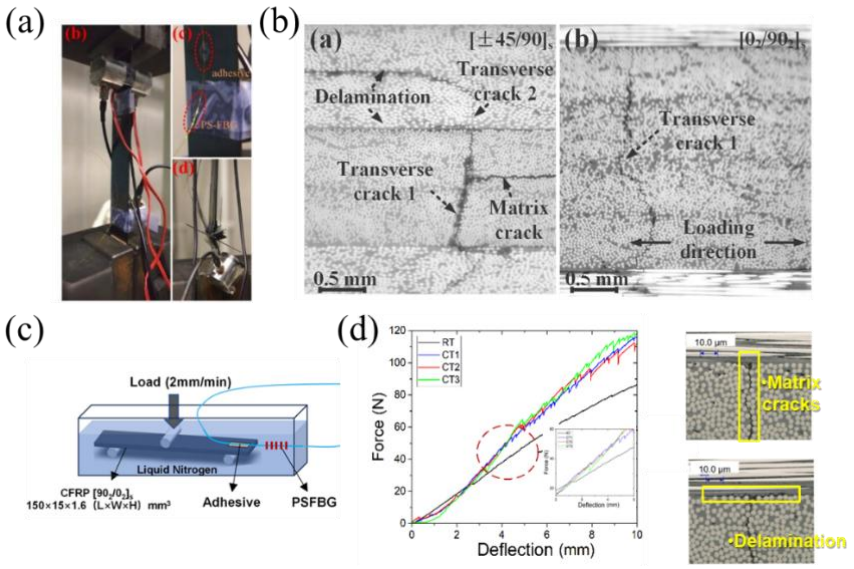

Figure 127: AE monitoring of composite in room and low temperature (a) experimental setup in room temperature (b) various types of microdamage (c) experimental setup in low temperature (d) mechanical properties and different types of microdamage

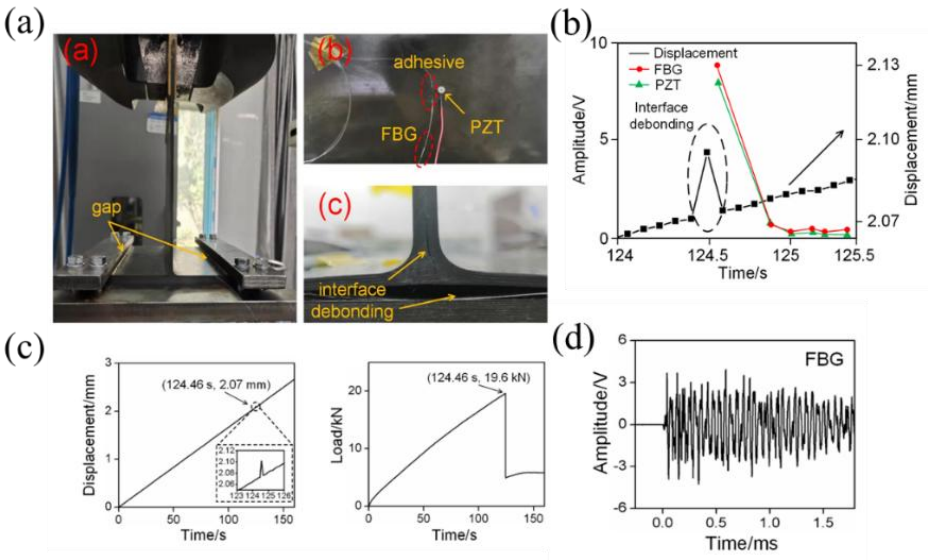

Figure 128: AE of composite T-joint (a) tensile test of T-joint (b) relationship of amplitude and load (c) displacement and load curves (d) typical signal

8.4 Aircraft structural health monitoring technology based on optical fiber sensing[45]

Considering the material properties, geometric characteristics, manufacturing processes, and service environment of aircraft structures, as well as the requirements for structural sensing parameters, optical fiber sensors and their integration strategies with aircraft structures are designed. These strategies aim to enable efficient and precise self-sensing of critical structural components without compromising structural efficiency. Additionally, multi-source optical fiber sensing data, including strain, temperature, deformation, and ultrasonic signals, will be analyzed in both the time and frequency domains to extract key features. A low-redundancy, high-dimensional feature set will be constructed to provide diverse and accurate measured data, serving as the foundation for subsequent performance degradation assessment, damage localization, and life prediction algorithms.

Application of technology

Based on the material system of the aircraft structure and structural production/assembly processes, the integration strategies were proposed for embedding or surface-mounting fiber optic sensors within/on the structure. Through the optimization of the sensing components, packaging, process stability, the reliability of sensors has been enhanced after structural integration while ensuring the integrity of sensing functions. By conducting simulated onboard environmental validation tests, the sensing capabilities of smart structures for parameters including strain, temperature, acceleration, and pressure were assessed. The overall process is shown in Figure 129.

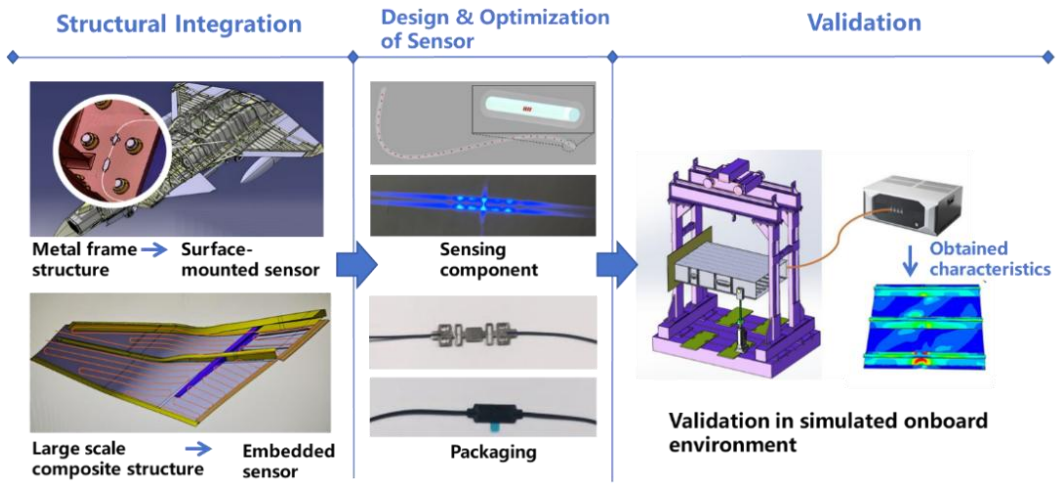

Figure 129: Evaluation process of aircraft structures

As illustrated in Figure 130, cracks and corrosion are the main forms of damage to aircraft metal structures, while fiber breakage and delamination are the main forms of damage to aircraft composite material structures. The methods of using optical fiber ultrasonic sensors for aircraft structural damage detection are mainly divided into passive and active types. When damage occurs accompanied by a significant acoustic emission phenomenon (cracks and composite material fiber breakage, etc.), passive detection methods are often used to capture the corresponding characteristic signals. However, during aircraft maintenance inspections for corrosion and other damages on the ground, active detection methods need to be adopted. In such methods, acoustic signals are excited. By capturing variations in the signal caused by the damages, the aircraft structures are evaluated utilizing the damage

[45] Changcheng Institute of Metrology&Measurement, Sui Guanghui , suigh@avic.com.

identification and localization reconstruction algorithms.

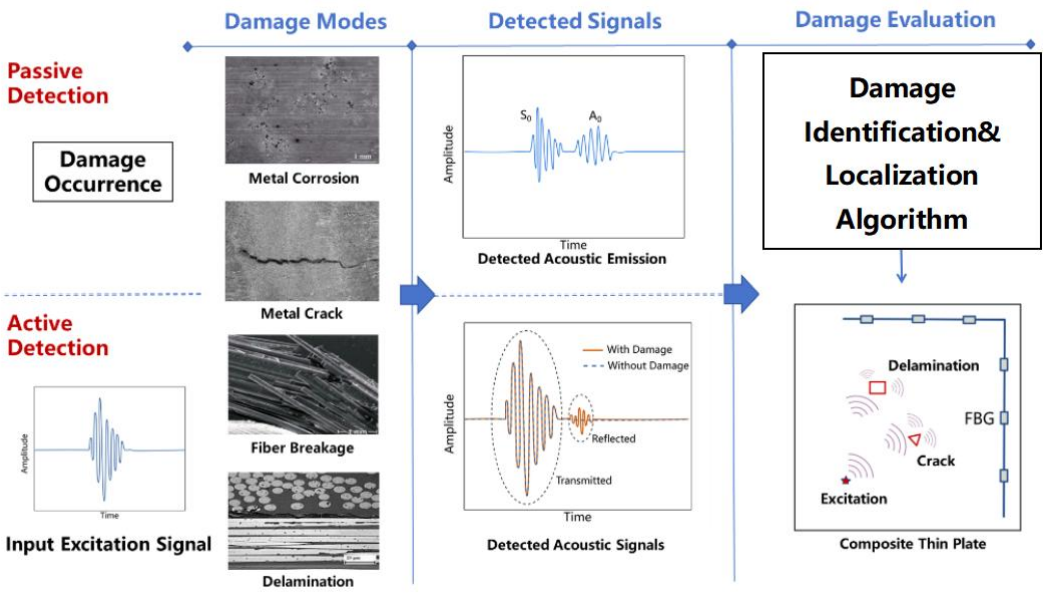

Figure 130: The passive and active detection of damages

The deformation measurement technology based on high-density weak reflection fiber Bragg gratings is a type of contact measurement method. The application of the sensors on the aircraft structures is not constrained by the structural characteristics. Moreover, it offers high real-time sensing capability, and immunity to electromagnetic interference. By considering the shape of the aircraft structure and its deformation characteristics, a sensor layout was proposed as shown in Figure 131. The deformation of the aircraft structure is reconstructed in real-time by analyzing the three-dimensional shape of the optical fiber.

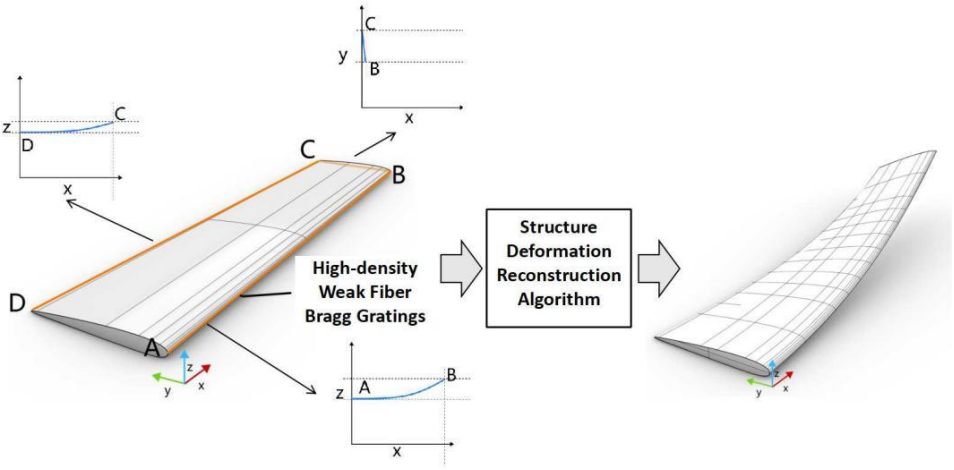

Figure 131: The deformation sensing using high-density weak reflection fiber Bragg grating sensor

8.5 Manufacturing of intelligent fiber-optic composite structures and applications[46]

The design, manufacturing, verification, evaluation, and maintenance technologies of intelligent composite material structures based on structural health monitoring are among the key technologies that promote the superior performance of composite materials and reduce the development and operational costs of civil aircraft. To achieve these goals, a fiber Bragg grating (FBG) sensing network with advantages such as small diameter, high-temperature resistance, large-scale networking capability, and bending resistance has been developed. Research has been conducted on the preparation technology of intelligent composite materials based on the fiber optic sensing network, and the application prospects of intelligent composite material structures in the manufacturing, testing, and service scenarios of commercial aircraft have been explored. This technology has already been applied to real-time temperature and strain monitoring during the curing process of a 1-meter-level L-shaped structural component, providing support for optimizing the R-zone springback process.

Development of Intelligent Fiber-Optic Composite Structures

A small-core FBG array was developed using the draw tower fiber grating fabrication technique. The developed gratings feature small diameter, high temperature resistance, suitability for large-scale networking, good bending resistance, and high accuracy in strain and temperature measurement when surface-mounted or embedded in composite materials. Feasibility verification was conducted for temperature and strain measurement at multiple positions and layers within the composite material using the fiber grating sensing network. The accuracy of strain measurement in integrated smart composite materials under high temperatures was validated, and the impact of embedding the fiber grating sensing network on the mechanical properties of the composite materials was studied. The preparation of a 1-meter-level L-shaped smart structural component and real-time monitoring of temperature and strain during the curing process were achieved.

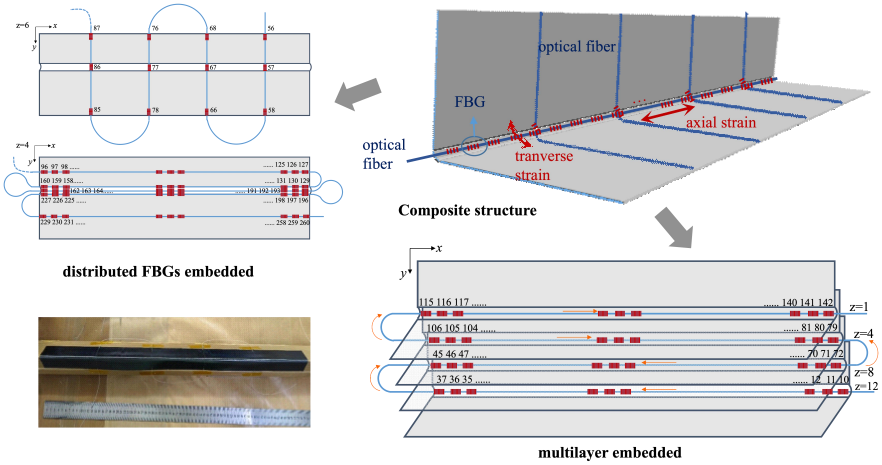

Figure 132: The intelligent composite component with embedded fiber Bragg grating sensor networks

The Prospect of the Application of Intelligent Fiber-Optic Composite Structures

Intelligent fiber-optic composite materials can be applied across various stages of aircraft development

[46] Shanghai Aircraft Manufacturing Co., Ltd, Composites Center, Qiu Xueqiong , qiuxueqiong@comac.cc,

and operation. During the manufacturing phase, by monitoring the curing process of composite structures, manufacturing processes can be improved, such as studying the relationship between R-zone strain and the degree of springback to predict R-zone springback and refining the processes to reduce it. In the testing and verification phase, the traditional strain gauges could be replaced and it could facilitate mechanical testing under high-temperature environments, as illustrated in Figure 133 showing thermal stress testing on large aircraft structures, significantly simplifying test setups and enhancing testing efficiency. During the service and operation phase, intelligent fiber-optic composite structures can provide real-time status data, enabling online or remote structural health monitoring and offering new approaches for condition-based maintenance.

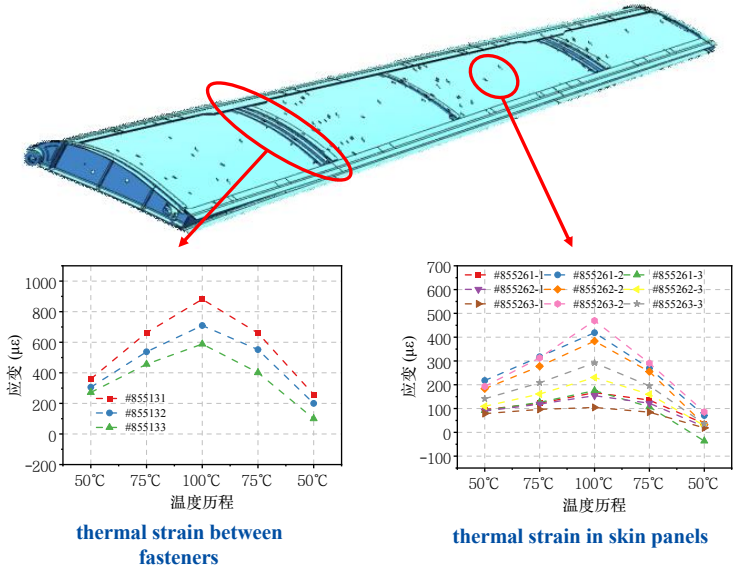

Figure 133: Thermal stress test of full size composite wing flap structures using FBG network

9 Full-scale fatigue testing

9.1 Civil aircraft flap high-reliability sinking hinge mechanism test technology [47]

The Civil Aircraft Flap Sinking Hinge, as a novel flap motion mechanism, necessitates component-level and assembly-level functional testing to verify and optimize its reliability design. To safely and efficiently conduct assembly-level flap mechanism functional tests, technical challenges in control, loading, fault simulation and measurement, and safety protection must be resolved. Based on this, four key technologies have been developed: flap attitude precision control technology, flap spatial motion process accurate load application technology, key parameter precision measurement technology, and multi-margin test safety protection technology

Key technology

Flap attitude precision control technology is achieved through a closed-loop precise control of flap attitude using a "control system+lower computer+encoder+tilt sensor" approach; flap spatial motion process accurate load application technology combines a screw module and a force controlled actuator to actively control the follow-up loading scheme, achieving accurate application of aerodynamic loads

[47] Aircraft Strength Research Institute, Li Yao, liy389@avic.com

during the automatic retraction and extension of flaps; key parameter precision measurement technology indirectly measures the hysteresis torque increment by adding torque sensors on the torque tube transmission path to characterize the frictional force increment of bearing hysteresis; multi-margin test safety protection technology is constructed by designing weak links in fixtures, adding torque sensors, angle sensors, and setting differential protection. In summary, a complete set of high reliability sinking hinge mechanism testing technology for civil aircraft flaps has been developed.

Application of technology

This project is applied to the flaps of a certain civilian aircraft model, which uses a sinking hinge mechanism. The component level test site of the high reliability sinking hinge mechanism is shown in the following figure.

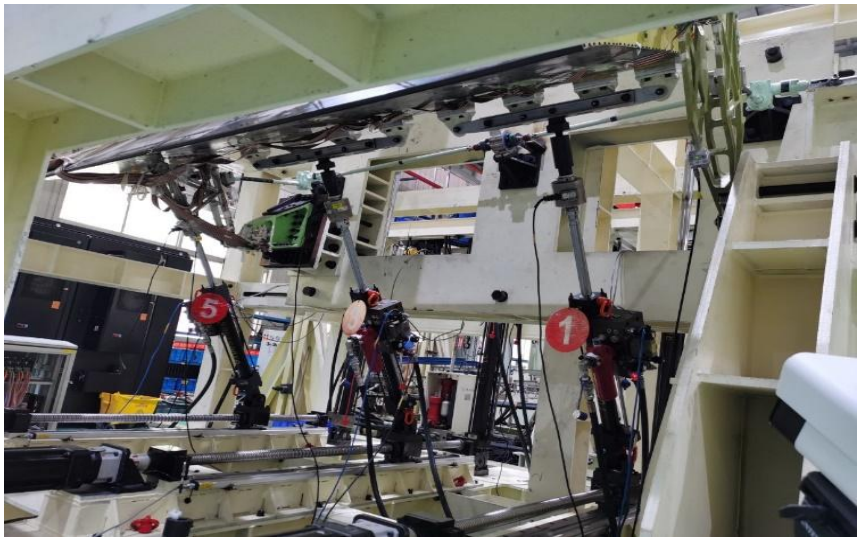

Figure 134: High-reliability sinking hinge mechanism test

The flap of this type must achieve 4,800 cycles of extension and retraction between 0° and 35°. Through flap attitude precision control technology, the control accuracy of the flap attitude encoder is maintained within 1%. By applying flap spatial motion process accurate load application technology, the displacement control accuracy of follow-up loading is kept within 1%, with substantial alignment between load commands and feedback at loading points, and load control accuracy within 5%. Key parameter precision measurement technology is utilized to measure the friction increment after bearing seizure. Multi-margin safety protection technology ensures the safe and smooth progress of the test.

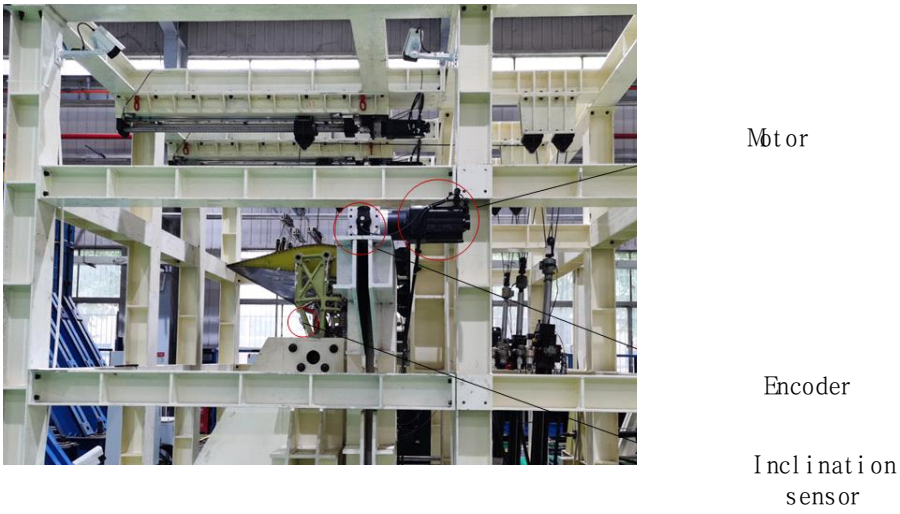

Figure 135: Flap attitude control field schematic diagram

The civil aircraft flap high-reliability sinking hinge mechanism test technology resolves key technical challenges including flap dynamic drive control, flap spatial motion process accurate load application, seizure fault simulation, key parameter precision measurement, and multi-margin test safety protection. It delivers robust technical support for assessing the structural lifespan and reliability of civil aircraft flaps and slats, holding critical significance for the development of both military and civilian aircraft.

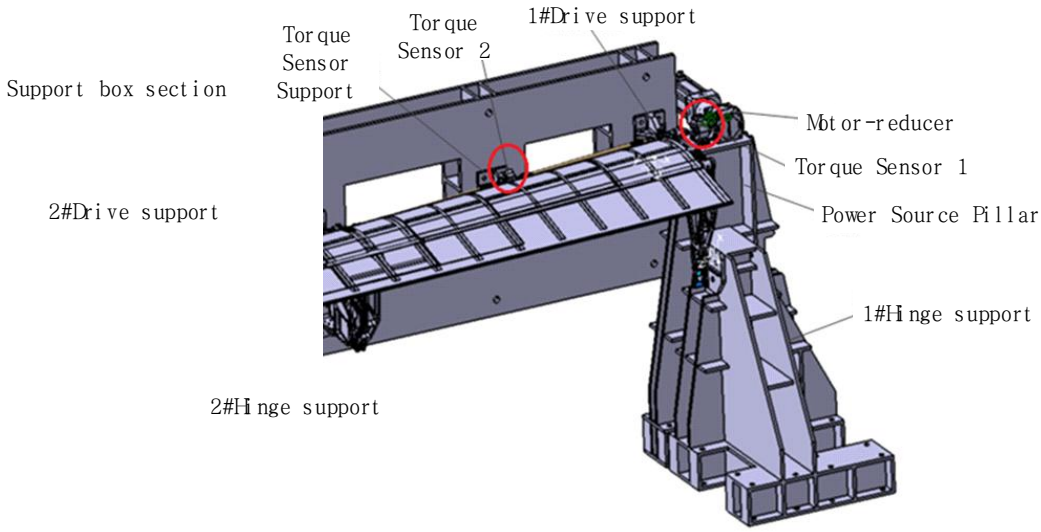

Figure 136: Torque sensor measurement scheme diagram

9.2 Safety protection technologies for full-scale fatigue testing of c919 aircraft[48]

Full-scale fatigue testing of the C919 aircraft was conducted to verify that it meets the requirements related to widespread fatigue damage in the airworthiness provisions. A cumulative total of 3 times life fatigue test needs to be completed. The long-period fatigue test poses a great challenge to the safety of the test system, and complete and reliable safety protection should be established for the various failure modes that may occur in each system.

[48] Aircraft Strength Research Institute, Wang Mengmeng, wangmm011@avic.com

Air inflation overpressure protection system

A multi-port collaborative low-noise rapid inflation/deflation system was developed, featuring 40 synchronized ports to enhance operational efficiency by 55% (Figure 137). Dual control systems—loading control and gas circuit safety monitoring—were implemented to prevent overpressure risks. The gas circuit system utilized five pressure relief valves with adaptive venting thresholds: 60 kPa initial relief and 85 kPa equilibrium pressure. Real-time pressure and flow monitoring via a dedicated interface ensured fail-safe responses, significantly reducing risks of cabin overpressure.

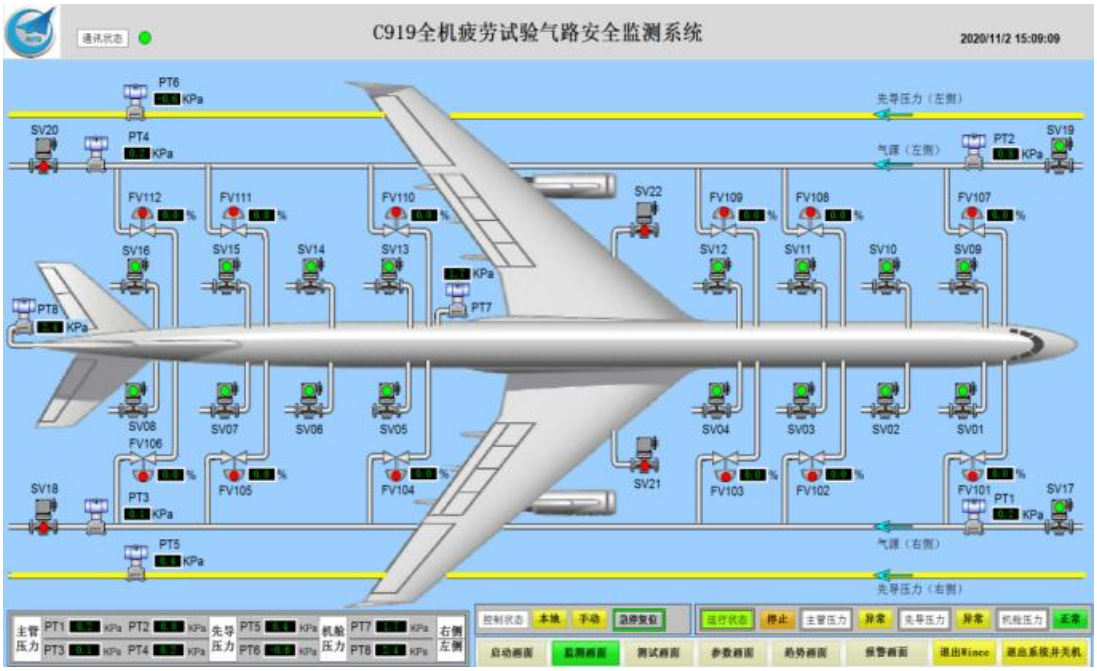

Figure 137: Schematic of the gas circuit safety monitoring system.

Hydraulic pipeline overpressure protection and monitoring

Pressure-regulating valves were installed at hydraulic substations to stabilize return oil pipeline pressure within predefined limits. A pressure relief tank connected to low-pressure pipelines enabled dynamic pressure dissipation, while a visualized oil circuit interface (Figure 138) provided remote monitoring and control via solenoid valves. Proactive pressure relief and automated oil recirculation through pumps minimized low-pressure pipeline failures, achieving 99.9% system reliability during cyclic loading.

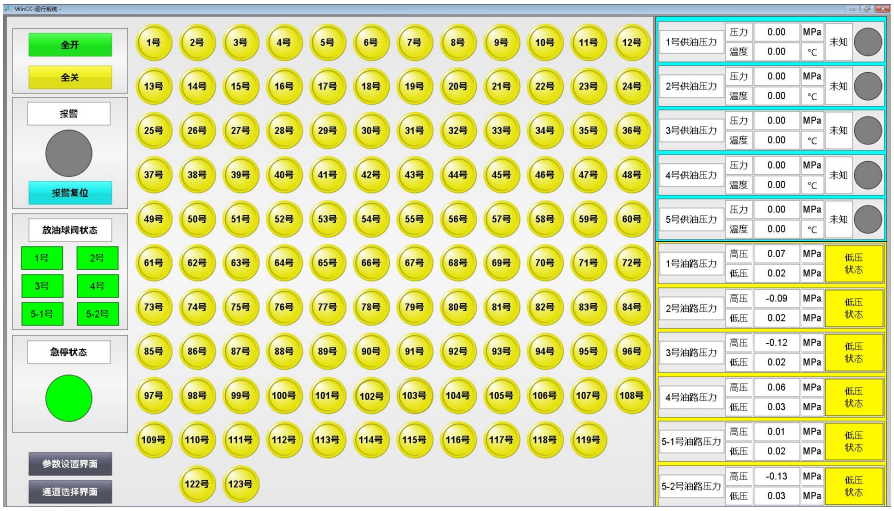

Figure 138: Operation interface of the visual oil circuit system.

Aircraft constraint protection system

A six-degree-of-freedom displacement compensation constraint system (Figure 139) ensured precise aircraft attitude control during testing. Safety measures included: Nose landing gear protection: A tray-pull rod assembly prevented bowing and abnormal pitch. Main landing gear protection: Dummy wheel trays mitigated adaptive support collapse risks. Actuator cylinder limiters: Restricted heading and lateral deviations during emergencies.

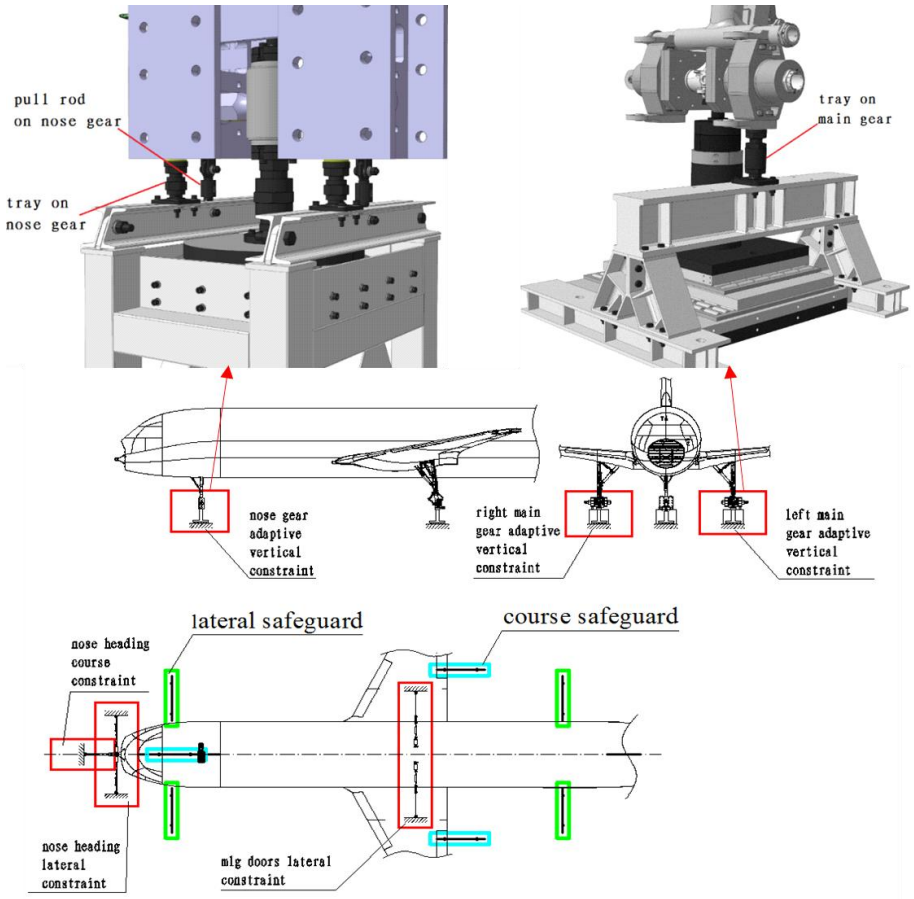

Figure 139: Schematic of the aircraft constraint system.

9.3 The full-scale fatigue test technology of the large-scale fire extinguishing/water rescue amphibious aircraft[49]

Full-scale fatigue testing provides the basis for determining the service life of aircraft structures, formulating maintenance plans, structural optimization, and process improvements. By detecting the initiation and propagation of fatigue cracks, it identifies weak points in fatigue resistance and evaluates aircraft safety. A certain large amphibious aircraft, due to its dual requirements for hydrodynamic and aerodynamic performance, as well as considerations regarding usage patterns and operational environments, presents significant differences from conventional land-based aircraft in structural design, load distribution, and testing. In the full-scale fatigue test of this large amphibious aircraft, multiple key technologies were successfully developed, including precise load processing, high-precision test loading, "0g" state enabling techniques (such as weight-offloading technology), and fatigue-resistant test platforms.

loads processing

The aircraft is used for both firefighting and rescue operations, with four task profiles (water scooping fire suppression, water injection fire suppression, airdrop rescue, and water landing rescue). During full-scale fatigue testing, the original inertial, aerodynamic, and hydrodynamic loads associated with all operational conditions across different task profiles and mission segments throughout the aircraft's lifecycle need to be converted into test implementation loads. To realistically simulate the actual loading conditions on the aircraft using limited loading actuators, various load processing methods were employed. Compared to the original loads, the calculated results ensured consistent loading on critical structural components while maintaining good fitting of shear force and bending moment distributions across different sections of the airframe.

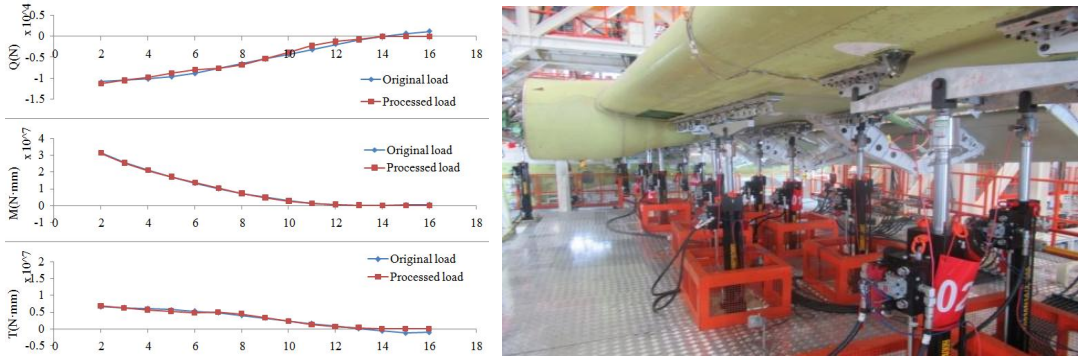

Figure 140: Comparison of shear force, bending moment, and torque before and after treatment

Test loading

The aircraft operates in a complex environment with diverse loads and differs significantly from conventional land-based aircraft in terms of structure. During testing, loading was conducted using different methods based on structural characteristics and load features, accurately reproducing the loads experienced by the aircraft during flight, takeoff/landing, and waterborne taxiing. This ensured that the structure underwent stress cycles identical to those encountered in actual use within the laboratory setting. The full-scale aircraft fatigue test utilized 151 hydraulic servo actuator loading points to

[49] Aircraft Strength Research Institute, Wang Zheng, wangz123@avic.com

simulate hydrodynamic, aerodynamic, and inertial loads on the aircraft. The test specimen was suspended using forward and main landing gear support fixtures at a height of 5000 mm above ground level along the aircraft's construction horizontal line. To maintain stability during testing, a six-degree-of-freedom statically determinate constraint method was employed.

Figure 141: Fatigue Test Loading System

Test Platform

The test loading platform is the main equipment used for operating, applying loads, inspecting, and monitoring the status of fatigue tests. It not only enables the application of partial vertical upward, heading, and lateral loads but also addresses issues such as test ballasting, inspection, and cable installation. The full-scale test framework adopts a modular design, facilitating rapid installation of the framework and loading points. The framework is divided into four spans and four levels in total. After verifying the overall strength, stiffness, and stability of the framework, modifications are made to strengthen its weaker sections based on analysis results, optimizing the overall design scheme continuously. Finally, under the condition of meeting the loading usage requirements, the selection of profile materials for each component, as well as their overall combination forms, is determined.

The hydraulic system mainly consists of main pipelines, distributors, remote control systems, and related fixed brackets. The hydraulic system includes four sets of hydraulic sub-stations and four sets of main pipeline systems in total.

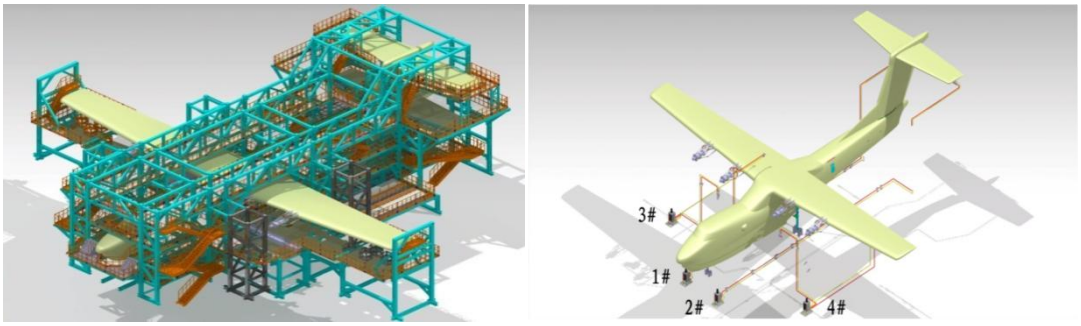

Figure 142: The Test Loading Platform and Hydraulic System Layout Diagram

9.4 Full-Scale Verification Technology for C919 Aircraft Rear Fuselage and Vertical Tail[50]

Construction of Strength Verification Framework for Composite Tail Section Structures

The full-scale structural strength verification of large composite components in civil aircraft occupies the apex of the "building-block" verification methodology, with its core focusing on integrated validation of damage simulation, repeated loading, and environmental coupling effects. To address these challenges, this study innovatively established a full-scale verification framework integrating fatigue, static, and damage tolerance assessments, in compliance with CCAR-25 airworthiness regulations and AC20-107B specialized guidelines. By systematically analyzing composite structural characteristics, a comprehensive solution was developed, encompassing test plan design, technical path optimization, and cycle control.

The verification path planning adheres to a "defect-environment-loading" triaxial logic, balancing safety margins with optimized cost and duration through humidity-temperature environmental simulation factors and load amplification coefficients. The static strength verification employs a three-stage protocol: " barely visible impact damage (BVID) introduction → 2× service life repeated loading → ultimate load test", effectively characterizing material property degradation under cyclic loading and environmental exposure while validating the ultimate load-bearing capacity of Class 1 damage structures throughout their operational lifespan.

For damage tolerance verification, a progressive procedure is implemented: " visible impact damage (VID) introduction → 2× inspection interval repeated loading → limit load test → limit load test - latent visible impact damage (LVID) introduction → limit load test". This sequentially verifies the residual strength of Class 2 damage structures to sustain limit loads within inspection intervals and the limit load-bearing capability of Class 3 damage structures. Finally, a structural load-bearing capacity test quantifies residual strength and failure modes.

Implementation of Verification Technologies for C919 Rear Fuselage and Vertical Tail

Building upon the above framework, the full-scale verification of the C919 composite rear fuselage and vertical tail achieved three technological innovations: A full-scale test platform integrating structures beyond Frame 64 (mid-rear fuselage, rear fuselage, and vertical tail) with a dummy horizontal tail, utilizing box-shaped end-cap fixation (Figure 143) and a 27-point loading system. A novel fully rigid loading method incorporating tension-compression pad-lever systems (Figure 144), enabling synchronized cabin floor beam and joint loading, improved operational efficiency. A distributed data acquisition architecture employing proximal analog-to-digital conversion, reducing on-site cabling by 60% and enhancing signal anti-interference performance. During implementation, load spectrum optimization and parallelized test design reduced the static/fatigue verification cycle to 333 days and damage tolerance verification to 265 days.

[50] Aircraft Strength Research Institute, Liu Wei, liuw103@avic.com

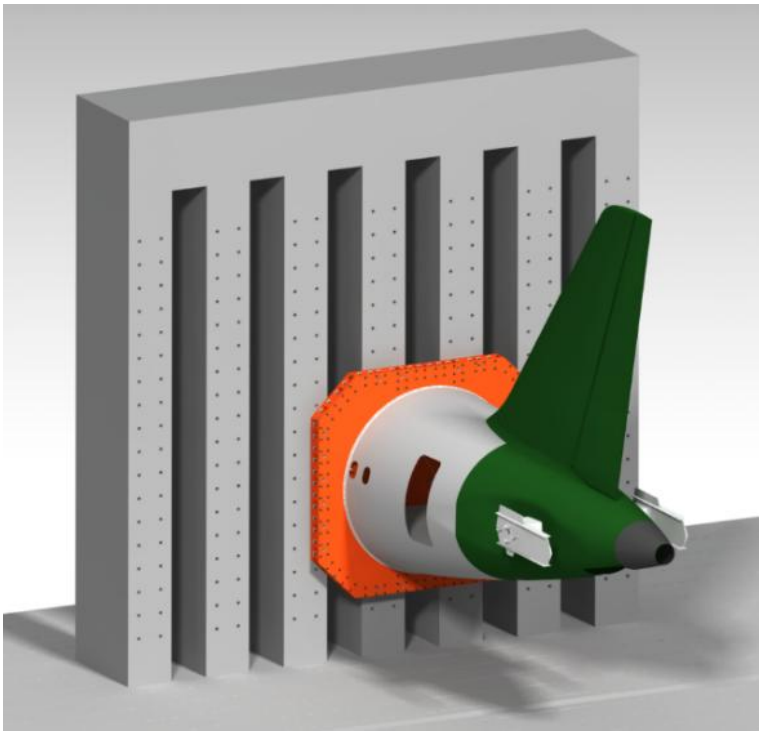

Figure 143: Schematic diagram of test specimen and constraint form

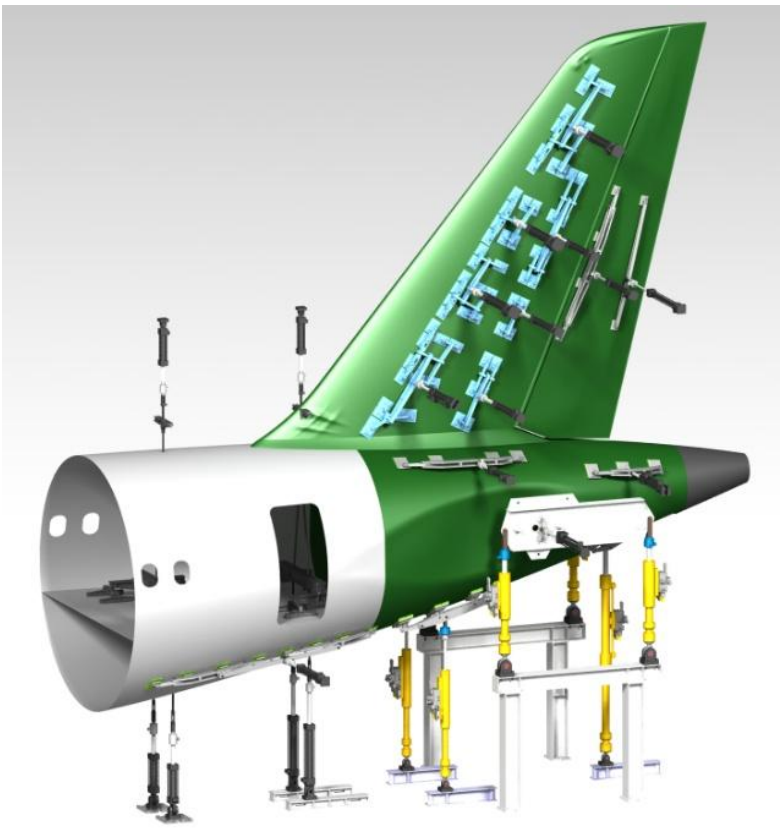

Figure 144: Schematic diagram of loading point layout

10 Airworthiness considerations

10.1 Thermal impact of metal-composite hybrid structure[51]

Due to the discrepancy in thermal expansion coefficient, the analytical strategies in fatigue and damage tolerance are distinguished with static strength analysis with metal-compound hybrid structures under temperature variation. Therefore, it is necessary to carry out a comprehensive study on this characteristic, in order to establish the static, fatigue and damage tolerance thermal evaluation methods, develop the corresponding analysis tool, and establish the airworthiness validation approach for the above method. To valide the compliance of CCAR25.571, if the traditional test verification method were continued to be used, it would lead to low efficiency and high cost during the aircraft development, and it would not be not universally applicable. The high proportion of composite materials applied in the new generation of civil aircraft implies a large number of metal-composite hybrid structures. This section gives the outlines of the strength analysis method of metal-composite hybrid structures under the influence of temperature, as well as the corresponding approach of airworthiness compliance validation.

Consideration of global stress introduced by temperature

Global temperature stress refers to the change of structural remote stress due to temperature variation. According to the most current analysis methods, the global stress caused by temperature can be regarded as part of the 1G stress in a certain service case. The verification of global temperature stress is currently one of the most difficulties in airworthiness compliance. Two temperature stress verification methods and approaches are given below.

Component-level global temperature stress test verification in a climatic chamber: The temperature test in a climatic chamber is limited by factors such as the size of the chamber, and is generally suitable for component, element and coupon tests. In the previous experience of such testing, the principle of linear superposition under the simultaneous action of temperature and mechanical load is verified. The test results manifest that for strain results from GFEM simulation are more conservative than those from temperature test.

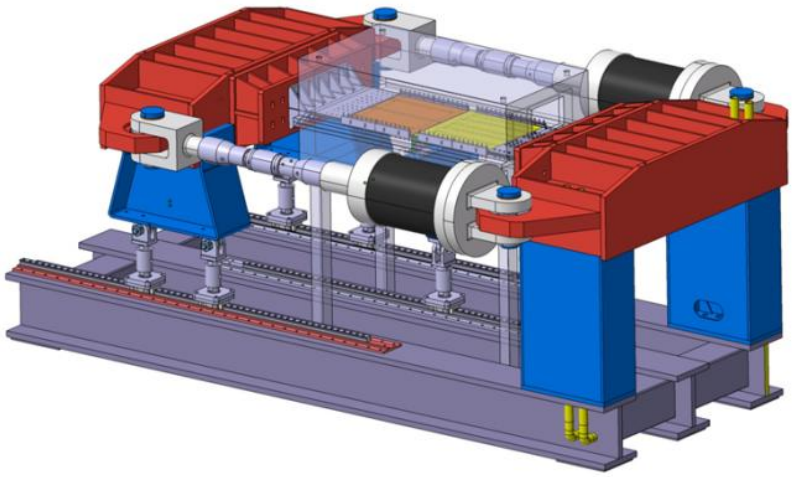

[51] Shanghai Aircraft Design and Research Institute, Li Xianchao, lixianchao@comac.cc

Figure 145: Schematic diagram of a thermo-mechanical test at various temperature in a climatic chamber

Electric blankets were applied to generate thermal field in the concerned areas in large-scale test specimens. It is worth noting that the accuracy of strain gauges depends very much on temperature compensation in a thermo-mechanical test. Therefore, it is necessary to arrange temperature compensation tests for different materials. Due to the influence of assembly clearance and other undesirable factors in large-scale specimens, and also because of low strain varition caused by temperature, the experimental procedure should be adjusted by firstly applying mechanical load, and then applying thermal load to improve the accuracy when analyzing the influence of temperature.

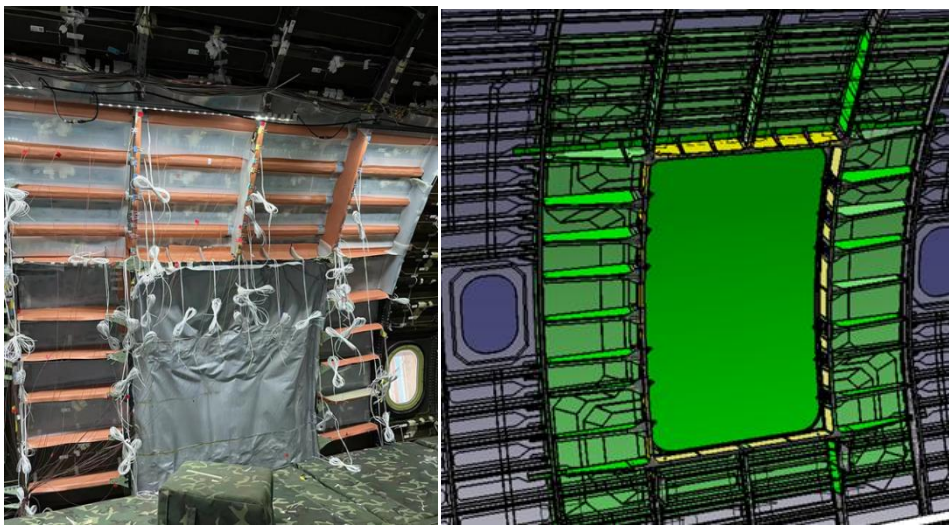

Figure 146: Electric blankets applied to entry door and its surrounding structures

Consideration of Local Stress Introduced by Temperature

For the hybrid joints, there is also a self-balancing load transmission through fasteners between metal and composite materials due to the different thermal expansion coefficients, and the additional working stress between the joints is induced by the load from fasteners.

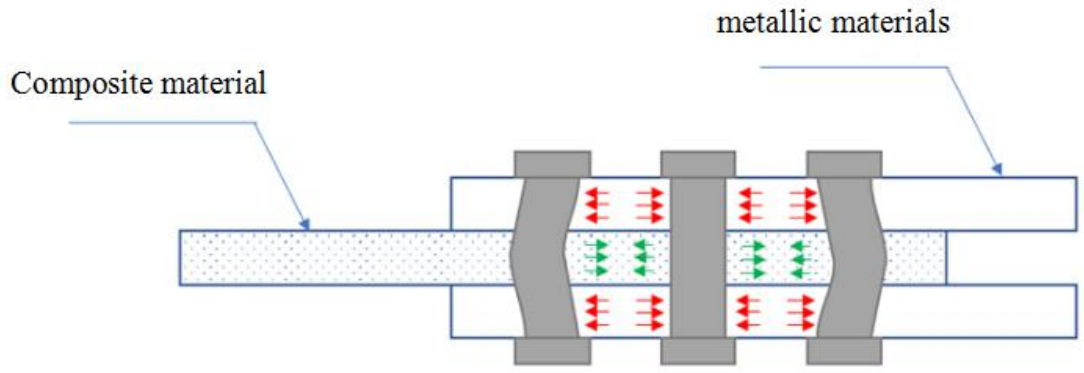

Figure 147: Test piece for docking zone between wing and fuselage

For this case, the thermal load is still a steady-state load. But it is necessary to combine the current fatigue analysis method, convert the hole edge stress concentration caused by the local fastener load transimission to remote stress field, and consider it together with the global temperature stress and mechanical stress. The advantage of this is that it does not need to alter the calculation procedures of

the original method.

The Airworthiness Validation for Wide-spread Fatigue Damage (WFD) Hybrid Structures

Regarding WFD, CCAR25.571(b) states that "Special consideration for widespread fatigue damage must be included where the design is such that this type of damage could occur. This demonstration must be by full-scale fatigue test evidence. The type certificate may be issued prior to completion of full-scale fatigue testing." Therefore, the WFD sensitive details in the hybrid structure must be verified by full-scale fatigue test. At the same time, according to the requirements of CCAR25.571(a), the adverse effects of temperature atmosphere must also be considered. It is time-cosuming and extremely difficult to carry out thermal cyclic loading on whether full-scale fatigue specimen or even component-levell fatigue test specimens in a climatic chamber. In this condition, the temperature cyclic stress can only be converted into equivalent mechanical stress, which is applied to the full-scale specimen. However, as evidence of airworthiness compliance, low-level experimental verification of the equivalent mechanical stress coefficients is still required. The verification approach is shown in Figure 148.

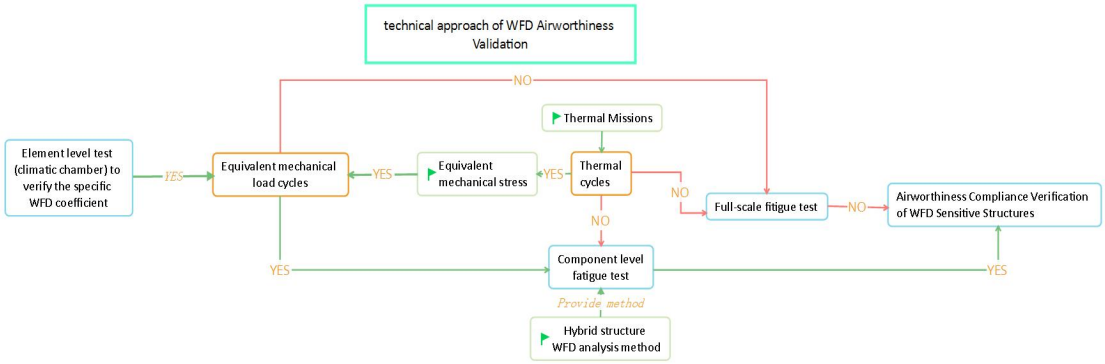

Figure 148: The technical approach of WFD Airworthiness Validation

10.2 Fatigue and damage tolerance substantiation for ac352 rotorcraft airworthiness certification[52]

The rotorcraft structure is under the influence of vibration and coupling environment caused by the continually rotating blades in unsymmetrical field, and the dynamic components of the rotorcraft as well as the adjacent fuselage structure is subject to cyclic stresses in every flight. The fatigue and damage tolerance substantiation of AC352 rotorcraft structure under CCAR-29R2 29.571&29.573 is mandatory to establish the retirement time and/or inspection interval which are specified in the Airworthiness Limitation Section for the safety of the transport category rotorcraft and to avoid catastrophic failure during the operational life.

Load and stress spectrum

The load and stress spectrum as severe as expected in operations is essential process for fatigue substantiation. The load and stress raw data for each component is measured during GIR flight test campaign, and the load cycle analysis is performed with rain-flow counting method. When the load cycle is ranged by enormous series, the fatigue load spectrum fatigue limit-life graph can be further

[52] China Helicopter Research and Development Institute, Wu Yanxia, wuyx74@avic.com

obtained by supplementing the material performance (the fatigue S-N curve), and make it easier to define service life. The safe fatigue curve (S-N curve) of the component is drawn based on structure fatigue test results (or the material performance) as well as load safety factor, and demonstrates the allowable number cycles to applied load. On the damage cumulative Miner rule, the service life or the retirement time can be calculated according to the number of cycle attach to the flight spectrum vs allowable cycle, or deduced from the fatigue load spectrum limit-life graph with safe fatigue limit.

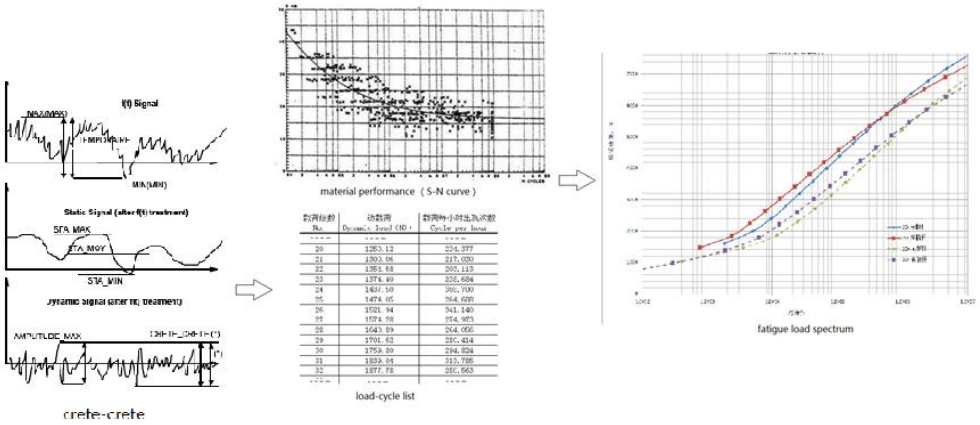

Figure 149: Load and stress spectrum

Retirement life and inspection interval

For metallic structure of AC352, the retirement life establishment is based on the fatigue curve due to as-manufactured full scale component test and the load spectrum measured. In general, 3-4 full scale component tests are performed for fatigue limit. In addition, the inspection interval is required to accommodate damage by manufacturing, maintenance, and in service, including corrosion, accidental damage, or manufacturing/maintenance flaws. The S-N curve with flaw tolerance can be deduced from full scale test of the metallic structure with the flaw. The typical flaw types including corrosion, scratch, impact as well as crack of multiple load paths are generally considered for inspection interval establishment. For AC352 metallic structure test parts, the critical areas of the component are subjected to cumulative scratch & impact and/or corrosion, and complete loosen the tightening torque on all bolts or remove the most critical bolt(s) during assembling the test. If necessary, bird strike and lighting should be substantiated for the safety of the transport category rotorcraft.

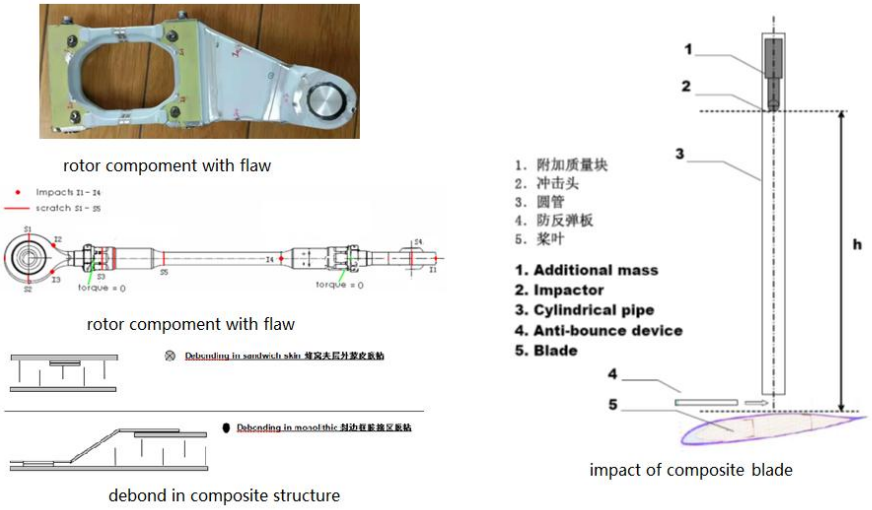

Figure 150: Component with flaw

For the retirement life of AC352, it is mandatory for the composite structure to consider environmental effects, allowable damage that may go undetected and allowable manufacturing defects including intrinsic flaws (e.g., small delamination, porosity) and BVID impact that may occur during manufacture, service or maintenance. The environmental effects including ageing, temperature and humidity can be considered in two different ways. Effect of both temperature and ageing can be assumed by the use of coefficients deduced from comparison tests on samples representative, or considered directly through full scale tests with moisture and mean temperature. Composite structure damage such as visible impact damage on blades and tailboom that can be reliably detected by scheduled or directed field inspections is performed at specified intervals, and the residual strength retained for the inspection intervals should be sufficiently above limit load.

10.3 Airworthiness research for hydrodynamic stability characteristics of amphibious aircraft[53]

In the requirements determination phase of an aircraft's airworthiness validation, it is necessary to determine the basis of validation of the aircraft, i.e. to determine its applicable airworthiness requirements. The major operational difference between amphibious aircraft and land-based aircraft is the surface take-off and landing. Amphibious aircraft in the water surface takeoff process and on the ground runway takeoff process has completely different characteristics, the aircraft in the water surface takeoff by hydrodynamic, aerodynamic and static buoyancy together, and these three forces and moments with the change of flight speed will be drastic changes, at the same time, the aircraft in the process of flexible water surface takeoff, prone to the influence of waves and wind to occur in the longitudinal swing, especially in the more severe water surface environment takeoff, the In order to reduce the aircraft bumps on the water surface, the aircraft is required to leave the water as soon as possible. In view of the surface operation characteristics of amphibious aircraft, it is necessary to assess the safety impacts of the special operating environment such as waves and splashes on the surface of the water, and it is also necessary to consider the development of special safety requirements for surface takeoff/landing performance, maneuvering characteristics and other characteristics that are

[53] General Huanan Aircraft Industry Co., Ltd, Xie Weiwei, xieww008@avic.com

different from those of land takeoffs.

Model Tests and Flight Tests

Model test refers to the towing test of a scaled-down model in a high-speed pool to simulate the hydrodynamic and aerodynamic characteristics of an amphibious aircraft subjected to the process of taxiing and takeoff and landing on water, to study and analyze the water surface takeoff and landing characteristics and water surface splash characteristics of the aircraft. Currently, for the requirements of 25.231(b) water surface stability boundary, 25.239(a) water surface splash characteristics, etc., considering the risk of test flight and the need for verification of special test conditions, the way of modeling test in the laboratory, i.e., the MC4 method, may be considered for conducting or assisting in conducting the conformity compliance demonstration. However, the prerequisite is to determine the similarity criterion, fully analyze and illustrate the influence of model scale effects, and ensure that the model test conclusions can represent the real aircraft test characteristics.

The splash level of the model was analyzed based on the video recordings of the model splash at the propeller and flaps at different test conditions (including the test speeds corresponding to different weight and center of gravity). The degree of sputtering can be categorized into three types: no sputtering, mild sputtering, and severe sputtering. In general, no splash corresponds to hardly any splash impacting the part, mild splash corresponds to occasional or small amounts of splash impacting the part, and severe splash corresponds to splash impacting the part severely.

Figure 151: Full aircraft model splash test

Due to the complexity of the real-world operating environment for amphibious aircraft, it is difficult for laboratories to simulate the real-world operating environment (other than calm water), and the splash pattern obtained from hydrodynamic model testing is different from the actual situation, model testing alone may not be able to fully satisfy the requirements for compliance verification of the splash characteristics of amphibious aircraft under CCAR 25.239. FAA Advisory Circular AC25-7C recommends a method for verifying compliance with the splash characteristics of FAR 25.239: Verification of the splash characteristics of amphibious airplanes should be accomplished by flight testing of the actual airplane, not by analysis or model testing. Hydrodynamic modeling can be used to identify problems, but is not a substitute for actual flight testing. However, validation can be done through a combination of MOC4 and MOC6 tests.

Figure 152: Splash characteristics (take-off)

During the acceleration of surface takeoff, there is no main hull splash water impacting the wings and flaps, and the actual accelerated taxiing results are in good agreement with the main splash characteristics of the model test results. With the increase of speed, the main hull splash position gradually moves backward, and the splash characteristics are further improved.

10.4 Rapid assessment of ALI projects for derivative models to airworthiness[54]

The upgrading or improvement of aircraft models is quite common. Generally, new models are derived by lengthening or shortening the fuselage, replacing with more advanced engines, and other modifications. In order to make full use of the airworthiness certification basis of existing models and efficiently evaluate the impact of new changes brought by derivative models on ALI (Airworthiness Limitations Items) airworthiness, the rapid assessment of ALI projects for derivative model to airworthiness has emerged. The key to this process is the development of a damage characteristics database and a rapid assessment method for damage tolerance based on changes in stress levels, which are essential for the efficient evaluation of ALI projects for airworthiness.

Damage characteristic database and rapid damage tolerance assessment method based on stress changes

The geometric parameters, stress calculation formulas, load spectra, crack extension data, inspection requirements and other relevant data from the crack propagation analysis of ALI projects for the certification model are centrally managed to establish a damage characteristic database. Using the load spectrum and fatigue internal force solution of the derivative model, the stress level of ALI projects for derivative model are calculated based on the parameters from the damage characteristic database. The damage ratio between the derivative model and the certified model is then determined by comparing

[54] Shanghai Aircraft Design and Research Institute, Li Xianchao, lixianchao@comac.cc

the stress changes. This allows for a rapid determination of the damage tolerance for the derivative model, thereby completing the airworthiness evaluation of ALI projects.

Application of rapid assessment of ALI projects for derivative models to airworthiness

Take, for example, the cracks in the fastener nail holes on the inner edge of the PSE structural reinforcement frame in the docking area of a civil aircraft, as illustrated in the figure below.

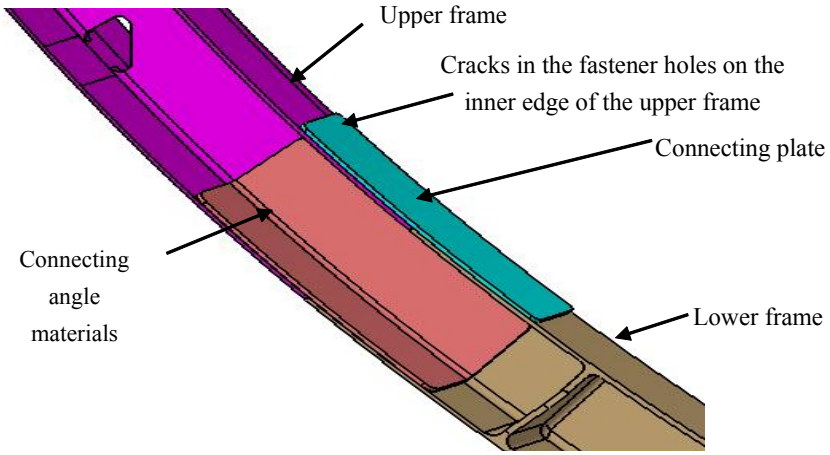

Figure 153: Crack in the fastener nail holes on the inner edge of the reinforcement frame in the docking area of a civil aircraft

During the ALI formulation process of the certified model, the strength engineer conducted crack propagation analysis on the cracks at the edge of the fastener hole, focusing on the inner edge of the frame. This analysis was based on the structural geometric parameters, materials, stress calculation methods and load spectrum of the reinforcement frame in the docking area. From this, inspection requirements were established and incorporated into the ALI for airworthiness. The structural geometric parameters, materials, stress calculation methods and crack propagation data used during the certification phase were then collected to form a damage characteristics database.

On the basis of the airworthiness of the certification model, the ALI project for the derivative model is formulated using the analysis methods from the damage characteristic database. The stress for the details of the derivative model's reinforcement frame are calculated, and the damage ratio between the derivative and certification models is determined based on changes in stress levels. A decision is then made to either maintain the inspection requirements from the certification model or adjust them accordingly. This process leads to a damage tolerance conclusion for the ALI project of the derivative model, confirming its airworthiness compliance.

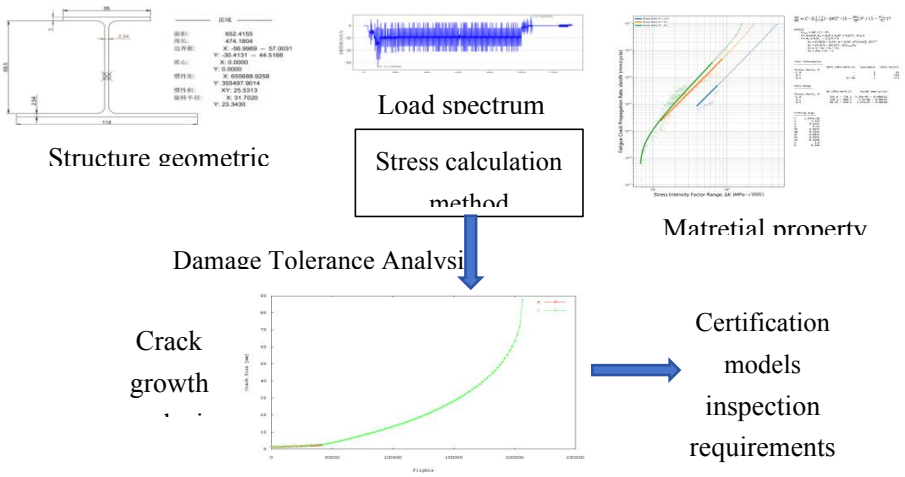

Figure 154: Establishment of damage characteristics database of certification aircraft models

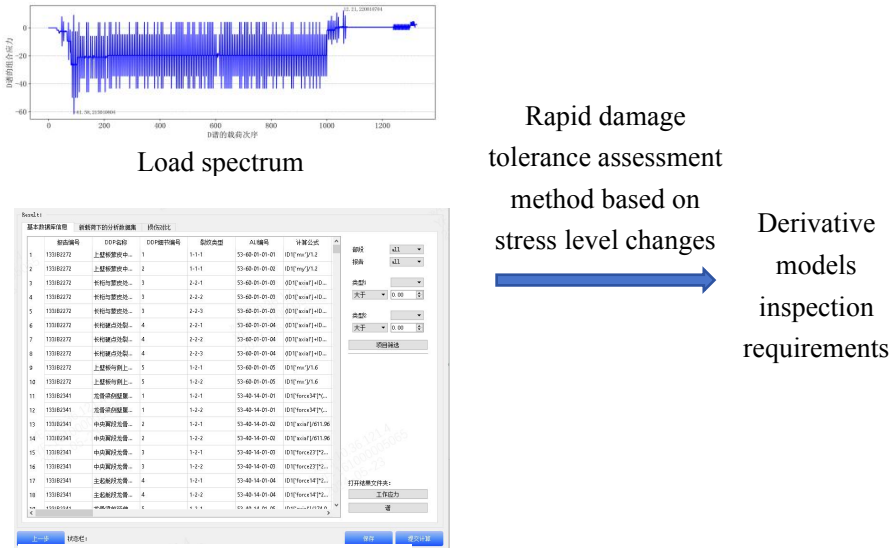

Figure 155: Rapid damage tolerance assessment based on stress level changes

11 Digital Engineering in aeronautical fatigue and structural integrity

11.1 Digital twin-based stress and fatigue tracking of aircraft structures based[55]

Tracking stress and fatigue evolution in aeronautical structures is of significant importance for achieving life-cycle management and ensuring flight safety. Many aircraft, such as general aviation aircraft and small unmanned aerial vehicles (UAVs) often lack onboard health monitoring equipment, making it difficult to monitor the structural damage states of critical components in real time. To track and assess the structural health of such aircraft, it is essential to effectively integrate available models and limited data to construct the airframe digital twin, enabling the online tracking and prediction of

[55] Beihang university, Dong Leiting, ltdong@buaa.edu.cn

structural loads and damage evolution with available flight data.

Airframe digital twin technology through the integration of model and data

The realization of airframe digital twin requires integrating structural, aerodynamic, and damage evolution models with operational and maintenance data, as illustrated in Figure 156. First, an aerodynamic model is employed to determine aerodynamic loads, and a multi-level structural model is used to analysis load transmission and obtain local stress distribution. The damage evolution model is then incorporated to assess structural health. Next, utilizing reduced-order modeling and surrogate modeling techniques, the integration of multi-disciplinary models is achieved while enhancing computational efficiency. Finally, a dynamic Bayesian network is used to fuse limited operational and maintenance data, enabling probabilistic assessment and prediction of structural health, thereby realizing the airframe digital twin.

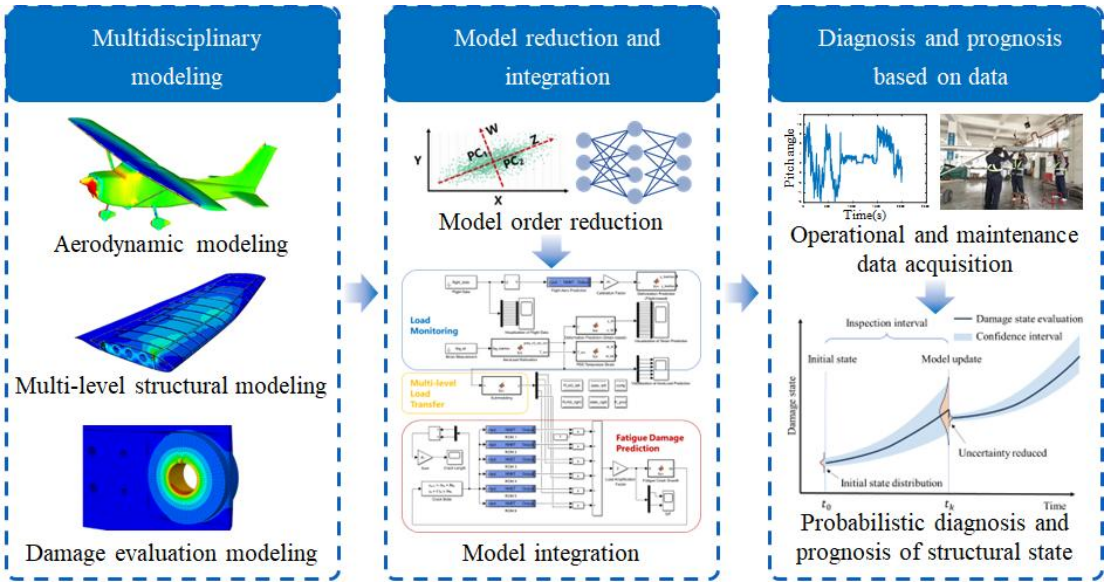

Figure 156: Airframe digital twin architecture

Structural health state evaluation of Cessna 172

In collaboration with the Civil Aviation Flight University of China and the Civil Aviation University of China, the aforementioned technology is applied to the Cessna 172, as illustrated in Figure 157. By leveraging multidisciplinary model simulation and analysis, this study addresses the challenge of structural health monitoring by overcoming the difficulty of installing relevant sensor equipment on general aviation aircraft. Additionally, aircraft inspection data are utilized to correct potential model biases in the multidisciplinary simulation, enabling a more reasonable diagnosis of structural damage through the coupling of data and physical mechanisms. This technology facilitates the development and implementation of digital platforms and risk analysis tools, which can assist users in inspection and maintenance while also supporting regulatory authorities in continuing airworthiness management. Currently, preliminary research has been conducted on this project, which is expected to improve the safety and continued airworthiness of the existing general aviation fleet.

Figure 157: Structural health management of Cessna 172 through the coupling of data and model

Airframe digital twin of an UAV

In collaboration with the Polytechnic University of Milan, the application of the aforementioned structural digital twin technology is demonstrated using an UAV with a 3.2-meter wingspan, as illustrated in xx. This study makes full use of flight test data, including flight parameters and limited strain measurements, along with multidisciplinary simulation models encompassing aerodynamics, structures, and fatigue. By conducting research on flight load tracking based on measured data and reduced-order simulations, fatigue crack growth modeling and prediction considering multi-level load transmission, as well as probabilistic diagnosis and prognosis of structural cracks, a digital twin of this UAV is constructed. Additionally, an UAV airframe digital twin system has been developed to achieve seamless integration and demonstration of the aforementioned technologies.

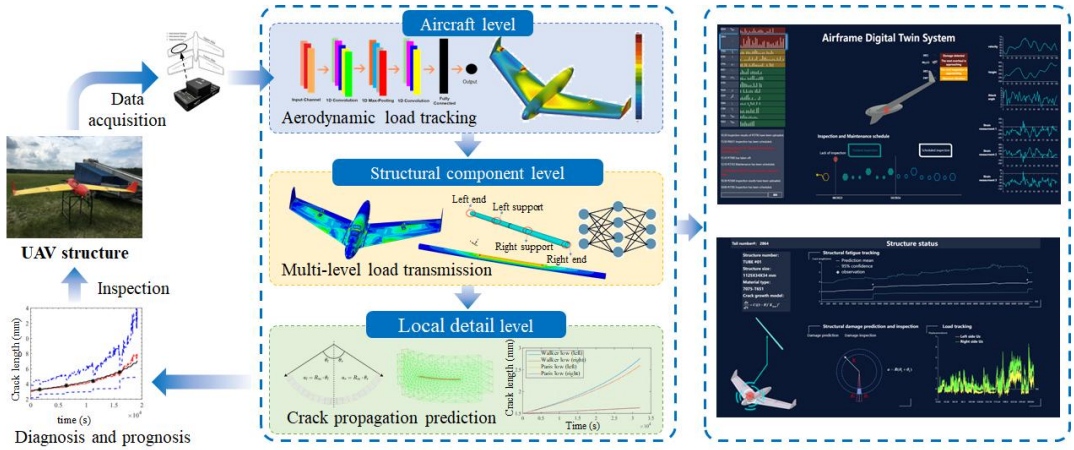

Figure 158: Airframe digital twin of an UAV

11.2 Neural network model fusing real data and virtual data for wing strain-load relationship[56]

When establishing a strain-load relationship model for aircraft structures, data obtained by ground calibration tests (stated as "real" data) and FE simulations (stated as "virtual" data) show different advantages and disadvantages. The "real" data show high accuracy but are trapped with narrow

[56] Beihang University, Bao Rui (rbao@buaa.edu.cn), Lu Songsong (11523@buaa.edu.cn), Li Chenxi (18375178@buaa.edu.cn)

application scope due to limited test ranges. The "virtual" data obtained via FE simulations cover a wide range of loading cases but are trapped with low accuracy. This leads to difficulties in achieving win-win situation of accuracy and application scope based on either “real” or “virtual” data. To solve this problem, a multi-level neural network model fusing “real” and “virtual” data was put forward, called compensation-based model. Sub-learners were embedded into the compensation-based model to measure this model's cognitive degree. The validation work of this model indicated that the model not only shows high accuracy and wide application scope, but also can effectively identify loading cases with poor cognitive degree.

Compensation-based Neural Network Model

The developed compensation-based neural network model is composed by prediction module and fusion module, see Figure 159. The prediction module is trained by a large number of "virtual" data and can give the low-fidelity prediction of loads parameters vector $\tilde{y}$ for structure’s strain vector x in wide application scope. The fusion module is a compensation module, which uses small amount of “real” data to calibrate prediction results of prediction module. The input vector of this fusion module is a new vector assembled by x and $\tilde{y}$, while the output vector of this module is the high accuracy prediction results of load parameters.

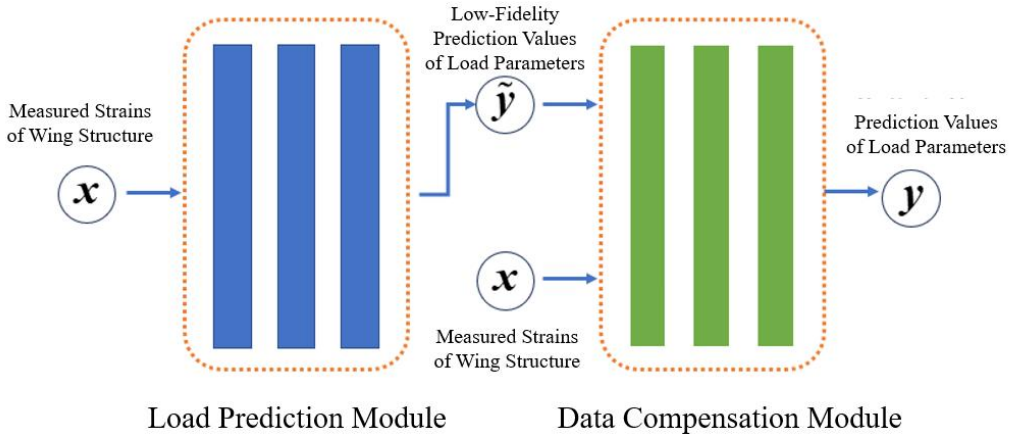

Figure 159: Compensation-based neural network architecture

Embedded Sub-learners to Represent Cognitive Degree of Predictions

Real data for some loading cases weren’t measured in ground calibration tests and therefore weren’t fused into the compensation-based neural network model. This leads to the low cognitive degree of model for some loading cases and thus resulting in significant prediction bias. In this research, variance of different neural network models trained with the same training set data is found to be an effectively way to recognize these cases. Based on this finding, a model cognitive degree recognition method was developed. It should be noted that an improved compensation-based neural network model embedded with several embedded sub-learners was developed in this research (see Figure 160). This model can easily provide multiple predicted results by multiple sub-learners, making it convenient to obtain enough data to ensure the requirement of variance calculation.

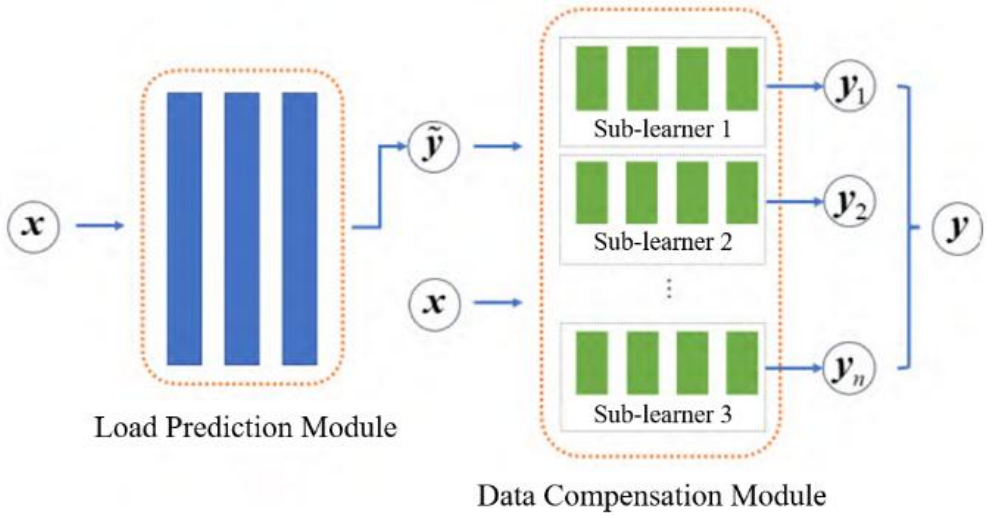

Figure 160: Model with embedded sub-learners

Verification and Analysis Based on Tests of a Scaled Wing

To verify above compensation-based neural network model, "virtual" data and "real" data for a scaled-down wing was obtained by conducting FE simulation on FE model shown in Figure 161(a) and ground calibration tests schematically shown in Figure 161(b). 50% of obtained data was used to train the compensation-based neural network model, other data were used to test the model.

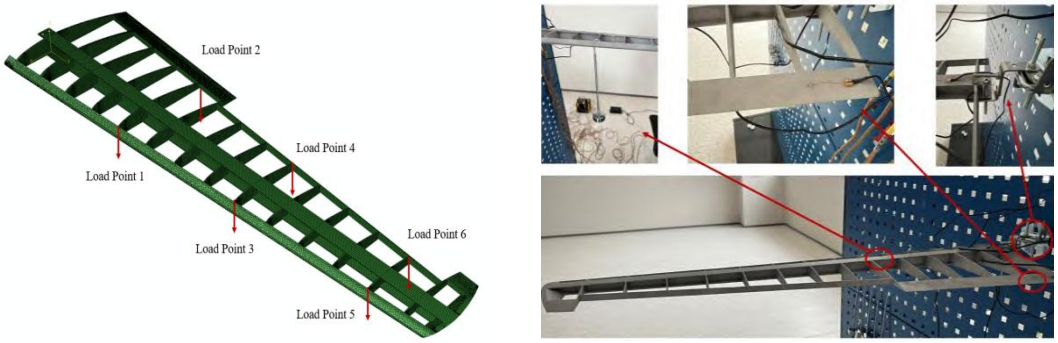

(a) (b)

Figure 161: (a) Finite element model and (b) calibration experiment of the scaled-down wing (additive manufactured by aluminum alloy)

The prediction results are shown in Figure 162(a) and compared with results predicted by non-fusion neural network trained by “real” data. It can be seen that the number of prediction cases with high accuracy increases and accuracy of most prediction cases are improved. This indicates the superiority of the developed compensation-based neural network model. The prediction error for torque and the corresponding prediction variances are also shown (see Figure 162(b) and (c)). The consistency between prediction error and variances can be found, verifying the efficiency of model cognitive degree recognition method in identifying unreliable prediction results.

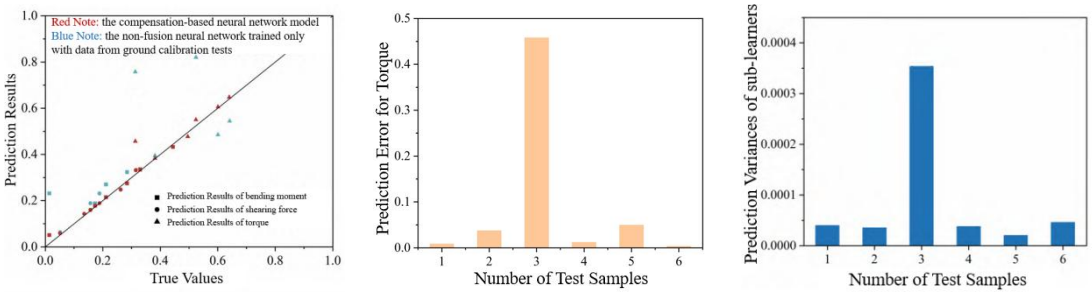

(a) (b) (c)

Figure 162 (a) Comparison between prediction results of the neural network model and real values, (b) prediction error for torque and (c) prediction variances of sub-learners

11.3 Research on digital twin model of aircraft structure based on machine learning[57]

In both static and fatigue tests of aircraft, the simulation data captures the full-field strain response, while the physical test data provides accurate strain data at specific points. However, the lack of an integrated method of simulation and physical data makes it difficult to obtain real-time and accurate full-field strain response of aircraft structure. Machine learning models possess the capability to integrate diverse types of data and to quickly modify the model with small amounts of data. When machine learning is used to obtain real-time strain field, training the strain distribution proxy model based on simulation data and quickly reconstructing the exact strain field based on real-time physical test data are two key techniques for constructing the twin model of aircraft structure.

Key technology

Constructing the digital twin model of aircraft structure based on machine learning is divided into two stages: 1. Before the test, through the simulation data, the testers built the strain machine learning model of the full-field aircraft structure. 2. In the test, the digital twin residual model is trained by real-time and accurate small sample strain data. The two models can characterize the relationship between spatial position, loading step, load case and physical strain field. For complex aircraft structures, researchers need to divide complex structures according to the principle of strain continuity, and then construct proxy models independently.

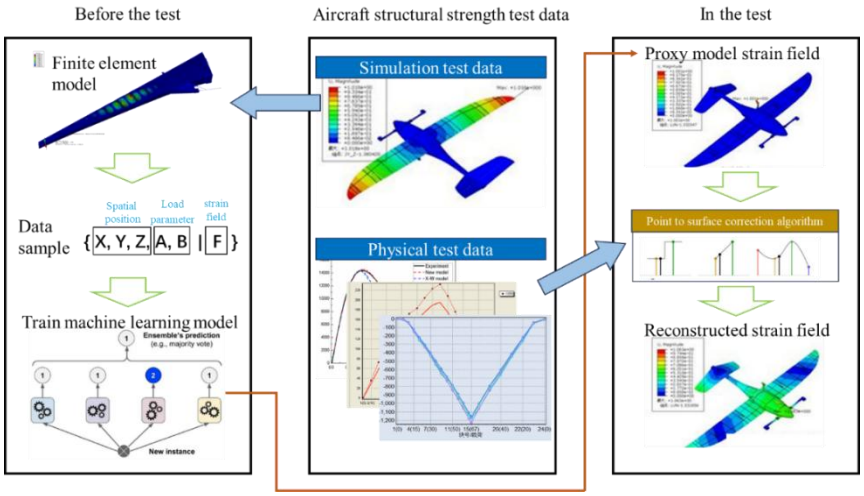

Figure 163: The two stages of constructing the digital model

[57] Aircraft Strength Research Institute, Duan Feng, duanf003@avic.com

Application of technology

With the development of virtual strength test, there is an increasing demand for real-time 3D visualization of aircraft strain in strength test field. The digital twin model based on machine learning not only has the ability to integrate simulation data and test data, but also helps to improve the efficiency of 3D test visualization.

First, the digital twin model can be applied to the lightweight display of aircraft structures. The more detailed the grid model is, the more clearly the strain distribution can be reflected, but the higher the display hardware requirements are. To ensure the real-time and accurate data of the physical test, the display model should be lightweight and efficient, and can respond to the test data in real time. The twin proxy model can be a bridge from the complex finite element model to the lightweight display model. Through complex simulation data, the proxy model clearly represents the mapping relationship between the spatial position and the strain value, and then the lightweight display model can quickly obtain the strain value just by the coordinates of the display element, so that the strain field cloud map can be efficiently drawn.

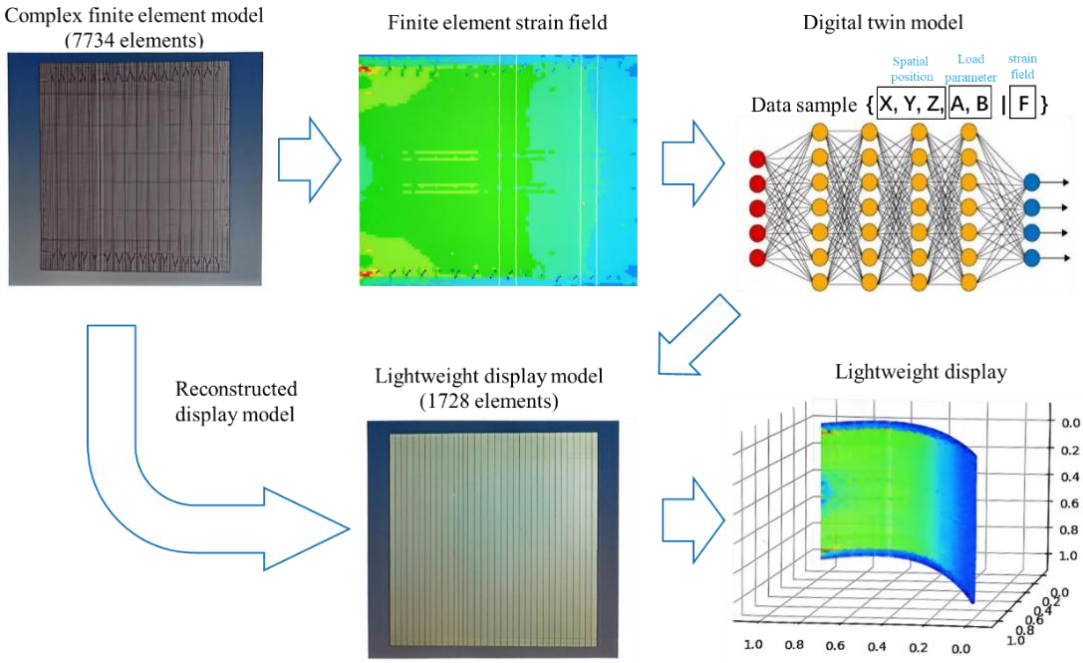

Figure 164: Twin model lightweight application case of typical panel structure

Secondly, this method effectively combines simulation data and physical test data, which is helpful for the testers to more intuitively and conveniently view the test data and analyze the strain distribution of the aircraft structure. The twin residual model records the gap between the simulation data and the test data, which is easier to evaluate the consistency of the strength test.

In summary, the digital twin model of aircraft structure has important engineering significance for making the decision of physical test.

11.4 Visual measurement method for dynamic pose of landing gear[58]

The measurement coordinate system is the benchmark for determining pose information. Accurately establishing the measurement coordinate system on the testing site has always been a major difficulty in visual measurement, especially for irregular measurement objects, it is difficult to determine a suitable measurement benchmark. This article adopts a combination of virtual and real methods to establish a measurement coordinate system on a virtual CAD digital model. By arranging key points on the surface of the landing gear physical model, the virtual digital model is registered with the coordinate system of the physical model, thereby achieving the consistency of the measurement coordinate system by aligning the coordinate system of the physical model with the virtual CAD digital model coordinate system.

Key point 3D coordinate photogrammetry reconstruction

To achieve the unity of the physical model coordinate system and the virtual CAD digital model coordinate system (i.e. measurement coordinate system), a close-range photogrammetry system is first used to reconstruct the three-dimensional coordinates of the key points arranged on the surface of the landing gear physical model. The software and hardware configuration of the close-range photogrammetry system used is shown in Figure 165. The system hardware includes Nikon D610 DSLR digital camera, circular coded markers, circular non coded markers, and scale bar. The system software can run on the Windows platform and includes functions such as calculation mode, deformation mode, and comparison mode.

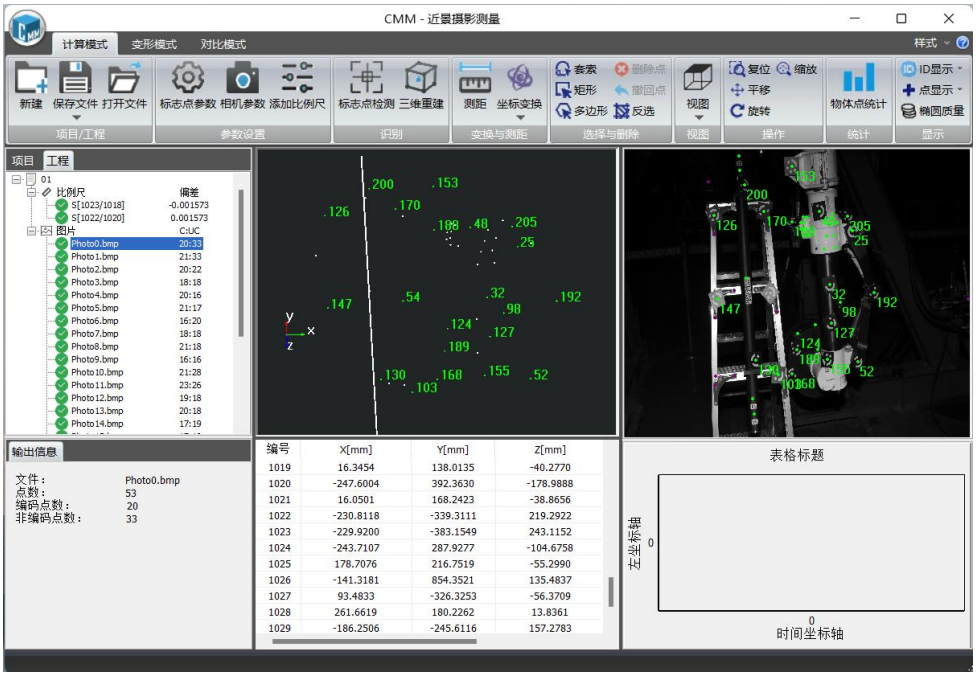

Figure 165: Close range photogrammetric system software

Dynamic pose measurement experiment of landing gear

At the testing site of a certain type of landing gear, dynamic pose measurement experiments were conducted. The acquisition and reconstruction frame rate of binocular stereo vision is 50Hz, and the

[58] Aircraft Strength Research Institute, Zhang Wendong, zhangwd003@avic.com

measured field of view size is 1.6 meters by 1.1 meters. Figure 166 shows the three-dimensional pose during the synchronous motion of the landing gear virtual and real models at different times. Figure 166 (a) shows the motion trajectory of a monitoring point on the landing gear, while Figure 166 (b) shows the variation of the attitude angle of that point over time.

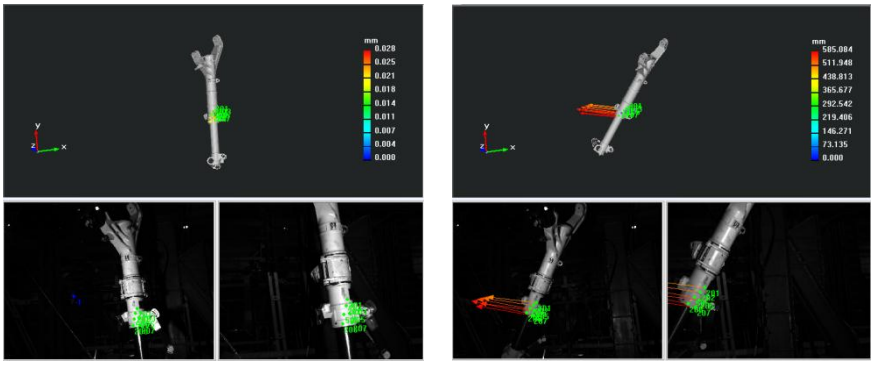

(a) t=0.04s (b) t=19.68s

Figure 166: Virtual and real model poses of landing gear at different times

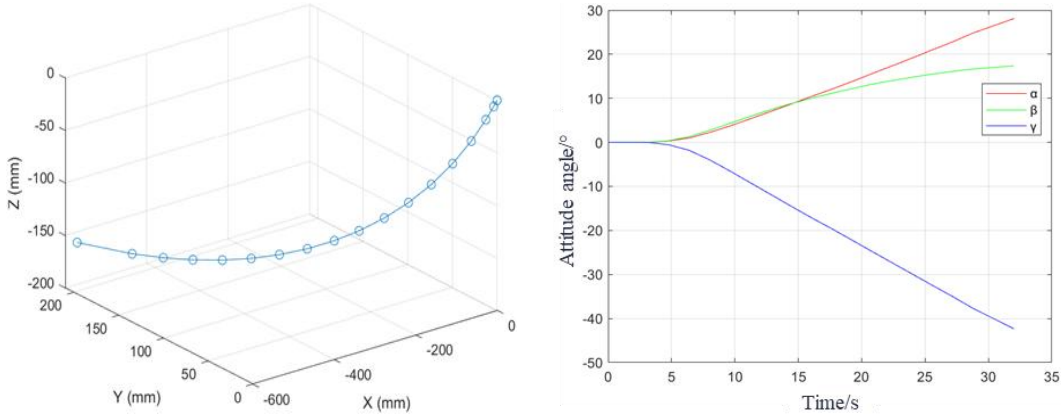

(a) (b)

Figure 167: (a) The motion trajectory of the landing gear. (b)The attitude angle of the landing gear

During the structural strength test of landing gear, the environmental conditions are usually complex, such as possible obstructions, which increases the uncertainty of the measurement process. The dynamic pose measurement method combining virtual and real elements proposed in this article only observes local areas and uses a small number of key points to drive the CAD model and the physical model to achieve synchronous motion, thereby obtaining the overall motion state and pose information. Therefore, this method is superior to traditional methods in terms of reliability, environmental adaptability, and monitoring efficiency.

11.5 Intelligent prediction technique for strength/rigidity of fusion structure based on digital twin[59]

In view of the requirement of real-time flight capability assessment and high precision life prediction of advanced aircraft, the key technologies such as multi-scale high-fidelity digital twinning simulation and digital twin drive strength/stiffness prediction are solved through multi-scale modeling techniques and

[59] Shenyang Aircraft Design & Research Institute, Liang Chen, liangc006@avic.com

large-scale stiffness prediction techniques based on large scale data. Characteristic intelligent prediction software aided tool, as the basis of application of twinning data for structural life and performance evaluation.

Key technology

Through the establishment of coverage design, manufacture and service of life cycle data management method, the key parts life evaluation model of aircraft structure driven by reduced-order model is built by the data of each stage and accurate evaluation of the health status of individual machines in the cluster and the conclusion of life consumption. At the same time, using the large data analysis and artificial intelligence technology, the conclusions of structural health assessment, structural maintenance data, training intensity, annual training plan and other constraints such as maintenance economy, fleet retention rate, etc. Establishing fleet life management model to achieve precise management of fleet life.

Application of technology

The object of the study is the docking zone between the wing and the fuselage of the fighter, which is the fatigue key part, and the multi-level model composed in this study is shown in the figure below.

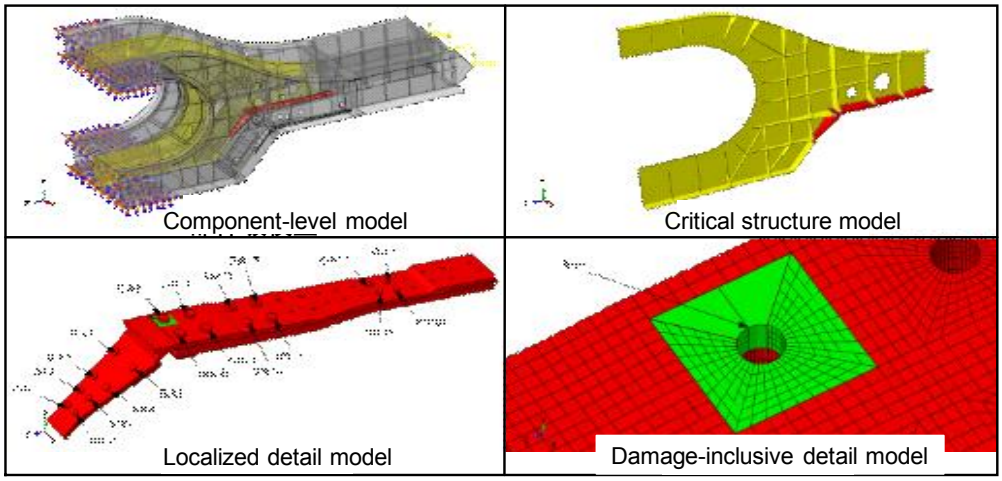

Figure 168: Multi-Level Model Diagram

For the simulation of damaged structures considering crack propagation, ZenCrack is employed. In the local detail model, full-contact solid elements are used, and the model is constructed based on the actual bolt standard information from the physical test rig. The mesh around the bolt holes was also refined. In the construction of component-level digital twin models, various bolt connection models in numerical simulation were investigated to balance computational accuracy and convergence. The end-fastener-screw contact model was adopted to approximate the simulation. The simulation results of the component-level digital twin model are shown in the Figure 169 below.

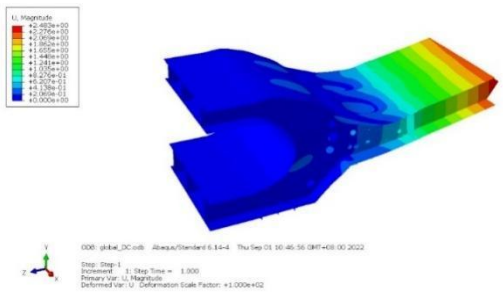

(a) Box Segment Displacement Cloud Diagram

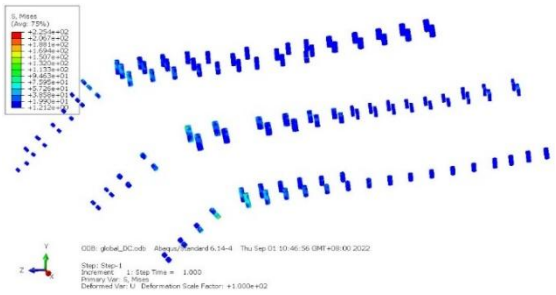

(b) Nail Load Distribution

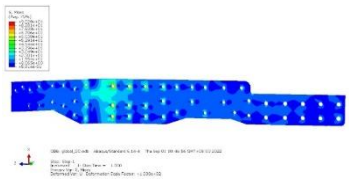

(c) 1# Frame Lower Edge Mises Stress

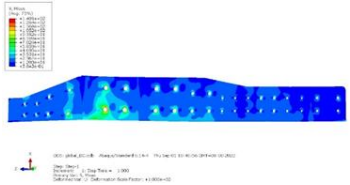

(d) 2# Frame Lower Edge Mises Stress

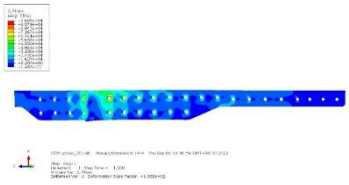

(e) 3# Frame Lower Edge Mises Stress

Figure 169: Finite Element Analysis Results of a Typical Load Cases for the Box Segment of a Wing-Body Fairing

Based on the constructed multi-scale parameterized model, combining flight parameters with load inputs, data samples for training real-time twin models are generated in batches. Multiple machine learning models, such as Dense, SVM, GBDT, and Ridge, are employed to construct multi-level strength/stiffness prediction models that predict the stress/strain at dangerous points based on flight parameter data like Mach number and altitude, followed by load data at key cross-sections.

Table 3: Comparison of the Accuracy of Stress Prediction Models

	Dense	SVM	KNN	RF	GBDT	Ridge
RMSE	0.01521	0.01204	0.01741	0.01964	0.01813	0.01157
MAE	0.00413	0.00471	0.00503	0.00442	0.00452	0.00310

11.6 An indirect stress monitoring method for aircraft critical locations based on flight data-bridge-stress model[60]

Within individual aircraft monitoring systems, two primary methods are employed to determine the stress spectrum of structural critical locations: the direct method and the indirect method. The direct method involves the installation of strain gauges at critical locations to directly measure stress or strain. In contrast, the indirect method, which is the most widely applied approach in engineering practice, involves monitoring the stress/strain of critical locations through load monitoring data in conjunction with a "load-stress" relationship model.

The traditional indirect method employs two primary models: the "flight data-structure load" model (hereinafter referred to as the "flight data - load" model) and the "structure load-stress of critical

[60] Chengdu Aircraft Design & Research Institute, Wang Qiang, wangq005@avic.com

location" equation (hereinafter referred to as the "load-stress" equation). This method presents two significant limitations. Firstly, it fails to account for the impact of load center position variations under different flight conditions on the load distribution across each station. Secondly, the stress prediction accuracy at critical locations is compromised due to the cumulative error propagation inherent in the "flight data-load" model.

In response to this context, this study proposes an innovative indirect stress monitoring technology for individual aircraft, which is based on a "flight data-strain bridge-stress of critical location" model. This approach takes advantage of the fact that the stress at critical locations exhibits a higher linear correlation with the strain bridge at the relevant station compared to the overall structural load. By leveraging this relationship, the methodology effectively mitigates the load prediction errors that would otherwise arise from the "strain bridge-load" equation. The technical framework for this approach is illustrated in Figure 170 and constitutes two primary components: the "flight data-physical bridge" model and the "physical bridge-stress" equation.

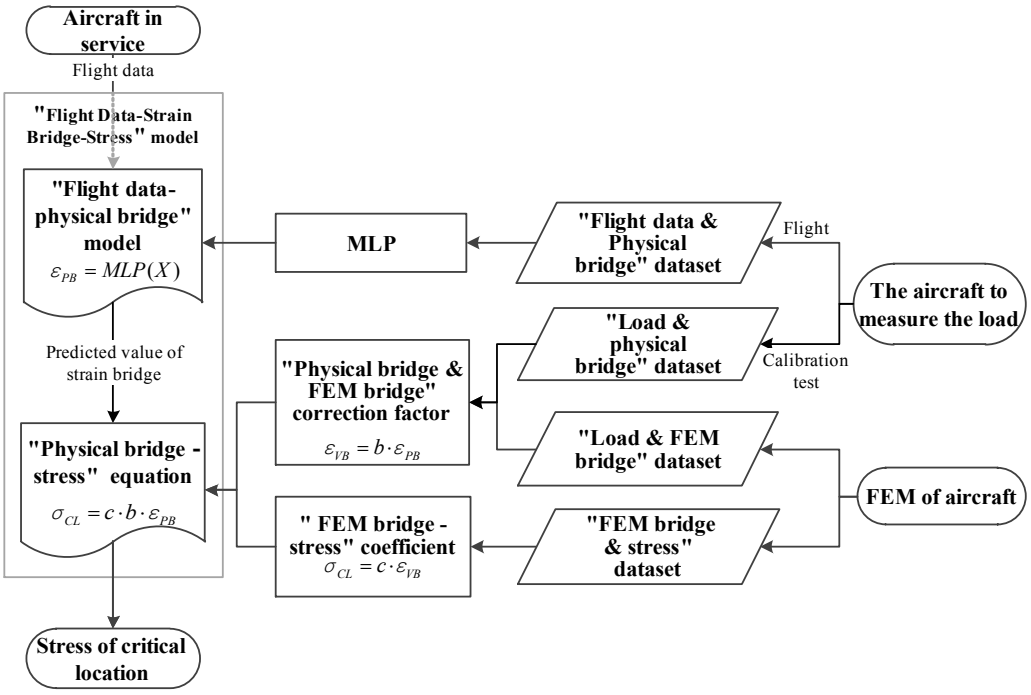

Figure 170: Technical flowchart of indirect stress monitoring for critical locations

Construction of "Flight Data-Physical Bridge" Model

Utilizing flight data closely correlated with load as input, the data processing methodology for the "flight data-physical bridge" model is implemented, as illustrated in Figure 171.

The Multi-layer Perceptron (MLP) model, as presented in Equation (1), serves as the foundation for this framework.

$$\varepsilon_{PB} = f(data_{flight}) \tag{1}$$

Where, $data_{flight}$ – means the flight data, ε_{PB} – means the value of the physical bridge on aircraft.

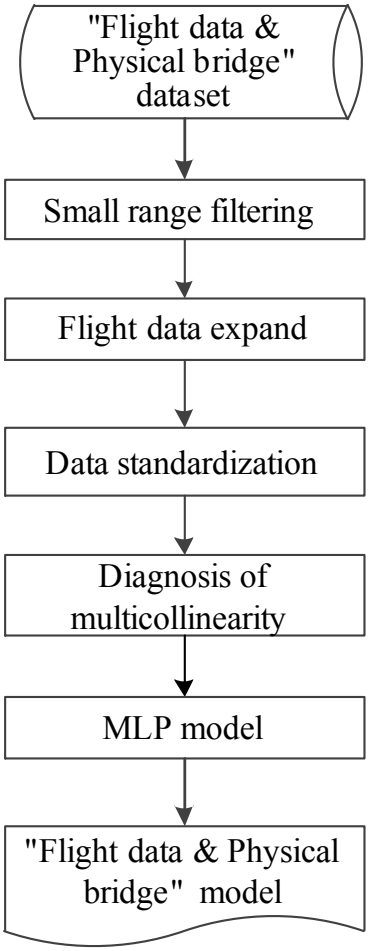

Figure 171: Flowchart of "flight data-physical bridge" model construction

Construction of "Physical Bridge-Stress" Model

Since the aircraft used for load measurement does not have strain gauges installed at critical locations, the direct mapping relationship between the physical bridge and the stress at these critical locations cannot be established. To address this limitation, this study proposes an indirect methodology for constructing a "physical bridge - stress of critical locations" model. This approach utilizes the "FEM bridge - stress of critical locations" relationship, derived from finite element method (FEM) simulations, as an intermediate bridge. The strained bridge correction factor between the virtual prototype and the measured aircraft is then determined to establish the model.

Data pairs corresponding to the FEM bridge (installed in the calibration FEM) and the physical bridge (installed in the aircraft) are obtained from FEM calculation data and physical calibration test data. Additionally, the correction factors for both the FEM bridge and the physical bridge can be derived, as expressed in Equation (2). Furthermore, the stress at critical locations and the FEM bridge values can be determined through FEM calculations, as shown in Equation (3).

$$\varepsilon_{VB} = b \cdot \varepsilon_{PB} \tag{2}$$

$$\sigma_{CL} = c \cdot \varepsilon_{VB} \tag{3}$$

Where, ε_{PB} – means the value of the physical bridge on aircraft, ε_{VB} – means the value of the virtual strain bridge in FEM of aircraft, σ_{CL} – means the stress of critical location in structure.

Therefore, the stress of critical locations can be obtained from flight data by using equation (4).

$$\sigma_{CL} = c \cdot b \cdot f(data_{flight}) \tag{4}$$

Case study

First, the flight data and physical bridge data from 145 flights of the load-measured aircraft are utilized as input. Following data processing, the MLP model is employed to establish the "flight data - physical bridge" model. The training accuracy of the model is presented in Figure 172.

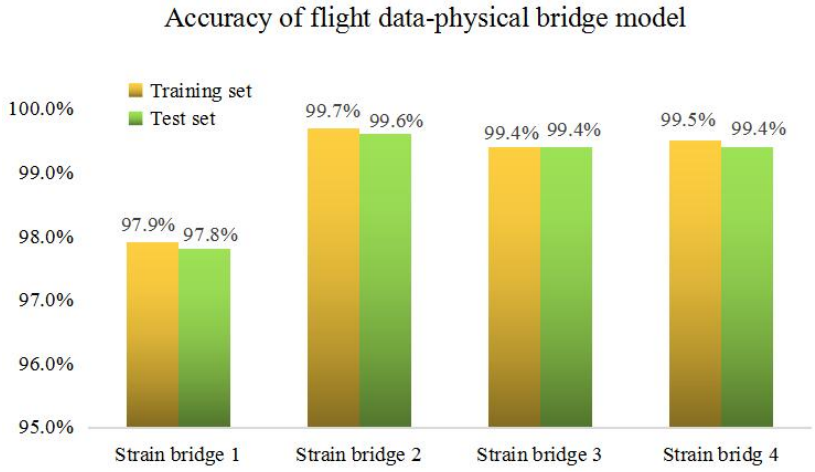

Figure 172: Accuracy of "flight data-physical bridge" model

Second, based on the FEM stress analysis of five representative fatigue load cases, the "FEM bridge-stress of critical location" equations are derived, as shown below.

$$\sigma_{CL} = 0.0658 \times \varepsilon_{VB} \tag{5}$$

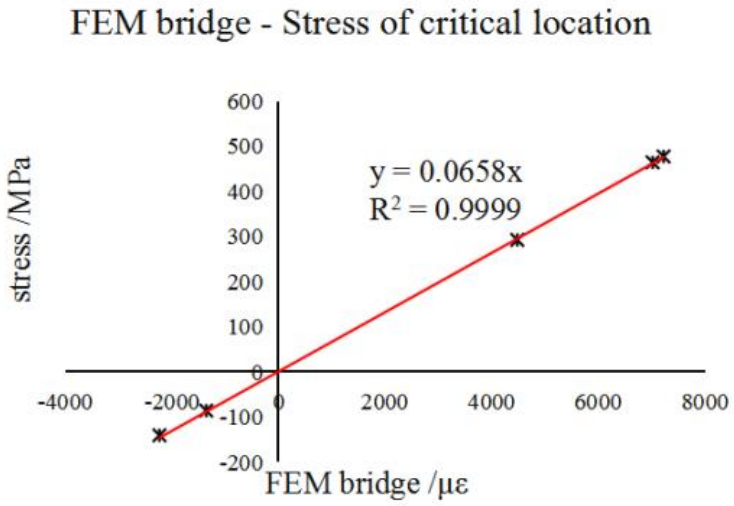

Figure 173: The linear regression of "FEM bridge - stress" model

Furthermore, the calculated FEM bridge and the physical bridge under ground calibration test conditions are paired to form datasets. Linear regression is then applied to determine the correlation between the measured aircraft physical bridge and the FEM bridge, as demonstrated below.

$$\varepsilon_{VB} = 265.79 \times \varepsilon_{PB} + 5.23 \tag{6}$$

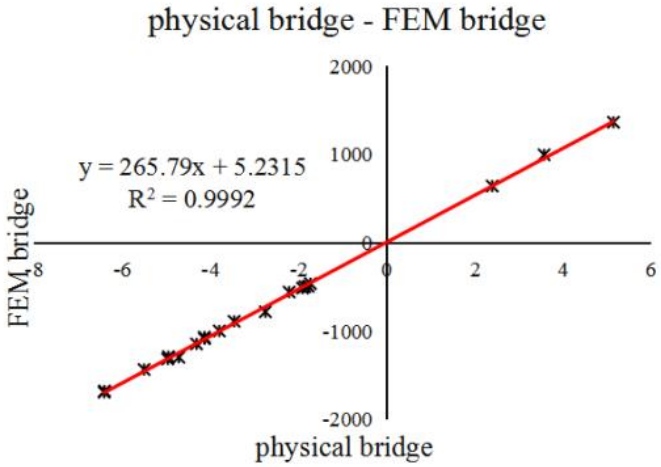

Figure 174: Linear regression of physical bridge - FEM bridge

By substituting Equation (6) into Equation (5), the "physical bridge-stress" model is established, as shown below.

$$\sigma_{CL} = 17.49 \times \varepsilon_{PB} + 0.34 \tag{7}$$

Using the full-scale fatigue test measurement data as an example, the aforementioned "physical bridge-stress" equation construction method is validated. In Figure 175(a), is the predicted strain in critical locations of Equation (7), while the abscissa in Figure 175 (b) is the predicted strain in critical locations by the "wing root bending moment-strain" equation. The ordinate is the experimentally measured strain. The results indicate that the "physical bridge-strain (stress)" equation construction method proposed in this study exhibits excellent predictive accuracy, with the linear fitting coefficient between predicted and measured strain approaching 1.0. Compared to the "wing root bending moment-strain of critical locations" equation, this method demonstrates improved accuracy for indirect stress/strain monitoring in individual aircraft.

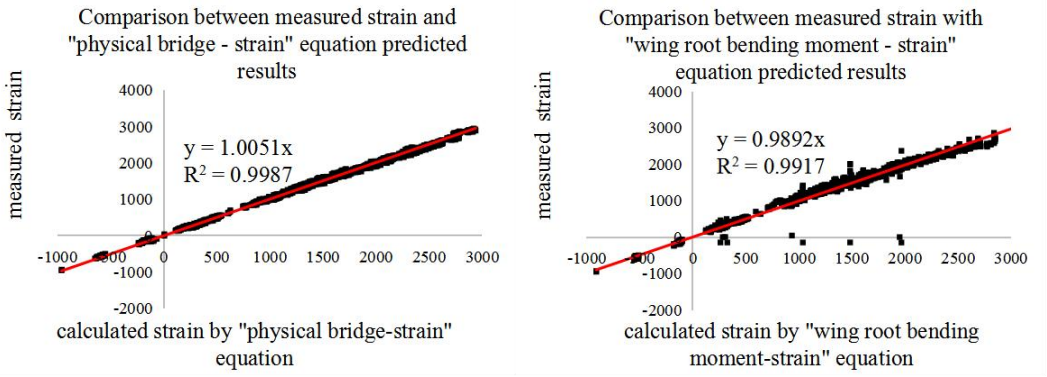

(a) (b)

Figure 175: Comparison between "wing root bending moment -strain" equation and "physical bridge -strain" equation